L-Università ta' Malta
Faculty of Engineering

MASTER OF SCIENCE IN ENGINEERING DISSERTATION

Investigation of a Surface Engineered Additively Manufactured Titanium Alloy

KELSEY ANN VELLA

Supervised by:
DR ING. ANN ZAMMIT

Co-supervised by:
PROF. ING. GLENN CASSAR
PROF. ING. JOSEPH BUHAGIAR

A dissertation submitted in partial fulfilment of the requirements for the degree of Master of Science in Engineering

by the

Faculty of Engineering

March 2024

Copyright Notice

L-Università ta' Malta

FACULTY/INSTITUTE/CENTRE/SCHOOL of Engineering

DECLARATIONS BY POSTGRADUATE STUDENTS

(a) Authenticity of Dissertation

I hereby declare that I am the legitimate author of this Dissertation and that it is my original work.

No portion of this work has been submitted in support of an application for another degree or qualification of this or any other university or institution of higher education.

I hold the University of Malta harmless against any third party claims with regard to copyright violation, breach of confidentiality, defamation and any other third party right infringement.

(b) Research Code of Practice and Ethics Review Procedures

Procedures.

Research Ethics & Data Protection form code ENG-2023-00015.

77 of the General Regulations for University Postgraduate Awards 2021, I accept that should my dissertation be awarded a Grade A, it will be made publicly available on the University of Malta Institutional Repository.

Abstract

Ti-6Al-4V is a titanium alloy widely employed for high-performance applications in the chemical, aerospace, automotive industries. This lightweight alloy offers an impressive combination of properties, featuring good fatigue performance accompanied, a high tensile strength, a low elastic modulus and excellent corrosion resistance. In recent years, there has been a significant increase in the use of additively manufactured components, driving by the advantages it offers over conventional processes. Additive manufacturing (AM) stands out for its ability to rapidly produce components, irrespective of their complexity. Additionally, AM parts are ready for use with minimal post-processing requirements. However, the AM technique also tends to promote porosity, surface roughness and tensile stresses. These factors can compromise the mechanical, corrosion, wear and anti-fouling performance of components in practical applications, particularly impeding its widespread adoption in the maritime industry. However, surface engineering may serve as a viable solution to address some of these limitations.

This work revolves around the investigation of a duplex treatment, involving shot peened followed by coating with a Ti/TiN/TiAlN/TiAlCuN layer via physical vapour deposition. The selection of shot peening was driven by its ability to improve the fatigue properties but also increases the material's wear resistance due to the induced hardening. The coating's significant hardness enhances the wear resistance, but it also enhances the corrosion resistance through barrier protection. Thus, this investigation aims to shed light on the effect the chosen treatments have on the microstructure, surface condition, hardness, and fatigue properties of AM Ti-6Al-4V. Secondly, this work also aims to show how in turn these properties affect the resulting corrosion, cavitation and cavitation-corrosion response, of the untreated and treated conditions, in a simulated marine environment. All surface treatments yielded a significant increase in hardness. The peening treatment generated compressive stresses extending to a depth of 150 μm, with maximum compressive stresses exceeding 700 MPa at around 30 μm below the surface. The coated-only condition showed excellent corrosion and cavitation-corrosion performance, attributed to the coating's high hardness and good adhesion. The roughness induced by shot peening was however detrimental for the corrosion, cavitation and cavitation-corrosion performance with no or minimal improvements observed. However, despite the presence of scatter, both treatments improved the fatigue life of the substrate.

Acknowledgements

I would like to first express my sincere gratitude to Dr. Ing. Ann Zammit, my project supervisor, and Prof. Ing. Glenn Cassar and Prof. Ing. Joseph Buhagiar, my project co-supervisors for offering their knowledge, guidance, and support throughout the duration of this research project. I would also like to thank Prof. Jian Chen and the research team at Southeast University, Nanjing, China for providing the additively manufactured material and for coating the samples. Additionally, I would like to extend my gratitude to Ing. James C. Camilleri, Mr. Daniel Dimech, Mr. Noel Tonna and Mr. Andrew Agius at the Department of Metallurgy and Materials Engineering laboratories for providing valuable advice and assistance during the testing phase of the project.

This research project was largely possible due to funding obtained through the attainment of the Endeavour II Scholarship Scheme, part financed by the European Social Fund. Acknowledgement is also extended to the Malta Council for Science and Technology (MCST) and the Ministry of Science and Technology of the People's Republic of China, which awarded funding to the SEAM (Surface Engineering of Additive Manufactured parts used in marine transportation) project, through the Sino-Malta Fund 2019 Call (Science and Technology Cooperation), of which this dissertation was a part of.

Finally, I am very grateful for the continuous patience, support and motivation provided throughout this demanding period, by my family members.

GOVERNMENT OF MALTA

FONDI.eu

The research work disclosed in this publication is partially funded by the Endeavour II Scholarship Scheme. The project may be co-funded by the ESF+ 2021-2027

May be co-funded by the European Union

ENDEAVOUR SCHOLARSHIPS SCHEME

Table of Contents

List of Figures

List of Tables

List of Abbreviations and Notations

3D	Three dimensional
AB	As-built condition
AM	Additive manufacturing
ASTM	American Society for Testing and Materials
at.%	Atomic percent
bcc	Body Centred Cubic
CAD	Computer Aided Design
CRS	Compressive Residual Stresses
DLC	Diamond-Like Carbon
DSS	Duplex Stainless Steel
DU	Duplex treated condition: shot peened and PVD coated
EBSD	Electron Backscatter Diffraction
EDS	Energy Dispersive Spectroscopy
ELI	Extra Low Interstitials
FWHM	Full width at half maximum
GAM	Grain Average Misorientation
GIAB	Glancing Incidence Asymmetric Bragg
hcp	Hexagonal Closed Packed
HIP	Hot Isostatic Pressing
HT	Built and heat-treated condition
IPF	Inverse Pole Figure
KAM	Kernel Average Misorientation
LOF	Lack of Fusion
LPBF	Laser Powder Bed Fusion
MDE	Mean Depth of Erosion
MDER	Mean Depth of Erosion Rate
MMPDS	Metallic Materials Properties Development and Standardization
NAB	Nickel Aluminium Bronze
OCP	Open circuit potential

OM	Optical Microscopy
PDF	Powder diffraction file
PTFE	Polytetrafluoroethylene
PVD	Physical Vapour Deposition / PVD coated condition
SCC	Stress Corrosion Cracking
SCE	Saturated Calomel Electrode
SEM	Scanning Electron Microscopy
SLM	Selective laser melting
SP	Shot peening / Shot peened condition
SS	Stainless Steel
TMN	Transition-Metal Nitride
WC/C	Tungsten Carbide/ Carbon
wt.%	Weight percent
XRD	X-Ray Diffraction

Glossary of Symbols

α	Alpha phase
α'	Acicular martensite phase
β	Beta phase
θ	Bragg angle
σ_ϕ	Stress along angle ϕ
ρ	Density
υ	Poisson ratio
λ	Wavelength
ψ	Tilt angle
C^*	Material loss due to the total corrosion component
C^*/E^*	Ratio of the total erosion component to the total corrosion component
C/T	Percentage of damage induced by corrosion relative to the total material loss
C	Material loss due to corrosion
C_E	Material loss due to cavitation enhanced corrosion
C_o	Material loss due to corrosion only
CW	Total loss due to corrosion-wear
d	Inter-planar spacing
d_n	Inter-planar spacing of planes parallel to the surface
d_ψ	Inter-planar spacing of stressed crystallographic planes
D_1 , D_2	Average depth value
E^*	Material loss due to the total cavitation component
E/T	Percentage of damage induced by erosion due to cavitation relative to the total material loss
E	Young's Modulus
E	Material loss due to erosion by cavitation
E_C	Material loss due to corrosion enhanced cavitation
E_{break} / E_{pit}	Pitting potential
E_{corr}	Corrosion potential
E_o	Material loss due to erosion by cavitation only
El	Elongation

F	Faraday's constant
H/E	Hardness-to-stiffness ratio
I	Anodic current
i_{corr}	Corrosion current density
J	Current density
L_C	Critical load
M	Atomic mass
M_i	Atomic mass of each element
M_S	Martensite start temperature
M_T	Melting temperature
n	Number of valence electrons / integer
Q	Charge
R_a	Arithmetic mean roughness
R_T	Room temperature
R_z	Mean roughness depth
S	Synergy between wear and corrosion
S_{dr}	Developed interfacial area ratio
t	Cavitation duration
T	Total material loss
T	Temperature
T_β	Beta-transus temperature
UTS	Ultimate tensile strength
V_{chem}	Volumetric material loss due to corrosion
V_{mech}	Volumetric material loss due to mechanical wear
V_{tot}	Total volumetric of material loss
W^*	Material loss due to the mechanical wear component
X_i	Atomic fraction of each element
YS	Yield strength

Chapter 1: Introduction

1.1 Introduction

The versatile properties of Ti-6Al-4V, have made it the primary choice for high-performance applications across industries including the marine industry. Materials designed for marine use necessitate excellent corrosion resistance, high specific strength and very good fatigue performance due to their exposure to wear mechanisms, such as cavitation wear, in corrosive environments [1], [2], [3]. In addition, recently a shift from conventional to additive manufacturing of components has been observed, driven by its various benefits. Apart from fabricating components with properties comparable to conventionally manufactured ones, the flexibility and rapid rate of additive manufacturing have been proven effective in reducing lead times [4],[5].

In the marine industry, long lead times pose a significant challenge, as the breakdown of critical components can ground the vessel or cease it operation. Consequently, additive manufacturing emerges as a viable solution to address this issue. However, this technique comes with its set of limitations. Suboptimal build parameters can result in porous and rough components. Moreover, the combination of high melting temperatures and rapid cooling rates, induces significant tensile stresses in components, fostering crack initiation and propagation [4], [6]. This is detrimental to the material's mechanical, corrosion and wear characteristics, which already exhibit subpar performance under sliding conditions [7], [8]. The overall solution to these challenges involves the implementation of surface engineering.

The author recognises that this solution is slightly counterintuitive as a multi-stage manufacturing process is being proposed which doesn't favour the advantages provided by AM. However, this investigation is considered as an initial step in determining the feasibility of the proposed process, particularly for highly customised or complex components, which can then be further optimised later on.

The aim is to apply treatments that improve the fatigue strength, wear resistance and corrosion resistance. This can be achieved by shot peening, a cold work process wherein a stream of shots impacts the surface, inducing compressive residual stresses. By eliminating the tensile stresses, the materials fatigue performance is significantly improved. In addition, the induced surface hardening enhances the wear resistance [9],

[10], [11], [12]. Despite a rise in the surface roughness due to peening, this can be mitigated by polishing prior to peening.

However, the induced roughness has been observed to contribute to a poor corrosion performance as a result of the increased surface area [13],[14]. Thus, the deposition of a ceramic multilayer coating, which does not eliminate the hardening induced by peening, is being proposed. Such coatings typically improve the wear resistance, due to their significant hardness and better load carrying capabilities, and also the corrosion resistance, by providing barrier protection [15], [16], [17]. Thus, the application of a duplex treatment is being proposed to achieve the required effects.

The bulk and surface characteristics of duplex treated substrates (shot peened and PVD coated) are as of yet not extensively studied. Even more so when applied to additively manufactured substrates. Similarly, in the majority of available research, cavitation and cavitation-corrosion testing was applied mainly to wrought Ti-6Al-4V. Limited information regarding the cavitation and cavitation-corrosion resistance of substrates treated with the highlighted surface engineering techniques can be found in literature. Thus, this research intends to contribute to existing knowledge and give further insight into the proposed areas of research.

1.2 Research Aim and Objectives

Via the proposed duplex treatment, an improvement in the corrosion, cavitation wear, cavitation-corrosion, and fatigue performance of Ti-6Al-4V manufactured via the 3D printing route, intended for marine applications, is expected. Thus, the main aim of this research is to test this hypothesis which shall be achieved by fulfilling the following objectives:

1. Adopt characterisation techniques to determine the effects imparted by the chosen treatments and the specific characteristics of the as-built (AB), heat treated (HT), shot-peened (SP), duplex treated (DU) and PVD coated (PVD) conditions including the residual stresses, hardness, roughness, phase transformation, microstructure, grain structure and coating adhesion.
2. Determine the mechanical properties of the heat treated (HT) sample via tensile and impact testing and of the heat treated (HT), shot-peened (SP) and duplex (DU) treated conditions via axial fatigue testing. Additionally, carry out micrographic analysis of the fractures resulting following impact and axial fatigue testing.

3. Investigate the corrosion, cavitation and cavitation-corrosion performance of the heat treated (HT), shot-peened (SP), duplex treated (DU) and PVD coated (PVD) conditions, in a simulated marine environment. Additionally, support all findings by micrographic analysis of the test areas and material loss quantification, in case of the cavitation and cavitation-corrosion tested samples.

Chapter 2: Literature Review

2.1 Background on Ti-6Al-4V Titanium Alloy

2.1.1 Introduction

Titanium and its alloys have found their use in numerous high-performance applications due to their well-combined properties. Ti-6Al-4V (Ti64), in particular, is arguably the most used titanium alloy, being used to produce nearly 50% of titanium components worldwide [6]. Originally, it was mostly employed in the aerospace industry due to being lightweight whilst having a high specific strength. However, it is being widely adopted by other industries due to its other desirable properties. In particular, it is becoming increasingly popular in the marine industry due to its excellent corrosion resistance in addition to the other properties, when compared to conventional marine materials [1], [2], [3]. Some current marine applications include its use for the production of mid-sized propellers and propeller shafts for small and large vessels, in marine piping systems, as well as for power and transmission equipment [1], [3]. Despite being very costly and energy-intensive to manufacture, these limitations can be balanced out by the increased service life and diminished maintenance costs that the material provides [18].

2.1.2 Characteristics of Ti64

Ti64 is a superior metal alloy typically employed on for high performance applications due to its excellent combination of properties. Having a density of 4.43 gcm^{-3}, it is classified as one of the lightest metals. It is particularly known for its high strength-to-weight ratio and superior corrosion performance [1], [19]. Thus, it is widely adopted in the aerospace, chemical and medical industries as it is able to withstand high loads, despite its minimal weight, and is impervious to corrosive environments. Its excellent corrosion resistance is due to its high affinity for oxygen which results in the formation of a thin and dense TiO_2 layer [1]. Additionally, it also has a minimal stiffness, good toughness and is capable of retaining its strength at temperatures as high as 550 ºC [1], [20]. It also has good formability and can be heat treated to alter its properties [20].

The TiO_2 layer forms via the passivation of the titanium alloy. It is typically composed of two layers, a compact inner layer and a porous layer on top. The compact inner layer contributes to the excellent corrosion resistance of the alloy as it eliminates contact between corrosive solution and the substrate thus hindering dissolution. An inner layer of large thickness allows for better corrosion resistance [21], [22].

2.1.3 Metallurgy of Ti64: Crystal Structure and Phases

Titanium is allotropic occurring in two different structures. These structures are hexagonal close packed (HCP), present at temperatures below the β transus temperature, and body-centred cubic (BCC), present at temperatures above the β transus temperature. Ti64 is typically a two-phase titanium alloy, composed of an α and β phase at room temperature, being classified in the α + β alloys category due to being alloyed with aluminium, which is an α-stabiliser, and vanadium, a β-stabiliser [6], [20]. The alpha phase has an HCP structure whilst the beta phase has a BCC structure. The combination of these two crystal structures, depending on the arrangement and volume fraction, allows Ti64 to have its specific combination of properties, which are derived from the individual properties of the phases themselves [1], [23]. In comparison with the β-phase, the α-phase is densely packed having an anisotropic structure and properties. It is less ductile having a greater resistance to plastic deformation and creep [1], [20].

The alloying element aluminium allows a decrease in the density of the alloy due to being more lightweight and it also provides the alloy with a higher strength via solid solution strengthening [20]. However, its content is limited to 6 wt.% as above this quantity, the alloy becomes more susceptible to stress corrosion cracking and embrittlement due to the formation of Ti_3Al intermetallic compounds [1], [20]. This element also aids to improve the oxidation resistance of the alloy. On the other hand, the addition of vanadium aids to strengthen the β-phase [20].

2.1.4 Microstructures of Ti64

The microstructure of a material is crucial as it directly influences the component's properties [6], [19]. Typically, Ti64 can experience the following phase transformations as observed in Figure 2.1(a):

$$\begin{array}{ccccccccc} R_T & \rightarrow & T_\beta \leq T < M_T & \rightarrow & M_T & \rightarrow & T_\beta \leq T < M_T & \rightarrow & T > M_S \text{ or } T < M_S \\ & & & & & & & & \text{(also depends on the cooling rate)} \\ \alpha + \beta & \rightarrow & \beta & \rightarrow & \text{liquid} & \rightarrow & \beta & \rightarrow & \alpha + \beta \,/\, \alpha' \end{array}$$

where, α, β and α' represent the alpha, beta and acicular martensite phases, respectively. During melting, the α + β phase present at room temperature, transforms into β before transforming into a complete liquid phase upon complete melting. With cooling, from liquid phase, it transforms again to the β phase and eventually to the α + β or α' phases. The phase transformation is dependent on the manufacturing process

particularly the temperature history and the cooling rates. Initially β grains form and with cooling from above the beta transus, the α phase starts to form as laths. The cooling rate dictates the amount and location at which these laths form. At moderate cooling rates, these α laths nucleate at the β grain boundaries and grow inside the β grains along specific planes. A faster cooling rate allows both the nucleation of the α phase within the β grains and at the grain boundary [6], [24]. A complete dual phase forms if the solidification process is very slow i.e. below 20 °C/s. In comparison, in case of fast cooling rates exceeding 410 °C/s, the β phase transforms into a martensite, α', phase as highlighted in Figure 2.1(b). The transformation to α' is a diffusion-less one and the decomposition occurs via non-equilibrium reaction [6].

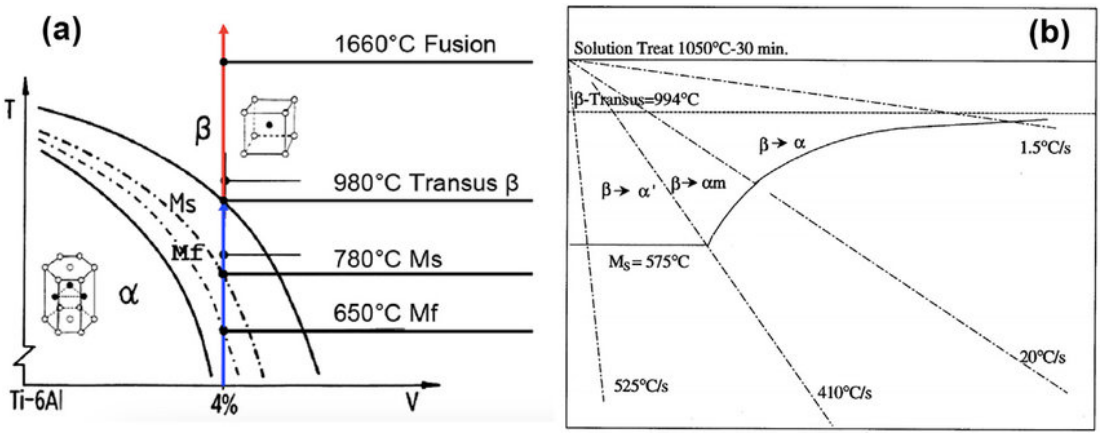

Figure 2.1(a) Phase diagram of Ti-6Al-4V and (b) Phase transformation expected at various cooling rates. Adapted from [6].

In addition, the thermal gradient is also an important factor to consider as it influences the type of growth and size of the microstructural features. Significant thermal gradients encourage columnar growth, where grains grow along the direction of heat extraction, and promote finer microstructures since they are accompanied by significant cooling rates, inhibiting grain growth. In comparison, lower thermal gradients promote the formation of an equiaxed structure as grains are given the time to nucleate and grow thus, a low gradient typically also results in coarser structures due to the accompanying slower cooling rates [6].

Thus, depending on the fabrication process and thermomechanical treatments adopted, Ti64 can have various microstructures such as equiaxed, martensitic, lamellar or bi-modal microstructures, either of which can be fine or course as observed in Figure 2.2 [21], [25], [26].

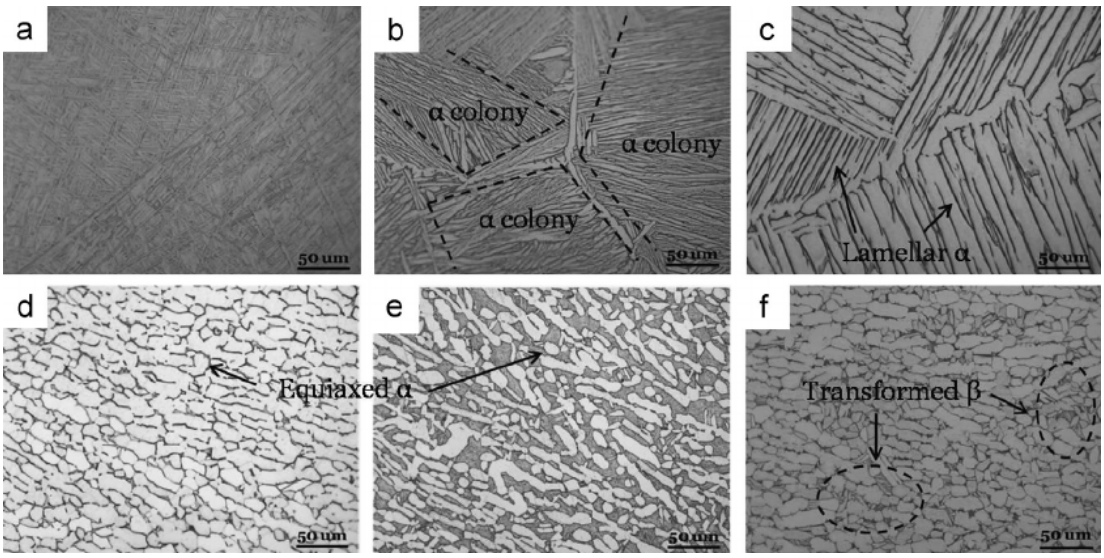

Figure 2.2 The various microstructures of Ti-6Al-4V (a) fine lamellar: water quenched (WC) from 1050ºC, (b) lamellar: air cooled (AC) from 1050ºC, (c) coarse lamellar: furnace cooled (FC) from 1050ºC, (d) fully equiaxed: furnace cooled (FC) from 950 ºC, (e) bi-modal: HT at 950 ºC, WC + HT at 550 ºC, AC and (f) bi-modal: HT at 950 ºC, AC + HT at 550 ºC, AC. Adapted from [6].

These varying microstructures result in varying properties. An equiaxed microstructure, is typically more ductile, more tough, has enhanced strength and a greater resistance to crack initiation compared to the other microstructures [1], [27]. In comparison, a martensitic structure has a higher hardness with recorded values in the range of 410 HV. This is beneficial for the corrosion resistance, as the higher hardness enhances the adhesion between the oxide layer and the substrate surface. Furthermore, a martensitic structure is typically more corrosion resistant as in a two-phase microstructure, galvanic interaction can occur between the phases arising from the occurrence of solute partitioning. The coarseness of the microstructure also plays a crucial role regarding the material's properties. A finer microstructure is generally stronger, more ductile, and resistant to fatigue crack initiation and exhibits a better oxidation behavior. On the other hand, a coarse structure is tougher and exhibits a better creep strength [1], [21], [25].

2.2 Additive Manufacturing of Ti-6Al-4V

2.2.1 Background

Typically, Ti64 products are manufactured via subtractive methods. However, throughout the last decade the production of components via additive manufacturing techniques, such as laser powder bed fusion (LPBF), has been gaining popularity. According to the ASTM F2792-10 - *Standard Terminology for Additive Manufacturing Technologies*, additive manufacturing is defined as the "process of

joining materials to make objects from three-dimensional (3D) model data, usually layer upon layer, as opposed to subtractive manufacturing methodologies" [28]. The laser powder bed fusion (LPBF) technique adopted in this investigation is known as selective laser melting. A schematic of the process can be observed in Figure 2.3 [29]. The initial step in all additive manufacturing techniques is the creation of a 3D model of the required component via computer aided design (CAD) software. The resulting file contains geometrical data which is processed into various layers of a specific thickness [6]. A layer of metallic powder particles is uniformly spread over the powder bed by the roller/rake system. Then via a scanner, which traverses in the coordinates required to produce the component, a laser beam is directed over the powder layer set on the bed. The beam selectively melts the powder according to the 3D data, which subsequently cools down and solidifies. This is repeated layer by layer until the desired component is manufactured. Typically, for building of Ti64 components, the process is carried out in an inert atmosphere due to the material's affinity to oxygen [6], [30].

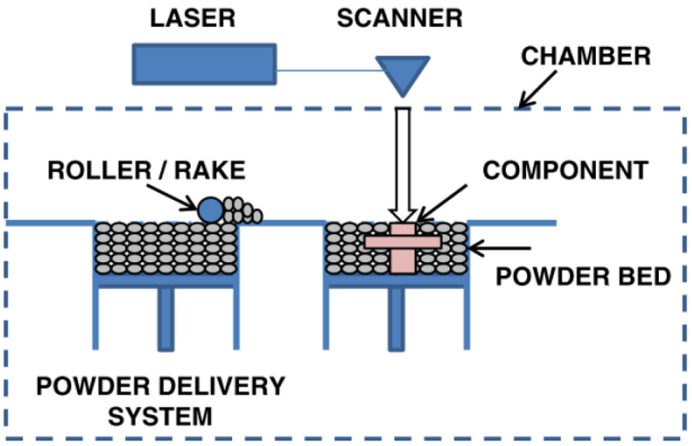

Figure 2.3 Schematic of laser powder bed fusion process [19].

2.2.2 Microstructure of AM Ti64

The microstructure of LPBF Ti64 is typically a fine needle-like structure composed of the acicular martensite, α', phase within the prior columnar β grains due to the very fast cooling rate, ranging between 10^4 to 10^6 K/s, and significant thermal gradients of the process [5], [6], [19], [25]. Additive manufacturing techniques present a complex thermal history when compared to subtractive techniques, and is dependent on the build parameters [19], [25], such as the power source, input power, scanning speed, and is also dependent on the part dimensions and geometry. This complex thermal history for one layer can be observed in Figure 2.4 [19]. Whilst building, each layer experiences a several thermal cycles. The very first layer has a temperature above the

melting point which is maintained during the printing of the second layer. By the time the fourth layer is printed, the first layer's temperature reduces but is still above the β transus temperature. Thus, this complex thermal history makes the prediction of the microstructure difficult. It also results in the epitaxial growth of the prior β grains. These grains nucleate and grow perpendicular to the build direction across the various layers. Unlike α laths, the size and thickness of these β grains does not depend on the cooling rate but on the total time during which a temperature between the melting point and the β transus temperature is maintained [19], [24], [25].

To obtain an α + β phase via laser powder bed fusion techniques, particularly by selective laser melting, according to Simonelli *et al*. [31] low laser power and scan speeds are required with the aim of reducing the cooling rate. Pre-heating the powder bed is also beneficial. These measures increase the interaction time between the material and the laser beam and the energy input. Thus, it allows higher temperatures in deposition giving more time for diffusion to occur.

These fine needle-like martensitic structures are typically characterized by a high strength but poor ductility. Hence, to enhance the ductility of AM components, heat treatments are employed. When heat treating below the T_β, α' either decomposes fully into the α and β phases in the prior β grains or partially which is in addition accompanied by the coarsening of α' phase. Above the T_β, any α' decomposes completely and the α laths formed coarsen significantly [19], [32], [33].

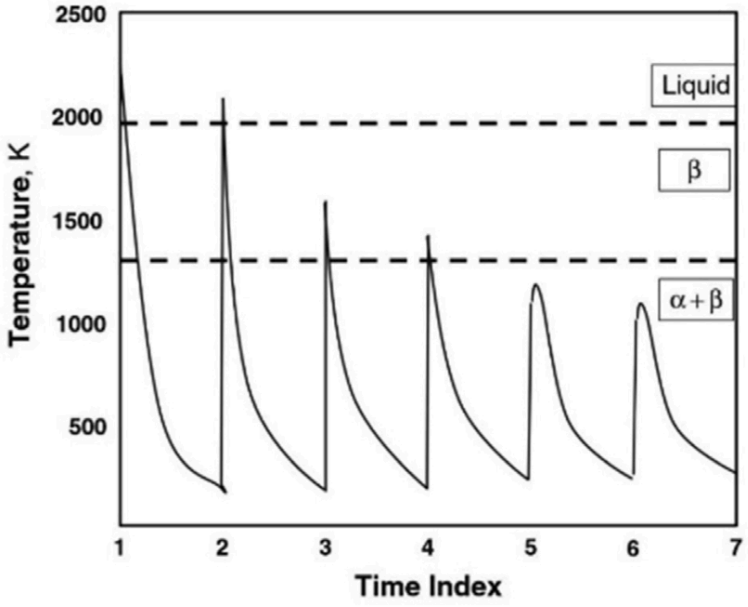

Figure 2.4 The thermal history of the successive layers of additively manufactured Ti-6Al-4V [6].

2.2.3 Advantages of AM

Certain geometries are challenging or otherwise difficult to manufacture via conventional processes due to their complexity. LPBF techniques can allow the layer-by-layer manufacturing of novel components, which is one of the most significant advantages of this process. Furthermore, LPBF allows the elimination of several manufacturing steps such as machining as it results in the fabrication of near net-shape components, thus the process has a shorter production time in comparison [4]. Furthermore, the near-net shape production as well as the re-using of the powder, allows a high rate of material utilization, minimizing material loss which is abundant in subtractive methods. Thus, increasing the cost effectiveness of the process. Furthermore, tooling is not required hence tool production time and expenses are significantly reduced [34]. In comparison to conventional processes, production of small batches of unique components via AM is economically feasible. LPBF techniques are also very flexible allowing for quick alterations to the component's design. Due to these various advantages, it can be a suitable replacement to subtractive manufacturing, allowing for potential reduction in lead times and associated costs.

2.2.4 Limitations of AM

However, additive manufacturing also presents its own limitations due to the layer-by-layer fabrication and the complex phenomena taking place during melting and particle fusion [6], [35]. Improper control over printing parameters can result in highly porous components and an associated poor surface finish. Furthermore, the high temperatures required to melt and fuse the metallic powder result in tensile residual stresses [4], [6]. The aforementioned can be very detrimental to the mechanical, corrosion, anti-fouling and wear characteristics of the material under typical marine conditions.

Theoretically, LPBF can produce components which are 100% dense. However, a slight deviation from optimal printing parameters can result in porosity. AM allows the production of components having controlled porosity, such as in case of load-bearing implants, in order to alter mechanical properties as desired. However, a degree of uncontrolled porosity still exists and unlike controlled porosity, this is detrimental to the mechanical properties. Pores act as stress concentrators and nucleation sites for shear bands and cracks. Furthermore, the ductility of the material is directly influenced by the shape and orientation of these pores. It is very difficult to eliminate uncontrolled porosity altogether. Even with the use of optimal parameters, a minimal amount of

porosity was still detected by Kasperovich and Hausmann [36] in SLM Ti64 and could only be eliminated via the application of post-processing, namely via hot isostatic pressing (HIP). The authors observed porosity to be present as an abundance of very small pores distributed throughout amounting to 0.08% of the total volume. Following HIP, a decrease in porosity by a factor of 8 was observed.

Two types of uncontrolled pores may be present: gas or lack-of-fusion (LOF) pores. As suggested, gas pores arise from the entrapment of gas in the molten pool thus are characterised by a spherical or mostly round shape and are also randomly distributed. Their diameter typically ranges between 1 and 100 μm. Such pores can be mitigated by employing a slower scan speed and higher laser power. In comparison, LOF pores are significantly larger, having an irregular elongated shape with sharp tips observed as thin flat cracks. Unlike gas pores, LOF defects are typically found at the interface between two adjacent layers. Such pores form under inadequate melting conditions. When laser energy is insufficient, complete melting cannot take place and subsequently bonding between layers is weak. These pores are detrimental to the load carrying capabilities of the component as typically, under a uniaxial tensile load applied in parallel to the build direction, premature failure is prone to occur as stresses become localized at the sharp tips of the pores. However, unlike gas pores, such pores may be avoided by increasing the applied energy density [6], [19].

LPBF techniques, in particular SLM, has been observed to result in surface roughness, R_a, values ranging between 5 and 40 μm [37], [38]. According to Li *et al*. [39], there are three major contributors to the resulting high surface roughness:

1. Due to the staircase effect, a phenomenon resulting due to the layer-by-layer deposition, which becomes more prominent with an increase in the number of layers and is more prominent in inclined or curved surface.
2. In SLM, unused powder particles remain on the powder bed thus, this can lead to the bonding of these partially melted particles at the top-most surface.
3. Due to presence of pores and lack-of-fusion defects at the surface.

Other sources of roughness include wetting which results in an unstable melt pool, evaporation leading to splashing of particles and spattering [35]. Whilst, this high surface roughness can be mitigated by optimizing the build parameters, only post-processing via polishing can remove the induced roughness. Moreover, polishing is

beneficial for mechanical properties as defects present at the surface are mechanically removed thus, removing potential sites where crack initiation can occur [6].

Such AM processes also induce high tensile residual stresses due to the large temperature gradients present. These stresses can have values as high as the yield strength of the material and typically reaches the peak at or near the top-most surface. The amount of stress induced is influenced by the number of layers, the scan length and the deposition strategy adopted. Moreover, their distribution is anisotropic with stresses being more significant along the scan direction which is exposed to greater thermal gradients. These tensile stresses are detrimental as they encourage crack initiation and formation leading to immediate component failure. Furthermore, such stresses result in warping and hence may lead to disconnection in the build. The warping can be mitigated through the designing of strategically placed supporting structures if required. Meanwhile, via stress relief or annealing heat treatment, these induced stresses can be significantly reduced [6].

2.2.5 Material Properties of AM Ti64

It is crucial that the material properties of LPBF Ti64 are comparable or superior to those of conventionally manufactured Ti64 in order for the additive manufacturing process to be considered as a replacement for conventional techniques. As mentioned previously, LPBF techniques typically result in a fine martensitic microstructure. This differs compared to microstructures obtained by conventional manufacturing, thus resulting in different properties. Moreover, the properties are impacted by other factors including the phases, grain size, prior β grain texture and defects [5], [6]. In Table 2.1, the various tensile properties of LPBF Ti64 in comparison with values typically observed for conventionally manufactured Ti64 are presented. Similar to marine applications, both aerospace and medical implant applications require excellent tensile and fatigue properties capable of withstanding the high loads and cycles the material is exposed to. According to the ASTM F136-13(2021) - *Standard Specification for Wrought Titanium-6Aluminum-4Vanadium ELI (Extra Low Interstitial) Alloy for Surgical Implant Applications* and ASTM F2924-14(2021) - *Standard Specification for Additive Manufacturing Titanium-6Aluminum-4Vanadium with Powder Bed Fusion* standards, the minimum values acceptable for Ti64 used for such applications are those listed in Table 2.1 [40], [41].

Table 2.1 Properties of conventionally and additively manufactured Ti-6Al-4V. 'H' and 'V' denote the build direction of the sample i.e. either horizontal or vertical.

		Yield Strength, YS (MPa)	**Ultimate Tensile Strength, UTS (MPa)**	**Elongation, El (%)**	**Young's Modulus, E (GPa)**
Min. values set by standards [40], [41]		758	827	8	-
Wrought Ti64 [1]		800 – 1100	900 - 1200	13 - 16	100 - 110
AM Ti64 [5], [23]	H	964	1041	7	113
	V	1058	1114	3	109
	H	802	1062	13	-
	-	1200	1280	2	-
	-	850	960	7	-
	H	1137	1206	8	105
	V	962	1166	2	102

The tensile properties of LPBF Ti64 have been the subject of numerous investigations. The majority observed that for a near 100% density, the built material has superior strength compared to its conventionally manufactured counterpart [5]. LPBF Ti64 typically has an enhanced yield and ultimate tensile strength and a higher hardness. This is a result of the α' martensite and the finer microstructure which hinders greatly dislocation motion. Its formation results in lattice strains and the phase itself consists of deformed lattice structures and a high dislocation density. The latter allows hardening to occur via the mechanism of dislocation strengthening [6]. These values are also well above those stated by the standard, however, the ductility is very poor, and many investigations report sub-standard values. A drop in stiffness is also typically observed for the built material. This is one of the primary reasons why LPBF Ti64 alloys are heat treated.

Heat treating the alloy improves both the stiffness and ductility, however results in a slight decrease in strength and hardness. A heat treatment below the β transus temperature results in the coarsening of the α' phase and allows the partial or full decomposition of the α' into α+β and the formation of α along the grain boundary. In comparison to a martensitic structure, an α+β in prior β grains structure is not as strong however it is still stronger than that of an equiaxed α+β structure. The strength is dependent on the thickness of the α-laths whose thickness is determined by the

maximum temperature and the cooling rate [5], [6]. As the laths become coarse, the effective slip length increases hence why a decrease in strength is observed [6]. Heat treatments above the β transus temperature leads to the total decomposition of α' phase however the final microstructure depends on the cooling rate. The slow cooling rates of furnace cooling allow a lamellar α+β microstructure whilst the faster rates resulting from quenching in water an α' microstructure is obtained [5].

The mechanical behaviour of LPBF materials is known to be anisotropic due to various sources. One of the main sources is the crystallographic texture. The microstructures produced by additive manufacturing are inherently textured due to the layer-by-layer processing of the metal powder. With solidification, columnar grains preferentially grow along the <100> direction thus LPBF Ti64 has a dominant β texture rather than having a random distribution of crystal orientations which results in isotropy [42]. Moreover, the present texture also influences the fracture mechanisms [31]. The build direction is another source of anisotropy. Its effect was observed by Yang *et al.*[42] who reported that horizontally built SLM Ti64 samples are stronger, whereas vertically built samples exhibit better ductility thus confirming that the build direction contributes to anisotropy. Similar conclusions were also drawn by Simonelli *et al.* [31].

Furthermore, the tensile properties are largely dependent on the material's densification and stress state. Tensile residual stresses and defects such as porosity and cracks induced by the printing process also negatively impact the ductility. The defects act as stress concentrators and crack initiation sites whilst tensile stresses promote the growth and propagation of cracks [6].

Compared to conventional Ti64, the as-built material typically exhibits a diminished fatigue performance. Walker *et al.*[43] noted that despite the scatter present in values quoted by the Metallic Materials Properties Development and Standardization (MMPDS) handbook for mill-annealed Ti64, as-built Ti64 exhibited a shorter fatigue life for the same stresses applied. The finer microstructures obtained by LPBF are beneficial to increase crack initiation resistance as the crack needs to initiate and break through a series of very closely spaced grain boundaries, thus it is delayed. However, the high probability of having build defects, because of improper build parameters, and the inherently poor surface condition of the as-built material far exceed the benefits of the finer microstructure hence, the poor fatigue performance [43].

Apart from optimizing the processing parameters, heat treatments and hot-isostatic pressing (HIP) have been observed to be highly beneficial in improving the fatigue performance of LPBF Ti64. HIP is the most effective as it has the ability of closing pores and reducing the size of internal defects. However, Leuders *et al.* [44] observed that heat treatments resulted in a near 240% increase in fatigue life after a sub-transus HT and a 970% increase after an HT above the β transus. This improvement was observed irrespective of the build direction. Moreover, Greitemeier *et al.* [45] observed that fatigue performance can be significantly improved by polishing or milling the surface irrespective of heat treatments.

As mentioned previously, as-built Ti64 is typically harder than wrought Ti64 due to the finer and harder α' phase. Wrought Ti64 has a hardness of approximately 314 HV, while various investigations observed values as high as 450 HV for LPBF Ti64, which decreased to 320 – 350 HV following heat treatment [5], [46], [47]. Generally, a higher hardness correlates to a better wear performance [5]. Following a review of numerous investigations, Bartolomeu *et al.* [5] noted that as-built selective laser melted Ti64 was harder, and more wear resistant compared to cast Ti64 obtaining the lowest wear rate. The authors concluded that this behavior is related to the varying microstructural features and hardness values. Similarly, Zhu *et al.*[48] observed that SLM Ti64 exhibited lower wear rates compared to the conventionally processed material also attributed to the higher hardness of the built material.

Interestingly, whilst testing SLM Ti64 and heat treated SLM Ti64 using a ring-on-disc rig, Zhu *et al.*[48] observed that the heat-treated condition was softer but more wear resistant when tested against soft and hard counterparts. In this case, this was attributed to the formation of a protective tribo-oxide on the heat-treated material which protected the underlying surface from wear and whose formation is dependent on the heat treatment parameters.

The varying microstructures and surface condition also influence the corrosion performance. For LPBF Ti64, the induced roughness and defects were observed to decrease the material's corrosion resistance, as they impact the soundness of the passive layer, increasing its dissolution rate. Heat treating was observed to enhance the resistance as present non-equilibrium phases such as the α' phase are minimised. Due to its high energy state, this phase is more prone to dissolution. This is confirmed by various investigations where as-built LPBF Ti64 tested in an artificial seawater was

observed to have an inferior corrosion resistance compared to conventionally manufactured Ti64, attributed to the varying microstructures [30], [49], [50], [51]. However, Yang *et al.* [30] confirmed that upon heat treating, the built material then exhibited comparable corrosion resistance to its conventionally manufactured counterpart.

2.3 Limitations of Titanium Alloys

Despite their various advantages and ideal properties, titanium alloys have various limitations as well. Its major limitation is its poor tribological behaviour, evidenced by galling, fretting and adhesive wear [7], [8]. This limits the use of the alloy in tribological applications. This poor behaviour is attributed to the alloy's: (i) low thermal conductivity, (ii) crystal structure, (iii) electron configuration and to (iv) its inability to be effectively lubricated as conventional lubricants have been observed to be insufficiently thick thus are not effectively adsorbed by the oxide layer [8], [52]. The low thermal conductivity increases the alloy's tendency to wear via adhesion. This is a consequence of the high flash temperatures observed under friction [52]. Metals having an HCP crystal structure, have one slip plane thus typically exhibit a good tribological performance as it is difficult for such metals to plastically deform. However, in comparison to other hexagonal metals, Ti64 has a smaller axial ratio allowing easier deformation system to be activated. A high enough critical resolved shear stress allows deformation via basal slip to take place. This behaviour is similar to cubic metals which are typically more ductile and prone to wear. Alloying Ti with Al aids to diminish slightly the co-efficient of friction as it improves the axial ratio. Ti and its alloys are more prone to adhesion due to their electron configuration. Over half of the valency electrons are non-localised and hence, can participate in donor interactions when in contact with a material which can accept electrons [8], [52]. Moreover, due to the high flash temperatures, conventional lubricants may undergo desorption and are not effectively adsorbed by the oxide layer due to forming a thin layer on the surface [52]. This TiO_2 oxide layer provides protection however, under friction conditions, this is undermined by the high flash temperatures thus resulting in plastic shearing of the layer due to its low shear strength. The layer undergoes de-passivation as particles of the oxide layer de-attach. Consequently, the wear rate increases due to detached particles contributing to three body abrasive wear [7]. This

limitation can be combatted through the application of surface treatments applied with the aim of enhancing the wear resistance of the substrate.

Additionally, the manufacturing of Ti64 products is also met with certain challenges. Ti64 products are typically manufactured through techniques such as forging, casting and rolling and subsequent machining. The transition from manufacturing Ti64 components using subtractive methods to the additive route is encouraged by various factors. It is very difficult to machine as it results in high cutting temperatures due to its: i) low thermal conductivity and ii) low volume specific heat [19], [53]. Furthermore, significant forces are required due to the alloy's ability to be work hardened and of retaining its strength at high temperatures. The complex deformation mechanisms of the material, especially under extreme working conditions, and poor dislocation motion also encourage this issue [6], [19], [53]. Moreover, the alloy is chemically reactive resulting in chemical wear of the cutting tools and in addition build-up edges are typically observed as the chips start to weld [19], [53]. These build-up edges form due to the high temperatures present which in turn aggravate further tool wear [19]. Due to the material's affinity to oxygen, machining cannot take place via alumina tools. Instead, tungsten carbide and high-carbide high-speed tools need to be used [20]. Additionally, its chemical reactivity also makes it challenging material to cast.

2.4 Material Degradation via Cavitation and Cavitation-Corrosion

2.4.1 The Cavitation Mechanism

Cavitation is a phenomenon whereby the material degrades due to the repeated application of dynamic loads. This repeated impact is applied via micro-jets which result from the implosion of cavitation bubbles. Cavitation can be detrimental, as it damages the component's surface, decreasing its efficiency and resulting in its eventual failure. Ideally, this is avoided to mitigate of costly repairs [54].

This phenomenon occurs when the liquid pressure rapidly decreases below a critical value and thus, the vapour pressure surpasses the liquid pressure without a change in temperature. This usually occurs due to the restriction of a fast-flowing liquid or high frequency vibrations. Initially, bubbles grow at present nuclei and nucleation sites which encourage their formation and are required for the cavitation phenomenon to occur [54]. Such nuclei include air bubbles present in the liquid varying from several microns up to an order of 1 mm. When the nuclei are in a region of low pressure, the

equilibrium of the forces acting at the surface is not established, and thus, cavitation initiates. Additionally external surfaces, such as the container walls or impurities, which are dissolved or suspended in the solution, can also be nucleation sites. Nucleation can be either homogeneous or heterogeneous. The former occurs when no additional gas phases are present in the solution, whilst the latter occurs due to small gas pockets which form in cracks and crevices found in hydrophobic insoluble solid impurities present in the solution. As the liquid pressure decreases, a minuscule bubble is released from the gas pocket as seen in Figure 2.5 [55].

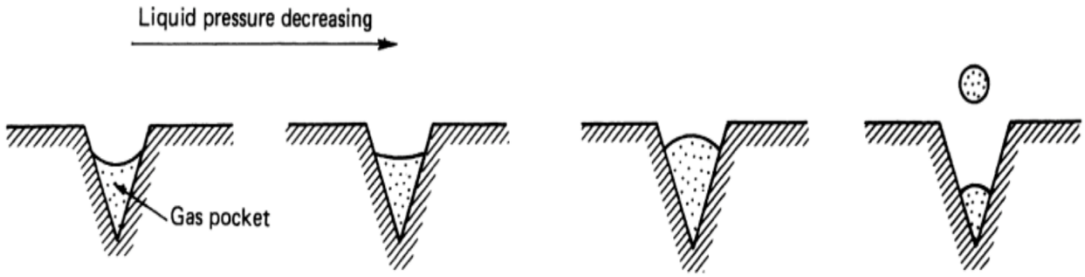

Figure 2.5 Schematic of heterogeneous nucleation [54].

Due to these nuclei, cavities form when there is a negative variation in pressure which fill up with the liquid vapour and gases present forming vapour bubbles. Essentially, due to the liquid pressure falling below the vapour pressure, the solution starts to boil locally. Upon an increase in pressure, above the vapour pressure, these bubbles implode and as they collapse, they undergo compression which is accompanied by the emission of high-pressure waves known as shock waves. These shockwaves can exert pressures as high as 400 MPa which are capable of inducing damage at the material's surface [54], [56]. If collapse occurs near or at a solid, its presence results in the formation of a re-entrant jet which travels through the bubble towards the solid exerting a high pressure on it [54]. This results in material loss if the exerted pressure from micro-jet or shock wave impact exceeds the solid's yield strength [54], [56].

Such micro-jets can have velocities ranging from 30 to 877 m/s. This value is dependent on size of the imploding bubble and its gas content. A high gas content, results in a damping effect and encourages the regeneration of the bubble. A low gas content results in smaller cavitation bubbles which form when the drop in the liquid pressure is significant. This then results in a high-speed micro-jet. The impact duration of micro-jets is very short due to their high velocity thus the repeated impact of micro-jets is referred to as cavitation pulses. The continuous impact of these pulses induces compressive residual stresses at the surface, pits and cracks. The latter propagate leading to significant material removal [54].

Due to the material loss imparted by this phenomenon, metal particles end up in the flowing liquid thus in various systems may be a potential source of further erosion. This phenomenon is evidenced by irregularly shaped craters having sharp edges which are characterised by an internal rough morphology as observed in Figure 2.6 [57]. Following extensive cavitation, the surface appearance assimilates that of a sponge. Additionally, this phenomenon generates a heat input and noises ranging in sound in some cases above 100 dB. The resulting shock waves can also result in vibrations which can contribute to material degradation via fatigue and eventual mechanical fracture [54], [56]. It is worth noting that this phenomenon differs from that of boiling where the formation of bubbles is a result of increasing temperature and change in pressure [54]. Moreover, the probability of cavitation in water increases with increasing temperature since it is accompanied by an increase in vapour pressure [55].

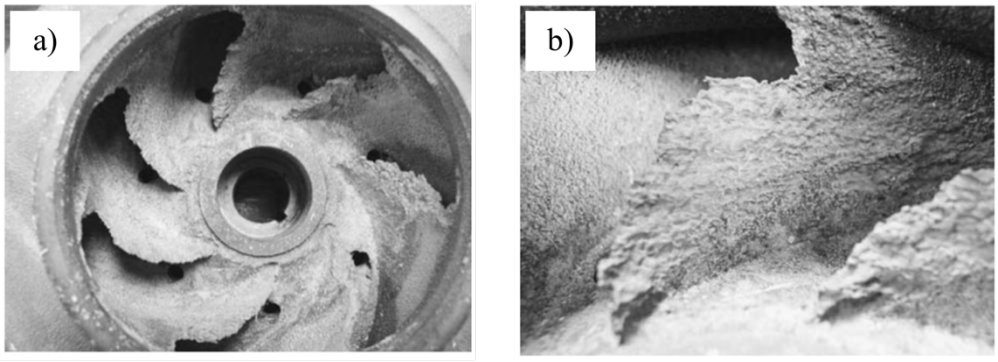

Figure 2.6 (a) Water pump impeller damaged by cavitation and (b) a high magnification image of one of the worn impeller blades where cavitation damage can be observed as the multiple dimples which increase the roughness significantly and also result in thinning of the blades [56].

Components and systems prone to experience sudden pressure drops are susceptible to the cavitation phenomenon. This typically occurs downstream in piping systems, such as vessel seawater cooling systems, which include valves and orifice plates. Such components restrict the liquid flow, increasing its velocity as the liquid passes through a constriction as observed in Figure 2.7 [56]. Accordingly, a drop in the static pressure is then observed. If static pressure drops below the vapour pressure, vapour bubbles form and then implode once the liquid's flow velocity decreases and the pressure increases. This effect is also observed in pump impellers, propellers, hydraulic turbines, and boiler blowdown lines which are likely to experience strong turbulence [56].

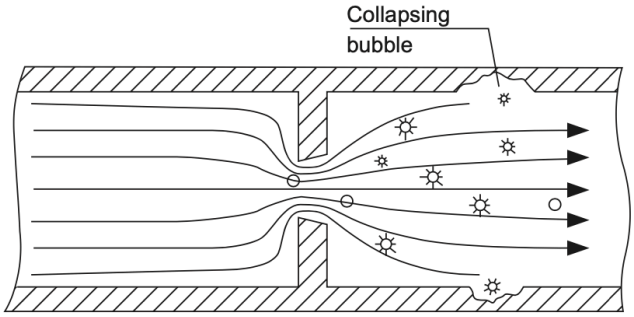

Figure 2.7 The occurrence of cavitation due to restriction of flow [55].

2.4.2 Cavitation Wear vs. Fatigue Failure

Various investigators have studied the correlation between cavitation wear and fatigue failure [55], [58], [59]. The continuous implosion of cavitation bubbles at the surface leads to local plastic deformation, thus local plastic strains, giving rise to the initiation of micro fatigue cracks which propagate and eventually once the material is no longer capable of withstanding the loads imparted by the implosions, the material fails and particle start to detach [55], [59].

Similar to components failing via fatigue, the micro-cracks have a tendency of nucleating at stress risers, including notches, welding defects and tears, or at heterogeneous areas such as at machining marks or inclusions [55], [59]. Hence, since rough surfaces exhibited a poor fatigue performance, similarly such surfaces exhibit a poor cavitation resistance which becomes gradually poorer as the surface is further roughened by cavitation [55]. Moreover, roughness is detrimental as it facilitates the easier separation of particles from the bulk and thus accelerates propagation [59].

Similar characteristics to those observed in fatigue damage were observed in areas which underwent severe cavitation. When testing an Fe-Mn-Si-Cr shape memory alloy, Wang *et al.* [58] determined that the observed cavitation is equivalent to low cycle fatigue failure with the propagation of fractures occurring along boundaries. Additionally, a strong correlation between the material loss rate and the testing parameters, including the frequency and amplitude applied, was observed. These parameters are the same as those adopted for fatigue testing thus can be considered as cyclic deformation parameters. Hence, this correlation provides a better indication the damage incurred by the cavitation mechanism is a fatigue process [58].

2.4.3 The Cavitation-Corrosion Mechanism: Cavitation in a Corrosive environment

Damage observed in cavitated regions is typically caused nearly entirely by mechanical mechanisms. However, evidence of damage due to electrochemical mechanisms have also been observed especially when cavitation occurs in an aggressive chemical environment [55], [56].

Various materials such as titanium alloys and stainless steels form an oxide layer at the surface which aids with the material's resistance against corrosion. Cavitation can encourage the removal of this oxide layer, exposing the underlying metal surface, which is more susceptible to corrosion, hence diminishing the material's corrosion performance. This gives rise to another phenomenon referred to as cavitation corrosion [56], [57]. Compared to for example carbon steel, titanium alloys are not as susceptible to cavitation corrosion, despite the ability of such steels to develop very thick oxide layers. This is due to the titanium alloys developing thin oxide layers having a better adhesion however, they are still susceptible to such degradation under the correct circumstances. Due to the addition of the corrosion mechanism, a synergy is created between cavitation and corrosion which aggravates and hastens the material's degradation resulting in the development of significant damage over shorter periods of time [56].

The cavitation corrosion phenomenon and the synergy between both mechanisms is heavily dependent on various factors. These include the chemical activity or corrosiveness of the surrounding environment, temperature, flow velocity of the medium and the medium properties [55], [56].

- **Effect of chemical activity and environment's corrosiveness**

This phenomenon is very likely to occur in corrosive environments such as the marine environment. Its corrosiveness and chemical reactivity are derived from the presence of various organic and inorganic particles, gases, chemicals and corrosive solutes amongst others which are dispersed in seawater. Subject to the ideal conditions, such foreign matter can chemically react with the component's material thus resulting in electrochemical reactions. The extent of these reactions is also dependent on the material's susceptibility to such chemical reactions which are further induced and encouraged by an increase in temperature [55], [60]. Materials which are not self-passivating, unlike for example NAB and titanium, are more chemically active hence

more susceptible. However, upon the destruction of the passive layer due to cavitation, whereby pits and pores are induced, the material's reactivity increases becoming more prone to corrosion as the induced defects encourage pitting and crevice corrosion [55].

- **Effect of flow velocity**

Additionally, a high flow velocity further enhances material loss as it increases the turbulence. Furthermore, certain obstructions such as bends, tee and elbow connections as well as deposits such as debris, dirt or weld spatter also encourage turbulence and hence enhance the damage due to cavitation corrosion [56]. On the other hand, it is likely that at very small flow velocities or in a static environment no cavitation corrosion occurs, but this is dependent on the material and medium. In comparison, even if the medium is slightly corrosive, cavitation corrosion damage still occurs given that the turbulence is sufficient. The probability of damage is further enhanced is solid particles or gas bubbles are present in the medium [56].

- **Other contributing factors**

Two other contributing factors are the temperature and the liquid properties. The temperature in the current investigation shall be kept constant at 25 ± 5 ºC. This is a relatively low temperature thus it will aid to maintain a low corrosion rate which has been observed to increase as the temperature increase [56]. It is worth noting that the cavitation phenomenon results in a local increase in temperature at the micro-environment level. However, an initially low temperature, is beneficial as it keeps the vapour pressure relatively low. Additionally, at low temperatures the quantity of dissolved or trapped gases is quite high. Therefore, minimal damage is observed as these gases dampen the impact induced by the collapsing bubbles [55].

Liquid properties, namely viscosity, also play a role. In the current investigation testing shall occur in artificial seawater which is characterised by low viscosity. This is not beneficial as higher viscosity liquids have been observed to dampen the effect of the collapsing bubbles thus, the resulting cavitation damage is minimal. Moreover, high viscosity liquid are characterised by low liquid pressures, which ais to hinder the occurrence of the cavitation phenomenon in the first place [55].

Thus, as observed all these factors play a major role in enhancing the synergy between cavitation and corrosion as by increasing the cavitation damage, the susceptibility to corrosion damage is automatically increased due to the defects and roughness induced

through mechanical damage. Depending on the previously mentioned factors and the material, cavitation corrosion can result in either uniform or local attack. The former is encouraged by high flow velocities and highly corrosive medium irrespective of the surface condition. It is further encouraged by the presence of solid particles. Local attack is encouraged by high local turbulence and is observed as grooves, gouging, dents or pits oriented along the direction of flow [56].

2.4.4 Test Methods for Cavitation Wear

Testing for a material's resistance to this phenomenon can occur via a vibration or flow device. The vibration test device consists of a horn which vibrates at a high frequency of 20 kHz and an amplitude of 50 μm. These vibrations result in the generation of cavitation bubbles as explained previously in Section 2.4.1. This test method follows the ASTM G32-16(2021) - *Standard test method for cavitation erosion using vibratory apparatus* [61]. In comparison, the generation of cavitation via a flow device includes the use of cavitation tunnels which propel the flow of water, forming a cavitating jet, towards the sample surface at varying flow intensities and velocities. This test method follows the ASTM G134-17 - *Standard test method for cavitation erosion via liquid jet impingement* [62]. The former is the most popular test method due to its simplicity and due to being considered as an international standard for investigating the cavitation behaviour of materials. The standard parameters at which tests should be carried out allow for easier comparison of results obtained for different materials by different investigators. However, care should still be taken when comparing as for the same material, a dispersion in the erosion rate may be observed due to existing differences such as in the surface roughness or in the quality of the testing solution [54].

During testing, the mass loss is monitored gradually and its relationship with time is represented by cavitation curves. Apart from mass loss other indicators used are volume loss, mean depth of erosion (MDE) or mean depth of erosion rate (MDER). Where mass loss is used for the comparison of materials with similar densities, volume loss is opted for when materials tested have different densities. From monitoring mass loss, the erosion rate is deduced as a function of exposure time. Initially, the erosion rate is negligible however then follows a rapid increase followed by a decrease eventually reaching a steady state. Thus, typically four different significant periods arise, as observed in Figure 2.8 [54], [55]:

(i) **Incubation**: this is the initial stage where the erosion rate is negligible. Cavitation damage during this stage includes the formation of tiny pits and exposure of grain boundaries. It also includes the nucleation of micro-cracks at grain boundaries and inclusions as the surface is exposed to both elastic and plastic deformation. Once the material's limit of deformability is exceeded, fractures and the detachment of particles occur. In certain cases, this period might not necessarily be visible as the effect of cavitation is significant and rapid in the first few seconds [55].

(ii) **Acceleration**: this is the second stage which is characterised by a significant increase in the erosion rate from negligible to maximum values. Pits created previously are aggravated forming craters. Additionally, further pits and cracks are created, grain boundaries become significantly visible and surface undulation takes place. Previously formed micro-cracks undergo rapid crack growth observed as splitting, shearing, and tearing. This rapid acceleration takes place as the material's strength is superseded by the induced internal tension [54], [55].

(iii) **Deceleration**: at this stage, the surface is saturated with cavitation pits some of which have become interconnected. These disturb the flow field diminishing the collapse of cavitation bubbles thus the erosion rate decreases significantly and stabilises at a lower value or may also oscillate at diminished values [54], [55].

(iv) **Steady state**: Upon decelerating, the erosion rate stabilises at a constant value as crack nucleation and propagation become constant for the remaining duration. This is observed as the damaged surface starts to behave as a buffer and the occurrence of implosions at the surface decreases. Thus, the erosion rate decreases and settles in a steady state [55].

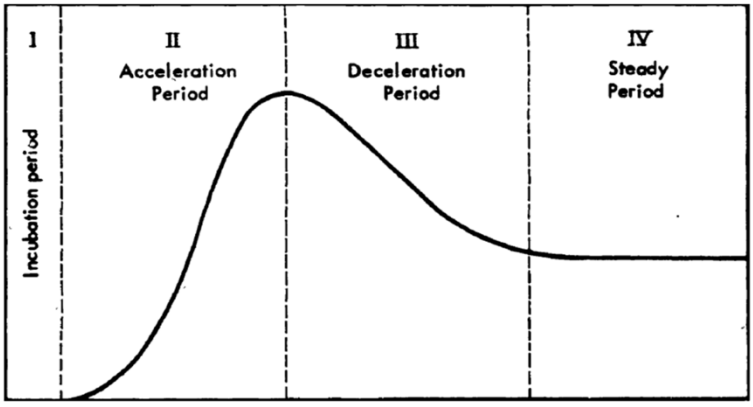

Figure 2.8 The different periods observed during cavitation testing [54].

2.4.5 Test Methods for Cavitation-Corrosion

Cavitation-corrosion testing follows the same concept as tribocorrosion testing (sliding wear testing in corrosive media), whereby a mechanical wear mechanism is applied to a material in a naturally corrosive environment or in an environment in which its corrosive effects are enhanced via electrochemical techniques. In this case, the mechanical wear i.e. cavitation is applied via methods explained in Section 2.4.3. From such testing, the material losses and synergy can then be quantified. Basumatary and Wood [63] carried out an extensive investigation into the various test methods which may be adopted to determine the material losses incurred due to the individual cavitation and corrosion mechanisms and their combined effect. Additionally, their main aim was to determine which methods provide the most reliable and accurate results.

The different test methods carried out to obtain the pure cavitation rate (E), pure corrosion rate (C) and total material loss rate (T) can be observed in Table 2.2. Following testing, the authors obtained the synergy, S, measurement by deducting the addition of E and C from T. After each test, the material losses for E, C and T were quantified via three different methods: (i) gravimetric mass loss, (ii) volumetric profilometry and (iii) mean depth of erosion rate (MDER). The latter was also obtained via profilometry [63].

Basumatary and Wood determined that the most accurate method for determining the synergy is method 5. Whereby, material losses for T and E were measured gravimetrically following cavitation testing in 3.5% NaCl solution and distilled water respectively and values for C were obtained through Faraday's law. The authors chose this method due to its minor limitations compared to the other methods. Data obtained via gravimetric measurements is accurate to around 0.01 mg however, water absorption by coatings or porous materials or the occurrence of selective phase attack may hinder the accuracy of the readings. Volumetric mass loss measurements are highly dependent on the precision of the profilometer. Magnification is typically limited thus data loss is expected for smooth and reflective surfaces. Moreover, it is unable to differentiate between cavitation damage, corrosion products, micro-scratches or burrs hence the measurement is not selective [63], [64].

Table 2.2 The five different test methods and the various methods adopted for material loss measurements by Basumatary and Wood [63].

<table>
<tr><th rowspan="2">Method of measuring material loss</th><th colspan="3">Testing methods to generate material losses due to erosion (E), corrosion (C) and their combination (T)</th></tr>
<tr><th>E</th><th>C</th><th>T</th></tr>
<tr><td>1. MDPR (By profilometry)</td><td rowspan="3">Cavitating in distilled water</td><td rowspan="2">Open circuit potential (OCP) and electrochemical impedances spectroscopy (EIS) analysis in 3.5% NaCl solution under static conditions</td><td rowspan="3">Cavitation in 3.5% NaCl solution</td></tr>
<tr><td>2. Volumetric mass loss (By profilometry)</td></tr>
<tr><td>3. Gravimetric mass loss (By mass balance)</td></tr>
<tr><td>4. Gravimetric mass loss (By mass balance)</td><td>Cavitating in 3.5% NaCl solution with cathodic protection</td><td></td></tr>
<tr><td>5. Gravimetric mass loss (Only T and E measured by mass balance, C by Faraday’s law)</td><td>Cavitating in distilled water</td><td>Potentiodynamic polarisation tests in 3.5% NaCl solution under static conditions</td><td></td></tr>
</table>

The authors considered cavitation testing in distilled water for measuring material loss purely due to the cavitation mechanism due to the negligible quantity of dissolved gases and radicals it contains compared to a 3.5% NaCl solution. Thus, the solution is significantly less corrosive [64]. Testing under cathodic protection is a popular method to obtain the material losses purely due to the mechanical wear mechanisms across all types of tribocorrosion tests however it also has its limitation. Whilst it prevents corrosion, hydrogen evolution is not suppressed, and this could eventually leads to embrittlement [63], [65]. Additionally, the hydrogen may also dampen the impact of cavitation [63]. Other test methods include testing at OCP or under an anodic potential in static and cavitation conditions, similar to tribocorrosion testing. Such tests allow the monitoring of the change in potential or current against time.

As observed, various test methods can be adopted to measure the material losses and synergy present thus, results are not always comparable due to the different methods used to calculate synergy and the different testing conditions adopted by the different

investigators. This was evidenced previously where for similar materials varying synergy contributions were obtained. Therefore, more research is required to determine the most ideal test method which may be standardised allowing for easier comparison of results.

- **Quantifying Material Loss: Mechanistic vs. Synergistic Approach**

Additionally, the material losses due to the various mechanisms can be calculated via two different methods, the mechanistic and synergistic approach. Using Equation 1, the mechanistic approach is used for material loss quantification by using volumetric measurements [66]:

$$V_{tot} = V_{mech} + V_{chem} \tag{2.1}$$

where, V_{tot} is the total volumetric material loss, V_{mech} is the volumetric material loss due to mechanical wear and V_{chem} is the volumetric material loss due to corrosion. To the author's knowledge, with regard to cavitation-corrosion, the use of the mechanistic approach to quantify material losses has not been adopted yet [63].

In comparison, the synergistic approach has been widely adopted [64], [67], [68], [69]. This method allows the quantification of synergy as per ASTM G119-09(2021) - *Standard Guide for Determining Synergism Between Wear and Corrosion* [70], the synergy can be calculated via Equation 2 where the total material loss due to cavitation-corrosion, T, is equivalent to:

$$T = E_0 + C_0 + S \tag{2.2}$$

where E_0, is the material loss due to cavitation only, C_0 is the material loss due to corrosion only and S is the material loss due to the combined effect of both mechanisms. Additionally, S can also be represented via:

$$S = E_C + C_E \tag{2.3}$$

where, E_C is the material loss due to corrosion enhanced cavitation and C_E is the material loss due to cavitation enhanced corrosion. However, this method is limited due to the inability of accurately measuring E_0 and C_0 which may be quantified via cathodic potential tests and static corrosion tests, respectively.

The synergistic approach adopted in this investigation shall follow that adopted by Mallia and Dearnley [71]. Via this method, the synergy component, S, cannot be

directly determined due to the test method adopted therefore the synergy calculations were modified as follows:

$$T = E_C + E_0 + C_E + C_0 \quad (2.4)$$

$$E^* = E_C + E_0 \quad (2.5)$$

$$C^* = C_E + C_0 = \frac{QMt}{nF\rho} + 0 \quad (2.6)$$

$$T = E^* + C^* \quad (2.7)$$

where, E* is the material loss due to the total cavitation component and C* is the material loss due to the total corrosion component. Additionally, for passive materials such as Ti64, C_0 is considered as negligible. Thus, C* is equivalent to C_E which can be obtained via Faraday's law, explained in further detail in Section 3.9.1.

Various investigations have been carried out which have proven the existence of this synergy and its various effects. When testing Zeron 100 (super duplex SS), 1050 mild steel, W1 tool steel, 304 and 316 stainless steel, grey cast iron, copper, brass and bronze using a sonic probe operated at a frequency of 20 kHz, amplitude of 30 μm and in both distilled water and 3.5% NaCl solution at 23 ºC, for synergy measurements where C was calculated from static potentiodynamic tests and E and T were calculated via the mean depth of penetration method following cavitation in distilled water and 3.5% NaCl water respectively, Kwok *et al.*[72] observed the following: (i) the greatest cavitation-corrosion resistance was provided by Zeron 100 followed respectively by the stainless, mild and tool steels, bronze, brass, cast iron and copper, (ii) for the copper alloys, the material loss due to corrosion (<1%) and due to the synergistic effect (<10%) of the mechanisms was minimal thus majority of materials losses occurred to cavitation only, (iii) for the cast iron and mild and tool steels, material loss due to the synergistic effect was significant accounting for 25, 66 and 15% respectively and (iv) for the stainless steels material loss due corrosion and the synergistic effect was negligible with the entire material loss being attributed to the cavitation-erosion mechanism only. The significant material losses due to synergy were attributed to the corrosive solution but were also dependent on the material and its properties including its strength, corrosion resistance, work harden-ability, microstructure and stacking fault energy amongst others. Materials characterised by a high corrosion resistance were observed to exhibit a greater resistance against the combined effect of cavitation-

corrosion. Additionally, from results obtained it was concluded that impact of the cavitation mechanism on corrosion depends on both passive film detachment and rate of material transport [72].

Similarly, Basumatary *et al.* [64] investigated the synergistic effects of cavitation-corrosion on nickel aluminium bronze (NAB) and 2205 duplex SS using an ultrasonic probe, operated at 20 kHz and an amplitude of 80 µm, in distilled water and 3.5% NaCl solution kept at 17 ºC while taking electrochemical measurements via a potentiostat. E and T were measured gravimetrically following cavitation in distilled water and 3.5%NaCl water respectively, whilst for C gravimetric measurements were carried out following potentiodynamic testing. The authors observed that for both materials, the synergistic effect was significant contributing to 74% and 37% of the total material loss for NAB and DSS respectively. In static conditions, DSS was more corrosion resistant however NAB was more resistant to corrosion whilst under cavitation in the seawater solution. Under cavitation, the OCP of NAB also stabilised at a faster rate and at a higher potential. On the other hand, NAB was observed to be more susceptible to cavitation owing to its smaller hardness compared to DSS. The authors noted that a significant synergistic effect can be attributed to the presence of dissolved gases and other minerals which affect the nucleation, growth, and impact of bubbles [64].

Zheng *et al.*[67] observed the synergistic effect of cavitation and corrosion on an austenitic and two martensitic stainless steels, one of which is alloyed with Zr, by testing in both 3.5% NaCl using a frequency of 20 kHz and amplitude of 30 µm. For synergy measurements, T and E were obtained gravimetrically following cavitation, whilst C was calculated using the measured corrosion current density. The authors observed that for all steels, the majority of material losses occurred due to the cavitation-erosion mechanism only accounting to over 80% of total losses. However, whilst losses due to pure corrosion were negligible, the loss due to the synergy of both mechanisms was low but still present amounting to more than 10% for all steels. From results obtained, the authors concluded that by enhancing the corrosion resistance or the mechanical properties of the material, it is less likely to experience damage due to synergy [67]. Thus, one possible method of achieving this is through surface engineering.

Whilst the impact of cavitation and corrosion combined on materials such as stainless steels and copper-based alloys has been well-studied, limited information exists on Ti-

6Al-4V in literature. One study was carried out by Neville and McDougall [73] on different Ti alloys. The alloys were cavitation tested at a frequency of 20 kHz and amplitude of 25 μm in 3.5% NaCl kept at 18ºC. The synergy was calculated by carrying out potentiodynamic testing in static and under cavitation conditions. The best cavitation-corrosion resistance was provided by Ti64 ELI alloyed with ruthenium followed closely by Ti64 ELI. Under cavitation conditions, an increase in current density values was observed however the Ti64 alloys remained in the passive regime. Additionally, the material loss due to corrosion only under cavitation was minimal amounting to less than 1% of the total material loss for Ti64 ELI [73].

2.4.6 Prevention Methods

These effects of cavitation are ideally prevented from the initial design stage. This can be achieved by planning for appropriate dimensioning with the aim of decreasing turbulence and susceptibility to pressure variations. A system can be designed to allow for a controlled and incremental decrease in pressure as opposed to a sudden drop. Ideally, cavitation-resistant materials having a smooth surface finish are adopted [56].

During service various preventive measures may also be adopted. These include maintaining a sufficient pressure level throughout the entire system to eliminate possible pressure variations, limit the occurrence of vibrations and avoid dispersed air from entering the system. On the other hand, generating or inducing large air or gas bubbles will aid to diminish cavitation damage by acting as a buffer for implosions. In case of systems exposed to a corrosive fluid or environment, the combined effect of cavitation and corrosion can be limited by cathodic protection or corrosion inhibitors [56].

Similar to cavitation, the occurrence of cavitation corrosion can be mitigated by adopting various measures including: (i) reducing the flow velocity and turbulence by applying design modifications such as avoiding flow obstructions, using flat and smooth hydrodynamic surfaces and enlarging curve radii, (ii) use materials of high resistance against cavitation corrosion such as stainless steel and titanium, (iii) avoid contamination and limit the quantity or air and solid particles in the system, (iv) apply abrasion-resistant coatings and (v) if possible, decrease the medium's corrosiveness by decreasing the solution temperature or improving its pH [56]. Additionally, corrosion inhibitors have been observed to impact the synergy as they diminish the corrosion mechanism's impact during cavitation [55].

Additionally, following an extensive review of various materials subjected to cavitation testing, Krella *et al*. [54] deduced that the material hardness is crucial for resistance against cavitation. Additionally, since this phenomenon impacts the surface, a viable solution to increasing the resistance is naturally to enhance the hardness at the surface via bulk or surface treatments. The authors noted that such treatments included thermo-chemical such as carburising or nitriding or quenching heat treatments, work hardening treatments, cladding, laser processing and deposition of coatings.

2.5 Surface Engineering of Titanium Alloys

2.5.1 Introduction

Over time, surface engineering techniques have become widely adopted as an effective solution for material performance improvement. The vast amount of existing surface treatments and endless combinations allow specific properties to be targeted and offer a cost-effective solution as opposed to altering the bulk of the material for property enhancement.

The material's performance can be enhanced via three main techniques [9]:

1. By the deposition of monolayer or multilayer coatings.
2. Via modification of surface metallurgy e.g. via shot peening.
3. Via modification of surface chemistry e.g. via nitriding.

The treatments proposed and which shall be focused on in this investigation are shot peening, a coating deposited via physical vapour deposition and the combination of both treatments.

2.5.2 Shot Peening

2.5.2.1 Background

Shot peening is classified as a cold work process since the surface is deformed at room temperature. Deformation is induced by a stream of metallic or ceramic spherical shots targeted at the surface. Upon impact, these shots elastically and plastically deform the surface inducing dimples at the surface. These dimples form as follows. As the shots impact the surface, the material is compressed downwards. As the material is not removed, it expands laterally. In turn, the compressive stresses are induced as a result of this lateral expansion [74]. Moreover, this mechanical impact strengthens and hardens the surface thus it is typically applied with the aim of increasing the service life by enhancing the fatigue, wear and stress corrosion resistance [9], [10], [11], [12].

Typically, treated materials have the stress distribution observed in Figure 2.9 [75]. The shots induce beneficial compressive residual stresses at the surface and up to a certain depth below it. These compressive stresses form as the materials attempts to resist plastic deformation. The maximum compressive stress is observed at the near-surface, then values decrease gradually altering from compressive to tensile [12], [76].

Strengthening occurs via two mechanisms: (i) stress-strengthening and (ii) microstructural-strengthening. An untreated surface is susceptible to fatigue cracking. However, the induced compressive stresses enhance the crack initiation and propagation resistance, encouraging crack closure and increasing the material's resistance to plastic deformation. The material's fatigue strength is enhanced as the induced stress increases the maximum cyclic stress required for crack formation to initiate. Additionally, the compressive stresses improve the performance by hindering crystal sliding along the direction of maximum shear stress under a shearing load [12], [77], [78]. Microstructural strengthening occurs due to the impact of shots, which forms a plastic deformation region in which the microstructure is modified. The grain structure in this region undergoes grain refinement resulting in an increase in grain boundaries, dislocation density and microstrains as observed in Figure 2.9 (b). Such refinement hinders the deformation of crystals via slip thus, delaying fatigue crack formation [12], [79], [80].

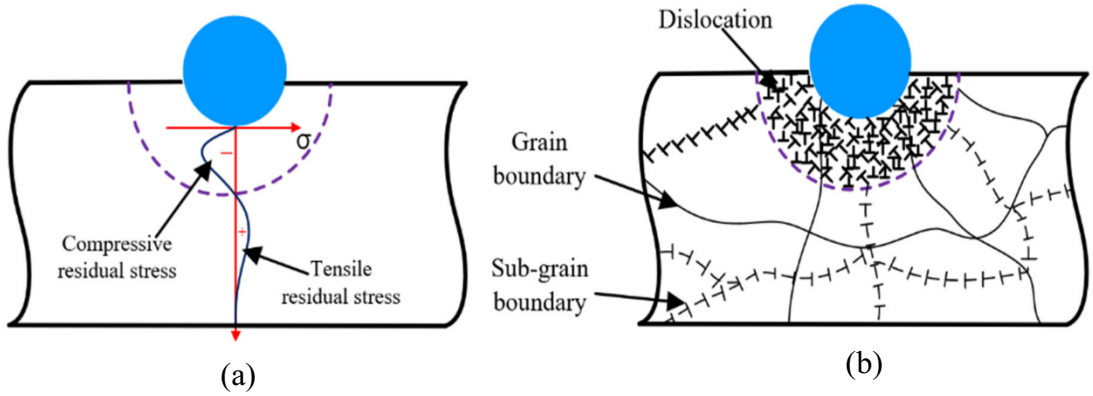

Figure 2.9 Schematics of (a) stress strengthening and (b) microstructure strengthening mechanisms [74].

2.5.2.2 Influence of SP on the Characteristics of LPBF Ti64

- **Effect of SP on the surface characteristics**

Various authors have investigated the effect of shot peening on wrought Ti-6Al-4V [10], [14], [81], [82], [83]. Ahmed *et al.* [14] observed that peening resulted in surface hardness up to 395 HV, a hardened layer 250 µm deep and a maximum compressive

residual stress of 1096 MPa just below the surface. These were accompanied by a significantly plasticly deformed microstructure near the surface. Such effects were also observed for shot peened LPBF Ti64 with values varying according to the peening parameters employed [83], [84]. Zhang *et al.* [83], following the shot peening of SLM Ti64 at an intensity of 0.2 mmA using 0.58 mm steel shots at a pressure of 0.2 MPa, observed an approximate 16% increase in surface hardness to 416 HV, a maximum compressive residual stress of 806 MPa and a hardened layer 180 μm deep. In comparison, Aguado-Montero *et al.* [85] recorded approximately a surface hardness of 400 HV, a maximum CRS of 900 MPa and a hardened layer 325 μm deep when peening SLM Ti64 at an intensity of 0.35 mmA using 0.58 mm steel shots.

By altering the peening parameters, the desired effect can be achieved. One of the most important parameters is the peening intensity and coverage. According to a study into the effect of shot peening parameters by Lin *et al.* [86], with higher peening intensities, finer grains are typically obtained, and an increased microhardness and a deeper hardened layer are generally observed [10], [11], [86]. In comparison, increasing the shot peening coverage does not typically increase the depth of the hardened layer but enhances the sub-surface maximum compressive residual stress induced and enhance the hardened layer's yield strength. However, an increase in these parameters also results in an increase in the surface roughness. This surface condition is also impacted by the shot size. A larger shot size is desired to obtain a uniform and homogenous surface as in comparison, smaller shots result in an increase in the number of dimples per unit area thus the increased roughness [14]. However, smaller shots then induce greater compressive residual stresses, thus parameter optimisation is crucial for obtaining the desired result.

This treatment is known to typically result in an increase in surface roughness following its application. Zhang *et al*. [83] recorded a surface roughness in the range of 1.8 μm however higher values in the range of 4.6 μm were recorded by Aguado-Montero *et al.* [85]. This value is also dependent on the prior condition of the surface whether it is machined, polished, or as built. This is not beneficial for the material's corrosion performance due to increasing the interaction area and resulting in the formation of an unsound passive layer allowing its degradation [14].

- **Effect of SP on the corrosion resistance**

To the author's knowledge, currently, there exists limited research on the impact of SP on the corrosion resistance of LPBF Ti64 in a simulated marine solution. However, present investigations on the effect of the SP treatment on the corrosion performance of materials provide varying results. Studies have shown that it tends to enhance the corrosion resistance as the treatment results in grain refinement thus increasing the grain boundary density which promotes the formation of the passive film [83]. Zhang *et al.* [83] investigated the effect that SP and ultrasonic shot peening treatments have on the corrosion resistance of SLM Ti64 in 3.5 wt% NaCl. The authors observed that both treatments enhanced the corrosion resistance however, in this regard the SP treatment was not as effective as the ultrasonic variety. This was attributed to the rougher surface generated by the conventional-SP treatment. A decrease in corrosion resistance due to the induced roughness was also observed by Zhan *et al.* [13] when investigating the effect different SP processes have on the corrosion resistance of S30432 steel in 3.5 wt% NaCl. The authors concluded that a single SP treatment was detrimental to the corrosion resistance in comparison with dual and triple SP treatments which cause limited roughening. Such a finding also suggests that the treatment parameters play an important role [87]. Additionally, Ahmed *et al.* [14] also observed a decrease in corrosion resistance when investigating the corrosion behaviour of wrought Ti64 having a duplex microstructure in Ringer's solution, which was peened at an intensity of 0.22 mmA using ceramic shots of different sizes: 125-250, 450 and 850 μm. The authors observed that the largest shot size had no effect compared to the untreated sample. However, as the shot size decreased, an increase in the corrosion current density values was observed. This was once again attributed to the higher roughness and heterogeneity imparted by smaller shots which encourage the passive film's degradation.

- **Effect of SP on the fatigue performance**

Whilst comparable tensile properties to traditionally manufactured Ti64 can be obtained via AM, the fatigue performance of AM Ti64 is inferior. It is severely compromised by characteristics including induced tensile residual stresses, porosity, roughness and anisotropy and the synergy present between them [74], [85]. These, in addition to the microstructure, influence significantly the material's crack initiation and propagation behaviour [74]. Consequently, these effects also result in significant

scatter in fatigue data due to their random and uncontrollable nature especially if printing parameters are not optimal [74], [85]. Fatigue cracks form under the application of cyclic load. Initially, micro-cracks form at the present surface defects. With continuous loading, these cracks grow and propagate until the material undergoes total failure [74].

Despite the various factors contributing to the fatigue performance, the most influential are the surface condition and porosity build defects thus, for improvement focus should be on measures which would mitigate these factors [74], [88]. The latter behave as stress raisers causing crack initiation to occur in the interior rather than at the surface [85].Thus specific surface treatments are applied with the aim of achieving any of the following effects: (i) reducing surface roughness, (ii) eliminate or reduce the size of defect at or near the surface and (iii) induce compressive stresses [74], [85]. Shot peening is mainly employed with the aim of replacing the surface tensile stresses with compressive stresses. Additionally, some researchers have also noted that the process is capable of reducing the size of pores found at the near surface [89], [90].

For LPBF materials typically an improvement in the fatigue performance is observed. Kahlin *et al.* [88] observed an approximate 70% increase in the fatigue strength of AM Ti64 following the application of a shot peening treatment. Similarly, Aguado-Montero *et al.* [85] observed an 75% increment in the fatigue strength of SPed LPBF Ti64 for high cycle fatigue and around 35% increase for low cycle fatigue. Additionally, the authors noted that for all SPed samples failure occurred within 200 μm from the surface and with the majority of failures initiating from surface or internal defects connected to the surface. It was observed that due to the induced compressive stresses, stress raisers were re-located to deeper depths in comparison to the as-built sample and thus, crack initiation occurred at the interior [85].

However, opposing results were also observed by Wysick *et al.* [89] when fatigue testing LPBF, polished and shot peened Ti64. The authors observed that while polishing alone enhanced the material's fatigue strength despite observing a scatter in data, upon the addition of shot peening a decline in the fatigue performance was observed. These authors attributed this to the increase in surface roughness of the previously mechanically polished surface. If significant, the effect of the poor surface condition and present defects may outweigh the positive effect of the induced stresses [85]. However, despite the resulting increase in roughness, when compared to the

surface condition of as-built samples, the surface morphology of the peened surface is more homogenous. Thus, shot peening is a widely accepted treatment for fatigue improvement [35], [36], [85].

- **Effect of SP on the cavitation resistance**

Material degradation via the mechanism of cavitation is classified as a fatigue process as material loss occurs via the cyclic loads induced by the continuous collapse of formed bubbles [91]. Compared to polished conventionally manufactured Ti64, Sasaki *et al*. [92] noted that polished LPBF Ti64 has a decreased cavitation resistance performance. The authors attributed this to the AM material having a weaker fatigue strength thus are not as capable in withstanding the fatigue fracture caused by the repeatedly collapsing bubbles. Thus, similar to fatigue performance, the cavitation resistance can be enhanced via shot peening [91].

To the author's knowledge the cavitation resistance of shot peened AM Ti64 is not yet extensively studied however various other investigations on the effect of shot peening on the cavitation resistance of different materials have been conducted.

Tomlinson *et al.* [91] had observed that shot peening was capable of enhancing the hardness of pure iron and austenitic stainless steel by an approximate factor of 2. Consequently, compared to the untreated samples, the mass loss due to cavitation in 1% NaCl water, decreased by a factor of 0.7 for pure iron and 0.1 for austenitic stainless steel. Similarly, for NAB shot peened with intensities ranging from 0.21 to 0.49 mmA, Zeng *et al.* [93] observed three times decrease in material loss when tested in 3.5% NaCl water. The authors attributed this increase in cavitation resistance to the mechanical strengthening induced by the peening treatment which outweighed the material loss aggravation caused by the corrosive solution. However, in comparison for LPBF Ti64, Sasaki *et al.* [92] observed that shot peening was not as effective as other peening methods in enhancing the cavitation resistance, as an 8% increase in resistance was observed during the first ten minutes of cavitation beyond which material losses were then similar to those of the untreated sample. Thus, overall, it was not capable of decreasing the erosion rate.

2.5.3 Physical Vapour Deposition

2.5.3.1 Background

PVD is a well-established technique widely used to deposit thin films with the aim of enhancing the wear and corrosion performance of the substrate. Such coatings are adopted for various functional applications including tools, dies, moulds and blades [94], [95]. This technique is widely adopted as coatings deposited are characterised with excellent adhesion, homogenous layers and allows the implementation of designed structures and graded properties. Additionally, coatings can be composed of any combination of materials [94].

The coating deposited in this investigation, was deposited using a PVD process known as magnetron sputtering [94]. The process consists of positioning a magnetron near various targets composed of the individual elements of the coating. It takes place in a vacuum chamber which is filled with an inert gas such as argon. A significant voltage present between the target and the substrate accelerates the inert gas' particles. The gas ions produced transmit their kinetic energy to the target, leading to the vaporisation of the target material which travels and condenses at the substrate surface gradually [94], [96]. The formation of the thin film results as the condensed particles undergoes various growth stages as observed in Figure 2.10 [96].

The coating's performance is influenced by the deposition parameters adopted particularly by the pressure and substrate temperature which directly impact the coating's structure and properties. Chang *et al.* [97] noted that for transition metal nitride coatings deposited by magnetron sputtering, an increasing pressure initially led to a denser columnar structure due to the increased collision rates, however increasing beyond a certain point reverted this effect resulting a porous coating having coarser grains. The effect was also observed for the coating's hardness. In addition, higher temperatures typically result in a smoother coating having finer grains and a more dense and uniform structure due to the increased sputtering power [98], [99]. Another influencing factor is the substrate's topography. A rougher substrate promotes the growth of a coating with a greater defect density and rough finish as underlying irregularities are transferred through the coating and magnified via the shadowing effect [100]. Thus, a good combination of deposition parameters and surface preparation is required to ensure the formation of an optimal coating.

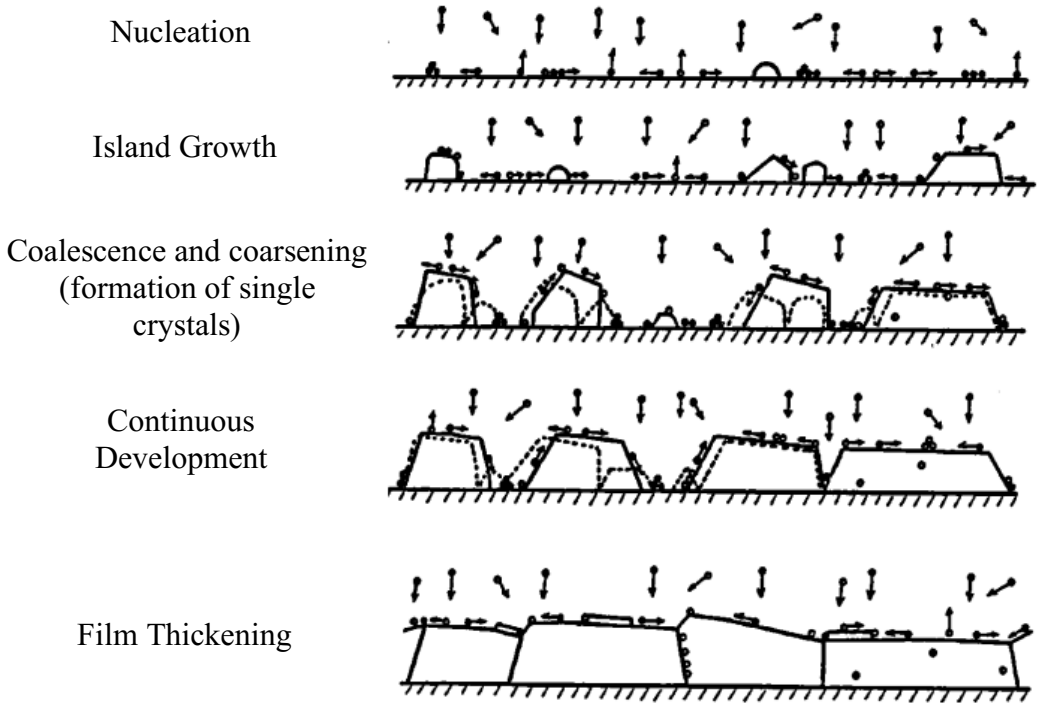

Figure 2.10 Schematic of the various growth stages a PVD coating undergoes [95].

2.5.3.2 Titanium Based Multilayer Coatings

PVD allows the deposition of three different coatings being monolayer, multi-graduated and multi-layer [94]. In this investigation, the coating applied has a multilayer construction. This is beneficial as compared to monolayer coatings, such coatings result in a dense structure with interfacial strengthening and have enhanced load carrying capabilities as the different layers aid to hinder the movement of dislocations [15]. Moreover, the various layers also prevent the propagation of the corrosive medium through any coating defects present to the substrate leading to an overall good corrosion resistance [15], [16], [17]. This was confirmed by Çomaklı [15] when investigating the corrosion-wear behavior of TiAlN/TiN multilayer (R_a of 0.23 μm) and TiN (R_a of 0.43 μm) and TiAlN (R_a of 0.38 μm) monolayer coatings deposited onto polished Ti45Nb, by applying a 6 mm alumina ball at a force of 3 N over the surface at a frequency of 1 Hz in simulated body fluid, whilst monitoring the OCP. The multilayer coated substrate, having the smallest R_a, obtained the lowest wear rate and coefficient of friction and exhibited the greatest resistance to corrosion.

The Ti/TiN/TiAlN/TiAlCuN coating investigated is classified as transition-metal nitride (TMN) coating. These are characterised by high hardness values and excellent wear and corrosion performances but are also brittle and highly stressed which in turn dictate the thickness and service life of the coating. However, these limitations can be

mitigated through depositing multiple layers and combining various metallic and transition-metal nitride layers to effectively reduce internal stresses and enhance the coating's toughness [101], [102].

Additionally, the properties of TMN coatings can also be altered by doping with other metallic elements. Aluminium is typically added to coatings designed to withstand wear as it increases the hardness of the coating significantly. This occurs as Al promotes solid solution strengthening. Aluminium substitutes titanium and due to the varying radii of the atoms, the structure of the coating is altered. This distortion results in an increase in the coating's residual stress and in addition to the solid solution effect, an increase in hardness is consequently observed [103]. However, the content still needs to be limited as this hardness increase is also accompanied with a sharp decrease in ductility resulting in brittle behaviour. It is generally limited to a maximum of 50 at% [104], [105], [106].

On the other hand, copper is added to contribute to an increase in toughness and hardness, reduce stresses and promote grain refinement given that its content is limited [104], [105]. This occurs as copper is not soluble in titanium nitride, attaching at the boundaries of the nitride phase nuclei hence limiting their growth. Typically, finer grains can accommodate more plastic deformation prior to failure hence the increased toughness. Additionally, copper is a ductile soft phase which also contributes to an improved toughness [107], [108]. The Cu content also enhances the biofouling resistance of the coating due to its toxicity [109], [110]. This is an important characteristic for components intended for marine applications to possess, as biofouling is abundant in the marine environment and can be the culprit of component failures.

Blinkov and Belov *et al.* [104], [105] investigated a similar (Ti,Al)N-Cu coating, of 0.3 μm roughness, deposited onto silicon and carbide slabs via cathodic vacuum arc deposition, extensively. The authors reached multiple conclusions, including:

(i) The Cu content, limited to 3.5 at% Cu, contributed to an increase in the coating's corrosion resistance, when undergoing potentiodynamic testing in lubricants of varying acidity (pH 2.5 – 10), and an increase in hardness from 25 to 49 GPa. Beyond 3.5 at% Cu, a decrease in hardness is then observed due to the softness of copper and the introduction of porosity.

(ii) The coating exhibited a high pitting corrosion resistance, tendency for self-passivation and low current density values despite the added Cu content, which can result in poor passivation properties due to nano-structurization.

(iii) The coating exhibited an excellent wear behaviour, where samples were rotated in chamber filled with water mixed with abrasive particles for 3 hours at 20 rps, evidenced by a high resistance to both abrasive and erosion wear.

(iv) The coating exhibited a degree of plasticity irrespective of its high hardness. No brittle fractures following the application of 250 N for 10^5 cycles were recorded and overall, it exhibited a high fracture toughness when subjected to various friction and loading conditions.

2.5.3.3 Influence on the Characteristics of LPBF Ti64

The specific effects of the proposed coating on the performance of AM Ti64 are as of yet very novel and limited literature if any can be found. Thus, the author aims to provide a review on PVD coatings and their performance in general and the effects such coatings typically impart on the substrate. PVD coatings are commonly applied with the aim of enhancing both wear and corrosion resistance [9]. Coatings primarily increase the corrosion resistance of the substrate as they eliminate contact between the substrate and the corrosive medium [111]. Such coatings typically have high hardness values thus are not worn easily [106], [111].

Titanium nitride coatings, as proposed for this investigation, are widely used due to the various properties such coatings possess. These high strength coatings with values ranging between 25 and 38 GPa are characterised by low internal stresses. Additionally, such coatings can retain most of their strength at temperatures as high as 800 ºC with low hardness losses recorded and are also very resistant to high temperature oxidation [104]. However, these coatings are very brittle being prone to brittle fracture. Thus, alloying elements are introduced to alter the properties of the coating as highlighted previously in Section 2.5.3.2.

In numerous applications, especially those related to marine, the components undergo complex mechanical-corrosive loads thus their performance is impacted significantly by the occurrence of wear, such as via cavitation, and corrosion which typically decrease the component's service time and efficiency. In such cases, a coating having the dual function of enhancing both the wear and corrosion performance is desired.

- **Effect of PVD coatings on the corrosion resistance**

The use of PVD coatings for wear performance enhancement is well established however in recent years such coatings have also been investigated for their use in corrosive conditions. Their performance in such conditions is dictated by the faultlessness of the coating layers as they provide protection solely by preventing the substrate from becoming in contact with the corrosive solution. By nature, PVD coatings are slightly penetrable due to their inherent micro-porosity and present defects such as pinholes. The latter are typically a consequence of impurities or particles which adhere to the substrate during the coating deposition. PVD coatings also typically have a columnar structure due to their growth mechanism which follows the surface topography. This results in the presence of pathways between adjacent columns which could allow the propagation of the corrosive solution towards the substrate diminishing its protective function [112]. Hence, the surface finish of the substrate is a major factor influencing the coating's integrity, including the amount of induced defects, and crucial for achieving a coating which possess good properties [112], [113].

Durst *et al.* [112] investigated the corrosion performance of various zirconium carbide and chromium carbide magnetron sputtered PVD coatings deposited on a low alloy steel in an artificial seawater solution. The substrate surfaces had a roughness varying between 0.01 and 0.3 μm. As expected, the polished surfaces resulted in lower current densities relative to the coatings deposited onto the rougher surfaces. For the latter, significant corrosion attack was observed whilst for the former the formation of pits was negligible. This effect was attributed to the increase in the amount of layer defects as a consequence of the greater surface roughness. Consequently, the deposited coating provides poor corrosion protection. Layer defects are initially induced by the peaks and discontinuities characterising a rough surface. The defects facilitate the transport of the corrosive solution to the substrate surface encouraging the corrosion of the substrate and subsequent blistering of the coating. In a similar investigation by Munemasa and Kumakiri [114], the authors observed that with increasing number of coating layers and decreasing substrate roughness the amount of pinholes induced in the TiN coating was reduced significantly. Beyond a roughness of 5 μm, the amount of pinholes in the TiN coating increased exponentially. Similar to this investigation, Durst *et al.* [112] deposited the coatings via magnetron sputtering ion plating. The authors noted that this particular PVD technique is ideal as it typically induces a

minimal amount of defects, results in an amorphous structure and provides a good corrosion resistance performance.

Additionally, a coating with good adhesion can delay the progress of corrosion [112]. Microporosity and build defects encourage loss of adhesion in such locations, negatively impacting its corrosion-barrier performance. Hence, an effective approach to enhance the coating's protective function is to decrease as much as possible the defect density. Generally, such defects are unpredictable and distributed in a non-uniform manner. The surface morphology and deposition conditions will dictate the defect density as well as their geometry and size. Surface anomalies including pits or peaks, contaminants such as foreign matter and an uncontrolled coating deposition all encourage the formation of defects. Foreign matter form cone defects which once in service or even following deposition, detach forming a hole in the coating. This then acts as a nucleation point at which failure can easily start and progress completely undermining the coating's integrity [113].

Various solutions have been proposed for improving the coating's corrosion protection function. These include the addition of layers, increasing the coating thickness, optimised deposition parameters and via alloying. Due to the consecutive deposition of layers which disrupts both the layer and defect growth, multilayering diminishes the impact of induced defects as it allows present pores, pits and defects to be covered and closed. Thus, blocking the pathways through which the solution could permeate. This technique allows the alternate deposition of soft and hard coatings resulting in a high hardness but low stiffness and the improvement of the fracture resistance by mitigating the propagation of cracks through the layers [15], [113]. Daure *et al.* [113] recorded the following observations after subjecting an M42 high speed steel, coated with a monolayer Inconel 625 and multilayer Inconel 625/Cr on surfaces of varying roughness, to salt spray testing: (i) overall the coatings decreased the corrosion current density, (ii) the coatings deposited on the polished substrate resulted in a significantly low corrosion rate, (iii) the roughest surface did not improve the corrosion resistance relative to the uncoated condition and (iv) compared to the monolayer coating, no significant difference in the corrosion resistance was obtained via multilayering.

- **Effect of PVD coatings on the fatigue performance**

The impact of these hard ceramic coatings on the fatigue and tensile behaviour is varied [102], [115]. Various investigations observed an enhanced low cycle and high

cycle fatigue performance when deposited on various bulk or wrought materials. The authors attributed this improvement, including in tensile properties, to the good coating-to-substrate adhesion, high coating strength and compressive residual stresses which aid to hinder the substrate from undergoing plastic deformation [115], [116], [117], [118]. Hein *et al.* [115] observed that the TiN coating deposited onto LPBF Ti-6Al-7Nb increased the hardness by a factor of 3, increased the overall strength but decreased the elongation and resulted in 60% improvement in the number of cycles to failure.

Puchi-Cabrera *et al*. [119] observed that the deposition of a TiN coating on 316L stainless steel improved the fatigue limit by 60 MPa relative to the uncoated substrate but did neither improve nor deteriorate the tensile performance. Costa *et al.* [120] investigated the impact of TiN, CrN and DLC coatings on the axial fatigue performance of wrought Ti-6Al-4V. In comparison to other investigations, these authors, for all PVD coatings, observed a decrease in the axial fatigue strength. This result was attributed to coating defects which encouraged the propagation of cracks from the coating, through the interface and into the substrate. Compared to the TiN and CrN coating, the DLC coating provided the best fatigue performance. The authors attributed this to the physical vapour deposition method. The TiN and CrN coatings were deposited via cathodic arc deposition whilst the DLC coating was deposited via magnetron sputtering which is known to result in fewer coating defects.

- **Effect of PVD coatings on the cavitation resistance**

Due to the high hardness and the occasional improvement in the fatigue performance make such PVD coatings of interest for components exposed to erosion mechanisms such as cavitation and particle erosion. The hardness in particular is of interest as it has the greatest effect on the cavitation, solid article erosion and wear resistance of the substrate. For cavitation resistance, the deposition parameters, coating thickness and the number of layers as well as the substrate properties play an important role. For cavitation testing of a ball bearing steel coated with a TiN monolayer, having a thickness ranging between 2.7 to 3.5 μm, an increase in the incubation period, thus in the cavitation resistance, was observed and was attributed to the coating's high hardness and compressive residual stresses [102]. However, this effect is not always guaranteed. For a TiN coating of similar thickness deposited onto Ti64, the incubation period was non-existent and the coated sample exhibited a high erosion rate compared

to the uncoated sample [121]. A decrease in the incubation period may be attributed to the formation of micro-droplets during the deposition of PVD coatings which are then pulled out because of cavitation and thus, accelerate the coating's failure as they result in pinholes which are essentially crack initiation sites. Additionally, a high resistance against plastic deformation translates to an increase in the coating's cavitation resistance as a greater impact energy is required to induce damage. For TiN coatings, an increase in resistance was observed as the coating's hardness-to-stiffness (H/E) ratio[1] increases from 0.049 to 0.058 [102], [123].

In addition to the hardness-to-stiffness ratio, the coating hardness-to-substrate hardness ratio also plays an important role. With an increase in ratio value an increase in resistance is typically observed however similar to the H/E ratio, this improvement is limited to a threshold value beyond which the resistance than decreases. A coating of high hardness, thickness and brittleness or an alloyed coating can be detrimental to its resistance [102].

For a TiN coating having a hardness of 2200 HK deposited onto Ti64 having a hardness of 405 HK, a decrease in the cavitation performance was observed compared to the uncoated substrate. Thus, for such coatings, a high coating to substrate hardness ratio can be detrimental [54]. Krella *et al.* [54] noted that for various coatings deposited onto various substrates, up to a ratio of three the resistance against cavitation peaked however beyond this value a decrease in resistance improvement was observed. A ductile substrate undergoes plastic deformation however due to the coating's high stiffness it is likely that the coating does not follow the substrates' deformation and hence undergoes brittle failure [54], [102].

Multilayer coatings were observed to exhibit a better resistance. Ma *et al.* [121] investigated the effect of a multilayer CrAlYN/CrN coating as compared to a monolayer TiN coating deposited onto Ti64 on the cavitation resistance. The authors concluded that the multilayer coating exhibited a better performance resulting in an improvement of 13.5 times. Similar observations were noted by Krella [124] when investigating the cavitation performance of deposited Ti/TiN multilayer coatings on an austenitic stainless steel. Additionally, compared to monolayer coatings, multilayer

[1] The hardness-to-stiffness (H/E) ratio is a measure of the elastic strain required to result in failure [122].

coatings are more wear resistant due to the increased fracture toughness provided by the increased number of interfaces which encourage the dissipation of fracture energy and deviate the crack propagation direction. Furthermore, the interfaces also function as defect barriers, storage sites, sources and sinks [125].

2.5.4 Application of Duplex Treatments

Typical duplex post-processing treatments applied to AM metals involve a combination of a heat treatment with another surface or bulk treatment. The heat treatment is applied with the main aims of homogenising the microstructure, relieving induced tensile residual stresses, and eliminating anisotropy. It is typically combined with treatments such as hot isostatic pressing, sand blasting or shot peening. These are then applied to eliminate the induced roughness, porosity and build defects or the tensile stresses induced by replacing them with compressive residual stresses.

The shot peening-coating duplex treatment is being proposed with the aim of combining the positive aspects of both processes. While still novel for AM Ti alloys, numerous investigations have studied the effect of such a combination of surface treatments on wrought Ti alloys. Evidence that shot peening improves the adhesion of the PVD coatings was presented in more than one investigation [79], [126]. Zammit *et al.* [126] observed that the shot-peened and WC/C coated wrought Ti64 had an excellent adhesion which surpassed that of the coated-only sample, thus the induced roughness had no effect on the adhesion. The ability of the coating-substrate system to transfer loads is determined by adhesion and for an optimal performance, good adhesion is required which is usually achieved by depositing the coating onto a smooth surface [83], [113]. Shot peening increases significantly the surface roughness which can promote the occurrence of mechanical locking which is however reversed upon exceeding a critical amount. Furthermore, via the work-hardening imparted by the peening process, the resistance of the substrate against deformation can be enhanced, thus improving the coating's resistance to delamination due to its inability of replicating the substrate texture [79], [83], [127].

The effect that the coating has on tribological, and corrosion resistance is also dependent on the coating's adhesion to the substrate. Poor adhesion causes the coating to easily flake off impacting negatively its performance [77]. Zhang *et al.*[80] observed a decrease of nearly by half, in the specific wear rate of duplex treated, via high energy shot peening treatment and TiN coating, industrial pure titanium

compared to the TiN coated-only sample. Similarly, Horiuchi et al. [115] observed a diminished wear rate for a DLC coating applied over a shot peened aluminium alloy surface compared to the DLC coated- only substrate which exhibited evidence of extensive adhesive wear. Such hybrid treatments were also observed by Zhang *et al.* [80] and Cao *et al.* [128] to result in higher values of hardness.

2.6 Summary

Throughout this chapter a background on, the investigated material, regarding the material degradation through cavitation and cavitation-corrosion and the effects surface treatments induce, was provided.

Additive manufacturing is being considered over conventional processes due to its various advantages such as rapidly producing parts having a complex geometry. However, additively manufactured Ti64 has various limitations because of the fabrication process itself which has a tendency of resulting in porosity, detrimental tensile stresses and a poor surface finish. These in turn negatively impact the wear, mechanical, corrosion and anti-fouling resistance of the material.

Moreover, components exposed to variations in pressure such as piping systems, pump impellers or propellers, are prone to material degradation via cavitation which causes pits, micro-cracks and cavities at the surface. Additionally, such components play a major role in marine transportation thus are also exposed to the marine environment which is corrosive by its nature. This enhances the material loss rate due to the synergy present between cavitation and corrosion whereby each mechanism aggravates the effect of the other. Thus, to combat all aforementioned limitations whilst enhancing the material's performance, the application of a series of surface treatments in addition to a prior heat treatment, is being proposed.

The bulk and surface characteristics of duplex treated Ti64 are, to date, not extensively studied. Even more so, when applied to additively manufactured substrates. Similarly, in the majority of available research, cavitation testing was applied to wrought Ti-6Al-4V. Limited information regarding the cavitation resistance of substrates treated with the highlighted surface engineering techniques can be found in literature. Thus, this research intends to contribute to existing knowledge and give further insight into the proposed areas of research.

Chapter 3: Materials and Methods

3.1 Substrate Material

The samples were manufactured via a laser powder bed fusion technique known as selective laser melting (SLM), from Ti-6Al-4V powder particles, having diameters ranging between 15 and 53 μm and the composition listed in Table 3.1.

Table 3.1 Chemical composition of Ti-6Al-4V powder particles [129].

	Ti	Al	V	Fe	O	N
(wt.%)	Bal.	6.16	4.30	0.16	0.09	0.01

An AmPro Innovations SP100 Metal 3D Printer (China), situated at Southeast University in Nanjing, China, was utilized to build the samples, as per the parameters listed in Table 3.2. These parameters were adopted as they resulted in minimal porosity, less than 1%, which is required due to its negative effect on the material's mechanical properties. Samples were built along the z-direction given their cylindrical geometry. Subsequently, all the samples were annealed, using a TAV Dualjet TPH-200 (Italy) furnace, in a nitrogen atmosphere at a ramp rate of 5 ºCmin^{-1} up to 800 ºC which was held for 2 hours followed by furnace cooling. Annealing was carried out in order to relieve detrimental stresses induced during the build process. The printed Ti-6Al-4V cylindrical coupons had a diameter of 20 mm and a thickness of 6 mm, whilst the dimensions of the tensile, impact and axial fatigue specimens are explained in further detail in Section 3.6.

Table 3.2 Laser powder bed fusion build parameters.

Build parameters	
Laser Power	100 W
Laser Speed	600 mms^{-1}
Beam Offset	10 μm
Layer Thickness	30 μm
Hatch Distance	70 μm
Internal Overlap	≥ 100 μm
Scanning Pattern	Stripe[2]
Stripe Width	10 mm
Scanning Orientation	Start at 45º, rotate by 66.66º

[2] A laser scanning pattern defined by the stripe width, the distance between adjacent stripes (hatch distance) and the scan direction [130].

3.2 Sample Preparation

The printed cylindrical coupons were metallographically prepared using standard metallographically techniques to a mean surface roughness, R_a, equivalent to approximately 45 nm using a Struers Tegramin-25 (Denmark) semi-automatic grinder and polisher. This was achieved by initially grinding the surface using SiC grinding papers starting from a rough P400 grit up to a finer P4000 grit. Once a cloudy appearance was obtained, the surface was polished to a mirror finish using an MD-Chem (Struers) polishing cloth lubricated with a solution composed of 10 vol.% hydrogen peroxide, H_2O_2, and 90 vol.% colloidal silica, OP-S (Struers). The aim of this step was to eliminate the resulting high surface roughness, characteristic to additively manufactured components. This procedure was also used for the axial fatigue specimen. A jig was constructed which facilitated the polishing of the specimen's flat sides, whilst the curved edges were manually ground using a grinding stone and grinding papers of increasing grit size and finally polished using a rotary polisher.

3.3 Surface Treatments

Following heat treatment and polishing three different sample batches were shot peened, PVD coated and treated with a combination of both surface treatments, respectively. Shot peening was applied with the aim of enhancing the fatigue performance and wear resistance of the built material via the induced hardening and compressive residual stresses. Whilst the PVD coating was designed with the aim of enhancing the wear resistance and providing the substrate with protection from corrosion. The treatments were then combined to determine whether a superior performance could be achieved.

3.3.1 Shot Peening

The shot peening treatment was carried out using a custom made set up consisting of a reservoir feeding the peening media to an air gun equipped with a PTFE nozzle, connected to a high air pressure source, in an Industrial Surface Treatments LTD. AB850 (UK) air blasting cabinet. Peening was carried out using the parameters listed in Table 3.3. Zirshot Z300 ceramic shots, supplied by Saint-Gobain were used. The shots had diameters ranging between 300 and 425 μm and the following composition: 60 – 70% ZrO_2, 20 – 33% SiO_2 and < 10% Al_2O_3. Ceramic shots were chosen due to

their chemical inertness which prevents any galvanic corrosion from occurring in case of embedded fragments at the sample surface.

In literature, the ideal Almen intensity adopted for peening Ti-6Al-4V ranges between 0.20 and 0.32 mmA, evidenced by the resulting hardening and significant residual stresses induced which have been observed to be beneficial in improving the substrate's resistance against wear [10], [11], [76], [131], [132], [133]. To determine the parameters, several Almen intensity tests were carried out varying the air pressure, specimen-to-nozzle distance, nozzle diameter and length were altered until an intensity of 0.20 mmA was achieved. This specific intensity was chosen as it has been associated with good hardening and significant residual stress generation without resulting in over peening or significant roughening. These tests consisted of peening A-Industrial Plus SAE 107 steel strips for different durations starting from 5 seconds up to a duration of 160 seconds, with successive doubling in the duration. For each strip, the arc height was measured prior to and following peening using a Mahr MarCator 1075R (Germany) Almen gauge. Shockform Saturation Graph Solver version 3.9 software (Canada) was subsequently used to calculate the saturation time and intensity. The saturation time corresponds to the point at which the peening duration has doubled and the increase in arc height is less than 10%. The peening intensity corresponds to the arc height obtained at the saturation point [134].

Following peening, all samples underwent ultrasonic cleaning in a soap-water solution for 15 minutes to remove any contaminants which may have become embedded during the surface treatment process.

Table 3.3 Shot peening parameters.

Shot peening parameters	
Shot Media	Z300
Nozzle Diameter	6 mm
Nozzle Length	80 mm
Shot Flow Percentage	100%
Pressure	7 bar
Nozzle-to-Specimen Distance	100 mm
Almen Intensity	0.20 mmA
Duration	60 s
Coverage	500%

3.3.2 Coating Deposition

Coating deposition was carried out using a Teer UDP800 closed field unbalanced magnetron sputtering ion plating system (China) situated at Southeast University in Nanjing, China. Before deposition, any oxide layers were removed by subjecting the surface to sputter cleaning via high energy bombardment up to 400 V and 0.5 A for 10 minutes followed by 10 minutes of cooling.

The coating deposited has a multilayer structure composed of the following layers: Ti, TiN, TiAlN and TiAlCuN. TiN coatings are known to exhibit a high hardness, excellent wear and corrosion performances [15], [16], [17]. A multiple layer structure was chosen as it provides better load carrying capabilities and corrosion protection whilst Aland Cu were chosen as alloying elements as they enhance the coating's hardness and toughness, respectively [103], [104], [105]. Whilst Cu also provides biofouling resistance [109], [110].

The various layers were successively deposited at a temperature of 148 ºC, using a bias of 90 V, a deposition pressure of 0.23 Pa, a target-to-specimen distance 14.5 cm. Four targets were utilised and the target currents were adjusted from 0.5 to 8 A with time according to the deposited layer. The deposition parameters used are listed in Table 3.4. The research team at Southeast University chose these parameters which following an optimization process, were observed to result in a structurally sound coating having a significant hardness and good adhesion between the layers and at the substrate surface.

The designations used for the sample conditions studied are explained in Table 3.5.

Table 3.4 Coating deposition parameters.

Layer number	Time duration and distribution (mins)		Bias voltage (V)	Nitrogen flow (%)	Target current (A)			
					1:Ti	3:Ti	2:Al	4:Cu
Cleaning	10	0	200	0	0.5		/	/
		Ramp up to 2	400					
		8	400					
Ti	15	0	90	0	0.5		/	/
		Ramp up to 10			8			
		5						
TiN	60	0	90	100	8		/	/
		Ramp up to 30		35				
		30						
TiAlN	60	0	90	35	8		2	/
		Ramp up to 5					8	
		55						
TiAlCuN	60	60	90	35	8		8	8

Table 3.5 Designations used for the different sample conditions investigated.

Designation	Sample Condition
As-built (AB)	Laser powder bed fused (LPBF)
Heat-treated (HT)	LPBF + heat treated + polished
Shot-peened (SP)	LPBF + heat treated + polished + shot peened
Duplex treated (DU)	LPBF + heat treated + polished + shot peened + coated
PVD Coated (PVD)	LPBF + heat treated + polished + coated

3.4 Surface and Near-Surface Characterization

3.4.1 Microscopy and Elemental Analysis

Micrographic analysis of the surface and cross-section (along the build direction) of the different sample conditions was carried out using a Carl Zeiss Axioscope 5 (Germany) optical microscope, for low magnification analysis and a Carl Zeiss Merlin Gemini (Germany) scanning electron microscope (SEM), for higher magnification analysis. The SEM was operated at 15 kV acceleration voltage and 1 nA probe current, using a Type II secondary electrons (SE2) detector. Prior to imaging work, the substrates were etched using Kroll's reagent composed of 5% HF, 13.5% HNO_3 and 81.5% H_2O from concentrated stock. For chemical composition analysis, Ametek

EDAX (USA) energy dispersive spectroscopy (EDS) analyser was used in conjunction with the SEM.

In order to analyse the coating, the sample was completely submerged and mounted in a cold mount resin to ensure that the coating is retained. The mounted sample was then sectioned using a Struers Accutom-10 (Denmark) precision cutting machine equipped with a SiC cutting wheel. Additionally, a minimal feed rate of 0.015 mms^{-1} was used. Once sectioned, the sample was ground and polished.

3.4.2 Scratch Testing

Scratch testing was carried out via a Bruker UMT TriboLab (USA) set up with a 60° Rockwell C indenter. Testing was carried out on the duplex treated (DU) and the coated only (PVD) substrates. Five scratches per sample were made, using the test parameters listed in Table 3.6. The scratch morphology was observed via a Carl Zeiss Axioscope 5 (Germany) optical microscope, and a Carl Zeiss Merlin Gemini (Germany) scanning electron microscope (SEM) to deduce the critical loads (L_C) at which failure took place. The critical loads were identified according to *EN ISO 20502:2005: Fine ceramics – Determination of adhesion of ceramic coatings by scratch testing* [135].

Table 3.6 Summary of scratch testing parameters.

Scratch testing parameters	
Indenter	60° Rockwell C
Type of load applied	Ramped
Initial contact force	1 N
Final contact force	40 N
Scratch length	10 mm
Scratch velocity	0.33 mms^{-1}
Loading rate	1.33 Ns^{-1}

3.4.3 Profilometry

An AEP Technology NanoMap-500LS (USA) contact profilometer was used to obtain linear scans of the surface topography of the different conditions. A single line scan consisted of a distance of 2500 μm scanned at 25 μms^{-1} with a lateral resolution of 1 μm and a vertical tip resolution of 0.1 nm. Five scans were performed, perpendicular to each other, to obtain average roughness measurements.

3.4.4 Electron Backscatter Diffraction (EBSD)

To analyse various microstructural features such as grain size and texture, the electron backscatter diffraction (EBSD) technique was employed. The specimens were sectioned along the build direction, and the cross-sections were mounted in a conductive mount. The samples were metallographically polished to a mirror finish using the procedure listed in Section 3.2 ensuring that no scratches or other surface imperfections were visible which could interfere with the analysis. Once polished, the samples were ultrasonically cleaned in a soap solution diluted with deionised water for 10 minutes followed by rinsing with ethanol and drying using compressed nitrogen to eliminate any contaminants.

EBSD scans were performed using Carl Zeiss Merlin Gemini SEM equipped with an EBSD/EDX Ametek (USA) EBSD detector on the various sample conditions. The mounted samples were fixed to a sample holder at an incline of 70º. This angle is used as it allows the easier detection of resultant Kikuchi bands[3] by enhancing their contrast. An area of 290 μm by 240 μm was scanned using a step size of 0.5 μm, a working distance between 12 and 14 mm, a working voltage of 20 kV and a probe current of 10 nA. Subsequently, analysis was carried out using the OIM Analysis™ version 8 (Germany) software. Scans obtained were filtered to eliminate any points having a confidence interval less than 0.1 and grain size less than five points. Furthermore, the resultant scans were cleaned using a grain dilation method ensuring that less than 25% of the scan data was altered.

3.4.5 X-ray Diffraction (XRD) Phase Analysis

For phase analysis, a Rigaku Ultima IV (Japan) diffractometer using a Bragg Brentano geometry was used. Scans were performed over a 2θ range of 20º to 90º with a step size of 0.02º and a dwell time of 2 seconds. The thin PVD coating was analysed using the same diffractometer but in the Glancing Incidence Asymmetric Bragg (GIAB) configuration. The same 2θ range, step size and dwell time were used however with a glancing angle of 3º. Both diffractometers employed a CuKα radiation source operated at 45 kV acceleration voltage and current of 40 mA. The resulting diffraction patterns

[3]Kikuchi bands are patterns resulting from Bragg reflections of inelastically scattered electrons [136].

were analysed using the Rigaku PDXL2 XRD (Japan) software and matched with peaks present in the software's databases.

3.4.6 X-ray Diffraction (XRD) Stress Measurements

Residual stresses were determined by using X-ray diffraction for the determination of crystal strain which in turn can be converted to stress assuming a linear elastic distortion of the lattice. To measure the stresses, present at different layers, electropolishing was used to remove very thin layers of material in the micrometre range. The various steps followed during this process are highlighted in Figure 3.1. This process was repeated until compressive residual stresses were no longer detected for the treated samples in order to generate representative stress-depth profiles.

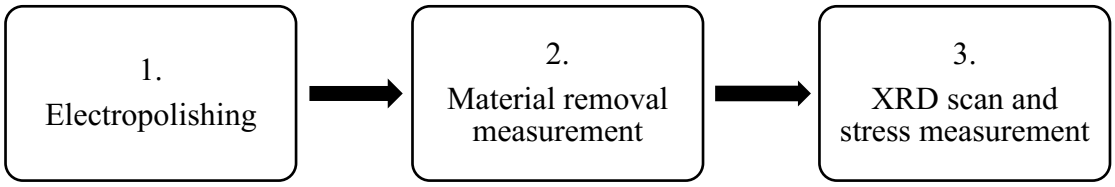

Figure 3.1 Processes involved to obtain XRD stress measurements.

3.4.6.1 Electropolishing

Layers were progressively removed via a Struers LectroPol-5 electropolishing machine (Denmark) equipped with a mask having a 1 cm^2 aperture. Flat samples were used and were masked accordingly using adhesive tape, which is impervious to the electrolyte, to expose an area of 1 cm^2. The whole surface did not undergo electropolishing to preserve a portion which can be used as a reference point for material removal measurements. The exposed area was then aligned with the aperture of the mask and the sample was held in place via adhesive putty.

An electrolyte composed of 10% perchloric acid and 90% ethanol from concentrated stock was used which was kept at room temperature. The process was carried out at an applied voltage of 70 V for a duration of 10 seconds which removes approximately 25 µm of material. Once electropolished, the sample underwent ultrasonic cleaning in acetone for 5 minutes to remove any residual material and was then dried using compressed air.

3.4.6.2 Profilometry

Following electropolishing, the depth of material removed was measured via contact profilometry. An AEP Technology NanoMap-500LS contact profilometer (USA) was

used to carry out linear scans 18 mm in length at a scan speed of 50 μms^{-1}, ranging across the 1 cm^2 exposed area, starting and finishing at the untouched areas. In total, six linear horizontal and vertical scans were carried out, at and 1000 µm above and below the centre to obtain an average depth.

Figure 3.2 depicts a typical scan obtained following electropolishing for a duration of 10 seconds. The obtained scans were then analysed using the SPIP- Scanning Probe Image Processor version 6.7.9 (Denmark) software. As observed Figure 3.2, the deepest point was taken a reference point, additionally five random positions were chosen at both the masked surface and the electropolished area. The difference between the chosen points for the masked area (blue points) and the reference point (red point) is calculated and averaged. Similarly, this is done for the electropolished areas (black points). Thus, resulting in two average depth values, D_1 and D_2, with respect to the reference point. The overall depth of material removed is then obtained by calculating the difference between the two average depth values ($D_1 - D_2$). The final average depth of material removed was then calculated by averaging the overall depth calculated for the six different scans.

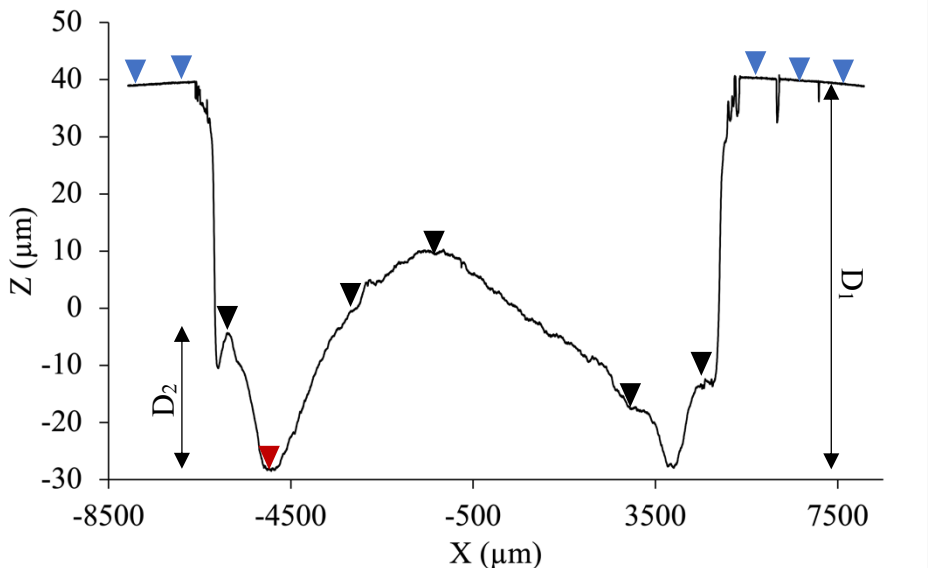

Figure 3.2 Surface profile of electropolished LPBF heat-treated Ti-6Al-4V with marked reference points used for the average depth of material removed calculations.

3.4.6.3 XRD Scans and Data Analysis

Stress measurements were obtained using the $Sin^2\psi$ method as per BS EN 15305 (2008) – *Non-destructive Testing – Test Method for Residual Stress analysis by X-ray Diffraction* [137], thus a Rigaku Ultima IV (Japan) diffractometer in the Bragg-Brentano configuration was employed for this analysis. The α-Ti (213) pyramidal plane peak was chosen to measure peak shifting therefore scans were carried out over a 2θ range of 139º to 144º at a step size of 0.02º and acquisition time of 5 seconds. This plane was chosen as it results in more accurate measurements due to its reflection occurring at high 2θ angles, at around 141.9º, which typically for minor interplanar spacing changes, exhibit more pronounced shifting. Additionally, this plane encompasses the *c* and *a*- axis thus, stress measurements more representative as values are averaged over both directions [138], [139].

Measurements were taken at seven ψ tilts, from 0º to 60º. The diffractometer employed a CuKα radiation source operated at 45 kV acceleration voltage and current of 40 mA. Prior to each scan, the sample underwent a theta auto-alignment process as with electropolishing changes in topography are observed. This process was carried out to ensure that the exposed area is properly aligned by compensating for any deviations which may impact the 2θ position and thus, the stress value.

The stress can then be obtained via lattice strain measurements. The latter are calculated by determining the chosen peak's 2θ position from which the inter-planar spacing, d, can be derived via Bragg's Law using Equation (3.1) [138].

$$n\lambda = 2d\sin\theta \tag{3.1}$$

where, n is an integer equivalent to 1, λ is the wavelength equivalent to 1.5406 x 10^{-10} m, θ is the Bragg angle which is determined by first obtaining the peak's 2θ position provided when analysing the obtained pattern using Rigaku PDXL 2 XRD (Japan) software. The software automatically determines the peak position via full width at half maximum (FWHM). Using Equation (3.2), the stress value can be calculated using the measured inter-planar spacing, d [138],

$$\sigma_\phi = \frac{E}{(1+\upsilon)\sin^2\psi}\left(\frac{d_\psi - d_n}{d_n}\right) \tag{3.2}$$

where, σ_ϕ is the stress along angle ϕ, E is the material's Young's modulus, υ is the material's Poisson ratio, ψ is the tilt angle, d_ψ is the inter-planar spacing of stressed

crystallographic planes and d_n is the inter-planar spacing of planes parallel to the surface. Via the $Sin^2\psi$ method, the inter-planar spacing, d, is calculated for each of the ψ tilts. Subsequently, a plot of d_ψ versus $sin^2\psi$ is obtained from which the values of the gradient, m, and y-intercept, c, can be derived. Thus, Equation (3.2) can be arranged in the format of Equation (3.3 and presented as follows in Equation (3.4) [138], [140]:

$$y = mx + c \tag{3.3}$$

$$d_\psi = \frac{d_n \sigma_\phi (1+\upsilon)}{E} \sin^2\psi + d_n \tag{3.4}$$

Considering the gradient component only, Equation (3.5) is then used to determine the stress value, σ_ϕ, substituting the y-intercept value calculated for d_n and the gradient obtained for m [140].

$$m = \frac{d_n \sigma_\phi (1+\upsilon)}{E} \tag{3.5}$$

Table 3.7 provides a summary of the parameters employed for XRD stress measurements.

Table 3.7 Summary of parameters used for XRD stress measurements.

X-ray diffraction stress measurement parameters	
ψ tilts	7 tilts from 0º to 60º in increments to 10º
2θ range	139º to 144º
Step size	0.02º
Acquisition time	5 s per step

3.5 Hardness Analysis

3.5.1 Surface Microhardness

Using a Mitutoyo MVK-H2 (Japan) microhardness tester in conjunction with a pyramidal diamond indenter, Vickers surface microhardness measurements were obtained. A load of 100 gf was applied for 10 seconds and a series of five indentations were carried out. Spacing between indents was kept equivalent to greater than two and a half times the indent's diagonal as stipulated by ASTM E97-17 *Standard Test Methods for Vickers Hardness and Knoop Hardness of Metallic Materials* [141].

3.5.2 Surface Nanohardness

A Nanomaterial NanoTest 600 (UK) was operated using the nano hardness test parameters in Table 3.8 to apply an array of thirty equally spaced indentations. Testing

was only carried out on the coating deposited on a metallographically polished built Ti-6Al-4V (PVD) sample to determine the properties of the coating, eliminating the effect of the softer substrate which is unavoidable for microhardness measurements. Additionally, nanoindentation could not be carried out on the duplex treated (DU) and shot peened (SP) samples conditions due to their high surface roughness.

Table 3.8 Summary of nano hardness testing parameters.

Nano hardness testing parameters	
Indenter	Berkovich 120º diamond tip
Initial load	0.1 mN
Maximum load	50 mN
Dwell time	5 s
Loading and unloading rate	1 mNs^{-1}

3.5.3 Profile Hardness

For profile hardness measurements a microhardness tester with a pyramidal diamond indenter was used applying a load of 100 gf. These hardness measurements were only carried out for the shot-peened (SP) and duplex treated (DU) sample to determine the extent of the peening treatment's impact below the surface. To obtain a microhardness profile of the change in microhardness with depth, measurements were made starting at the surface into the bulk with, five indentations 20 μm apart were made at every depth location. The successive sets of indents were made 30 μm below the previous set and each time shifted to the right by 5 μm to ensure that all indents were equally spaced. Measurements were gathered up to a depth of approximately 200 μm.

3.6 Mechanical Properties Analysis

All test specimen were built horizontally since horizontally built specimen typically exhibit better tensile and fatigue strength due to the applied loads being perpendicular to the columnar grains thus, there are more grain boundaries which aid to hinder crack propagation. Similarly, for impact specimen, horizontally built samples have been observed to absorb more energy prior to fracture. [6], [142]

3.6.1 Tensile Testing

Tensile specimens were manufactured according to the geometry and dimensions as shown in Figure 3.3. These were tested using an Instron 5982 (USA) electromechanical universal testing system equipped with an Instron 2620-604 (USA) dynamic extensometer. A strain rate of 3 mm min^{-1} was applied, and testing was carried out at a temperature of 25°C and a humidity of 62%. Testing was carried out on as-built and heat treated (HT) specimen to determine the actual mechanical properties of the substrate material investigated with five repeats being conducted. The specimens were manufactured and tested as per ASTM E8/E8M-16 - *Standard Test Methods for Tension Testing of Metallic Materials* [143]. From data recorded by the machine and extensometer, the Young's modulus, 0.2% yield strength, ultimate tensile strength and elongation were calculated. For the determination of the Young's modulus, the extensometer data was used whilst the 0.2% yield strength was deduced using the 0.2% offset method via the Origin (USA) software.

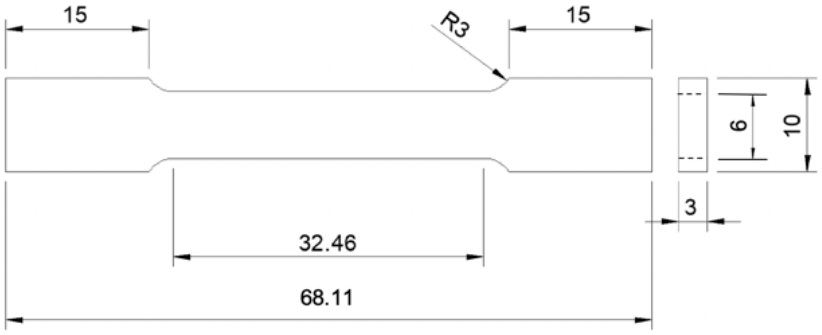

Figure 3.3 Dimensions of tensile testing specimen.

3.6.2 Impact Testing

Charpy impact specimens having the geometry and dimensions shown in Figure 3.4 were tested via an Instron 450MPX-J2 (USA) motorised pendulum impact testing system. The specimens were manufactured and tested as per ASTM E23-16 - *Standard Test Methods for Notched Bar Impact Testing of Metallic Materials* [144]. During impact, the maximum load, time to reach max load, impact velocity, total duration and total energy absorbed were recorded. The material tested was in the as-built and heat-treated (HT) condition and a total of five repeats were carried out. Following testing, the fractures were analysed via scanning electron microscopy to determine the nature of the fracture.

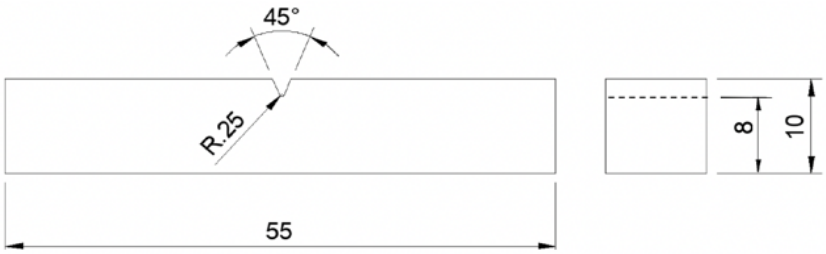

Figure 3.4 Dimensions of impact testing specimen.

3.6.3 Axial Fatigue Testing

Specimens having the geometry and dimensions as observed in Figure 3.5, in the as-built and heat-treated, shot-peened, and duplex treated conditions, underwent axial fatigue testing to quantify the amount of cycles the material can endure until failure and the impact of the applied surface treatments on the material's fatigue performance. The PVD coated only condition was not tested as such coatings are not typically deposited with the aim of improving the fatigue strength and contradicting results have been reported on their impact on the axial fatigue performance [119], [120]. By testing the duplex treated condition, the aim was to determine whether the process of the coating deposition impacts the effect imparted previously by shot peening. The dimensions chosen and testing methodology followed were as per as per ISO 1099:2017(E): *Metallic materials- Fatigue testing- Axial force-controlled method* [145]. To conform with the standard, the gauge section of the specimen was ground and polished using the sample preparation method listed in Section 3.2, ensuring that any visible and significant scratches and defects were removed.

Axial fatigue testing was performed using an Instron 8802 servo hydraulic fatigue testing machine at room temperature under load control at a frequency of 20 Hz and an amplitude of 2.25 kN. The load range applied was from 8 kN to 12.5 kN, with the maximum load being equivalent to 570 MPa which is approximately 70% of the yield strength. As the samples were loaded, measures were taken to ensure that samples are perpendicularly aligned to eliminate the effect of shear stresses. Six repeats for each condition were tested and for each test the total number of cycles endured was recorded. Following testing, fractured samples were analysed via scanning electron microscopy to determine the cause and nature of the fractures.

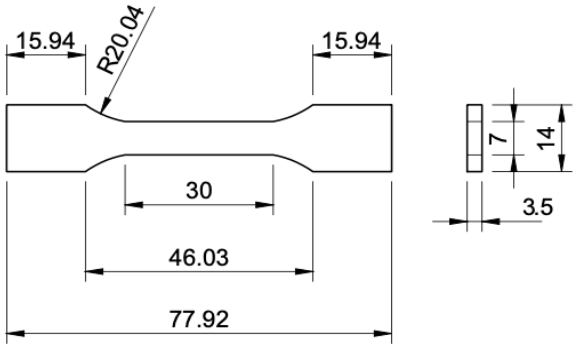

Figure 3.5 Dimension of axial fatigue specimen.

3.7 Corrosion Testing

Testing was carried out using a Gamry Interface 1000™ (USA) potentiostat connected to a 3-electrode setup as shown in Figure 3.6. The working, counter and reference electrodes were the titanium-based test coupon, a platinum coated rod and a saturated calomel electrode (SCE), respectively.

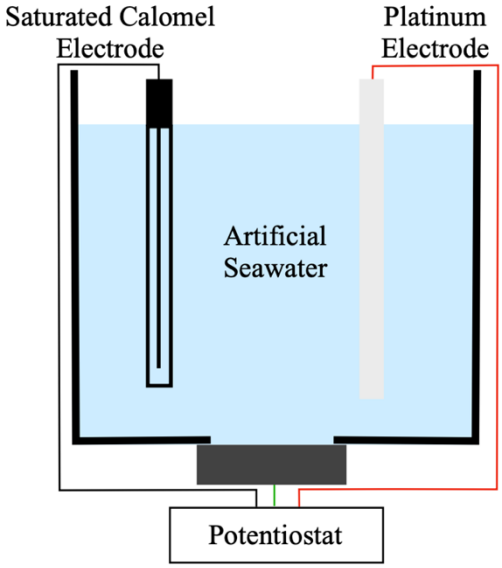

Figure 3.6 Corrosion testing set up.

The samples were exposed to 300 ml of artificial seawater, which was kept at a temperature of 25 ± 2 ºC, to simulate the marine environment. This temperature was chosen to simulate the seawater's surface temperature which generally ranges between - 2 and 30 ºC depending on the region [146]. Additionally, it is considered that as rule a of thumb, an increase in temperature by 10 ºC typically doubles the corrosion rate [147]. Thus, a higher temperature was chosen to observe the material's behaviour under aggravated conditions as much as possible. The electrolyte was formulated in accordance with ASTM D1141-98 (2021) - *Standard Practice for the Preparation of Substitute Ocean Water* [148]. Table 3.9 provides the chemical composition of the

substitute ocean water. It is composed of two stock solutions, 6 ml of solution No.1 and 3 ml of solution No.2. These are then diluted in 300 ml deionised water in addition to 1.23 g of Na_2SO_4 and 7.36 g of NaCl.

Table 3.9 Chemical composition of stock solutions.

Chemical Compound	Concentration (gL^{-1})
Stock Solution No. 1	
$MgCl_2.6H_2O$	555.6
$CaCl_2$	57.9
$SrCl_2.6H_2O$	2.1
Stock Solution No. 2	
KCl	69.5
$NaHCO_3$	20.1
KBr	10.0
H_3BO_3	2.7
NaF	0.3

Theoretically, a surface area of 0.785 cm^2 was exposed to the electrolyte, however this is only true for the heat-treated (HT) and PVD coated (PVD) conditions as their surface roughness is less than 0.14 μm. For the shot-peened (SP) and duplex treated (DU) samples, the surface roughness exceeds the stipulated value thus the actual exposed area is derived by determining the developed interfacial area ratio or S_{dr} parameter which accounts for the additional area owing to the morphology of the surface. To obtain this parameter, 3D maps of the surface were obtained via an AEP Technology NanoMap-500LS (USA) contact profilometer and were analysed using the SPIP-Scanning Probe Image Processor version 6.7.9 (Denmark) software which calculated the S_{dr} parameter automatically. Given that both the SP and DU samples had a similar surface topography, for both sample conditions the S_{dr} parameter was equivalent to 1.03% thus, the actual exposed area is 0.793 cm^2.

Initially, the open circuit potential (OCP) was monitored for 2 hours to allow for its stabilisation. This was followed by potentiodynamic polarisation sweeps from a range of - 200 mV versus OCP to + 1.5 V versus reference at a sweep rate of 0.1667 mVs^{-1}. The test was repeated three times for each of the sample conditions to ensure repeatability. Following corrosion testing, the exposed areas were then observed via optical and scanning electron microscopy. A summary of the corrosion test parameters is provided in Table 3.10.

Table 3.10 Potentiodynamic test parameters.

Potentiodynamic testing parameters		
Voltage range		- 200 mV vs. OCP to + 1.5 V vs. SCE
Sweep rate		0.1667 mVs^{-1}
Testing solution		Artificial seawater
Solution temperature		25 ± 2 ºC
Test area:	**HT**	0.785 cm^2
	SP	0.793 cm^2
	DU	0.793 cm^2
	PVD	0.785 cm^2

3.8 Cavitation Testing

For cavitation testing, the set up shown in Figure 3.7 Cavitation testing set up. A Hielscher UIP500hd (Germany) transducer, equipped with a titanium horn having a 15.9 mm Ti-6Al-4V replaceable tip, was used to generate cavitation. The indirect cavitation method was adopted following closely the ASTM G32-16 *Standard Test Method for Cavitation Erosion Using Vibratory Apparatus* [61]. Samples were fixed onto a holder such that the distance between the tip and the sample is approximately 2 mm. This indirect method was adopted as the direct method, whereby the tip is the test sample, does not allow for electrochemical analysis since the tip is not isolated and could also result in inaccurate material loss measurements due to galvanic corrosion occurring between the sample and the horn [55]. As per the standard, the transducer was operated at a frequency of 20 kHz and an amplitude of 50 μm.

Testing was conducted in artificial seawater, formulated as stated in Section 3.7, and kept at a temperature of 25 ± 2 ºC for uniformity across the different tests. During testing, the temperature was monitored to ensure that it is still within range as the generation of cavitation is typically accompanied with an increase in temperature due to the fluctuating pressures. To aid with keeping the temperature constant, the artificial seawater solution itself was continuously circulated using a pump. Samples underwent cavitation for a total duration of 4 hours and mass loss measurements were conducted in intervals using a Radwag AS60/220.X2 PLUS (Poland) high precision weighing balance. Measurements were recorded to an accuracy of ± 0.01 mg at 10-minute intervals for the first hour, at 20-minute intervals for the second hour and at 30-minute intervals for the third and fourth hours. Before weighing, the samples were

ultrasonically cleaned and rinsed with alcohol then thoroughly dried using hot air each time to ensure that no water retention or foreign particles are present which could impact the accuracy of the measurements.

From data gathered, the cumulative mass loss and mass loss rates were quantified. Additionally, the condition of the surface was analysed via optical and scanning electron microscopy at intervals of 30-, 120- and 240 minutes. A summary of the test parameters is provided in Table 3.11.

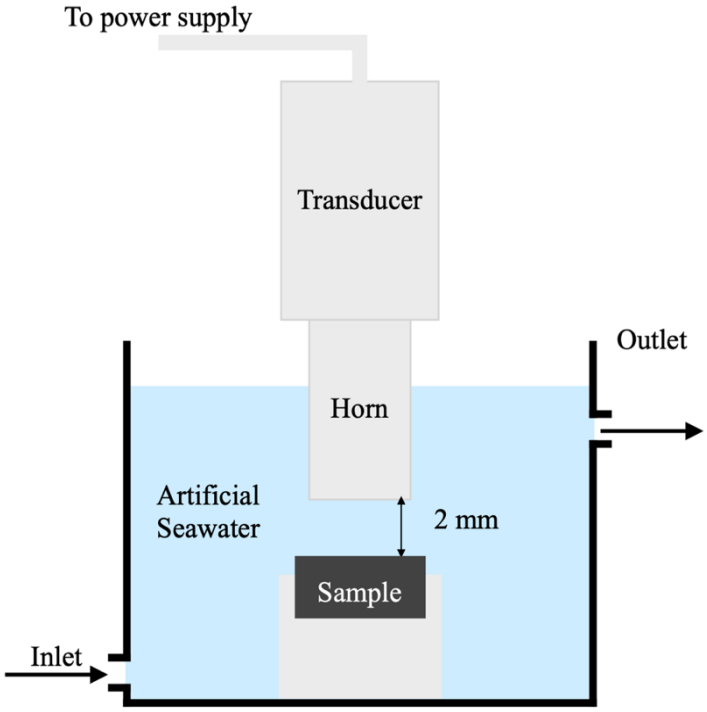

Figure 3.7 Cavitation testing set up.

Table 3.11 Cavitation testing parameters.

Cavitation testing parameters	
Frequency	20 kHz
Amplitude	50 µm
Tip diameter	15.9 mm
Horn-to-sample distance	2 mm
Duration	4 hrs
Testing solution	Artificial seawater
Solution temperature	25 ± 2 ºC

3.9 Cavitation-Corrosion Testing

To investigate the cavitation-corrosion behaviour, the cavitation testing set up and parameters detailed in Section 3.8 were used in addition with the use of a potentiostat and electrodes for electrochemical analysis as depicted in Figure 3.8.

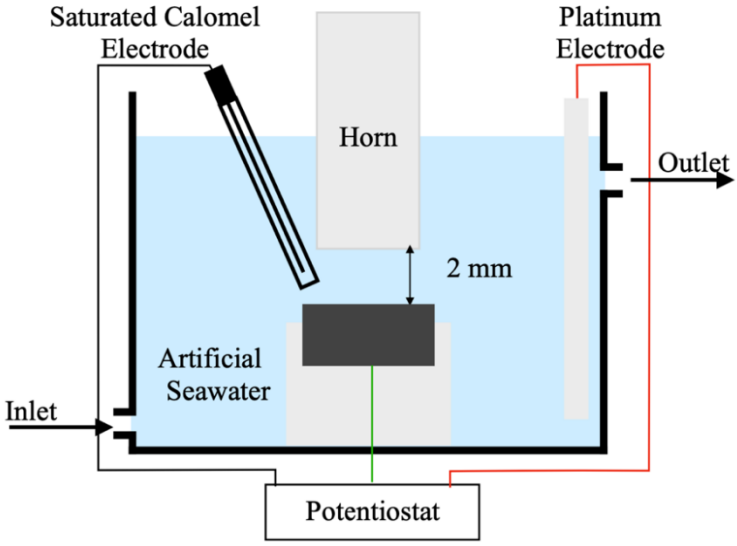

Figure 3.8 Cavitation-corrosion test set-up.

A Gamry Interface 1000™ (USA) potentiostat, to which the sample, reference and counter electrode were connected, was used to induce an anodic potential of 0.2 V with respect to the saturated calomel reference electrode. This value is determined from polarisation curves obtained from potentiodynamic tests. However, this value could not be determined from curves obtained under static conditions as the effect of cavitation is expected to shift the curves upwards and to the left since it compromises the naturally occurring oxide layer via the impact of bubbles. Hence, potentiodynamic testing using the same parameters as in Section 3.7, was carried out under cavitation conditions. Testing was conducted on the HT and SP sample conditions as for the DU and PVD samples, the removal of the coating due to cavitation midway during the PD scan resulted in conflicting results. A value of 0.2 V was chosen since at that value the samples were in the passive region thus, this ensures that all samples are in the passivating regime when undergoing cavitation.

Similarly, testing was conducted in circulating artificial seawater kept at a temperature of 25 ± 2 ºC. Prior to testing, the samples were thoroughly cleaned and then weighed using a high precision weighing balance. Via potentiostatic testing, the voltage was then induced for a total of 4,200 seconds. During the initial 1,200 seconds the current was monitored under static conditions. At 1,200 seconds, cavitation was initiated for

1,800 seconds and upon stopping, the current was monitored for a further 1,200 seconds under static conditions. The potentiostat recorded the change in the dynamic anodic current with time and this data was then used to quantify material losses as described in 3.9.1. Additionally, all tests repeated three times for each condition. Similarly, to Section 3.7, the change in the actual test area due to the induced roughness was also accounted for during potentiostatic testing under cavitation.

Following testing, all samples were ultrasonically cleaned and rinsed with alcohol then dried using hot air prior to weighing using a high precision weighing balance. The surface was then analysed via optical and scanning electron microscopy. Elemental analysis of any debris and artefacts present was also carried out using energy dispersive spectroscopy. A summary of the test parameters is provided in Table 3.12.

Table 3.12 Cavitation-corrosion testing parameters.

Cavitation-corrosion testing parameters	
Frequency	20 kHz
Amplitude	50 μm
Tip diameter	15.9 mm
Horn-to-sample distance	2 mm
Duration	4200 seconds (1800 seconds under cavitation)
Testing solution	Artificial seawater
Solution temperature	25 ± 2 ºC
Potential	+ 0.2 V vs. SCE

3.9.1 Material Loss Quantification

From data collected during testing and gravimetric measurements taken, the material losses due to the various mechanisms were then quantified. The total wear and corrosion components can be quantified using the following equation [71]:

$$CW = C^* + W^* \quad (3.6)$$

where, CW is the total loss due to cavitation-corrosion (g), W* is the loss due to the mechanical wear component (g) and C* is the loss due to the corrosion component (g). CW was obtained via mass loss measurements from mass values obtained prior to and after cavitation-corrosion testing. C* was obtained via Faraday's Law (Equation 3.7) using the data from the dynamic anodic current versus time plots obtained during cavitation-corrosion testing. Upon obtaining CW and C*, W* can be derived from the

subtraction of C* from CW. The error of W* was then obtained through the addition of both C* and CW errors.

$$C^* = \frac{IMt}{nF\rho} \tag{3.7}$$

where, I is the current derived from the area under the current against time plot (A), M is the atomic mass ($gmol^{-1}$), t is the test duration (s), n is the charge no. for the oxidation reaction (obtained from the passive region of their respective Pourbaix diagrams), F is Faraday's constant (96,487 $Cmol^{-1}$), ρ is the density of the substrate (gcm^{-3}). Equation 3.7 yields a result in terms of volume loss thus, this was converted to mass loss by multiplying the volume loss with the substrate's density, or the coating's density in case of the coated conditions.

The valence number, n, and the atomic mass, M, required to calculate C* were derived from Equations 3.8 and 3.9.

$$n = \sum \frac{(at\%).(\text{oxidation number})}{100} \tag{3.8}$$

$$M = \sum X_i M_i \tag{3.9}$$

where, at% is the atomic percentage and X_i is the atomic fraction both of which were determined from EDS elemental analysis of the samples and M_i is the atomic mass of each element which was obtained from the periodic table. The at%, oxidation number and the resulting n and M values are summarized, for each of the sample conditions, in Table 3.13 which includes all parameter values required to calculate C* using Faraday's law. The density values listed were calculated in previous work carried out by the author [149], [150].

The oxidation number, required to calculate the valence, n, of each element was determined from the passive region of each element's Pourbaix diagrams since testing is carried out at a potential at which the material is in a passive state. However, certain metals having varying valences for active dissolution and passive state. This leads to the possibility of uncertainties in the quantification of corrosion's contribution on the total material loss, if both states are present under test conditions [151]. While Pourbaix diagrams simplify the deduction of the likely oxidation state, it should be kept in mind that these diagrams are a simplified model which assume equilibrium conditions and as such kinetic factors arising from electrochemical reactions are ignored. Additionally, these diagrams also do not consider changes in temperature and pressure conditions which may alter the element's stability [152]. Due to these

constraints on accuracy, the resulting values should be considered as an approximation of the actual values.

For the HT and SP sample conditions, the atomic mass is assumed to be equivalent since the peening treatment does not impose any chemical changes. Additionally, for the DU and PVD samples, the atomic mass, density, and oxidation number of the coating were considered due to it being the outermost layer exposed to the electrolyte. This would no longer be valid if gross delamination was to occur exposing the substrate to degradation. However, this was avoided by adopting a short testing duration during which if any coating loss occurred, the exposed area is negligible compared to the coated area thus had no significant impact on the results.

Table 3.13 Faraday's Law parameters calculated for the different sample conditions.

Sample	Main constituents (at%)	Density, ρ (gcm^{-3})	Atomic mass, M ($gmol^{-1}$)	Oxidation number	n
HT	Ti 85.23 Al 12.19 V 2.58	4.43	45.41	+ 4 + 3 + 5	3.904
SP	Ti 85.23 Al 12.19 V 2.58	4.43	45.41	+ 4 + 3 + 5	3.904
DU and PVD Ti/TiN/ TiAlN/ TiAlCuN	Ti 23.77 Cu 0.32 Al 27.27 N 48.63	3.47	27.58	+ 4 + 2 + 3 -	3.100

3.10 Summary

Throughout this chapter, a detailed description of the materials investigated, and methods used was provided. The sample conditions were characterised using surface and near-surface characterisation techniques including microscopy, profilometry, EBSD, XRD phase and stress analysis. Additionally, the mechanical properties of the additively manufactured material were investigated via hardness, tensile, impact and axial fatigue testing. The latter also provided an insight into the effect of the surface treatments on the fatigue performance, while scratch testing allowed for a more detailed analysis of the coating's cohesive and adhesive properties.

Through corrosion, cavitation, and cavitation-corrosion testing the performance of the different sample conditions in a simulated marine environment could be tested providing an insight on the applicability of the chosen material, manufacturing method and surface treatments for such applications. Table 3.14 provides a summary of all the methods and techniques adopted and to which sample conditions these were applied.

Table 3.14 Summary of all analysis techniques and test methods carried out and the respective sample conditions these were applied to.

Analysis techniques and test methods	AB	HT	SP	DU	PVD
Surface and near-surface characterisation					
Microscopy	✓	✓	✓	✓	✓
Scratch				✓	✓
Profilometry	✓	✓	✓	✓	✓
EBSD	✓	✓	✓	✓	✓
XRD phase analysis	✓	✓	✓	✓	✓
Stress measurements	✓	✓	✓	✓	✓
Mechanical testing					
Surface microhardness	✓	✓	✓	✓	
Profile microhardness		✓	✓	✓	
Nano hardness					✓
Tensile		✓			
Impact		✓			
Axial fatigue		✓	✓	✓	
Marine environment simulation testing					
Corrosion		✓	✓	✓	✓
Cavitation		✓	✓	✓	✓
Cavitation-corrosion		✓	✓	✓	✓

Chapter 4: Results and Discussion

In this chapter, results obtained from all the techniques adopted and tests conducted, outlined previously in Chapter 3, shall be presented and discussed. This chapter is organised into seven sections, each delving into the outcomes of specific aspects including, surface and near surface characterisation, mechanical testing, together with corrosion, cavitation and cavitation-corrosion testing.

4.1 Surface and Near-Surface Characterisation

In this section, observations arising from the characterisation of the surface and near surface of the various conditions shall be discussed. To carry out this analysis various techniques were adopted including optical and scanning electron microscopy (SEM), energy dispersive spectroscopy (EDS), profilometry, electron backscatter diffraction (EBSD), and X-ray diffraction (XRD). These results collectively offer an understanding of the surface and near surface condition of the as-built sample prior to and following the application of various treatments.

4.1.1 Micrographic Analysis

Micrographic analysis was conducted to analyse the evolution of the surface and cross-sectional microstructures following the application of microstructure- modifying treatments as discussed in Section 4.1.1.1. Additionally, Sections 4.1.1.2 and 4.1.1.3 delve into the effect of all treatments applied on the as-built surface and the structure of the coating, respectively.

4.1.1.1 Microstructural Modifications: Bulk Heat Treatment and Shot Peening

From the treatments applied, significant modifications in the microstructure were observed following bulk heat treatment and shot peening treatment . Thus, in order to analyse these alterations, micrographs were captured for the as-built (AB) and heat-treated (HT), as observed in Figure 4.1.

The micrographs of the as-built condition, observed in Figure 4.1(a), reveal a microstructure composed of acicular α’ martensite including fine needles in prior columnar β grains (highlighted by the dotted lines) as recorded in literature [4], [153], [154], [155]. The fine α’ phase forms due to the rapid cooling and solidification which results in a nondiffusion transformation from the β phase [155]. The β grains grow epitaxially on the surface of the previously built layer, nearly parallel to the build direction as the bcc β phase grows preferentially along the <100> direction thus its

columnar formation [4], [19], [153], [154]. The fibre-like texture is owed to the grains having a random rotation around the <100> direction [4].

The as-built samples were underwent heat treatment at a temperature of 800 ºC, a temperature below the β transus temperature, followed by furnace cooling. Such high temperatures encourage the coarsening and eventual breakdown of the α' phase into a dual α + β phase [6]. As observed in Figure 4.1(b), the resulting microstructure is composed of a combination of a fine lamaller α phase, presented by the coarser white laths, and β phase, presented by the fine dark regions, forming a basket weave network in prior columnar β grains. With heat treating, the α phase intially nucleates at grain boundaries of the α' phase and as vanadium atoms become expulsed, the β phase starts to form at the α phase grain boundaries [4]. This structure is characteritics of sub-transus heat treatments, such as the one carried out in the current investigation, as observed by various investigators [4], [155], [156].

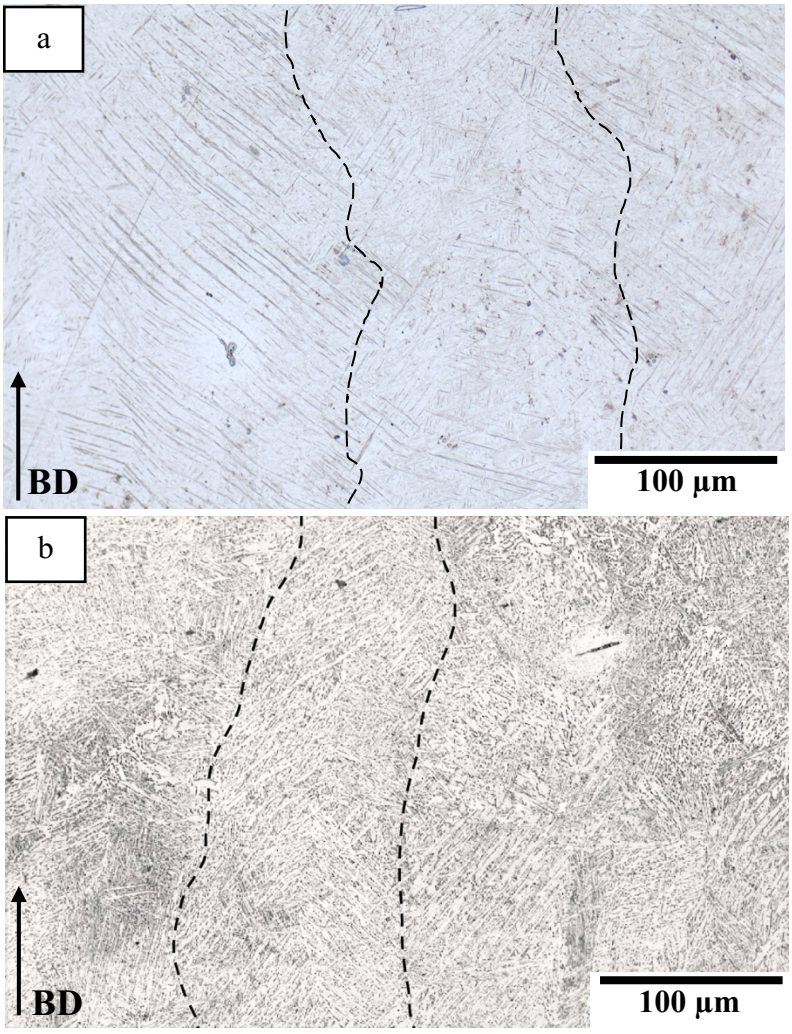

Figure 4.1 Low magnification cross-section micrographs of a) as-built and b) heat treated LPBF Ti64. The dotted lines highlight the prior columnar β grains boundaries.

At the chosen heat treating temperature of 800 ºC it is well documentat that the full breakdown of the α' phase occurs. With further increase in temperature, the grains coarsen, the growth of the β phase is encouraged whilst the α phase is further stabilised [153], [155]. This is likely due to the α' phase decomposing at around 730 ºC [157]. This is the most important parameter as the final microstructure is eventually determined by the HT temperature [153], [155]. Its impact is more significant than that of the hold time, heating and cooling rates particularly when the HT temperature employed was below the beta transus temperature. This is due to the significant α phase fraction present at such temperatures which hinders the growth of the β phase. Thus, this effect diminishes only upon increasing the HT temperature as consequently the α phase fraction is reduced [153]. However, Nguyen *et al.* [19] also noted that very low cooling rates, below 20 ºC/s, ensure the elimination of the α' phase. For furnace cooling, as adopted in the current invstigation, cooling rates can be a low as 0.6 ºC/s thus ensuring that negligible amounts of the α' phase remain, if any [19], [158].

Micrographs were obtained for the shot-peened (SP) sample were obtained and are presented in Figures 4.2 and 4.3. The peening treatment is a cold work process which induces a number of modifications in the microstructure including grain refinement exhibited by a plastically deformed layer, twinning and phase transformation. On the microstructural level, whilst the grains appear to be more populated at the surface, the effect of grain refinement was not very obvious as observed in Figure 4.2. Moreover, even at higher magnifications (Figure 4.3), the presence of twins was also not apparent which is a typical mechanism by which hcp crystals deform [149], [159]. In both cases, this may be attributed to the initial grain size being small or to the chosen peening intensity not resulting in sufficient strain rates. For additively manufactured Ti64, the microstructure is inherently fine thus it is likely to be a contributing factor in this case. Additionally, the aluminium content can also be a contributing factor to the lack of twinning as a high content (over 6.6 wt.%) suppresses twin formation and inhibits slip systems [11], [132], [149]. The absence of twinning in shot-peened additively manufactred Ti64 as observed by Zhang *et al.* [83] and Slawik *et al.* [84] aligns with findings presented here. Both studies documented significant grain refinement and a decreased crystallite size. Despite this lack of visual evidence, the effectiveness of the peening treatment was confirmed later on in Sections 4.1.5, 4.1.7 and 4.2 via EBSD analysis, XRD stress measurements and microhardness measurements, respectively.

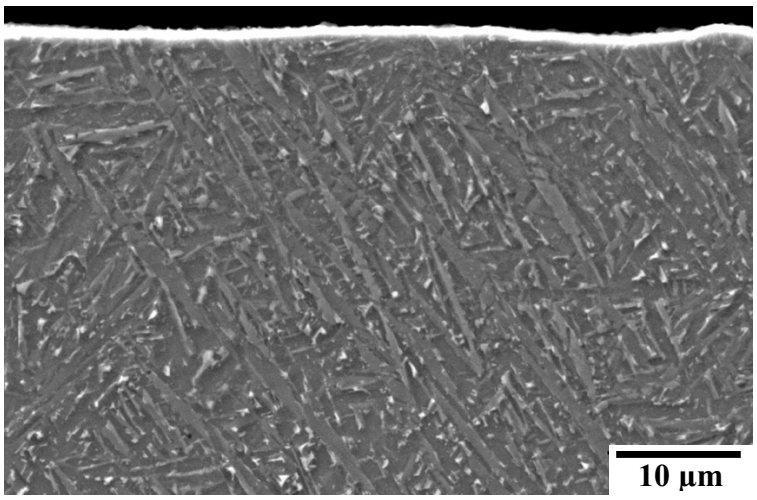

Figure 4.2 High magnification micrograph of shot-peened LPBF Ti64.

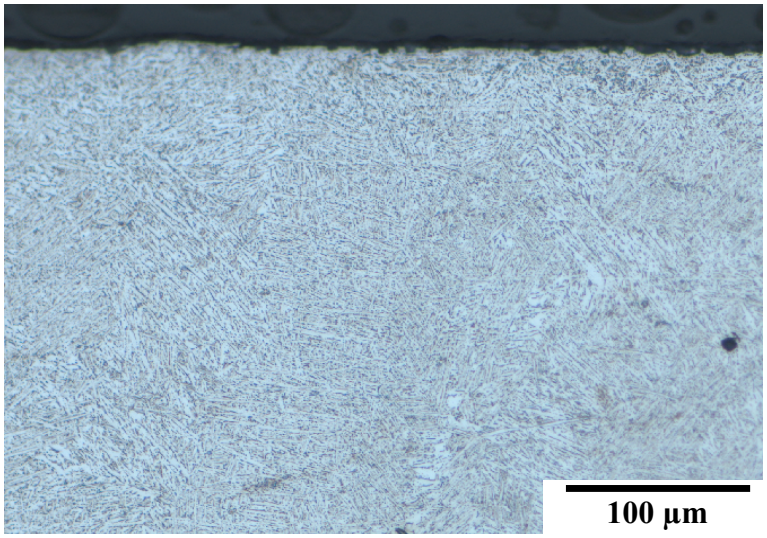

Figure 4.3 Low magnification micrograph of shot peened LPBF Ti64.

4.1.1.2 Comparison of Sample Surfaces

Figure 4.4 depicts low and high magnification micrographs of the surface of the various samples allowing their comparison. The AB sample has a significantly rough surface morphology, as observed in Figure 4.4(a), which is attributed to the LPBF process. For the HT sample, the induced roughness is eliminated upon polishing as observed in Figure 4.4(b) however, this led to the exposure of underlying porosity confirming that the samples are not 100% dense. Similary, for the PVD sample (Figure 4.4(e)), which was polished prior to the coating deposition, a smooth highly polished surface can be observed. Thus, the deposited coating retained the reflectivity of the underlying substrate and resulted in no change except for the colour of the surface which adopted a bronzish hue.

Upon shot peening, the impact of shots induced dimples at the surface, roughening it significantly thus losing its highly polished appearance as observed in Figure 4.4(c). Moreover, the impact was visually observed to encourage the growth of existing pores and the opening of new ones. The high magnification micrographs of the SP sample also exhibit multiple white patches scattered across the surface. These were confirmed, by EDS analysis in Section 4.1.2, to be fragments of the ceramic shot media which became embedded at the surface.

The coating replicated the texture and appearance of the underlying surface when deposited onto the previously shot peened surface and as observed in Figure 4.4(d) no apparent levelling occurred. Similarly to the PVD sample, the DU surface has a bronzish hue however it is more dull compared to the PVD surface oweing to the increased roughness of the underlying substrate due to shot peening.

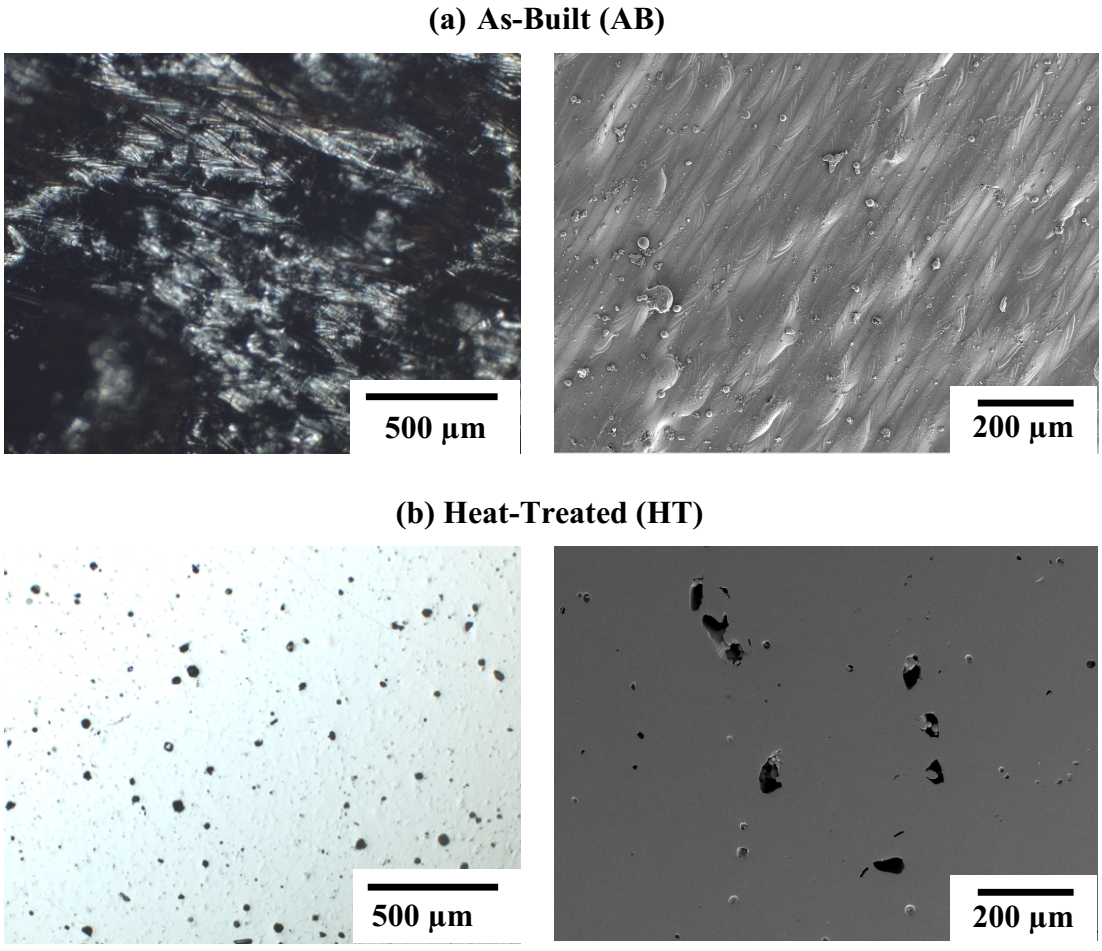

Figure 4.4 Low magnification surface micrographs of a) as-built and b) heat treated, and then polished, LPBF Ti64. On the left hand-side low magnification optical micrographs whilst on the right hand-side shows electron micrographs of the surface

(c) Shot Peened (SP)

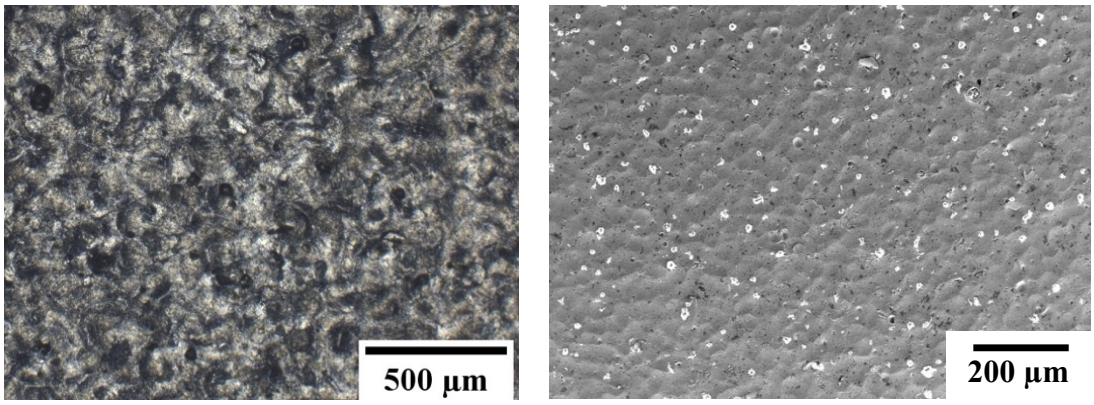

(d) Duplex Treated (DU)

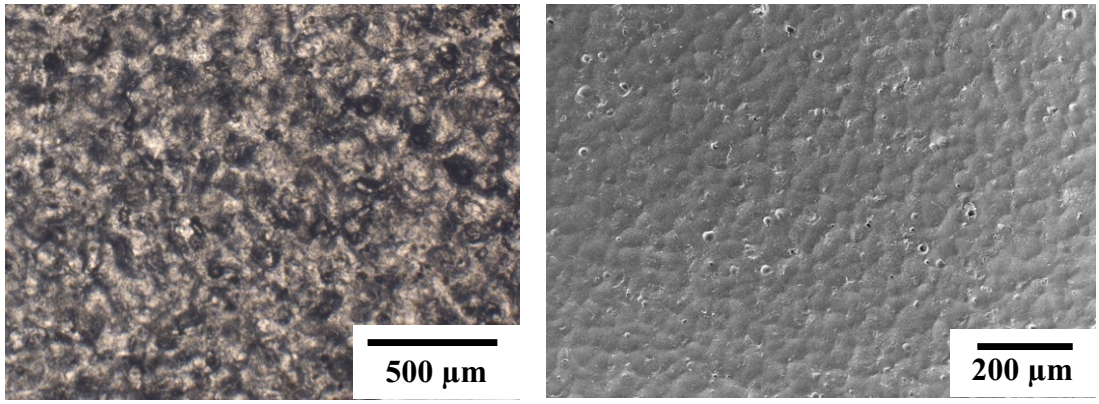

(e) PVD Coated (PVD)

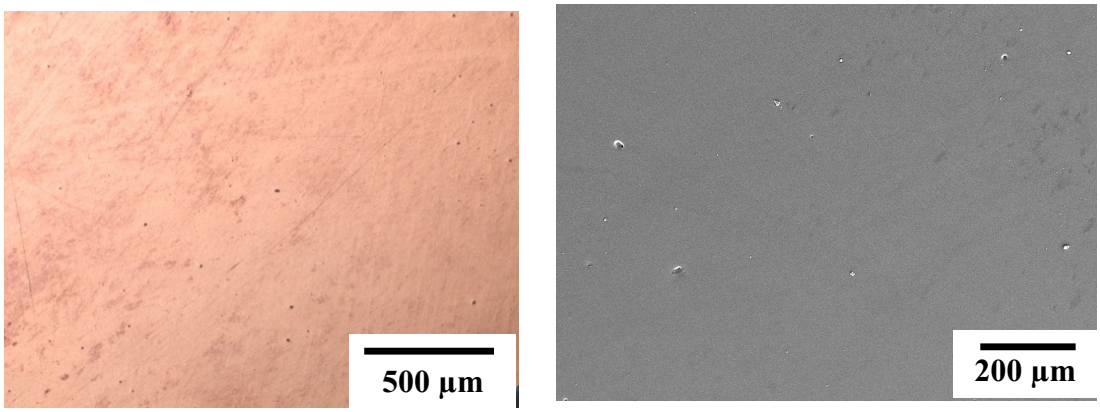

Figure 4.4 Cont. low magnification surface micrographs of c) shot peened, d) duplex treated and e) PVD coated only LPBF Ti64. On the left hand-side low magnification micrographs of the surface are depicted, obtained via an optical microscope, whilst on the right hand-side higher magnification micrographs of the surface are depicted, obtained via an SEM.

The coating was further analysed at higher magnifications to look for any morphological defects in the coating. Figure 4.5 exhibits artefacts tpyical of PVD coatings including overgrowths, craters and voids which form during the deposition process. Overgrowths, as observed in Figure 4.5(b) and 4.5(e) for the DU condition, typically result from protruding surface features including asperities and foreign matter thus, are likely to be further encouraged by rough substrates. Such features act

as nucleation sites which encourage the growth of nodules composed of the coating. Moreover, present craters (Figure 4.5(a) and 4.5(d)) may be attributed to the detachment of such overgrowths. Voids, visible in Figure 4.5(c), 4.5(d) and 4.5(e), are the consequence of shallow depressions or pits at the substrate surface which the coating replicates during deposition. Due to the shadowing effect, coating growth inside the void is minimal thus such defects are not likely to be covered up during deposition.

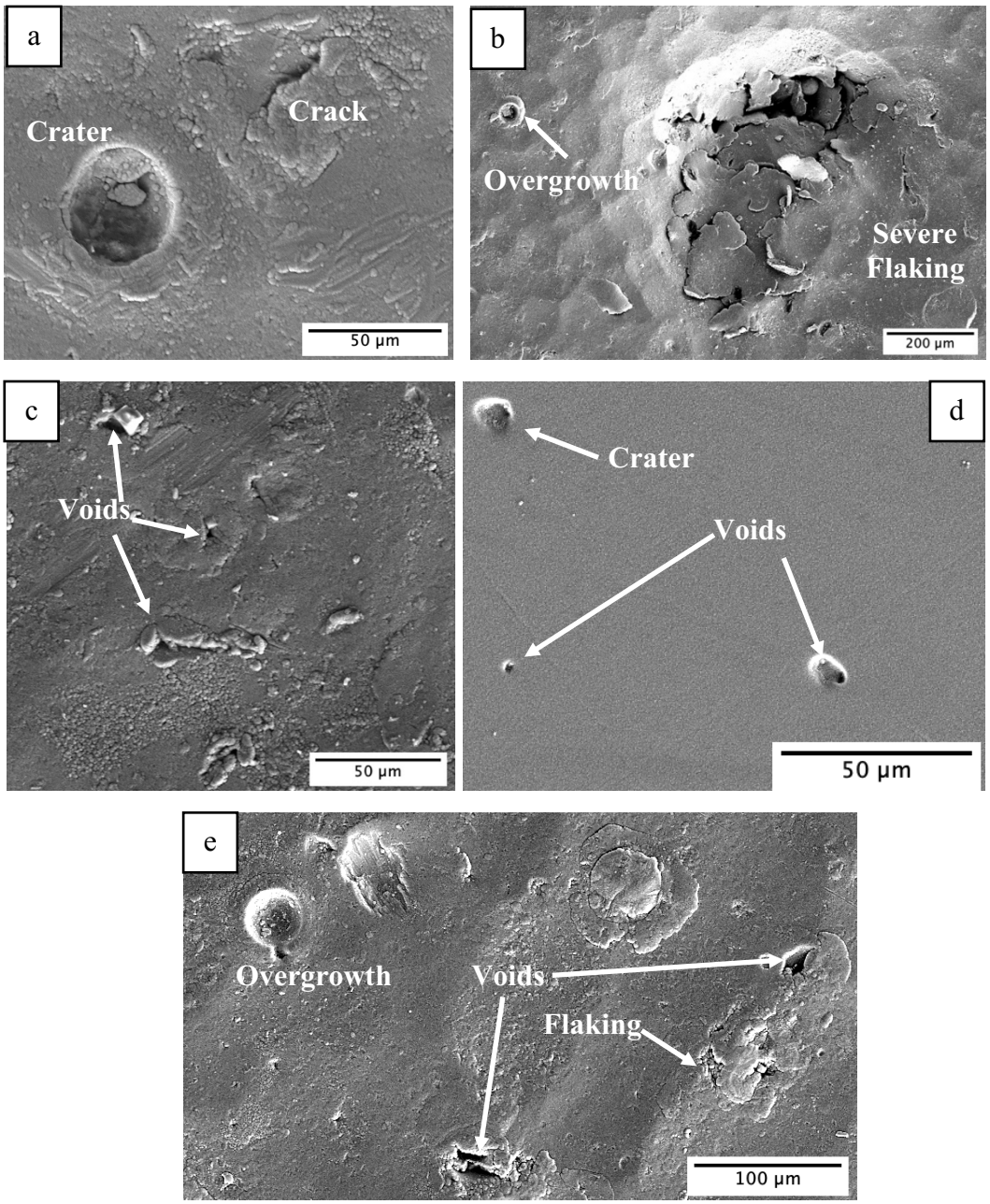

Figure 4.5 High magnification micrographs of coating defects observed on both DU and PVD conditions.

Additionally, evidence of flaking and minor cracking (depicted in Figure 4.5(b) and 4.5(e)) has been observed, potentially attributed to high compressive stresses during deposition or the thermal stresses induced upon cooling [160]. Alternatively, these defects might stem from pre-existing fatigue delamination of the underlying substrate caused by the repetitive high velocity impact, as observed by Zhang *et al.* [78]. Cracks observed (Figure 4.5(a)) may also be a consequence of cuts caused during the peening process which hinder the growth of a uniform layer. Such defects were expected for the DU sample in particular, due to the highly textured and deformed underlying substrate which provides various nucleation sites from which defects can develop.

4.1.1.3 Coating Profile Analysis

The deposited coating was further studied, along its cross-section, via microscopy. A series of high magnification micrographs of the cross-sectioned coating, presented in Figure 4.6 and 4.7, were obtained via scanning electron microscopy. As typically observed for such titanium nitride coatings, the coating deposited in this work is composed of a dense columnar structure as seen from a fractured section of the coating depicted in Figure 4.6. According to Çomakli *et al.* [15], the coating's density can be attributed to its multilayer structure. With each layer being sequentially deposited, the columnar growth is typically interrupted each time, thereby enhancing the structural density of the coating. However, as observed in Figure 4.6, this effect was not evident. The deposition of multiple layers gives rise to a dense columnar structure composed of small grains. This is beneficial, since columnar structured coatings are inherently porous due to the voids present between the adjacent columns. A dense coating aids to mitigate the permeation of the corrosive media towards the substrate's surface allowing the coating to provide better corrosion protection [15], [16], [17]. Additionally, this dense structure is beneficial for the load carrying capabilities.

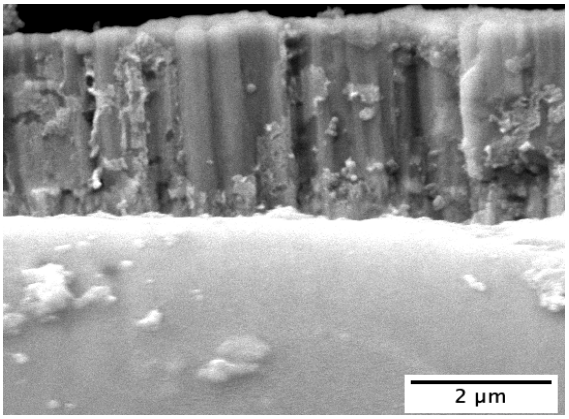

Figure 4.6 High magnification micrograph of the columnar structure of the coating deposited onto the polished surface (PVD condition).

The defects indicated by the arrows in Figure 4.7(a), observed on the coating deposited onto the substrate previously subjected to shot peening, appear to be overgrowths. These features may arise due to either entrapped foreign matter at the surface or the asperities resulting from the peening process. These may result in the formation of significant cone shaped defects running along the cross-section and are characterised by poor adhesion thus impact the durability of the coating [161]. Such macro defects were expected for the DU condition as the coating was deposited onto a rough surface which encourages the formation of defects.

The presented micrographs depict a highly conformant coating, a conclusion supported by the surface roughness analysis detailed in Section 4.1.4. The coating conforms to the topography of both the smooth (PVD condition) and peened (DU condition) substrates onto which it is deposited, maintaining a consistent thickness throughout. Additionally, the coating appears to be well adhered especially between the layers with no obvious defects such as microcracks or detachment. The detachment observed between the coating and substrate surface in Figure 4.7(a) may be attributed to the cross-section preparation and polishing process as it is not observed in Figure 4.7(b) which depicts the various layers and measured thickness of the coating.

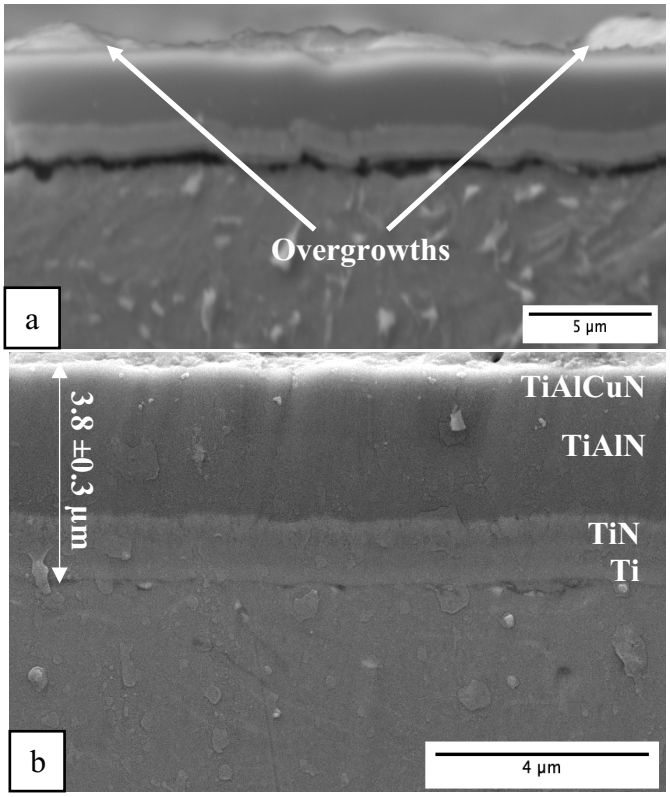

Figure 4.7 High magnification micrographs of a) observed overgrowths on the coating deposited onto the previously shot peened surface (DU condition) and b) the cross section, highlighting the various layers, of coating deposited onto the previously shot peened surface.

Table 4.1 provides a summary of the overall average thickness of the layers constituting the coating deposited onto the polished (identified as PVD) and shot peened (identified as DU) substrates and the specified thickness (by the supplier) of the various layers. The difference in the thickness of the coatings of the PVD and DU conditions is insignificant. Thus, the surface condition did not influence the coating's growth. Additionally, all thicknesses are within the ranges specified by the supplier.

Table 4.1 Thickness measurements of the PVD coating layers.

Layer	Average Thickness (µm)		Specified Thickness (µm)
	PVD	DU	
1: Ti	0.33 ± 0.03	0.35 ± 0.05	0.1 – 0.5
2: TiN	0.94 ± 0.17	1.25 ± 0.26	0.4 – 3
3: TiAlN	1.55 ± 0.28	1.80 ± 0.40	0.4 – 3
4: TiAlCuN	0.76 ± 0.10	0.86 ± 0.12	0.1 – 1.5
Ti/TiN/TiAlN/TiAlCuN	3.88 ± 0.58	4.26 ± 0.83	1 – 8

4.1.2 Elemental Analysis

Table 4.2 lists the various elements detected for the different sample conditions when analysing three different surface areas for each condition. This analysis confirmed that the different surface treatments affected the surface chemistry of the various samples.

For both the as-built (AB) and heat-treated (HT) samples, similar titanium (Ti), aluminium (Al), and vanadium (V) content, in line with the Ti-6Al-4V designation, was detected except for some minimal iron (Fe) content which was detected for the AB condition. However, the presence of Fe was expected as the powder itself contains around 0.16 wt.% as highlighted in Table 3.1 in Chapter 3.

Table 4.2 Elements detected for all conditions via EDS analysis.

Condition	Element (wt.%)									
	Ti	Al	V	C	O	Fe	Zr	Si	Cu	N
AB	89.28	6.05	4.35	-	-	0.32	-	-	-	-
HT	89.39	6.30	4.31	-	-	-	-	-	-	-
SP	67.08	5.47	2.59	4.82	14.71	1.23	2.72	2.00	-	-
DU	49.24	15.04	-	-	-	-	-	-	0.76	34.97
PVD	47.98	14.52	-	-	-	-	-	-	0.50	37.00

In the shot peened (SP) condition, the presence of additional contaminants has been confirmed in conjunction with the anticipated detection of Ti, Al, and V. This is not uncommon for shot peened surfaces [14], [162]. Main contaminants include high traces of oxygen and minor traces of zirconium (Zr), silicon (Si), and iron (Fe). The peening media used was likely the source of these detected contaminants as the shots used were composed of a combination of ceramics, mainly of 70% ZrO_2 and 30% SiO_2 and Al_2O_3. During peening, upon impact shots may fracture and become embedded in the surface. Meanwhile, the iron content detected, in one of the areas analysed, can be attributed to the contamination of ceramic shots with steel shots remaining from previous treatments within the shot delivery system. This may be mitigated by ensuring that the delivery system and chamber are thoroughly cleaned.

The detection of contaminants was correlated with the presence of various bright specks observed at the surface of the peened sample. Further analysis was carried out on one such bright patch as observed in Figure 4.8. These specks appear to be around 50 to 100 µm in size, and significant amounts of Zr, Si, O and some Al were detected confirming its ceramic nature and the likelihood that these bright specks are remnants of fragmented shots. Their ceramic nature is further confirmed by their bright appearance, as non-conductive materials cannot be properly imaged via scanning electron microscopy due to charging, manifested as glowing. Fragmented shots are undesirable as they result in cuts and tears due to their uneven morphology whilst embedded fragments may disrupt the growth of the naturally occurring oxide layer. In instances where metallic shots are used, embedded fragments may result in galvanic coupling impacting the corrosion performance of the substrate however, the use of ceramic shots as in this investigation, eliminates this possibility. Whilst Fe was also detected, the quantities detected were minimal thus, it is highly unlikely that it will have a significant impact on the corrosion performance [163].

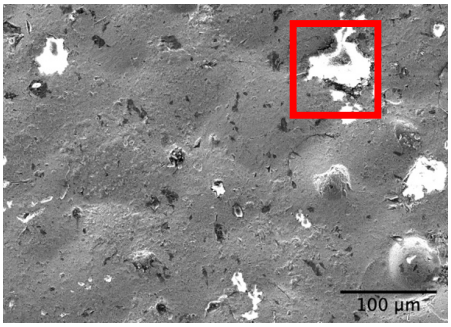

Element	wt.%
Al	3.74
C	14.21
O	16.40
Si	20.61
Ti	1.77
Zr	43.27

Figure 4.8 High magnification micrograph of the shot peened condition including elements detected for the highlighted white patch.

Following the deposition of the coating, the elements detected were Ti, Al, Cu and N which are all part of the coating's make up. For the duplex treated (DU) sample, none of the previously detected contaminants were observed, likely due to the coating itself concealing any contaminants present. In addition, the surfaces were primarily subjected to high energy bombardment to remove any oxidation.

Additionally, due to the coating's multilayer structure, elemental analysis of the various layers was carried out via a line scan, carried out over a length of 6.2 µm starting from the bulk as observed in Figure 4.9. From 0 to 2.2 µm, the elements detected correspond to the bulk material. The bottom of the coating, being the initial Ti layer, was detected at an approximate distance of 2.2 µm. Towards the end of the scan, a slight increase in the Cu content is observed, corresponding to the final TiAlCuN layer and reflecting the diminished values detected via spot analysis carried out at the surface, in Section 4.1.2. The absence of vanadium in the measurement profile over the distance from 2.2 to 6.2 µm confirms that this range is equitable to the coating thickness. Therefore, the line scan conforms with the structure of the coating observed in Figure 4.7(b).

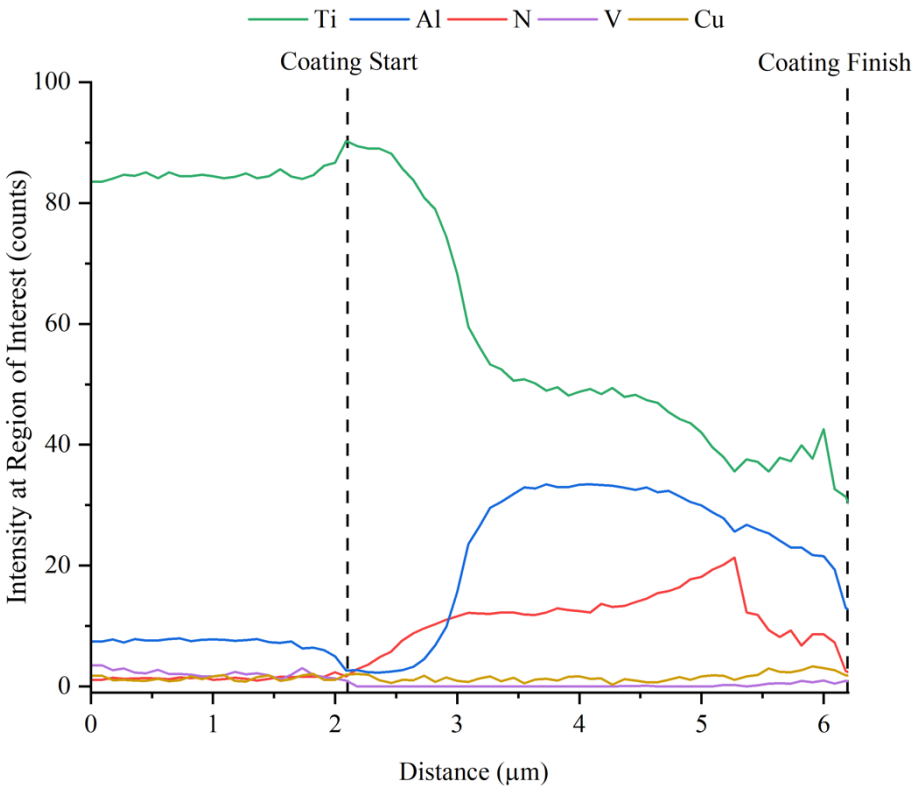

Figure 4.9 Line scan resulting following elemental analysis of the coating.

4.1.3 Scratch Testing

To investigate the adhesion characteristics of the coating, two sample conditions underwent scratch testing, the duplex treated (DU) and the coated-only (PVD). Figure 4.10 depicts low magnification micrographs of selected representative scratches carried out on the DU and PVD sample. Despite the scratch being less distinct for the DU sample, towards the higher load end of the scratch, the coating deposited onto the previously shot peened substrate suffered comparatively more damage up to complete delamination in comparison to the PVD sample scratch.

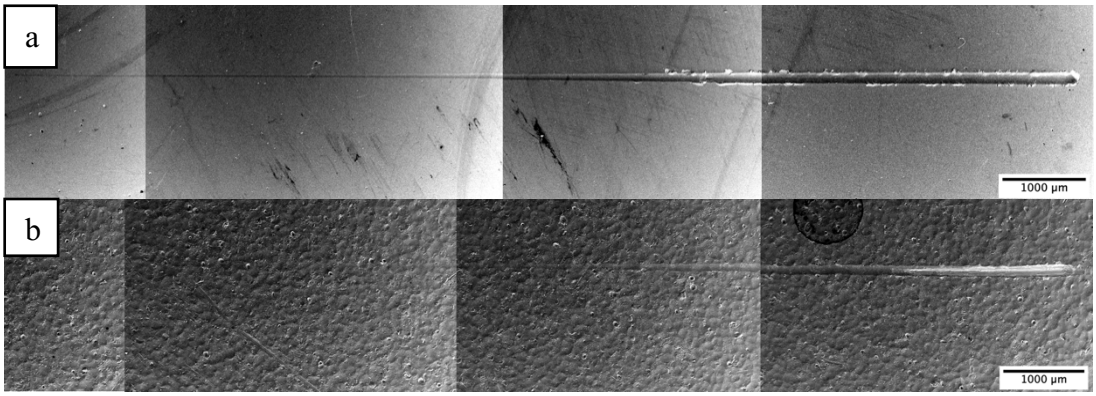

Figure 4.10 Low magnification micrographs of the scratch on the a) PVD and b) DU samples.

The critical failure loads are presented in Figure 4.11 whilst, Figure 4.12 shows the details of the characteristics observed following scratch testing. The main aim of scratch testing is to determine the critical loads, referred to as L_C, at which various characteristic failure modes occur. L_{C1}, L_{C2} and L_{C3} are the loads at which, the onset of cracking, the first occurrence of substrate's exposure and continuous gross coating removal, also regarded as a guideline for the coating's load bearing capacity are respectively observed [164], [165], [166]. For both samples, similar L_{C2} loads were recorded and occurred at similar distances, at 6.8 mm and 6.5 mm respectively, from the starting point of the scratch. For the DU sample, the coating could withstand a load, L_{C3}, of 33 N prior to failure. In comparison, for the PVD sample, complete coating removal did not occur for all repeats, thus it can be assumed that the coating deposited onto the polished surface has better load carrying capabilities, capable of withstanding at least 40 N. This was the maximum load permissible by the set up hence why the PVD coating could not be tested to failure. This discrepancy in performance can be attributed to the increased roughness of the DU sample, which alters the interaction of tip with the surface and increases the coating's defect density, contributing to a local loss of adhesion [113].

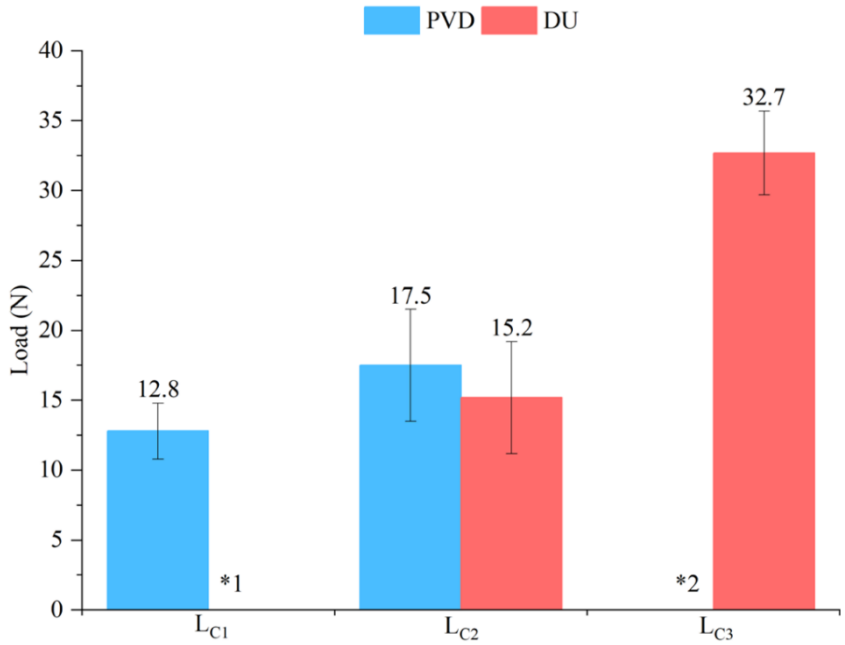

*Figure 4.11 The critical loads endured and the corresponding characteristics. *1 No values could be identified for L_{C1} on the DU sample. *2 No values were obtained for L_{C3} as the PVD coated only substrate sustained no such damage.*

However, it is worth noting that the hardness of the substrate also plays a significant role since the failure of the coating is determined by the substrate's deformation. In an investigation by Bonnici *et al.* [167], when the same coating was deposited onto SLM 316L SS, the maximum load decreased to only 17 N. The AM Ti64 substrates are less rough and 46% and 12% harder than the AM 316L SS substrate in the untreated and shot peened condition, respectively. Thus, the harder and less rough AM Ti64 substrate allowed the coating to outperform the 316L samples.

From microscopical imaging of the scratch track, for the DU treated sample, no L_{C1} characteristics could be identified due to the very rough surface of the sample. For both sample conditions, L_{C2} characteristics were observed while L_{C3} was observed for the PVD sample only. This suggests that scratch testing portrayed an overall better coating adhesion when applied to polished untreated alloy compared to that deposited on the shot peened surface. This is shown by a continuous removal of the coating for the DU samples at a normal load of 33 N which is not evident for the PVD sample. The L_{C1}, L_{C2} and L_{C3} characteristics can observed in Figure 4.12.

The L_{C2} characteristics observed for both the DU and PVD samples, represent recovery spallation observed as chipping at the track edges which occurs due to residual stress relaxation. This is evidence of brittle failure, attributed to the high hardness of the coating, where coating removal is concentrated at the edges of the track rather than

across it which is observed in case of ductile failure typically exhibited by softer coatings. These characteristics are observed along the scratch track of both conditions as the load progressively increased. Ruan *et al.* [168] attributed such failure to the coating's poor crack resistance due to having high internal stresses. Further evidence of brittle failure is presented by the L_{C3} characteristic observed for the DU sample, identified as gross spallation.

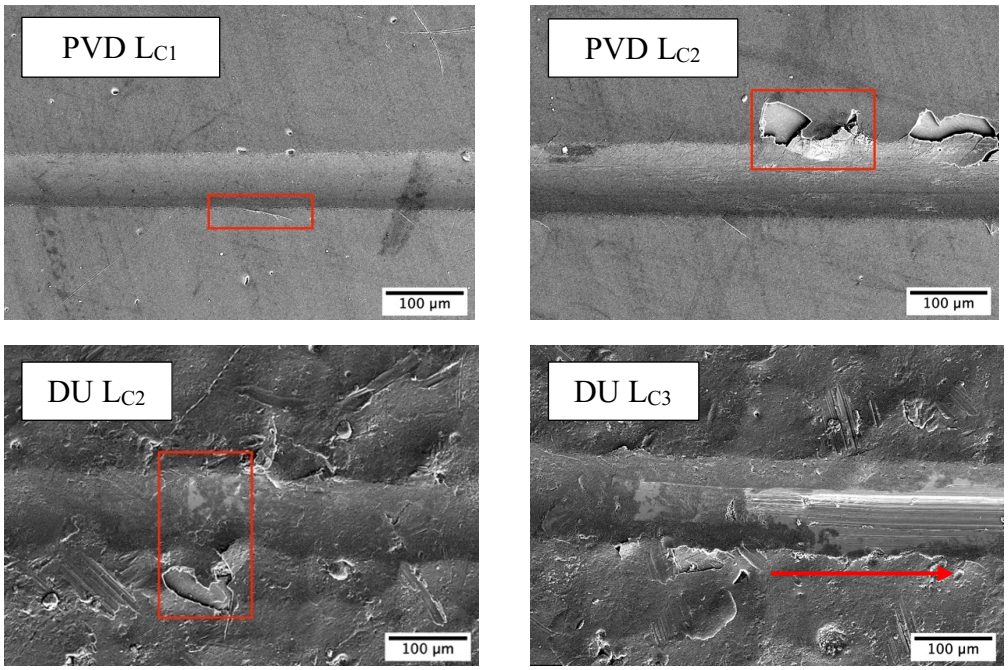

Figure 4.12 Characteristics corresponding to the critical loads identified following scratch testing, highlighted by red annotations.

Moreover, as observed in Figure 4.13 along and at the end of the scratch tracks, for both samples failure was mostly adhesive as supported by the EDS analysis conducted on the end of the scratch track. Such observations were also noted by Ruan *et al.* [168] for a multilayer Ti/TiN/TiAlN coating deposited onto wrought Ti64. The authors observed that as the load was increased, complete coating removal with large peeled-off areas at the edges occurred.

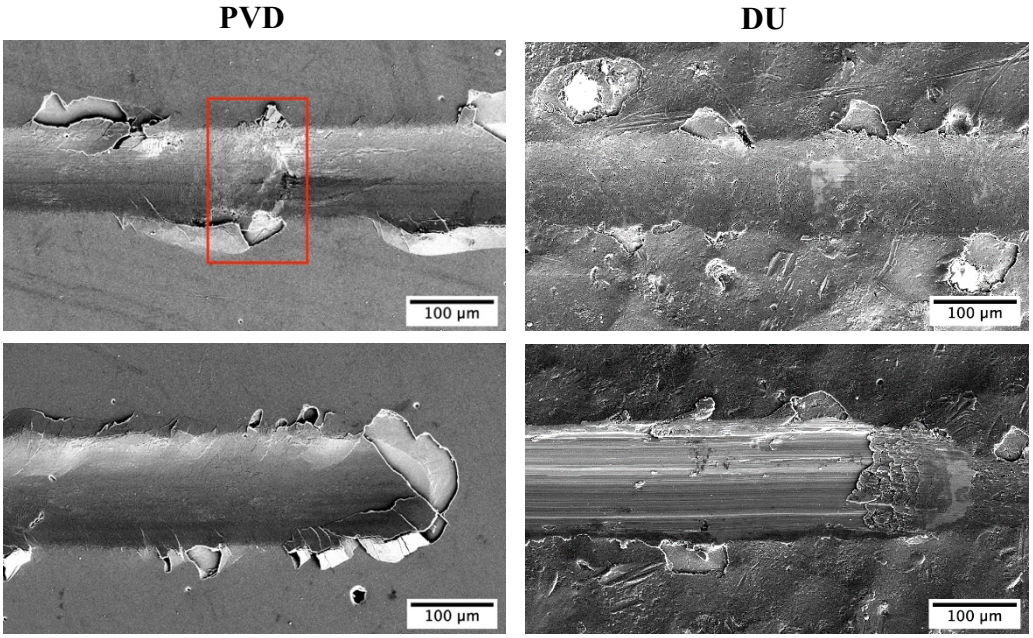

Figure 4.13 Further characteristics observed along the scratch tracks of the PVD and DU samples, adhesive failure annotated by red outline.

As mentioned previously, EDS analysis was carried out at the end of the scratch tracks to determine what elements are present in various selected areas, as observed in Figures 4.14 and 4.15. The main areas chosen were outside the scratch track, inside the scratch track and at delamination and spallation sites. For areas 1, 3 and 4 of the PVD sample, the coating was detected with the Cu content being very minimal in comparison to the quantity of the other elements. Moreover, no vanadium was detected thus confirming that cohesive failure did not take place. However, adhesive failure is confirmed by the analysis of area 2, where the coating was completely de-bonded from the substrate, as elements of the underlying Ti64 substrate were detected in the appropriate proportions. It is worth noting that such failure was not significant and was concentrated at the tracks' edges. In comparison, for the DU sample, elements from both the coating and the substrate were detected in all areas ranging from 2 to 5.

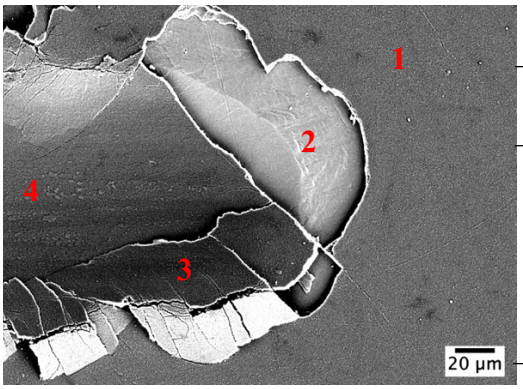

Element	Wt. % in each area			
	1	2	3	4
N	37.00	7.89	32.54	35.36
Al	14.52	5.44	14.76	14.67
Ti	47.98	82.79	52.22	49.97
V	/	3.89	/	/
Cu	0.50	/	0.47	/

Figure 4.14 Areas at the end of the PVD scratch track analysed and the elements detected.

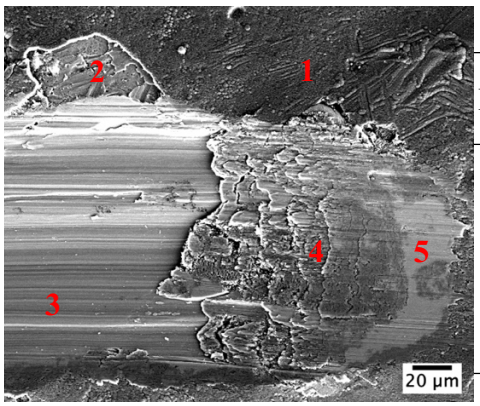

Element	Wt. % in each area				
	1	2	3	4	5
N	34.79	7.51	6.61	26.80	9.98
Al	14.86	5.36	4.85	11.79	5.61
Ti	49.06	82.58	77.72	59.65	80.70
V	/	3.78	3.55	1.31	3.30
Cu	0.58	0.76	0.38	0.46	0.42

Figure 4.15 Areas at the end of the DU scratch track analysed and the elements detected.

4.1.4 Surface Topography Analysis

Figure 4.16 depicts representative profiles of the surface of the various sample conditions and the chart in Figure 4.17 provides a comparison of the mean surface roughness, R_a, and mean maximum depth, R_z, values of each condition.

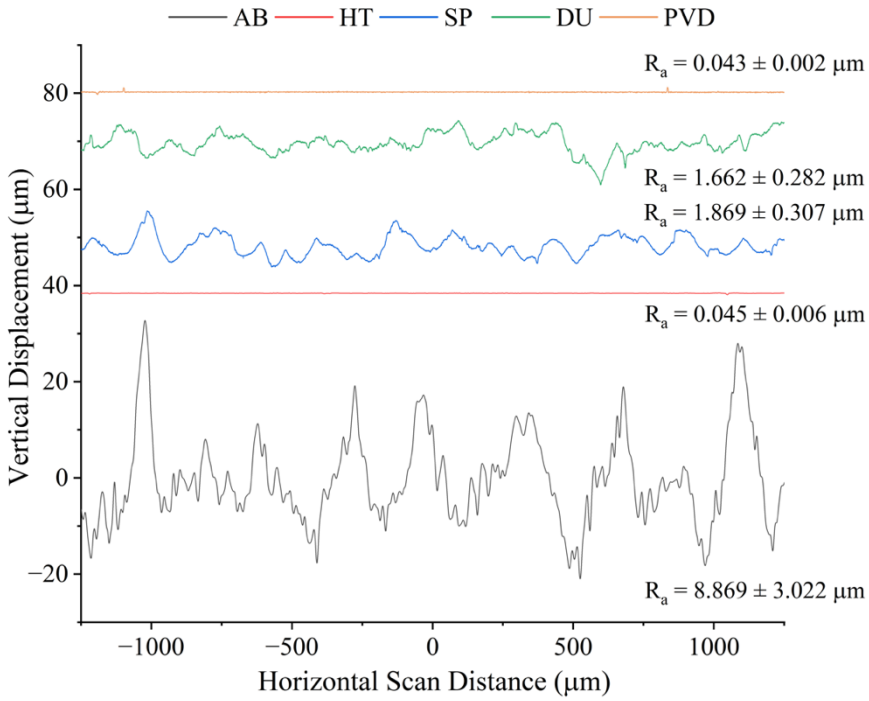

Figure 4. 16 Surface roughness scans of all sample conditions.

Initially, the as-built sample exhibits notably rough topography, with an R_a value in the range of 8.87 ± 3.02 µm. The resulting surface roughness, following fabrication via AM, has been widely documented since it has been observed to correlate to a decrease in the overall performance of the material. Mean surface roughness values recorded in literature, for selective laser melted components, start around 5 µm and reach values as high as 40 µm [37], [38]. For as-built SLM Ti64 in particular, Wang *et al.* [169] recorded R_a and R_z of 7.59 and 42.60 µm respectively. Significant values are attributed

to: (i) non-optimised printing parameters which encourage porosity and LOF defects at the surface, (ii) the staircase effect which becomes more prominent with an increase in thickness, (iii) the partial melting and consequent bonding of unused powder particles at the surface and (iv) an unstable melt pool [35], [39].

Optimal printing parameters aid to diminish the roughness however post-processing techniques such as grinding and polishing eliminate the induced roughness entirely [6]. Upon polishing the roughness is significantly reduced by a near 100% to an R_a value in the nanometric range as observed for the HT sample. Additionally, an R_z value of 0.47 ± 0.35 µm, was recorded as observed in Figure 4.17. This value is attributed to the porous nature of additively manufactured samples. Whilst polishing diminishes the surface roughness, it also encourages the growth of pores present at the surface and the exposure of new pores which were positioned just below the surface due to the removal of material. Such a value is significant compared to R_z values recorded for conventionally manufactured Ti-6Al-4V. In previous work by Vella *et al.* [149], the authors recorded an R_z value, for wrought Ti-6Al-4V, equivalent to 0.07 ± 0.02 µm.

As highlighted in Figure 4.17, upon shot peening, the surface roughness, R_a, and maximum depth, R_z, increase significantly by approximately 41 and 31 times the initial values, to 1.87 ± 0.31 µm and 14.47 ± 3.47 µm respectively. This increase is a direct consequence of the impact and deformation caused by the shots. As the ceramic shots impinge the surface, the surrounding material deforms forming dimples mirroring the shot's geometry. This process leads to the creation of sharp protrusions and deep valleys, giving rise to the high R_a and R_z values recorded.

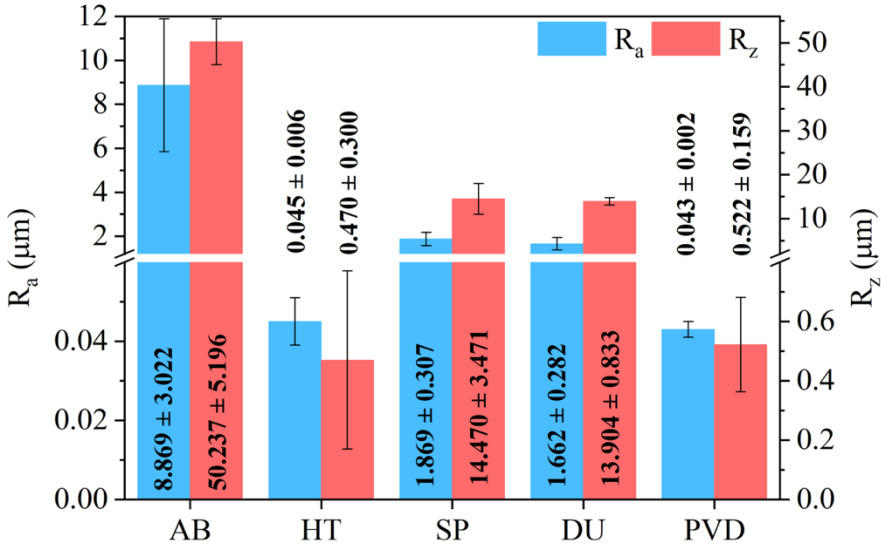

Figure 4.17 Comparison of the different conditions' surface roughness measurements.

Due to being one of the major effects imparted by shot peening, the impact on the surface topography has been thoroughly investigated in literature. From available literature, the most closely related investigation to the present one with respect to peening parameters, was that carried out by Ahmed *et al.* [14]. The authors shot peened wrought Ti64 using 450 μm diameter ceramic shots propelled from the nozzle, situated 90 mm away from the sample surface, at a pressure of 5 bar and intensity of 0.22 mmA, over a duration of 40 seconds. The authors observed R_a and R_z values equivalent to 0.74 μm and 4.71 μm respectively which are approximately 61% and 66% less than values recorded in the present investigation. Despite the similarity in process parameters, the higher values recorded in the present case are likely attributed to the higher pressure (7 bar), longer peening duration (60 seconds) and slightly smaller shot diameters, ranging between 300 and 425 μm, employed in this work.

The impact of peening parameters on the surface morphology has been experimentally proven by various investigators. Ahmed *et al.* [14] observed a gradual increase in R_a and R_z values as the shot size was decreased from 850 μm to 125-250 μm. This increase, observed with a decrease in shot size, has been attributed to the smaller shots' ability of penetrating to deeper depths in the material due to their smaller surface areas, thus are exerting larger pressures upon impact. Furthermore, both the peening intensity and pressure have been observed to directly determine the magnitude of surface roughness. Zhang *et al.* [83] recorded R_a and R_z values of 1.8 μm and 9.5 μm respectively, when peening additively manufactured Ti64 at an Almen intensity of 0.2 mmA and a pressure of 2 bar, using steel shots having a diameter of 580 μm. By duplicating the Almen intensity to 0.4 mmA but using the same shots as Zhang *et al.* [83], Slawik *et al.* [84] recorded R_a and R_z values of 3.1 ± 0.2 μm and 21.7 ± 0.9 μm respectively, for AM Ti64,nearly twice that recorded by Zhang *et al.* [83]. Additionally, a 36% increase in the surface roughness of SPed wrought Ti64 was recorded by Ganesh *et al.* [10] when increasing the peening pressure from 3.5 to 4.5 bar.

The deposition of the coating on both the polished and shot-peened surface did not induce significant changes in surface topography. For both the DU and PVD conditions, similar R_a and R_z values to SP and HT respectively were recorded. PVD coatings can have an inherently rough finish due to their growth occurring across different crystallographic planes [81], [126]. However, Harlin *et al.* [170] followed the assumption that if the coating is less than 5 μm thick, as in the current investigation

(Section 4.1.1.3), then the final surface finish is similar to that of the uncoated substrate. Additionally, the deposition of the coating on a polished surface allows for the formation of an equally low roughness coating having an associated low defect density as there are significantly less features which could interrupt its growth. As opposed to the DU sample where the coating was deposited onto the peened surface.

When depositing coatings onto rough substrates differing results have been observed. In certain cases, the coating growth mimicked the surface morphology retaining a high surface roughness whilst in other, the surface morphology was improved as the coating provided a levelling effect [127], [171]. The former results in a coating characterised by a constant thickness whilst the latter occurs when non-uniform coating growth takes place. where the coating essentially fills the dimples induced by peening, reducing the overall roughness. In the current investigation, the deposited coating inherits the rough surface morphology of the substrate resulting in a highly conformant coating. This can be attributed to the line-of-sight behaviour of deposited atoms in magnetron sputtering [127]. In addition, levelling is not always desirable, as the non-uniform growth results in a coating having an uneven thickness with shallow thicknesses observed at asperities. Such locations promote crack initiation and thus subsequent coating failure via fragmentation as observed by Jiang and Arnell [127] for multilayer DLC coatings deposited on an M42 tool steel substrate having a surface roughness of 1.15 μm. Once coated, a decrease to 0.7 μm in surface roughness was recorded.

In contrast, Bobzin *et al.* [171] reported no discernable reduction in the surface roughness following the deposition of a TiAlCrSiN PVD coating on a shot peened HSS substrate. Furthermore, when Zammit *et al.* [81] deposited a multilayer WC/C coating onto previously shot peened Ti64, the authors recorded similar R_a and R_z values to the shot peened only substrate. In addition, the authors concluded that the multilayer structure of the coating did not contribute to a reduction in roughness. Similarly, in the current investigation, despite the coating's multilayer structure, the number of layers is limited, thus their thicknesses were likely insufficient to cause smoothing or result in levelling. Hanabusa *et al.* [172] observed that the surface roughness of TiN and TiAlN multilayer coatings can be improved through an increase in layers and thus an increase in the overall coating thickness. Zimmer and Kaulfuβ [173] noted that such an improvement in surface roughness with an increase in the number of layers, may be attributed to the smoothing of surface anomalies as the sharp interfaces between

each layer alter the growth orientation of the various layers thus, the structure of the top layer differs slightly to that of the underlying layer.

Ideally, for components designated for marine applications, it is imperative to minimise substrate roughness in order to diminish its impact on the performance of the component and on the integrity of the deposited coating in case of the coated substrates. For the SP condition, despite the peening treatment resulting in a roughened surface, the induced compressive stresses and improved fatigue strength shall outweigh the negative effect induced by the increased roughness. Additionally, polishing the surface prior to peening, aids to mitigate the extent of roughnening induced by the process.

4.1.5 Electron Backscatter Diffraction (EBSD) Analysis

To analyse the impact of the manufacturing process and the surface treatments, grain size plots, observed in Figure 4.18, and grain average misorientation maps, observed in Figure 4.19, were obtained. The microstructure is composed of various laths after transformation from columnar prior-β grains. This columnar growth parallel to the building direction is typical for LPBF as it is driven by the steep temperature gradients resulting from the heat flow towards the substrate together with the epitaxial growth in between layers resulting from re-melting of previously solidified layers [174]. These columnar grains will undergo a diffusionless transformation to α' laths upon the rapid cooling as shown in Figure 4.19(a) for the as-built (AB) condition [175].

The thin and long lath morphology makes grain size analysis using the grain diameter inaccurate. Therefore, grain area measurements are presented in this work. To obtain the distribution, the grain area was plotted against the area fraction values of the various sample conditions (Figure 4.18) for the near-surface area equivalent to 290 μm by 100 μm. Due to the large spread in lath sizes observed, typical after AM processes due to the variation in thermal gradient throughout the specimens, significant overlap in measurements was observed. Following heat treatment, the lath structure is retained (as shown in Figure 4.19(b)), however the lath thickness increases as the average width of the laths increases from 0.66 μm to 0.74 μm.

Contradictory results emerged post shot peening, as shown in Figure 4.18. Following peening, no significant refinement was observed. A contributing factor may be the pre-existing fine microstructure present prior to the application of the peening treatment [176]. On the other hand, for the DU sample, a small degree of refinement was

observed with its grain area plot shifting slightly to the left towards smaller values. Yeo *et al.* [48] also observed a slight decrease in the average size of the grains following laser shock peening of LPBF Ti64 however, when considering the standard deviation, overlap between the values obtained in their work was present. The significant statistical overlap observed here suggests that, if refinement occurred, it was minimal and not deemed statistically significant. Grain refinement is a function of dislocation generation and movement. For Ti64, which has a hexagonal close packed structure, refinement at ambient temperature via severe plastic deformation is very difficult due to the structure's high deformation resistance [178]. Plastic deformation induced, initiates dislocation motion and accumulation which become immobile. Sub-boundaries then form due to dislocation annihilation, resulting in refinement as low angle grain boundaries transform into high angle grain boundaries [81]. An initial fine microstructure inhibits dislocation mobility, thus requiring excessively high peening intensities for any significant grain refinement to occur.

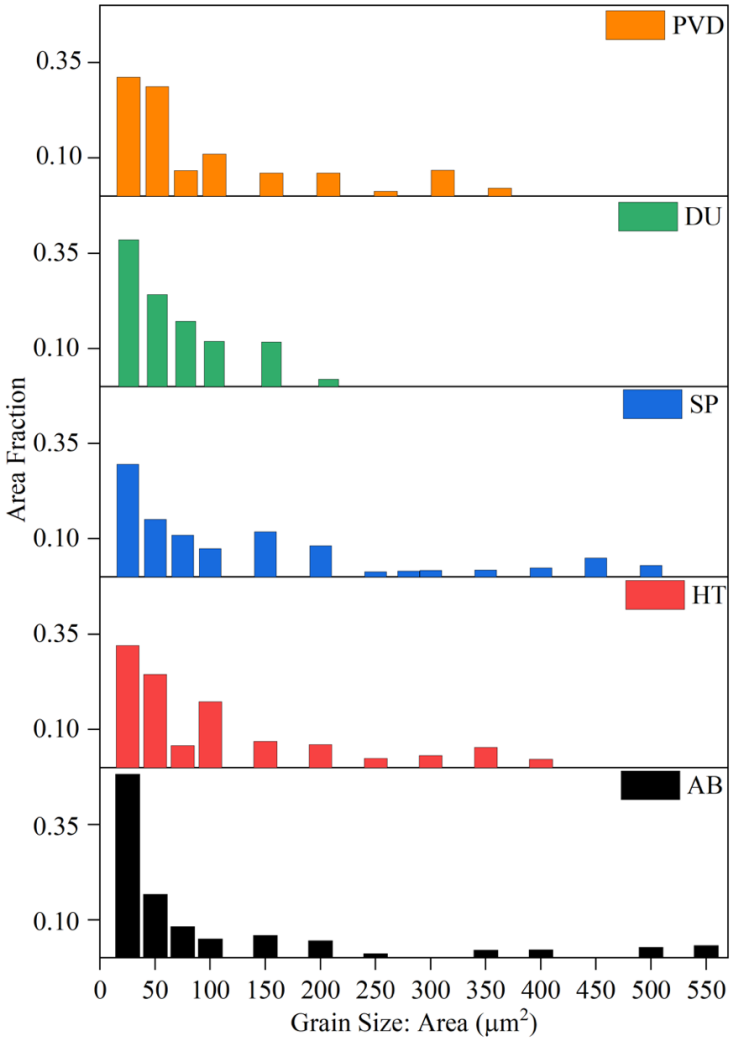

Figure 4.18 Grain size distribution represented by area fraction for the various conditions.

The aspect ratios of the generated microstructures near the surface are presented in Table 4.3. A marginal decrease in aspect ratios is noted for the values of the shot peened and duplex treated conditions compared to the heat-treated specimens indicating that a deviation from an elongated to a more globular shape may have occurred.

Table 4.3 Average aspect ratio values of all conditions derived from cropped maps of 290 μm by 100 μm (from the surface) calculated as a function of the area fraction .

Sample Condition	Aspect Ratio
AB	3.37
HT	3.68
SP	3.27
DU	2.90
PVD	3.60

The impact of the shot peening treatment is discernible through misorientation analysis as depicted in Figure 4.19 which compares the grain average misorientation (GAM) maps of the different sample conditions. Such misorientations are expected to be induced following the application of localised stress. The as-built (AB) sample has a significant misorientation distributed over the cross-section which can be attributed to the tensile residual stresses induced by the high thermal gradients generated by the LPBF process. Following the application of a heat-treatment, the misorientation is significantly reduced. However, misorientation is then pronounced for the surface of shot-peened (SP) and duplex treated (DU) conditions. In this case, this can be attributed to the induced compressive residual stresses by the shot-peening treatment. The depth of the increased misorientation is evident up to ~100 μm under the surface, corroborating stress and hardness measurements of the near-surface area. There appears to be no evidence of twinning, a typical mechanism through which hcp crystals deform [159]. A small initial grain size, insufficiently high peening intensity and high Al content which suppresses twin formation may all be contributing factors to the lack of twinning [11], [132], [159].

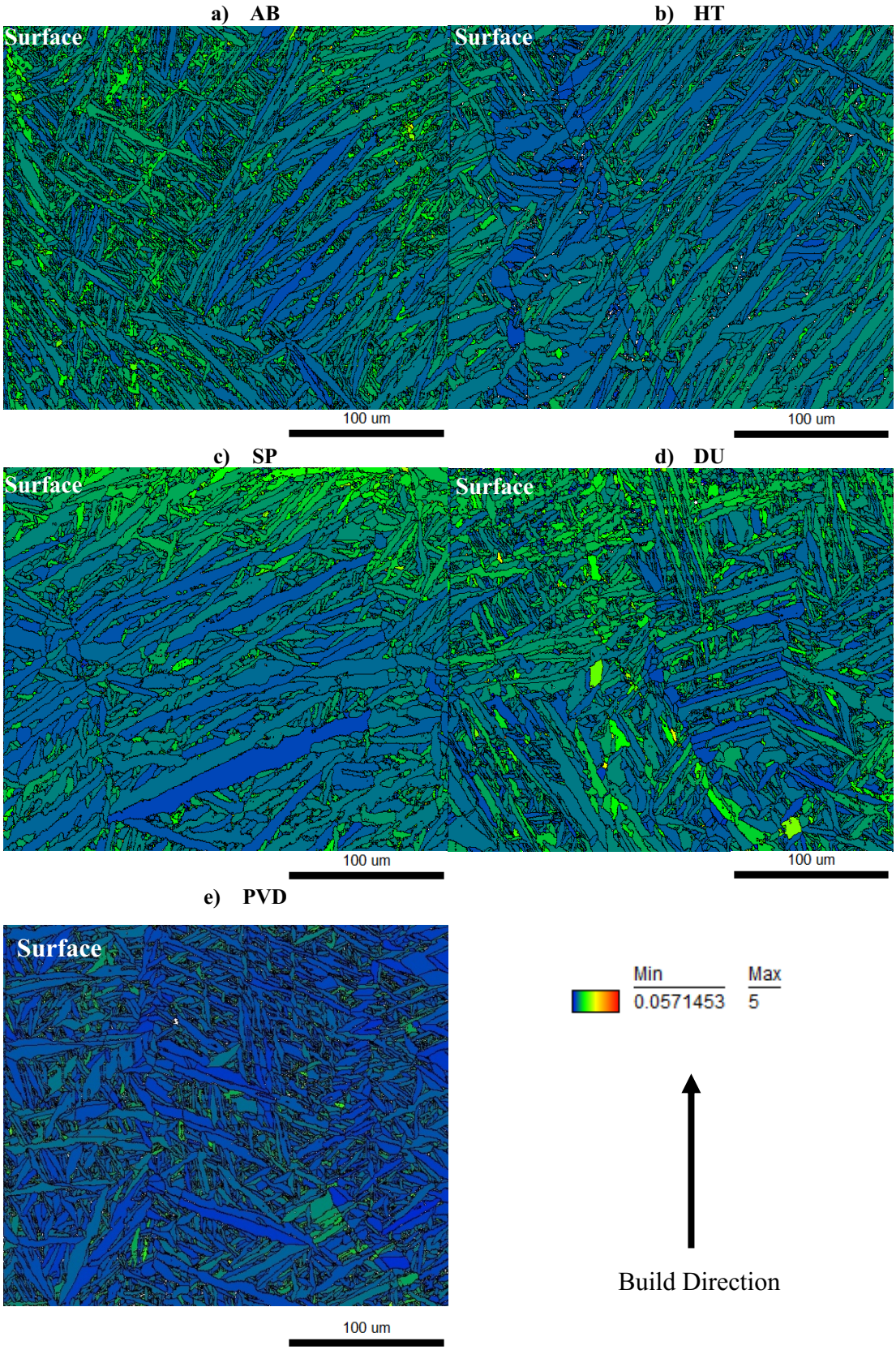

Figure 4.19 Grain average misorientation maps for the different conditions. Blue, equivalent to 0.05 (no units), representing negligible misorientations up to a maximum value of 5 equivalent to red in the maps.

To precisely quantify the impact of the induced stresses, the Kernel average misorientations (KAM) were plotted as observed in Figure 4.20. After heat treating, the KAM value reduced from 0.76 to 0.67. This decrease is attributed to the stress relief caused by the heat treatment. However, an increase near the surface can be observed for the shot-peened and duplex treated samples which is an indication of high local strain concentration and induced residual compressive stress.

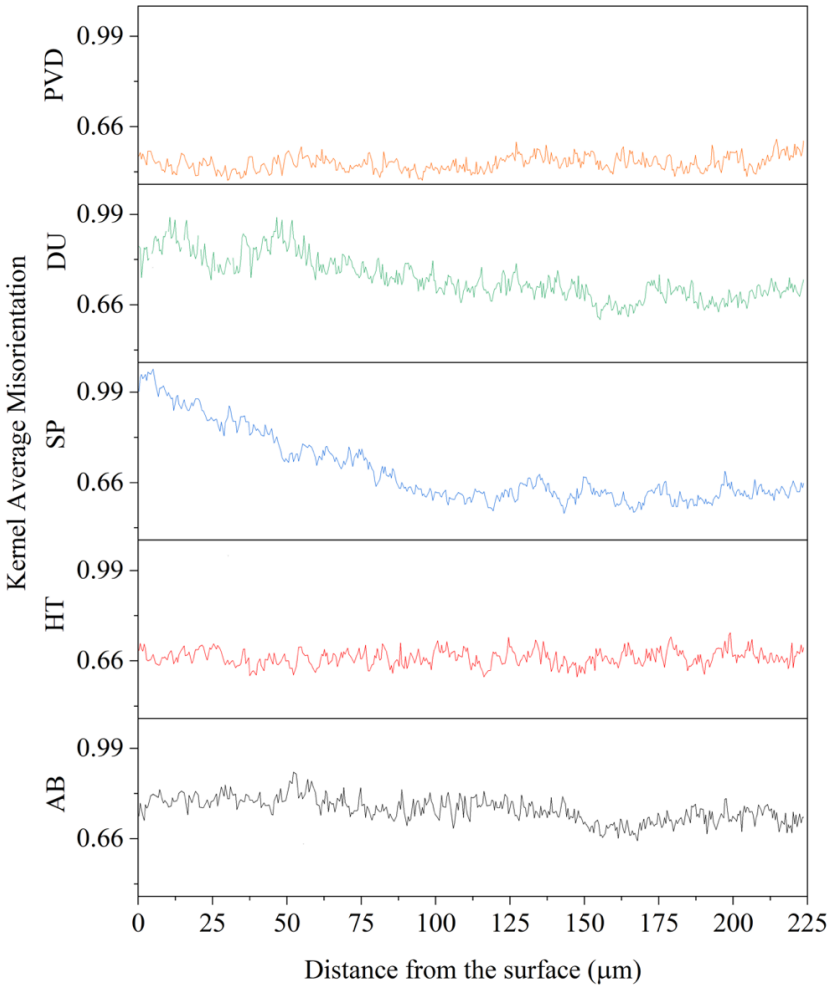

Figure 4.20 Plots of the Kernel Average Misorientation values and their variation along the depth of the different conditions.

The induced stresses led to an increase in dislocations and a change in grain orientation at the near-surface. The rotation of the laths is caused by movement of dislocations through the lattice thus the increase in the KAM value in the near surface area. This rotation effect is more evident through inverse pole figure (IPF) maps obtained after parent beta grain reconstruction, observed in Figure 4.21. For the SP and DU conditions, a change in orientation due to the peening treatment is evidenced by changes in lath orientation within the individual grains, highlighted by the arrows. Such differences are not observable in the HT condition shown in Figure 4.21(a).

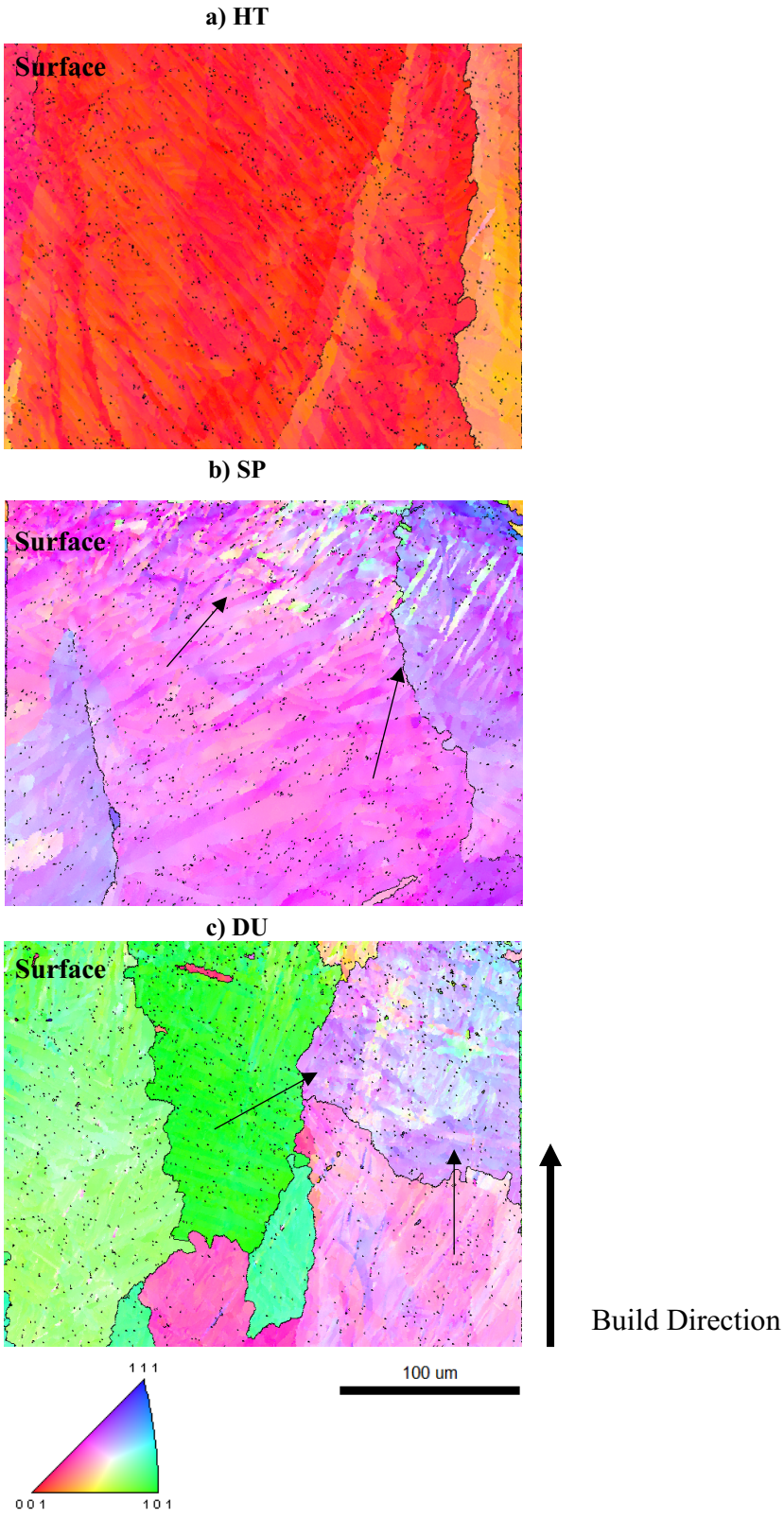

Figure 4.21 Parent beta reconstruction maps of the a) HT condition compared to the b) SP and c) DU conditions. Changes in lath orientation highlighted by the black arrows.

4.1.6 X-ray Diffraction (XRD) Phase Analysis

Figure 4.22 depicts the various diffraction peaks detected, for the different sample conditions, during XRD phase analysis. For the AB, HT and SP samples, the positions of the detected peaks were similar to those of the standard peaks observed in the hcp α-Ti (04-002-2539) and bcc β-Ti (04-018-5433) powder diffraction files. This is supported by the micrographic analysis carried out in Section 4.1.1 where micrographs obtained for the AB sample depict a microstructure composed of a α' grains and those obtained for HT and SP depict a microstructure composed of a majority of α grains in columnar β grains. For the PVD and DU samples, peaks detected coincided with the standard peaks of the cubic TiAlN powder diffraction file (01-077-6809).

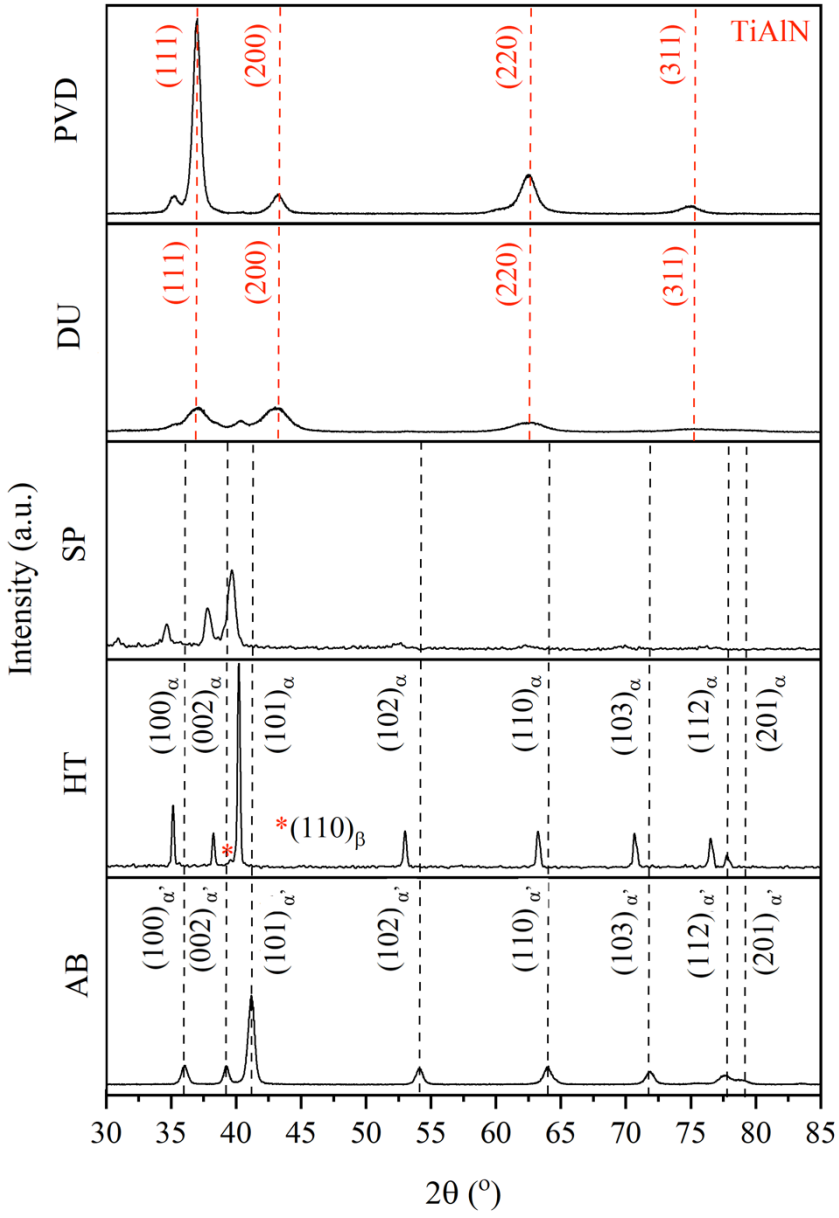

Figure 4.22 X-ray diffraction spectra for all conditions. The '' symbol is used to highlight the position of the beta peak.*

As observed in various investigations, the peaks detected for the as-built sample actually represent the single acicular-martensite α' phase rather than the α phase [179], [180], [181]. However, the peaks roughly conicide with those of α-Ti as despite being two different phases, α' and α have the same hexagonal close packed crystal structure thus differentiating between the peaks is difficult [180]. Additionally, compared to the heat treated condition, the peaks detected for the AB sample are also less intense. This can be attributed to the rougher surface of the AB sample, quantified in Section 4.1.4, where diffracted ray absorption occurs by the present surface asperities [182]. However, Rafi *et al.* [180] also attributed low intesities to the finer structure, as observed in Section 4.1.1.1, by which selective laser melted Ti64 is characterised.

The spectrum detected for the polished and heat treated sample evidenced that the transformation from the α' phase to the dual α and β phases occurred as previously observed by various investigators [179], [181], [183]. This occurred as when heat treating at 800 ºC, which is above the β transus temperature equivalent to 730 ºC, the α' phase decomposes and tranforms into the α and β phases. The previous α' phase peaks are replaced with high intensity α peaks and the β-Ti(110) peak which can better observed in Figure 4.23. The limited intensity of the β peak could be attributed to the HT parameters adopted which were aimed to result in stress relief rather than the coarsening of the grains thus, not enough time was given for significant growth of the β phase to occur. In comparison with the peaks of the AB sample, the peaks detected for the HT condition are more intense, narrower and shifted towards lower 2θ values. The higher intensity of the HT peaks may be attributed to the surface finish of the sample, which as opposed to the AB sample, was that of a mirror finish. Kaschel *et al.* [183] attributed the leftwards shifting and narrowing of detected peaks to the transformation occuring where as a consequence the crystallinity increases whilst the strain decreases. Common sources of strain include dislocations, grain boundaries, chemical heterogenities, precipitates or internal stresses which via heat treatment are eliminated or relieved thus the decrease in strain [183]. During the transformation, the crystal parameters such as the crystallite size, d-spacing and lattice parameters start to change. The lattice parameters typically undergo an increase since the lattice expands as the solute atoms undergo diffusion during the α' to α + β transformation. The lattice expands as the vanadium atoms diffuse from the α' phase to the β phase. Thus, via increasing the heat treatment temperature, more intense β peaks may be detected as

higher temperatures encourage further the occurrence of diffusion, in the process enriching further the β phase therefore increasing its volume fraction [184].

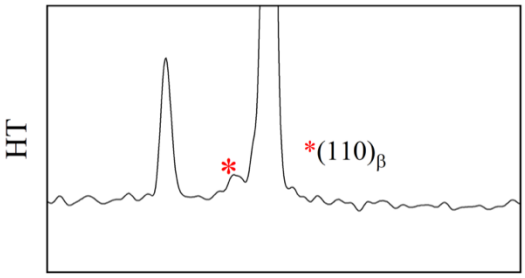

Figure 4.23 Magnified section of the detected beta peak for the HT sample.

Following shot peening, the XRD spectrum detected underwent a number of changes however no new peaks were detected confirming that phase transformation did not occur. The most notable were shifting to lower 2θ values, peak broadening, a decrease in the majority of peak intensities and a poorly defined β peak. Such observations were also recorded by Zammit *et al.* [81] for shot peened wrought Ti64 and Zhang *et al.* [83] for shot peened selective laser melted Ti64. Both shifting and broadening are attributed to the induced residual stresses by the peening process, quantified in Section 4.1.7. Residual stresses are further classified into two classes being type 1, known as macro strains, and type 2, known as micro strains. Macro-strains are typically constant and contribute to peak shifting. These result when materials having a polycrystalline structure undergo elastic deformation which induces a uniform strain that alters the inter-planar spacing. The extent of the changes undergone by the inter-planar spacing is proportional to the applied stress. On the other hand, peak broadening is a consequence of induced non-uniform microstrains which result when the material undergoes plastic deformation, thus the applied stress exceeds the yield strength of the material. Such deformation distorts the crystal lattice. Both macro and micro strains are experienced by materials undergoing plastic deformation techniques such as shot peening [139], [185], [186]. Diminished grain sizes also encourage peak broadening since there are less lattice planes available to generate diffraction peaks via constructive interference [187].

As mentioned previously, diminished peak intensities and also broadening are a consequence of the induced surface roughness in this case by the peening treatments. The impingiment of shots induces dimples resulting in numerous protrusions which interfere with the detection of the diffracted X-ray as they absorb these rays [81]. The induced roughness is also a contributing factor to the poor definition of the β-Ti (110)

peak as roughness enhances the signal noise [81], [126]. Additionally, this may also be due to peak broadening causing the β-Ti (110) and the α-Ti (101) peaks to overlap one another or also due to the slight increase in intensity and broadening of the adjacent α-Ti (002) peak. An increase in intensity of the α-Ti (002) peak may be an indication of modifications occurring in the crystallographic texture i.e. a change in grain orientations which are known to arise in the application of plastic deformation techniques [81], [188].

The spectra obtained for the DU and PVD samples consisted of reflections along the (111), (200), (220) and (311) planes which are typical to TiN and TiAlN coatings [15], [168]. Apart from the peaks related to the coating's phases, a slight α-Ti (100) peak and α-Ti (101) peak related to the bulk were also detected for the PVD and DU sample respectively. This is to be expected as the penetration depth of the X-ray is likely to be greater than the coating thickness. Additionally, no peaks related to the copper phase were detected suggesting that the element is X-ray amorphous or else not present in sufficient detectable quantities [189].

For the PVD sample, the peak detected for the reflection along the (111) plane has a very high intensity. Similarly, this was observed by Pugal Mani *et al.* [190] when investigating a multilayer PVD TiN/TiAlN coating confirming that the coating is highly crystallised along the (111) plane. Furthermore, an identical spectrum, with respect to the detected peaks and their positions, was obtained for both the PVD and DU samples indicating that the prior peening treatment did not affect the crystalline growth of the coating. However, for the DU sample, broader and less intense peaks were dectected. As mentioned previously, these changes can be attributed to the induced residual stresses and the rough surface condition of the prior shot peened DU sample. The broader peaks detected also confirm that residual stresses imparted previously by the peening treatment were retained during and following the deposition of the coating. This was confirmed further via residual stress analysis found in the following Section 4.1.7.

4.1.7 X-ray Diffraction (XRD) Stress Measurements

The residual stress-depth profiles of the various sample conditions can be observed in Figure 4.24. Whilst a summary of each condition's recorded surface stress, maximum stress and its location with respect to the surface as well as the estimated depth of the hardened layer where applicable, are provided in Table 4.4. For the AB and PVD

conditions, only the surface stress was recorded as it was sufficient for comparison purposes to determine the immediate effect of the heat treatment and coating deposition processes.

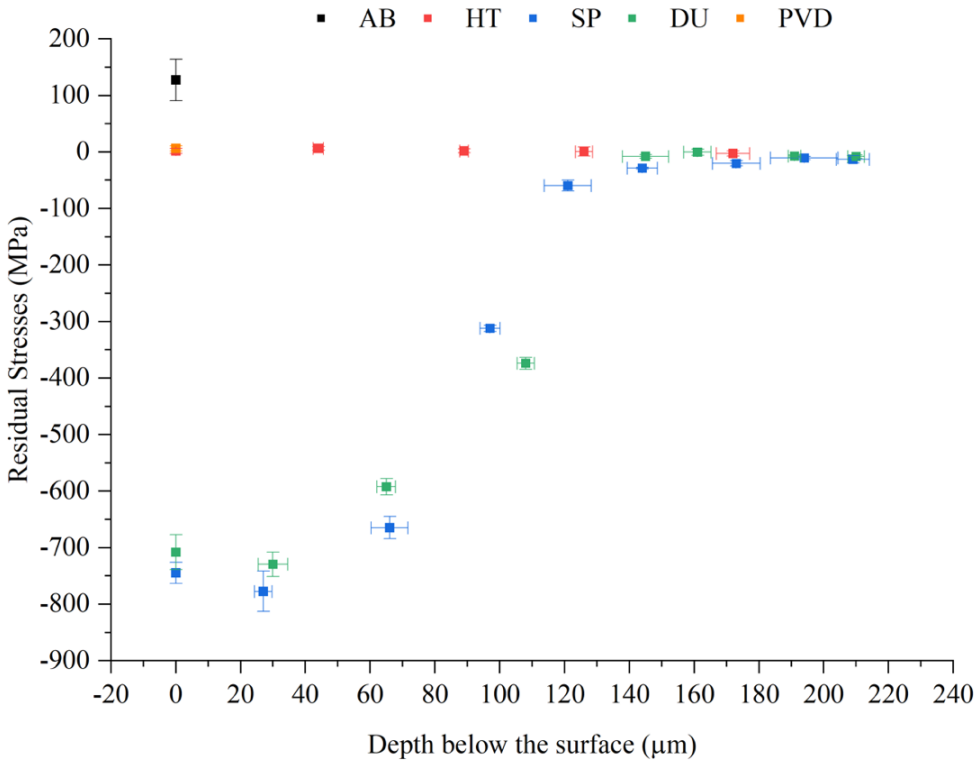

Figure 4.24 Stress profiles of the various sample conditions.

Table 4.4 Summary of stresses and hardened depth measurement.

Condition	Surface stress (MPa)	Maximum stress (MPa)	Depth of maximum stress (µm)	Estimated hardened layer depth (µm)
AB	127.5 ± 36.9	127.5 ± 36.9	/	/
HT	1.8 ± 4.5	1.8 ± 4.5	/	/
SP	-744.3 ± 18.7	-777.2 ± 36.0	27.0 ± 2.7	150
DU	-708.0 ± 31.1	-729.2 ± 21.6	30.0 ± 4.6	150
PVD	6.4 ± 4.7	6.4 ± 4.7	/	/

In the untreated as-built (AB) condition, a high surface stress of the tensile nature was recorded as observed in Table 4.4. It is assumed that below the surface, tensile stresses of similar magnitude are present. The stresses are anticipated and ascribed to the additive manufacturing process due to various factors. Firstly, the temperature gradient experienced during fabrication plays an important role. Due to the use of a laser, the

material onto which the laser is directed, undergoes a rapid increase in temperature locally, consequently resulting in expansion. However, the surrounding material is cooler thus it counteracts this expansion inducing compressive stresses in the process. Upon cooling, the previously heated area contracts but once again, the surrounding material restricts the extent of contraction due to its different temperature hence the previously induced compressive stresses transform into tensile stresses. Additionally, the repeated melting and solidification of built layers may contribute to this phenomenon. During layer deposition, the underlying solid layers experience complete or partial re-melting due to the high temperatures present. Upon cooling, these layers shrink pulling and stretching the newly deposited layer thus, inducing tensile stresses. Lastly, the non-homogenous microstructure may also result from the non-equilibrium nature of the build process, leading to an inhomogeneous lattice spacing [191].

Following the application of a heat treatment, the surface stress decreased significantly to 2 MPa which is deemed as insignificant. This confirms that the heat treatment was effective in relieving the induced detrimental tensile stresses. Additionally, it is also beneficial as it homogenises the microstructure and diminishes the induced anisotropy [35]. Upon the deposition of the coating onto the previously heat-treated sample, a similar surface stress of 6 MPa was recorded. This suggests that the coating itself does not impart residual stresses. The coating's diminished stress measured may be a consequence of various factors including the deposition temperature, the coating's structure or its thickness. In this investigation, the coating deposited had a multilayer structure composed of various thin layers and was deposited at a low temperature reaching a maximum of 148 ºC. A diminished temperature prevents extensive contraction from occurring during cooling as it diminishes the effect of the differing thermal properties of the substrate and coating [185]. Low PVD coating stresses have been previously reported by Zammit *et al.* [81] for a multilayer WC/C coating deposited onto wrought Ti64 and were ascribed to the multilayer structure of the coating. Whilst, Yanfeng *et al.* [192] attributed lower stresses to the presence of a metallic Ti interlayer in a multilayer Ti/TiN coating. The more ductile metallic layer aided the relief of high stresses present in the ceramic layer. Similarly, this Ti interlayer was the initial layer deposited of the coating in the current investigation.

It is worth noting that the overall stress state of coating is also dependent on the substrate's stress state prior to deposition. Sprute *et al.* [193] observed that the

deposited multilayer Ti/TiAlN coating had higher compressive residual stresses when it was deposited onto a nitrided substrate as compared to a ground substrate since the nitriding process induced greater CRS in the substrate. As observed later on, this was also confirmed in the current investigation as upon the deposition of the coating onto the highly stressed previously shot peened substrate, a similar high compressive residual stress was measured at the coating surface unlike for the coating deposited onto the polished only substrate.

Additionally, the induced stress is also dependent on the coating thickness. Vogli *et al.* [194] deposited three different designations of a Ti/TiAlN PVD multilayer coating onto a high-alloy hot work tool steel. The difference between each designation is the thickness of the TiAlN ceramic layer with designation 'A' having the thickest TiAlN layers at 500 nm each, whilst the Ti interlayer thickness was kept constant throughout all designations. The authors observed that for designation 'A' lower compressive residual stresses were measured in the TiAlN layer as compared to the other conditions. This was attributed to the higher thickness of the ceramic layers which allows the better growth of the layer consequently resulting in an improved microstructure. In the current investigation, all ceramic layers had a thickness exceeding 500 nm thus, the diminished stress values measured may be attributed to this.

At the surface of the SP sample, a measured compressive residual stress (CRS) of 744 MPa implies significant plastic deformation, a conclusion supported by the KAM data and GAM maps presented in Section 4.1.5. A maximum CRS of 777 MPa was observed at a depth of 27 μm. These induced stresses contribute to the strengthening of the material by enhancing the material's resistance against crack initiation and propagation [12], [77], [78]. Similar values were observed for the DU sample whereby at the coated surface a CRS of 708 MPa was recorded and a maximum CRS of 729 MPa was recorded a depth of 30 μm. The difference is statistically insignificant indicating that the coating deposition process did not result in any significant relaxation of previously induced stresses. The absence of stress relaxation could be attributed to the deposition temperature, which as mentioned earlier reaches a maximum of 148 ºC - well below the Ti64 phase transition temperature (~800 ºC). The similar surface stress values of the PVD and DU samples compared to those of the HT and SP samples respectively could also be due to the X-ray's depth of penetration being similar to or greater than the coating's thickness. Thus, the stress

state of the underlying substrate rather than that of the coating was detected. However, obtained values are still useful as they confirm that the coating deposition process did not influence the stress state of the underlying substrate.

As observed in Figure 4.24, the stress profiles of both SP and DU conditions are characterised by very high compressive values at the near surface (depth < 40 μm) which exhibit minimal variation. Values are observed to decline at the middle depth ranging between 40 and 150 μm beyond which values reach minimal values and stabilise at depths deep below the surface. Higher stresses are confined close to the surface, in comparison to other peening methods such as laser shock peening, due to direct impact occurring at the surface thus the plastic restriction is concentrated at and just below the surface [11], [12], [85]. For both sample conditions, the effect of the peening treatment was observed to extend up to 140 to 150 μm from the surface, beyond which residual stresses were no longer of a compressive nature. This depth gives an indication of the stressed layer induced and is in correlation with that observed via the microhardness measurements.

Comparable stress magnitudes and hardened layers have been documented by Zhang *et al.* [83] and Xie *et al.* [11] for shot peened LPBF Ti64. The stress magnitude was observed to be dependent on various peening parameters [83], [86]. Impingement at higher velocities, correlating to an increased peening intensity, induces greater plastic deformation thus typically an increase in the CRS at the surface is observed [83]. Higher peening velocities also increase the thickness of the compressive stress layer and induce a maximum CRS at deeper depths [86]. In comparison, increasing the coverage does not thicken the hardened layer but enhances the subsurface maximum CRS [85], [86].

4.2 Hardness Analysis

4.2.1 Surface Microhardness

To determine the effect of the applied treatments imparted on the as-built Ti64, the surface hardness of each condition was measured, observed in the bar graph shown in Figure 4.25. This allows a direct comparison of hardness measurements recorded.

For the as-built sample, a hardness equivalent to 346 $HV_{0.2}$ was recorded. This is inline with values obtained by Hattal *et al.* [195] where values equivalent to 350 ± 13 HV were recorded. Such values are attributed to the fine acicular α' martensitic

microstructure, characterised by a high hardness and brittleness, resulting from the rapid cooling rates experienced during the build process [5], [46], [47]. Upon heat treating, the surface hardness of LPBF Ti64 decreased by approximately 4% to a value of 332 $HV_{0.2}$. The magnitude of the hardness drop is closely related to the heat treatment temperature. This is evidenced by hardness values recorded by Li *et al.* [196] for selective laser melted Ti64 heat treated at four different temperatures: 650 ºC, 750 ºC, 850 ºC and 950 ºC. As the temperature increased, the hardness was observed to drop to values below that of the as-built material which was equivalent to 375 HV. With heat treating, the phase transformation from α' to α and β, which is significantly softer, initiates and as the temperature increases a complete dual α and β phase is garuanteed whilst the phase fraction of the β phase progressively increases. The cooling rate also plays an important role since a slower cooling rate, such as that obtained through furnace cooling, encourages grain growth. Subsequently, this coarsening of the microstructure results in a decreased hardness [6], [47], [156].

Following the treatment of the surface by shot peening, the hardness of the built and heat treated sample increased by 40% to a value of 464 $HV_{0.2}$, confirming the occurrence of work hardening imparted by the impingement of shots. Similar increases in hardness were observed by numerous investigators for shot peened Ti64 [10], [81], [90], [197]. For broadly similar peening parameters, a 37% increase was observed by Zammit *et al.* [81] whilst a 35% increase was recorded by both Ganesh *et al.* [10] (and Yilidran Avcu *et al.* [197] where hardness values recorded reached 475 HV.

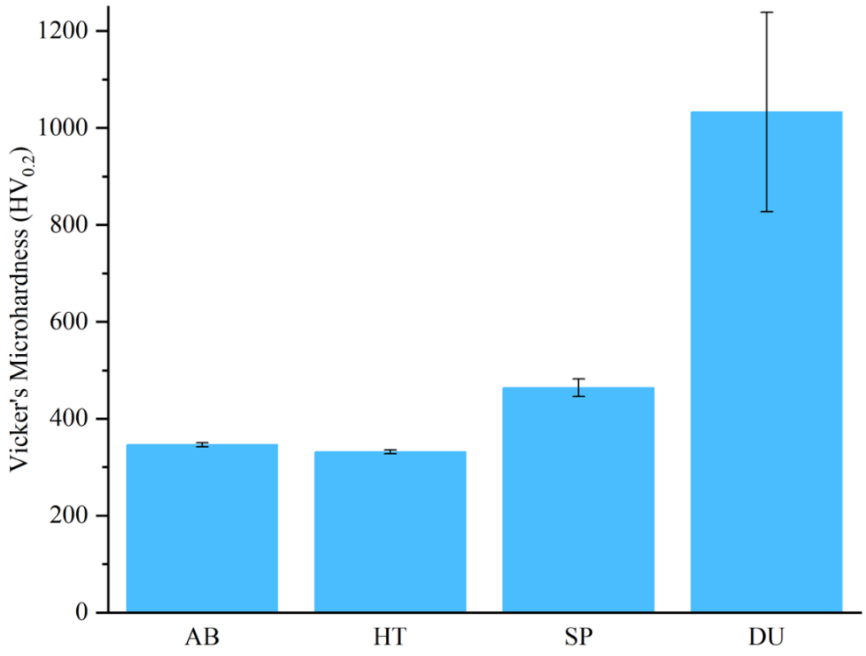

Figure 4.25 Comparison of the surface microhardness of the various conditions.

Surface hardening via shot peening has been attributed by investigators to two main mechanisms, being: (i) stress-strenghtening via the induced residual stress and (ii) microstructural-strenghtening via grain refinement [10], [11], [77]. Grain refinement significantly contributes to the reduction in grain size and the concurrent substantial increase in grain boundaries, primarily attributed to the occurrence of impingement. Grain boundaries hinder dislocation motion, essential for material deformation. Therefore, increasing the number of these boundaries restricts dislocation motion, resulting in enhanced material hardness and hence contributes to the overall strengthening of the material [10], [11], [83]. Shot peening can also impart a martensitic transformation, which can contribute to hardening, however in this case, this most likely did not occur as no apparent martensite peaks were detected by XRD phase analysis (in Section 4.1.6). For Ti alloys, this transformation is unlikely to occur due to their small crystal lattice distortion [198].

The most significant increase in hardness was observed for the duplex treated sample where the coating was deposited onto a previously shot peened surface. For the DU sample, a hardness of 1033 $HV_{0.2}$ was recorded contributing to approximately a 210% increase. This significant increase was expected since such ceramic coatings are characterised by high hardness values. Additionally, the coating investigated consists of multiple layers and such a structure has been observed to improve the coating's load carrying capabilities. This effect is observed as dislocation motion and crack propagation along the coating are hindered, attributable to the numerous interfaces formed by the distinct layers, which act as boundaries [15]. The load carrying capabilities also depend on the underlying substrate. Depositing the coating onto a hardened shot peened surface is beneficial as a harder substrate provides the coating with better load carrying capabilities, compared to softer substrates, since it can alleviate the stress concentration and minimise the strain at the substrate-coating interface to prolong the service life of coatings in harsh environments [198], [199], [200].

Microhardness measurements were not carried out for the substrate with only PVD coating; instead nanoindentation testing, detailed in Section 4.2.2, was employed to determine the actual hardness of the coating.

4.2.2 Surface Nanohardness

Nanohardness testing was conducted on the HT and PVD conditions only due to the high surface roughness resulting from deposition of the coating onto the previously shot-peened surface (DU condition), rendering the surface unsuitable for such analysis. Table 4.5 provides a summary of the hardness, modulus of elasticity and elasticity index of the PVD condition obtained via nanoindentation in comparison to values of uncoated HT condition obtained from Section 4.2 and 4.4.1.

Table 4.5 Data obtained from nanohardness testing of the multilayer coating compared with the data of printed and heat-treated Ti-6Al-4V.

	Hardness, H (GPa)	**Modulus of Elasticity, E (GPa)**	**Elasticity Index, H/E**
HT	3.00 ± 0.03	99 ± 3	0.030 ± 0.001
PVD	26.00 ± 2.00	337 ± 38	0.080 ± 0.011

The coating provided a ninefold increase in the hardness of the uncoated substrate, while concurrently multiplying the elastic modulus of HT LPBF Ti64 by nearly 3.5 times. This significant increase was expected since such transition metal nitride coatings are known for their high hardness, resulting from their minimal valence electron concentration, with values ranging between 25 and 38 GPa recorded for TiN coatings [104], [168], [201]. Additionally, alloying with elements such as Cu and Al has also been observed to influence the hardness of such ceramic coatings typically resulting in a slight increase [105], [202].

Moreover, the measured hardness is significantly greater than that recorded for the DU sample, which might be attributed to the indentation depth resulting during Vickers microhardness measurements, approximated to 1.90 μm, more than 10% of the coating's thickness. Thus, the softer underlying Ti64 substrate likely influenced the hardness measurements of the DU condition. In comparison, for nanohardness testing of the PVD condition, the indentation depth was observed to be around 320 nm only.

Whilst in the current investigation high hardness and elastic modulus were recorded, both values are still towards the lower end of the range observed in literature. This may be attributed to the inclusion of the initial Ti monolayer in the coating structure which has a considerable thickness in comparison to the other layers. This effect was observed by Ruan *et al.* [168] for a multilayer Ti/TiN/TiAlN PVD coating where, with increasing thickness of the softer Ti layer, an overall decrease in hardness, from 39 to

26 GPa, and stiffness, from 509 to 268 GPa, was observed as the Ti layer contributed to an overall decrease in the residual stress.

Additionally, the elasticity index provides an indication of the coating's ability to absorb elastic deformation without failure, it describes the elastic strain to failure of the coating [81], [203]. A high index, specifically a high elastic-to-strain failure ratio, is desired. This signifies that, when subjected to high cyclic stresses, the coating possesses the capability to deflect and follow the substrate's deformation without fracturing. This ratio can also be considered as a measure of the coating's ability to absorb energy elastically. For Ti and TiN layers, H/E values are typically around 0.044 and 0.067, respectively [203]. In comparison, for multilayer Ti/TiN coatings these values are observed to increase by 40 to 50% depending on the number of layers and thickness ratio [203]. Similarly, the value recorded in this investigation is around 50 ± 31% greater than typical figures quoted for Ti and TiN layers confirming that the application of the chosen multilayer coating is beneficial.

4.2.3 Profile Microhardness

Through hardness-depth measurements, the effect of the peening treatment below the surface could be determined. Figure 4.26 provides a comparison of the variation in hardness along the depth of the heat treated, shot peened and duplex treated conditions.

As observed, the effect of the peening treatment is very clear. For the HT sample, hardness measurements were mostly constant along the depth whilst for the SP and DU samples, initial values recorded were higher and decreased gradually until bulk hardness values were reached. From Figure 4.26**,** the peening treatment appears to be effective up to a depth of approximately 180 µm for both the SP and DU conditions. A similar affected depth for shot peened LPBF Ti64 was observed by Zhang *et al.* [83]. The authors observed that the effect of the treatment extended to 180 µm below the surface of selective laser melted Ti64 which underwent shot peening at 0.2 mmA and 2 bar using 600 µm steel shots. However, various other hardening depths are also observed in literature, as outlined below.

Aguado-Montero *et al.* [85] recorded a hardened depth of 325 µm for shot peened SLM Ti64 impinged by 600 µm steel shots at an intensity of 0.35 mmA for 500% coverage. This difference in results may be attributed to the varying shot size and peening intensity where, in the current investigation, a smaller shot size (300 to 425 µm) and intensity (0.20 mmA) were utilised [14], [27], [197], [204]. The shot size

has been observed by both Ahmed *et al.* [14] and Yilidran Avcu *et al.* [197] to have a significant effect on the depth of the hardened layer. Ahmed *et al.* [14] observed that an increase in shot size contributed to a deeper hardened layer which was however limited up until a certain depth.

Similarly, Yilidran Avcu *et al.* [197] recorded varying depths of hardened layer when shot peening wrought Ti64 under different conditions. At a constant pressure of 7 bar but with increasing intensity and shot size, a significant increase in the hardened depth was observed from 120 µm to 550 µm.This was attributed to the amount of plastic deformation induced by peening which is dependent on the kinetic energy exerted by the shots. Larger shots exert greater kinetic energy thus the increased magnitude of the hardened depth. The effect of the peening intensity was observed by Yang *et al.* [204] where for shot peened Ti64 using intensities ranging from 0.2 to 0.4 mmA, the hardened layer was observed to increase from 90 to 135 µm with increasing intensity.

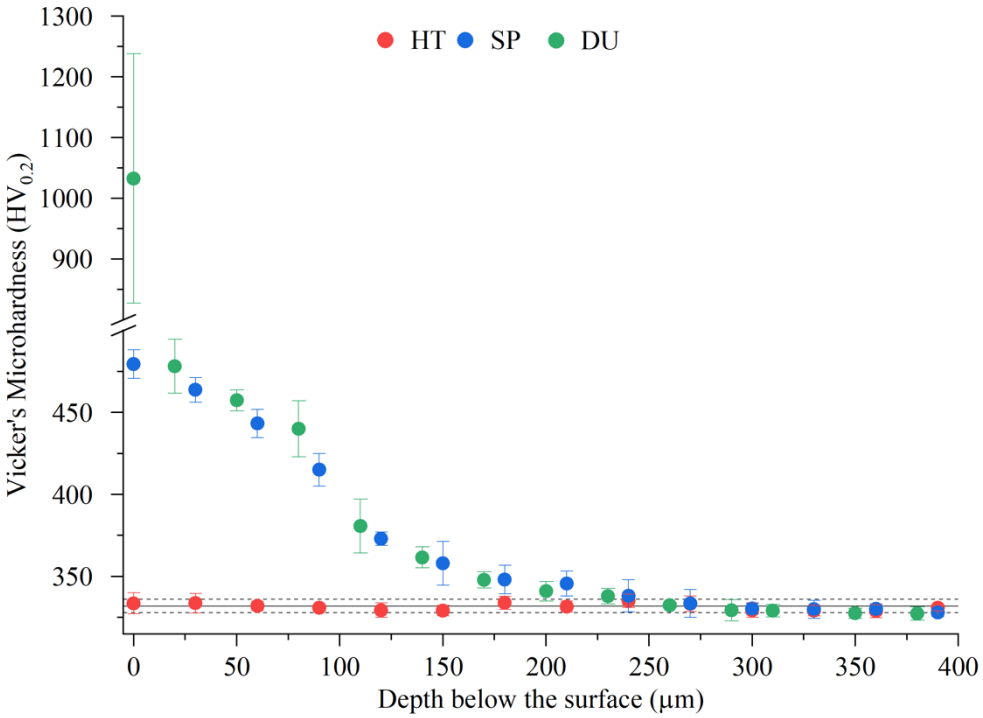

Figure 4.26 Variation in hardness along the depth of the HT, SP and DU conditions.

Although achieving a significant hardened depth is a desireable outcome, it is important to consider that larger shots and peening intensities may result in a significantly rougher surface. Surface roughness should ideally be minimised due to its negative influence on the material's performance especially in high cycle applications and corrosive environments [197]. Additionally, smaller shots have then been observed to induce greater compressive stresses [14]. Hence, for the envisioned

application in the current investigation, a good balance of peening parameters is crucial.

4.3 Mechanical Properties Analysis

4.3.1 Tensile Testing

To determine the ultimate tensile strength, yield strength, Young's modulus, and elongation of the LPBF Ti64 substrate, tensile testing was conducted for which the results are presented in in Table 4.6. The values obtained were also compared to values extracted from literature obtained for built and heat treated and wrought Ti64. These were compared with built Ti64 that underwent as similar heat treatment to that conducted in the current investigation. The comparison between the various values can be observed in Figure 4.27 for the yield strength (YS), ultimate tensile strength (UTS) and Young's modulus of elasticity (E) and in Figure 4.28 for the elongation (El).

Table 4.6 Mechanical properties derived from tensile testing of the printed and heat-treated (HT) LPBF sample.

Sample	UTS (MPa)	YS (MPa)	E (GPa)	El (%)
Printed + HT	893 ± 52	817 ± 50	102 ± 8	7 ± 1

Both strength and modulus of elasticity values recorded in the current investigation, as observed in Figure 4.27, are in line with those recorded in literature for heat-treated LPBF Ti64, within the range of values recorded for conventionally manufactured Ti64 and exceed minimum values set by standards, rendering the studied material acceptable for use in application.

Various researchers have reported ductility ranging from 1 to 8 % for as-built untreated Ti64 [6]. As observed in Figure 4.28, a wide range of values have been observed for built and heat treated Ti64 in literature, however values as high as 14% were also recorded. Such high values are comparable to those recorded for wrought Ti64 and exceed the minimum set value of 8%. Such high ductility values are typically observed as the heat treatment encourages the transformation of the brittle martensitic phase into a more ductile alpha and beta dual phase [149], [180], [205], [206].

The ductility value recorded in the current investigation is at the lower end compared to literature values for as-built and heat treated Ti64, suggesting that the applied heat treatment did not result in a significant change, however it is still within the range. Additionally, it is significantly less than values recorded for wrought Ti64 and is

marginally within the minimum values identified by the standards [40], [41]. This diminished ductility, may be correlated to the low quantity of beta phase formed following the heat treatment, which is more ductile than the alpha phase due to its bcc structure since, as compared to the hcp structure of the alpha phase, has more available slip planes [1], [20], [149].

Another factor affecting the ductility is the presence of defects such as micro-cracks, lack of fusion and pores which as-built materials are prone to due to their layer-by-layer manufacturing. Additionally, such defects negatively impact the mechanical properties by contributing as stress concentration sites [149], [196], [207]. In the current investigation these defects could have likely contributed to the diminished ductility as their presence was confirmed later in Section 4.3.2 during the microscopic analysis of impact fractures. Such defects may be mitigated by employing optimal printing parameters.

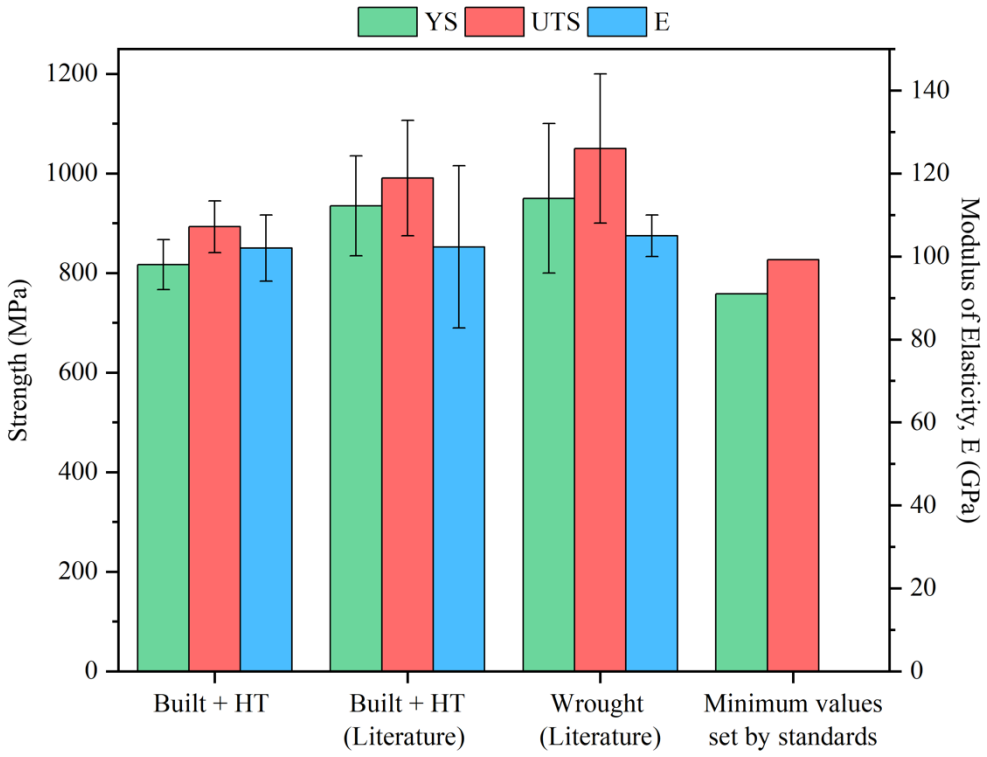

Figure 4.27 A comparison of the yield strength (YS), ultimate tensile strength (UTS) and Young's Modulus (E) of the printed and heat treated sample compared to (i) values observed in literature for the same condition and wrought Ti64 and (ii) the minimum values set by standards [90], [91]. Errors were calculated via the min-max method.

The material's ductility is also dependent on the build orientation for additively manufactured components as the orientation will influence the direction along which tension is applied. For a horizontal build direction, as adopted in this investigation, low elongation values, less than 10%, were expected since tension was applied perpendicular to the formed columnar grains. In this orientation, there are less effective grain boundaries, which are initially required due their interference with crack growth [149], [205].

Thus, following heat treatment, the built material has properties comparable to those recorded for wrought material with an exception for the elongation. This is a very common observation and it is attributed to the difference in microstructures resulting from the varying manufacturing techniques [5].

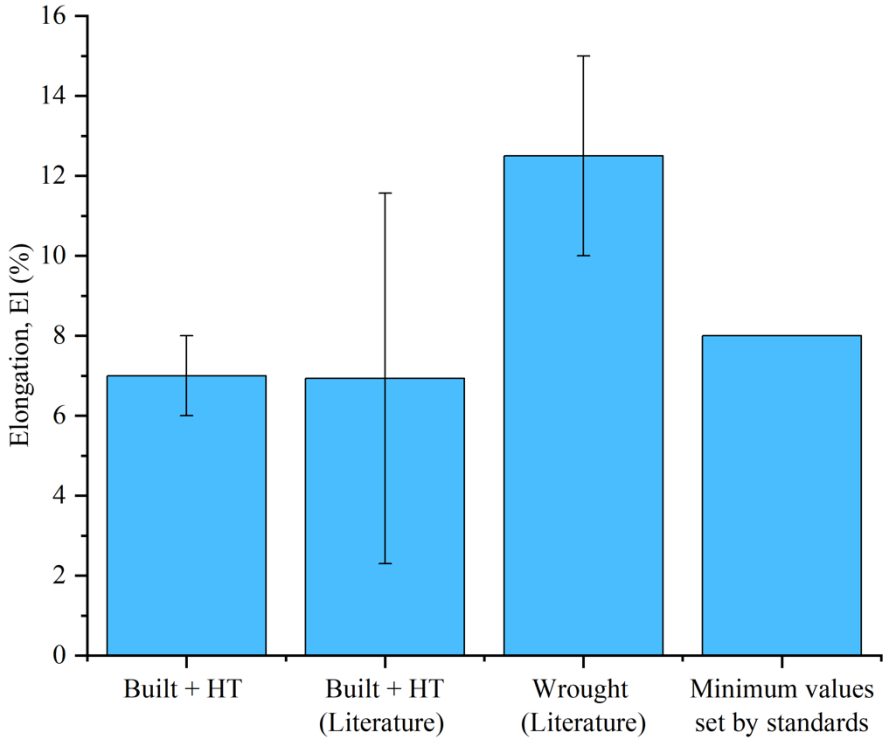

Figure 4.28 Recorded ductility values in comparison the values observed in literature and to minimum values stipulated by standards [90], [91]. For measured values the error was calculated via the min-max method whilst for quoted values, the error bars represent the range.

4.3.2 Impact Testing

Following the impact testing of built and heat treated Ti64 specimens, it was observed that the specimens were capable of absorbing a total energy of 14.3 ± 2.0 J. Typically, for as-built Ti64 values ranging between 4 and 10 J have been recorded in literature. Such diminished values are a consequence of the highly brittle martensitic structure of the as-built material [142], [179], [208], [209], [210]. Thus, in comparison the specimen in this investigation have exhibited an improved performance which may be

attributed to the prior heat treatment conducted resulting in the decomposition of α' into α and β. Similarly, this was observed by Lee *et al.* [179] whereby a 20% increase to 7.3 J, in the absorbed energy was recorded following annealing.

The improved performance observed in the current investigation may also be attributed to the build orientation, a factor known to influence the absorbed energy values [209]. In the current investigation, the test specimens were built horizontally. Numerous investigators observed that horizontally built samples can absorb more energy than vertically built samples due to the crystallographic texture of the as-built material [209], [142], [211]. Unlike wrought Ti64, which exhibits a random distribution of crystal orientations, as-built Ti64 is strongly oriented along the <100> direction resulting in anisotropy [42], [142]. Thus, horizontally built samples exhibit a better performance since the notch and fracture direction are perpendicular to the individually built layers which aid to hinder crack propagation [142]. This build orientation dependent performance is unwelcome as it restricts the material's use in industrial applications. However, its effect can be mitigated by ensuring that layer adhesion is excellent and devoid of defects [208].

Values recorded in the current investigation are significantly reduced compared to those of wrought Ti64, for which values as high as 49 J were recorded [212]. This difference can be attributed to the varying microstructures where the typically equiaxed microstructure of wrought Ti64 is much more ductile in comparison to the fine needle-like structure of as-built Ti64 [179], [211]. This difference in values also exists as it is dependent on the volume fraction of the phases [179]. As confirmed in Section 4.1.6, the HT sample contains only a very minimal fraction of the more ductile β phase exhibited by the minor β peak detected among the numerous α peaks.

The fractured surfaces were observed via microscopy to determine the nature of the fracture. The high magnification micrographs in Figure 4.29 depict regions at the top of the fracture where final fracture occurred (Figure 4.29(a)), the middle section (Figure 4.29(b)) and at the bottom where fracture initiated (Figure 4.29(c)). The fractures mainly exhibit characteristics of brittle fracture as significant plastic deformation does not appear to be visible. Additionally, as highlighted in Figure 4.29(b) and (c), various cleavage facets can be observed, further evidence of brittle fracture. Some dimples are also evident which are typical characteristics of a ductile fracture (highlighted in Figure 4.29(a) and (c)). For AM Ti64, brittle fracture has been

observed by various investigators including Yasa *et al.* [208] and Lee *et al.* [179]. However, the possibility of a mixed-fracture, characterised by the presence of both brittle and ductile fracture features, as observed in this case, has been documented by Kazachenok *et al.* [212] and Hacisalihoglu *et al.* [211]. It is plausible that a mix of both fracture types is present due to the heat treatment which allowed the decomposition of the martensitic phase, thus enhancing slightly the ductility but still retaining some brittleness due to the resulting fine microstructure.

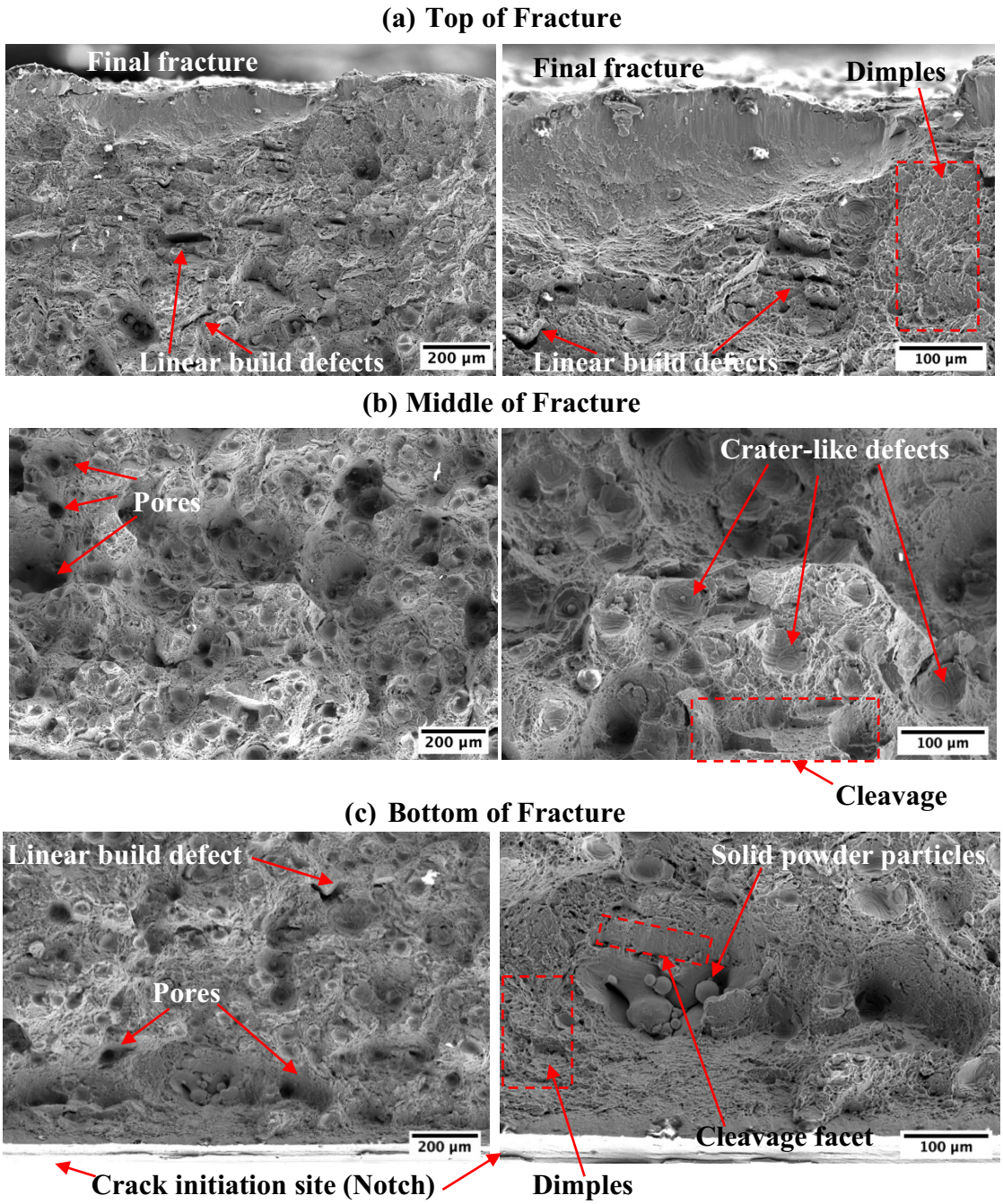

Figure 4.29 High magnification micrographs of the impact fractures of the built and heat treated sample (HT) depicting (a) the final fracture zone, (b) middle fracture zone and (c) the crack initiation zone.

The micrographs also expose the presence of various build defects, which the additive manufacturing parts often retain, including porosity and solid un-melted powder particles as highlighted in Figure 4.29(b) and (c). Such defects negatively impact the toughness of the as-built material thus are a contributing factor to the large difference present between values recorded for wrought and as-built Ti64 [208], [209]. Similar to Wu *et al.* [213], numerous linear building defects (Figure 4.29(a)) were observed in the current investigation. Such defects are an indication of an inconsistent build quality having sub-standard adhesion and cohesion between the several layers. Their presence diminishes the material's load bearing capacity subsequently reducing its impact toughness [213]. In addition, several crater-like defects, highlighted in Figure 4.29(b), were observed. Such defects exhibit characteristics of cleavage fracture which may be evidence of the event of particle detachment or pull-out.

4.3.3 Axial Fatigue Testing

The results obtained following axial fatigue testing of the HT, SP and DU sample conditions can be observed in Table 4.7. Runout was set at 3×10^6 cycles to limit the maximum test to a reasonable duration. As observed, despite overlap in the quantity of life cycles endured across all conditions, all HT samples failed before the runout setpoint, whilst for both the SP and DU conditions, instances of run out were recorded. This suggests that the chosen surface treatments can improve the fatigue life of the as-built material however, the degree of improvement is highly dependent on various factors as will be discussed.

While all results presented show a degree of scatter when comparing the number of cycles survived at the selected load, for the HT sample this is minimal. This sample was observed to withstand an average of 190,003 ± 71,999 cycles. However, whilst instances of run-out were recorded for both the SP and DU conditions, failures at cycles in the range of 2×10^5 were also recorded exhibiting a significant scatter in values. Additionally, some failures undergone by both sample conditions were within the range of the HT sample implying that in such cases, the treatments were not beneficial and neither enhanced nor decreased the fatigue life of the untreated material.

In relation to the effect of surface roughness, Walker *et al.* [43] conducted a similar study where SLM Ti64 samples machined to a surface roughness of 0.8 μm, underwent axial fatigue testing at an applied stress of 600 MPa. All samples failed after an average of 266,517 cycles [43] i.e. similar to the number of cycles survived in this work.

Nonetheless, samples tested in the current work were heat treated. This suggests, that given the surface finish is optimal and defect density is low, heat treatments might not necessarily be required for improvement in the fatigue performance.

Table 4.7 Cycles endured by the samples following axial fatigue testing including statistics based on obtained results where applicable. No failure relates to the occurrence of run out, where samples reached 3,000,000 cycles without failure. Errors were calculated via the min-max method.

Condition		Life at 570 MPa (cycles)	Average cycles to failure (cycles)	Minimum life (cycles)	Maximum life (cycles)
HT	**1**	232,547	190,003 ± 71,999	125,101	269,100
	2	125,101			
	3	230,531			
	4	269,100			
	5	150,084			
	6	132,658			
SP	**1**	295,349	N/A	259,425	> 3,000,000
	2	No failure*			
	3	330,021			
	4	259,425			
	5	No failure*			
	6	No failure*			
DU	**1**	No failure*	N/A	223,165	> 3,000,000
	2	294,441			
	3	845,538			
	4	837,025			
	5	223,165			
	6	No failure*			

Considering the average cycles endured by the failed shot peened samples, it can be approximated that peening resulted in an increase in the fatigue strength. This increase can be attributed to the induced residual stress field whose effect surpasses that imposed by the increased roughness. Similarly, Kahlin *et al.* [88] and Aguado-Montero *et al.* [85] observed a 70% and 75% increase in fatigue strength of AM Ti64 following shot peening. The authors also noted that the induced stress field promoted the closing

of pores thus reducing possible crack initiation sites [85]. However, this effect was not investigated here. Whilst overall an improvement was observed, in one instance for SP4, the cycles endured overlap with those endured by the HT samples. This could be attributed to significant LOF defects, evidenced in Figure 4.31, which hastened its failure or it could be an instance where the roughness induced by the peening process outweighed the beneficial effects of hardening and compressive stresses induced by the peening treatment. This was observed by Wysick *et al.* [89] where polishing AM Ti64 improved the fatigue limit significantly more than shot peening.

Whilst shot peening has had an overall positive impact, the same cannot be attested for the coating under study. Literature presents a disputed view of the effect of PVD coatings in relation to fatigue, for instance whilst Puchi-Cabrera *et al.* [119] observed an increase in the fatigue limit following the deposition of a TiN coating on 316L SS, Costa *et al.* [120] observed the opposite effect for Ti64 coated with a TiN layer. Results presented in this work suggest that the coating did not have a significant influence as the DU condition presented a similar behaviour to that exhibited by the SP condition.

The significant scatter in values determined via axial fatigue tests may be attributed to a number of factors which introduce an element of variability including: lack-of-fusion (LOF) defects and porosity, a high surface roughness, tensile stresses or anisotropy [43], [85], [89], [214]. Defects vary from one sample to the next and furthermore, their shape, position, and orientation with respect to the direction of applied stress also varies thus resulting in scatter. LOF defects typically form perpendicularly along layer boundaries due to the insufficient energy. Such features were also observed to be the main locations at which failure originated from [43]. In the current investigation, these are likely the main source of the observed scatter as their presence was observed when analysing the fractures optically (Figure 4.30 – 4.32). The effect of the surface roughness can be eliminated via polishing or machining whilst the effect of the induced tensile stresses can be mitigated via the application of a heat treatment of shot peening. Both measures were adopted in the current investigation to mitigate their effect as much as possible. The build direction also plays a role. The samples tested in the current investigation were horizontally built which were observed by Leuders *et al.* [44] to exhibit less scatter than vertically built samples and in addition endure more cycles. Dispersion in fatigue life values of LPBF materials, is also related to the

different mechanisms by which samples fail, observed to be dependent on the build parameters and loading method [89], [214].

From the review of micrographs of the fracture surfaces, the origins of crack initiation could be determined. Observation of crack surfaces show that initiation points coincided with existing surface defects such as pores and other internal build defects which in turn impacted the lifetime significantly. All HT samples failed with HT2, HT4 and HT5 failing due to LOF defects and porosity present just or at below the surface, as observed in Figure 4.30. In comparison, for HT1 and HT3, no surface defects or pores were observed. In both cases, fracture could have been encouraged by improper mounting resulting in the contribution of shear stresses, in addition to the applied axial stress, during testing. On the other hand, HT6 likely failed due to an improper surface finish at the side of the samples as various shallow grooves and scratches were observed.

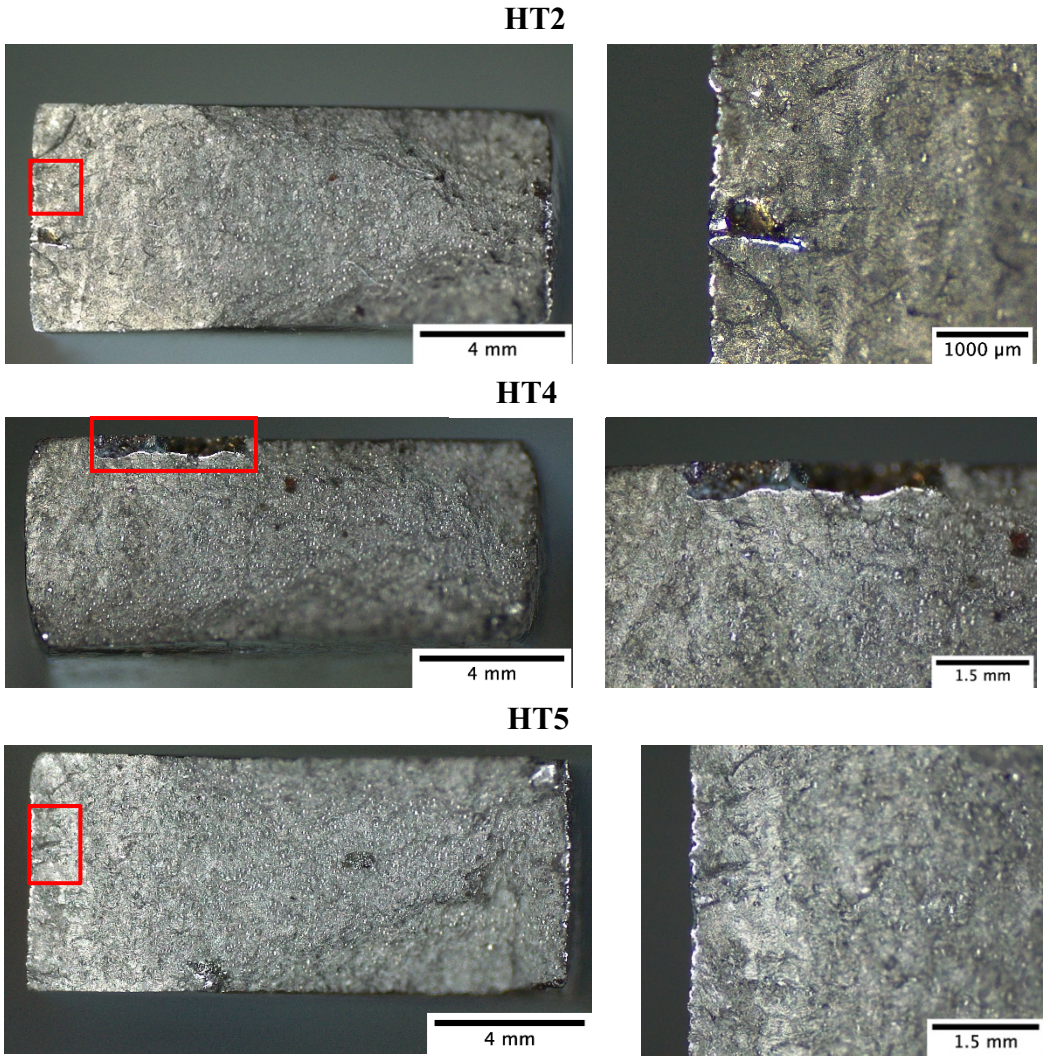

Figure 4.30 Optical micrographs of the fractures and fracture initiation point observed for HT2, HT4 and HT5.

For both SP1 and SP4, failure occurred at an LOF defects just below the surface originating from the manufacturing process as observed in Figure 4.31. Whilst, for SP3, failure initiated from a large pore present at the surface. Moreover, for samples DU3 and DU4, the occurrence of failure at a significantly higher cycle counts was attributed to the lack of defects observed both at and below the surface. Thus, as compared to HT1 and HT3 which were also mostly defect free, the application of the duplex treatment was successful in enhancing the fatigue performance of the material. On the other hand, the shorter life of DU2 and DU5 was due to significant LOF defects and pores present at the surface and sub-surface, as highlighted in Figure 4.32, similar to the SP sample which underwent failure.

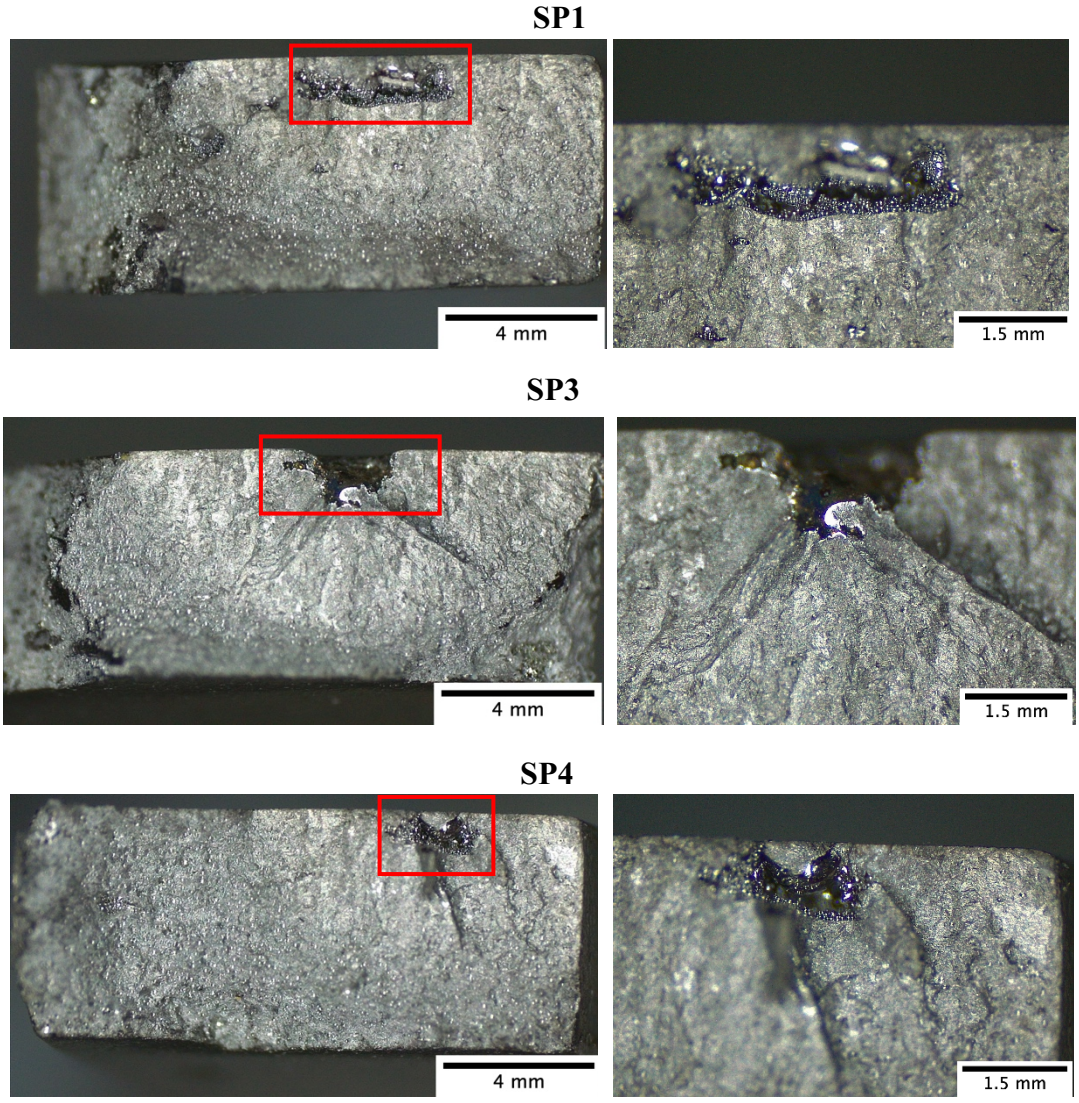

Figure 4.31 Optical micrographs of the fractures and fracture initiation point observed for SP1, SP3 and SP4

Chastand *et al.* [214] identified porosity and surface defects as the least and most critical failure mechanisms, respectively. Failures occurring from pores were observed impact the fatigue life less severely whilst surface defects were observed to be the most critical as they easily encourage fissure initiation. Consequently, most failures were observed to occur within 1 mm from the surface as at such locations, fracture propagation and creation of emerging cracks are promoted rather than impeded. Thus, the authors theorise that the position, size and concentration of defects is more critical for the occurrence of crack initiation than the quantity of such defects. A high concentration of microscopic defects positioned at the near surface are the ideal combination for the promotion of crack initiation [214].

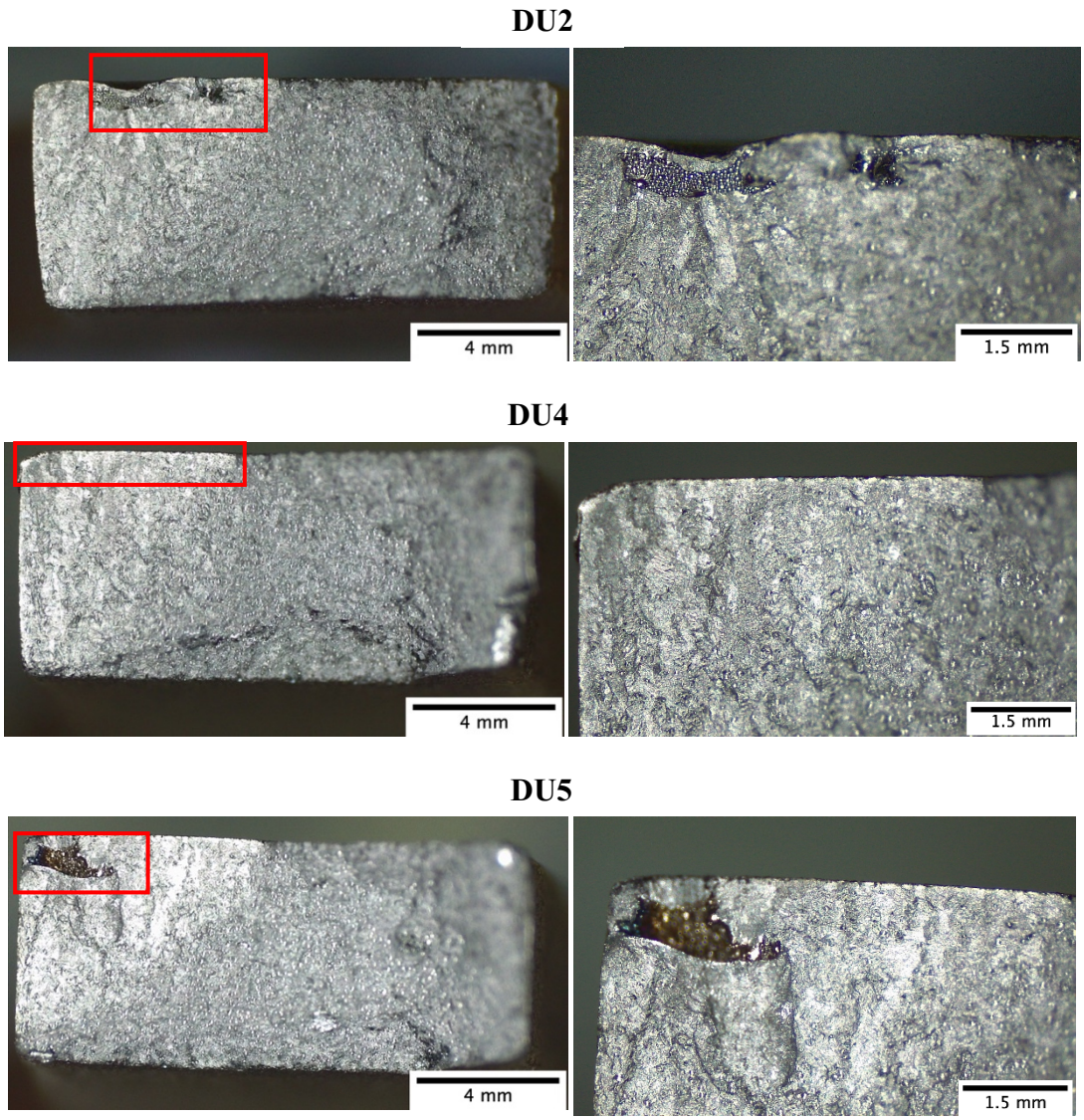

Figure 4.32 Optical micrographs of the fractures and fracture initiation point observed for DU2, DU4 and DU5

Fatigue cracks typically present different textures. Close to the defect which acts as the crack initiation point, the fracture is shiny and smooth even as it propagates. However, at the point of catastrophic rupture, the fracture surface appears dull and very rough. These variations in textures arise from the transitioning crack growth. At the initiation point, the fracture undergoes short crack growth as plastic strain is minimal and the change in the stress intensity factor is low. With propagation, plastic strain and change in the stress intensity factor increase thus crack growth transitions from short to long [85]. At this stage, Aguado-Montero *et al.* [85] observed that long crack growth is typically characterised by striations. At the point of final fracture, crack growth is significant, and fracture is static characterised with microvoids. A similar change in textures was observed in the current investigation for all fractures. As observed in all Figures 4.30 – 4.32, close to the initiation point the surface is shiny. Its appearance then gradually becomes darker and rougher at the final fracture point.

In conclusion, while it appears that the surface treatments do enhance the fatigue life of the samples it also important that defect density is kept minimal mainly via the adoption of optimal build parameters. This combination would allow for improved fatigue life coupled with a reliable and more repeatable performance.

4.4 Corrosion Testing

Representative potentiodynamic curves obtained for all sample conditions tested in simulated ocean water, can be observed in Figure 4.33. For comparison, a bar graph of the corrosion potential, E_{corr}, corrosion current density, $i_{corr,}$ and the current density, J, at 400 mV vs SCE values, depicting a range of three repeats, was plotted as observed in Figure 4.34.

From the PD curves and as observed from the bar graph, the overall best resistance against corrosion was provided by the PVD condition, where the coating was deposited onto polished and heat-treated LPBF Ti64. This was exhibited by the minimal i_{corr} values and more positive E_{corr} values. The HT sample exhibited a similar behaviour to the PVD condition, exhibited also by the minimal i_{corr} values however, in comparison the obtained plots were shifted further to the left suggesting that from both conditions, the PVD coated sample is superior. This is further encouraged by the much smaller current density values recorded for the PVD condition at 400 mV. However, at around 1400 mV for all three repeats, the current density of the PVD condition undergoes a steep increase in current values which was not observed for the HT condition. This

increase indicates that pits are starting to form thus this value is regarded as the pitting potential, E_{break} or E_{pit}.

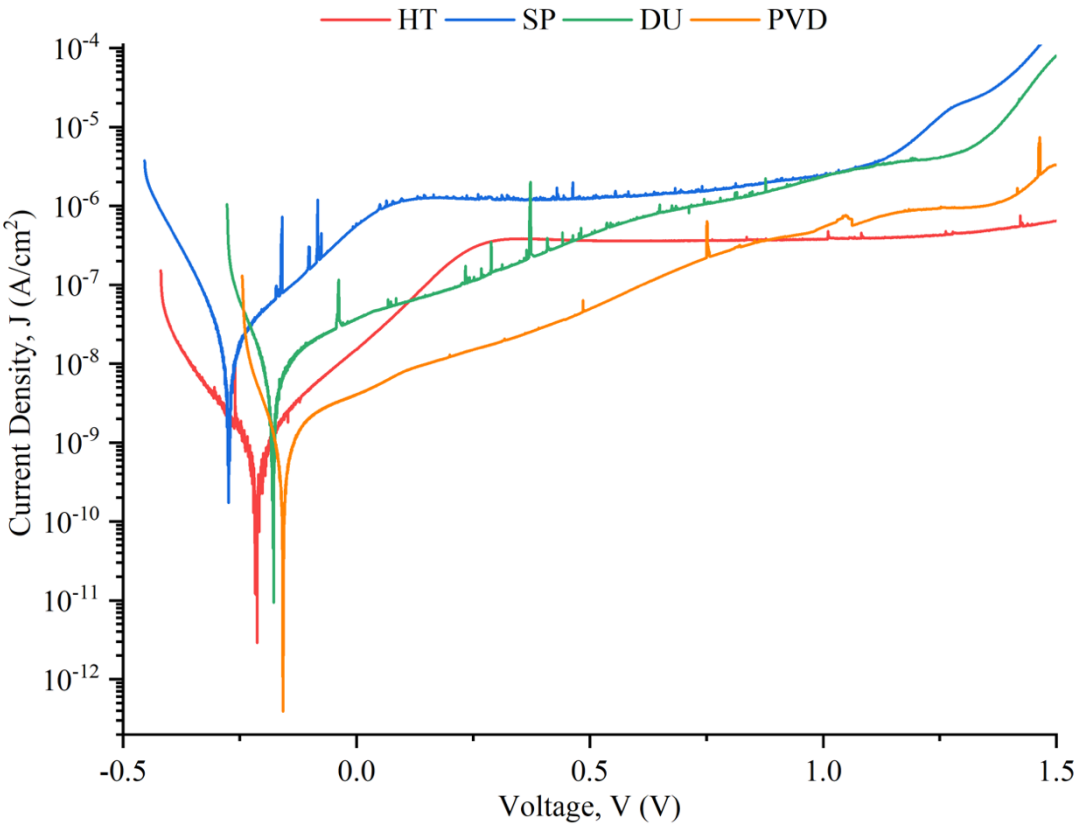

Figure 4.33 Representative potentiodynamic (PD) curves obtained for each of the tested conditions.

On the other hand, it can be deduced that both peening and duplex treatments were not effective in improving the corrosion resistance as evidenced by their significant i_{corr} values. The SP and DU conditions exhibited a similar behaviour to the HT and PVD samples respectively, however in both cases the obtained plots were shifted upwards and towards more negative voltage values, highlighting their inferior performance. Additionally, in comparison to the HT condition, the SP sample exhibited an E_{break} potential of around 1000 mV. The DU condition also exhibited the occurrence of this phenomenon at around 1200 mV.

As depicted by both Figures 4.33 and 4.34, the HT condition where the as-built sample was heat treated and then polished exhibited a good corrosion performance without the application of any other treatments. Commercial Ti64 itself without any treatments has an excellent corrosion performance, however additively manufactured Ti64 has exhibited an inferior resistance which has been attributed to the present phases. Unlike commercial Ti64, which is typically composed of equiaxed α and β phases, as-built Ti64 is overall composed of the acicular α' martensite as observed in Figure 4.1(a) in

Section 4.1.1.1. This α' phase is metastable existing in a high energy state, thus is more susceptible to dissolution in corrosive environments [30], [50]. Hence, the utilisation of heat treatment in the present study proved advantageous as it facilitated the removal of the α' phase, ensuring that the material, in its as-built, heat treated, and polished state, will demonstrate an adequate resistance to corrosion.

However, other investigations have shown that heat treating does not always guarantee an improvement. Both Yang *et al.* [30] and Dai *et al.* [215] conducted investigations into the influence of heat treating at different temperatures on the corrosion performance of additively manufactured Ti64, in a simulated seawater solution. In both investigations, the authors observed that heat treating at a temperature beyond 850 ºC was not beneficial, resulting in greater corrosion current density values. Thus, these investigations contradict the assumption that higher heat treatment temperatures are more beneficial for the corrosion performance as, whilst eliminating the α' is beneficial for improving the corrosion resistance, other factors also have a major influence including the grain size and phase fraction [30]. In particular, the mode of diffusion and the speed at which it occurs during corrosion is different for the various phases [216].

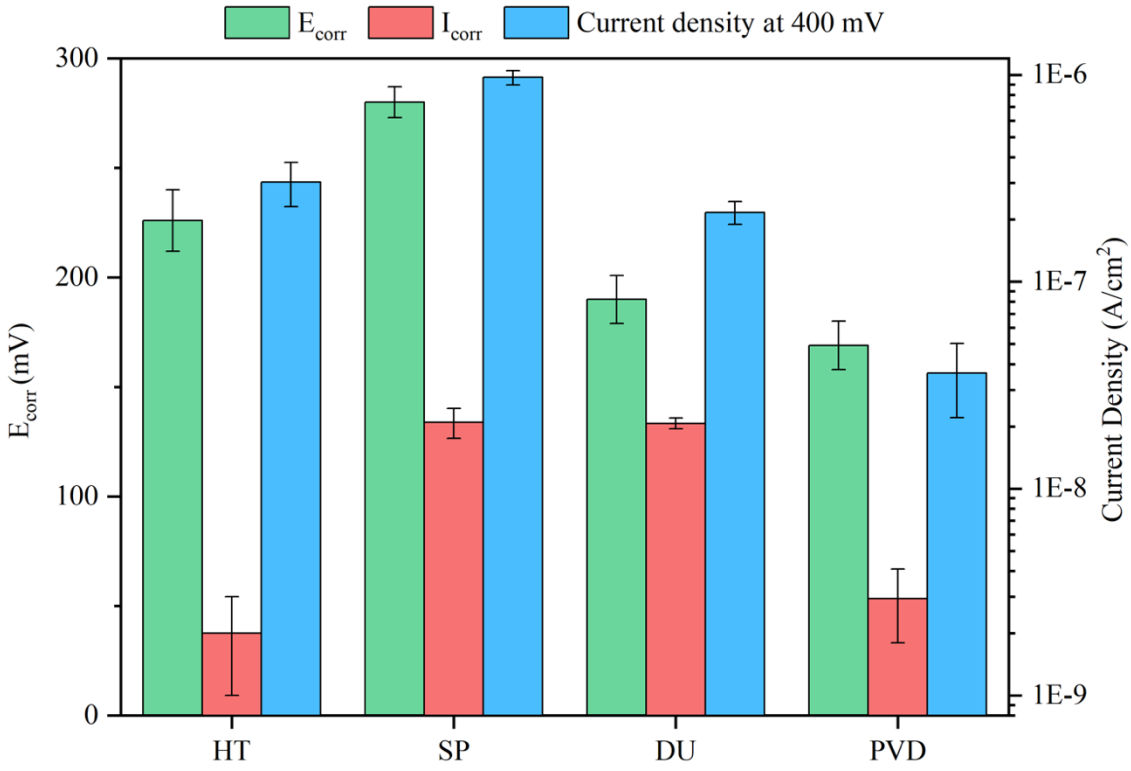

Figure 4.34 A visual comparison of the corrosion potential, E_{corr}, corrosion current density, i_{corr}, and the current density at 400 mV vs SCE values for each of the tested conditions.

As mentioned previously, the higher energy state of α' phase results in its easier dissolution as compared to the α phase. On the other hand, the β phase has a higher vanadium content which improves its resistance against dissolution. Therefore, the corrosion resistance of the phases can be ranked as follows: β > α > α' [30]. The β content can be increased by adopting higher heat treatment temperatures however this is also accompanied by an increase in grain size, especially if furnace cooling is adopted. For Ti and its alloys, the general consensus is that the smaller the grains the better the material's resistance against corrosion. This is typically attributed to the more rapid passive film formation which occurs, encouraged by the finer grains. Additionally, the higher grain boundary density, as a result of the finer microstructure, has also been observed to enhance the passive film's adhesion [217].

To summarise, the corrosion performance is very sensitive to the heat treatment adopted. From these investigations, it can be inferred that the ideal heat treatment should result in a thermally stable, dual α and β phase consisting of fine grains having the perfect balance between eliminating the α' phase and having enough β content without significantly increasing the grain size [30]. Such a microstructure appears to have been achieved in the current investigation as observed previously in Figure 4.1(b) in Section 4.1.1.1 and as confirmed by the phase analysis carried out in Section 4.1.6. Thus, as compared to other materials, the initial corrosion performance of the built, heat-treated and polished material, prior to any surface treatments, is considered to be very good.

The poorer corrosion performance exhibited by the SP condition in the present study can be attributed to numerous factors. In literature, contradicting results have been observed. Zhang *et al.* [83] observed an improvement in the corrosion performance of LPBF Ti64, which underwent shot peening and ultrasonic peening separately, as compared to the untreated condition, in 3.5 wt.% NaCl. This improvement was attributed to the induced grain refinement which, in the present study was not obvious as highlighted in Sections 4.1.1.1 and 4.1.5. Grain refinement is sought after as it promotes passive film formation [83]. Another factor which impacts the corrosion performance is the resulting surface topography following peening which, as highlighted in Section 4.1.4, was observed to increase by around 41 times to 1.9 μm. Its limiting effect was observed by Zhang *et al.* [83], as although the shot peened sample exhibited an enhanced corrosion resistance, it was constrained by the greater

roughness induced when compared to ultrasonically peened sample which exhibited the best corrosion performance overall due to the limited roughness and grain refinement induced by the process. In addition, several previous investigations observed no change or a decrease in corrosion resistance following shot peening when testing in 3.5 wt.% NaCl, 0.9 wt.% NaCl and Ringer's solutions [13], [14], [218]. In all cases, this lack of improvement in corrosion resistance was correlated to the high surface roughness as it increases the interaction area and promotes the growth of an unsound passive film [13], [14].

The effects of the induced roughness were also reflected in the results obtained for the coated substrates. As highlighted in Section 4.1.4, for the PVD condition a surface roughness of 43 nm was observed whilst for the DU condition a value of 1.7 μm was recorded. The coating deposited onto the polished surface (PVD condition) exhibited significant resistance to corrosion as compared to the coating deposited onto the previously shot peened surface (DU condition). The main difference between both conditions was the induced roughness which is known to increase the defect density of coating, diminishing its protective abilities. Additionally, irrespective of the effect imparted by the substrate's surface condition, the coating's performance was likely improved via the addition of copper in the top-most layer. Blinkov *et al.* [104] observed that as compared to a TiAlN coating, the addition of 3 at.% Cu improved the performance of the coating by enhancing its pitting resistance and tendency to self-passivate. Additionally, the deposition of the coating via magnetron sputtering was essential as this technique has been observed by Durst *et al.* [112] to result in sound coatings having minimal defects and a good corrosion resistance.

However, for all conditions except the HT condition, a sudden increase in current density values was observed. The voltage at which the sample exhibits this increase is regarded as the pitting potential, E_{break} or E_{pit} and it was recorded for all three repeats of the SP, DU and PVD sample conditions. It indicates that at these potentials, the passive layer is undergoing localised corrosion, likely being manifested as pitting. The HT sample did not exhibit this phenomenon, most likely due to having a more stable passive film which was less likely to breakdown [154]. The high surface roughness of the SP (1.9 μm) and DU (1.7 μm) treated samples, compared to that of the HT sample, is likely contributing to the formation of an nonuniform and unstable passive film with more active sites that encourage its breakdown, as evidenced by the pitting observed

in Figures 4.35 and 4.36 [83]. On the other hand, for the PVD condition, the coating was deposited onto a surface of minimal roughness. In this case, this phenomenon may be attributed to localised corrosion occurring due to the seawater solution propagating towards the substrate via the pathways created by the columnar structure of the coating, observed in Figure 4.6, or defects present, observed in Figure 4.5(d). It is worth noting, that the impact of the surface roughness is further highlighted by the fact that for the DU sample, this increase in current density values is occurring earlier in comparison to the PVD condition. However, the coating is then effective in delaying its occurrence when comparing the DU and SP conditions.

To understand better why a poor corrosion resistance was observed for the SP and the DU treated samples, the samples were observed using a scanning electron microscope. As shown in Figure 4.35, for the HT sample negligible corrosion damage was observed whilst for the PVD sample, minimal damage was observed with pit-like features occurring sparsely in the test area. However, as evident from Figures 4.35 and 4.36, notable depressions resembling pits were observed in both the SP and DU samples. Craters and cracks observed on the surface of the shot-peened sample are attributed to damage sustained during the application of the peening treatment. Such defects, allow the solution to penetrate and become trapped, resulting in a more corrosive environment. Consequently, this increases the likelihood of localised corrosion, specifically of the crevice corrosion type, to take place. Moreover, for the SP sample, various white patches can be observed both inside and outside the test area. These were confirmed in Section 4.1.2 to be embedded ceramic fragments from the shot media. Surrounding such patches, no evidence of a corrosion attack was observed due to ceramics being unreactive unlike other metallic materials which in comparison, would have resulted in galvanic corrosion due to their reactive nature and dissimilarity with the substrate. For the DU sample, several defects such as cracks and delamination were observed. Additionally, several pits formed in the coating deposited. Thus, its poor performance similar to that of the shot-peened sample, is attributed to such defects which allow the propagation of the corrosive medium, enhancing the corrosion under the coating rendering the coating unprotective. The formation of such defects in coatings is also linked to the high roughness of the underlying substrate. In literature, as the underlying substrate's surface roughness is increased, the corrosion protection provided by the coating is observed to decrease [112], [113]. As PVD coatings are

deposited, their nucleation and growth are dependent on the surface topography. A smooth surface promotes a lower defect density and improves adhesion. In comparison, a rougher surface encourages the formation of porosity and growth defects. This results in a local loss of adhesion and increases the coating's permeability allowing the solution to permeate through the coating forming a stagnant corrosive environment between the substrate and the coating, thus decreasing its corrosion-barrier performance [112], [113].

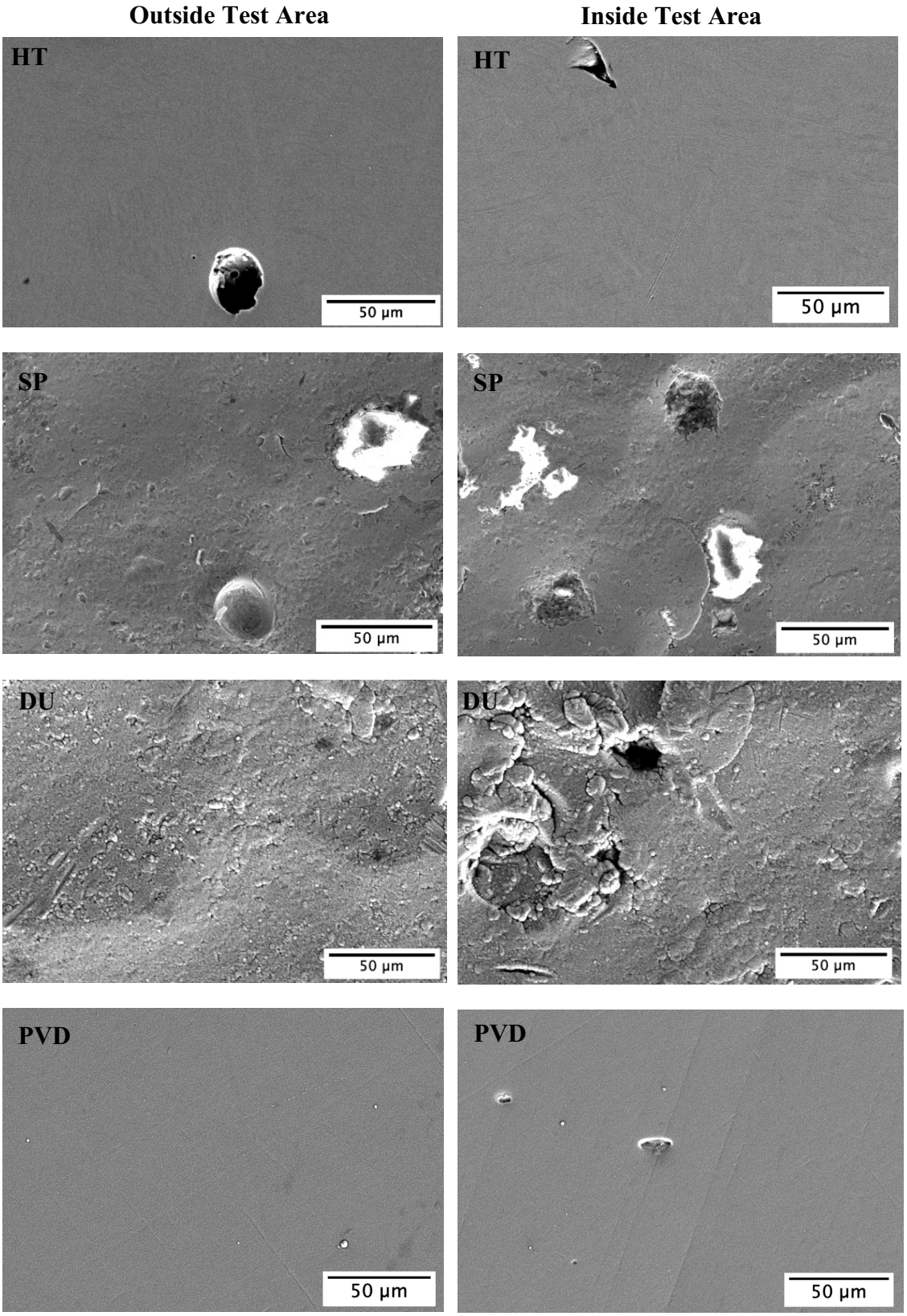

Figure 4.35 High magnification images of outside and inside the corrosion test area for all sample conditions.

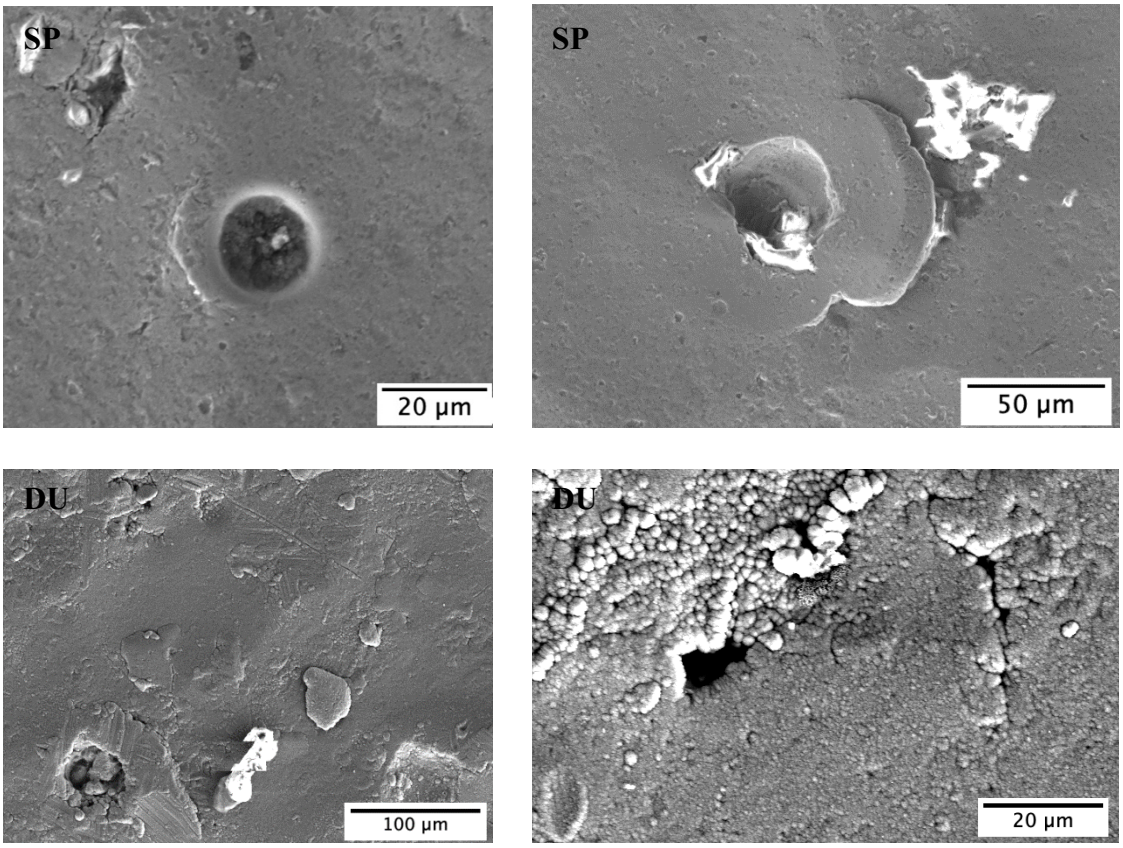

Figure 4.36 High magnification micrographs obtained post corrosion testing in simulated ocean water, of a pit and surface damage in the form of cracking and craters, observed in the SP test area, and pits and coating defects including cracks and delamination observed in the DU test area.

The corrosion current density, i_{corr}, provides a good indication regarding the corrosion resistance of the samples. A small corrosion current density value reflects a minimal corrosion rate and also suggests that the surface has a greater tendency to be passive [154]. From Figures 4.33 and 4.34, it was observed that at around 400 mV, where all the samples are in the passive regime, the corrosion resistance, can be ranked as follows based on the current density values recorded at 400 mV: PVD > DU ≈ HT > SP. Therefore, it is confirmed that the application of the coating alone led to an improvement in the corrosion resistance of the material. In contrast, the shot peening treatment resulted in a decrease in corrosion resistance. On the other hand, the duplex treatment neither enhanced nor compromised the substrate's corrosion resistance.

4.5 Cavitation Testing

4.5.1 Material Loss Analysis

During cavitation testing, the material losses were monitored at various intervals for all sample conditions. Based on the results obtained, the plots illustrated in Figures 4.37 and 4.38, depicting the time trends of cumulative material loss and material loss

rates, were generated. These plots facilitate a comparison of the behaviour exhibited by the various samples.

The data presented below shows that the surface treatments were ineffective in enhancing the cavitation resistance of the substrates. Additionally, for all conditions the presence of the plots show no incubation period (whereby material losses are initially negligible), suggesting that the impact of cavitation was significant and rapid within initial seconds. Typically, surface treatments are applied with the aim of extending this incubation period as this would highlight further the substrate's improvement against degradation via cavitation. Its absence highlights further the ineffectiveness of the chosen surface treatments in the current investigation. In addition, these results highlight that a ductile material, i.e. the HT and SP substrates, exhibit greater resistance to cavitation compared to brittle materials, such as the coating under examination.

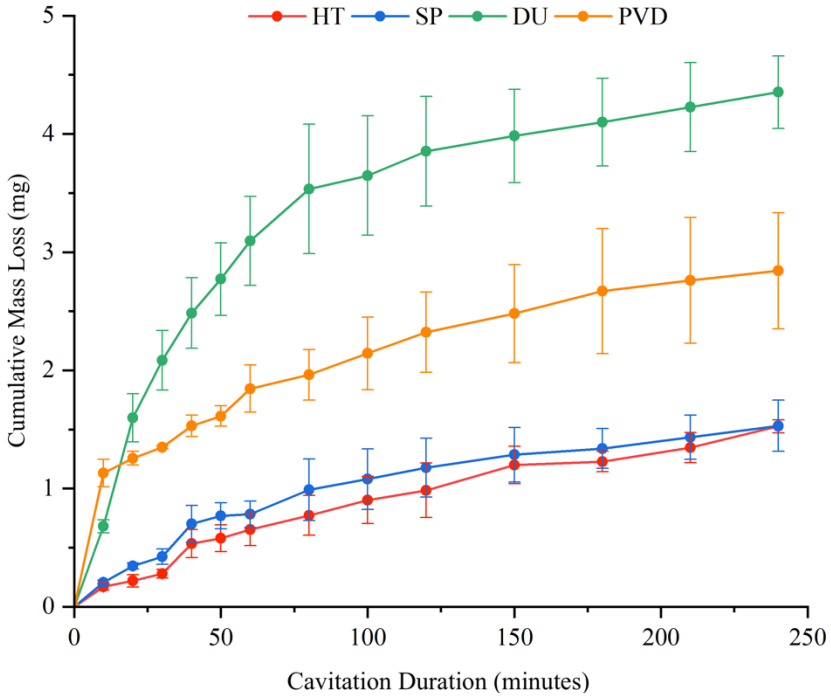

Figure 4.37 Cumulative mass loss recorded with increasing cavitation duration for all conditions which underwent cavitation testing in simulated ocean water.

This incubation period has been recorded for wrought Ti64 by numerous investigators [73], [92], [219]. However, in an investigation into the cavitation resistance of wrought and additively manufactured Ti64, Sasaki *et al.* [92] observed that in comparison to wrought Ti64, for its additively manufactured counterpart having a similar surface finish, this incubation period was not observed. Additionally, for the built and polished material an erosion rate 13 times that of the wrought material was recorded. The

authors attributed this lower cavitation resistance to the material's inferior fatigue strength thus its inability of effectively resisting the repeated impact of cavitation bubbles and shock waves. For the polished as-built material, the inferior fatigue strength may be attributed to build defects including, porosity and lack-of-fusion defects, induced by the building process which generally result from non-optimised build parameters [43]. In Section 4.3.3, the effect of these imperfections on the fatigue performance of the material was previously witnessed. It was noted that such defects served as sites for failure initiation during fatigue testing. Moreover, greater material losses are encouraged in highly porous materials as with cavitating, the impact enlarges present pores and exposes new pores, pre-existing in the bulk. As highlighted in Figure 4.4(b) in Section 4.1.1.2, the HT condition was not devoid of pores at its surface thus, these features may have contributed to the material losses depicted in Figure 4.37.

The peening treatment resulted in no change as cumulative material losses of 1.53 ± 0.22 mg and 1.53 ± 0.06 mg were recorded for the SP and HT conditions respectively. Material losses increased gradually with time almost at a constant rate as reflected by the trends in Figure 4.38. Beyond the 10-minute mark, at which the erosion rates peaked at 0.017 ± 0.003 mg/min and 0.021 ± 0.002 mg/min for HT and SP respectively, the erosion rate decreased to minimal values remaining mainly constant throughout. Such results imply that the induced roughness by the peening process is not resulting in any significant changes. Additionally, shot peening has been observed by various investigators to improve the cavitation resistance of materials mainly due to the induced mechanical strengthening by the impingement of shots [91],[93]. However, in the present study the peening treatment neither improved nor diminished the cavitation resistance of the material.

Similarly, Sasaki *et al.* [92] reported no overall discernible improvement in the cavitation resistance of shot peened LPBF Ti64. The authors proposed that this lack of improvement could be attributed to the inability of shot peening to access and treat existing miniscule surface features, such as fine gaps. This limitation arises from the size disparity between the shots used and the metallic powder particles. Such fine gaps however can be penetrated by the cavitation generated bubbles resulting in mass loss [92]. Additionally, Tomlinson *et al.* [91] observed an improvement in cavitation resistance attributed to the high work hardening capacity of austenitic SS and pure iron whose hardness increased by 70% and 100% respectively following shot peening. In

comparison, whilst hardening did occur, only a 40% increase in hardness was observed in the current work.

It was also observed by both Sasaki *et al.* [92] and Si *et al.* [220] that the material's resistance against cavitation erosion increases as the roughness decreases. The former determined that polishing the AM Ti64 sample improved its erosion rate by approximately 6 times that of the as-built sample [92]. Si *et al.* [220] presented the effect of induced roughness by ultrasonically peening an aluminium alloy using intensities ranging between 0.056 and 0.24 mmA. The sample peened using the largest intensity was observed to be the roughest, having an R_a equivalent to 2.5 µm, and from all peened samples obtained the greatest material loss rate. The authors also highlighted that cracks and tears induced by the peening process are also of a disadvantage as such features weaken the cavitation resistance further [220].

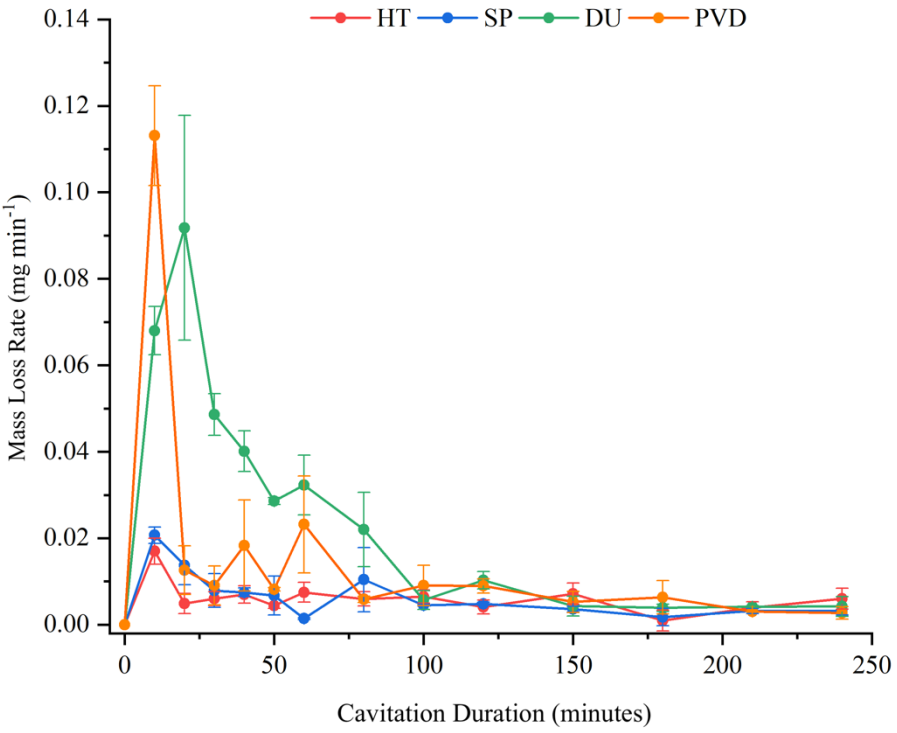

Figure 4.38 The behaviour of the mass loss rate throughout the cavitation testing duration.

Thus, the lack of improvement in the current investigation may be attributed to insufficient hardening induced by the peening process or the resulting roughness. Moreover, shot peening has been proven to enhance the fatigue strength of the material however, it has not yet been observed to definitively enhance the material's resistance to cavitation, which is regarded as a fatigue process. Therefore, it can be concluded that the surface condition has a greater influence on the material loss rate than the improved fatigue strength and hardening effect induced by the peening treatment.

Hence, it is more probable that no change is occurring as the negative effects resulting from the increased roughness are being neutralised by the compressive stresses induced on the surface.

In comparison, for the DU and PVD conditions, material losses amounted to 4.35 ± 0.31 mg and 2.84 ± 0.49 mg respectively implying that the application of the duplex treatment and the sole deposition of the coating decreased the cavitation resistance of the component. For the DU sample, a rapid acceleration in material losses is observed up until around 100 minutes beyond which values then stabilise. Whilst for the PVD condition, a rapid increase is only observed within the first 10 minutes. This is reflected by the erosion rate where maximum material loss rates of 0.092 ± 0.026 mg/min and 0.113 ± 0.012 mg/min were recorded for DU and PVD, respectively. For the DU sample, this maximum rate was observed at the 20-minute mark after which values gradually decreased. Values eventually settled reaching constant rates similar to those of HT and SP at the 100-minute mark, at which point the coating in the test area was completely removed. In comparison, for the PVD condition, despite the initially significant material loss rate, values immediately decreased resulting in a mostly constant material loss rate beyond the 20-minute mark. Furthermore, unlike the DU condition, complete coating removal at the test area was not observed for the PVD condition after 240 minutes of testing. For both the DU and PVD conditions, the high material losses recorded can be attributed mechanical failure where the coating's adhesion was not able to withstand the loads applied through the impacting bubbles and shockwaves, thus resulting in its near immediate but not complete removal as observed later in Section 4.5.2.

Varying cavitation performances have been observed for PVD coated substrates in literature. For a TiN coating, of maximum 3.5 μm thickness, deposited onto a steel an improved cavitation resistance was observed exhibited by a prolonged incubation period and attributed to the high hardness and compressive residual stresses of the coating [102]. This is opposed to that observed in the present study where the coating failed immediately, likely due to the presence of coating defects such as micro-droplets which become easily detached upon cavitation, resulting in pinholes which act as crack initiation sites encouraging the coating's failure [102]. Evidence of such defects existing prior to testing has been provided previously in Section 4.1.1. In Figure 4.40(c) and 4.40(d), later in Section 4.5.2, the effect of these defects during testing can

be observed, as most coating removal was initiated at existing defects for both PVD and DU samples. This was observed by Ma *et al.* [221] TiN coated Ti64 sample exhibited an inexistant incubation period and a higher erosion rate compared to untreated Ti64.

Additionally, Krella [124] noted that for Ti/TiN multilayer coatings deposited onto austenitic stainless steel, coating's having a high roughness exhibited high material loss rates upon cavitation. Rather than attributing the DU condition's poor behaviour to the coating's hardness and strength, it is more likely due to the substrate's rough surface condition prior to the coating deposition, recorded to be around 1.9 μm, which encouraged the formation of defects, evidenced in Section 4.1.1, that are detrimental to the coating's adhesion and cavitation performance. The negative influence of the substrate's roughness on the coating's adhesion was exhibited in Section 4.1.3 where the coating of the DU condition was capable of withstanding 32 N however that of the PVD condition did not undergo complete failure at the maximum load.

For the PVD condition, where the coating was deposited onto a smooth surface, material losses are significantly less compared to those of the DU sample. This further confirms the negative influence that high surface roughness has, promoting an increase in the defect density which is detrimental to the coating's adhesion. The defect density of the PVD condition was observed to be minimal compared to DU from micrographic analysis (Section 4.1.1). However, despite this, defects were still present thus it is likely that its poor behaviour was encouraged by existing surface defects which act as failure initiation sites upon cavitation. It was observed that, the batch of samples onto which the coating was deposited were highly porous. Thus, unless the coating is very well adhered and the surface is free from any defects, it is useless for such applications.

The poor performance could also be attributed to the high hardness-to-stiffness (H/E) ratio of the coating. The coating investigated in the current study was observed to have an H/E ratio of 0.08. In literature, for TiN coatings having an H/E ratio ranging between 0.049 and 0.058, the cavitation resistance was observed to increase with the increasing ratio. However, 0.07 is considered to be a threshold value beyond which the erosion rate is then observed to increase rather than decrease, as recorded for a TiN coating having a ratio of 0.078 [54], [102]. This occurs as despite the increasing hardness, the stiffness and thus the coating's brittleness are also increasing. A brittle coating deposited onto a ductile substrate, as is the case in the present study, undergoes

damage via brittle failure under dynamic loads easily, since brittle failure requires less energy and thus an increase in the erosion rate is observed [54], [102], [123].

4.5.2 Micrographic Analysis of Test Area

As observed in Figure 4.39**,** which depicts images of the different conditions and their change in surface appearance over time, all samples underwent gradual degradation. SEM micrographs are also provided to allow for comparison of each sample's test area condition at the 30, 120 and 240- minute intervals (Figures 4.40, 4.41 and 4.42).

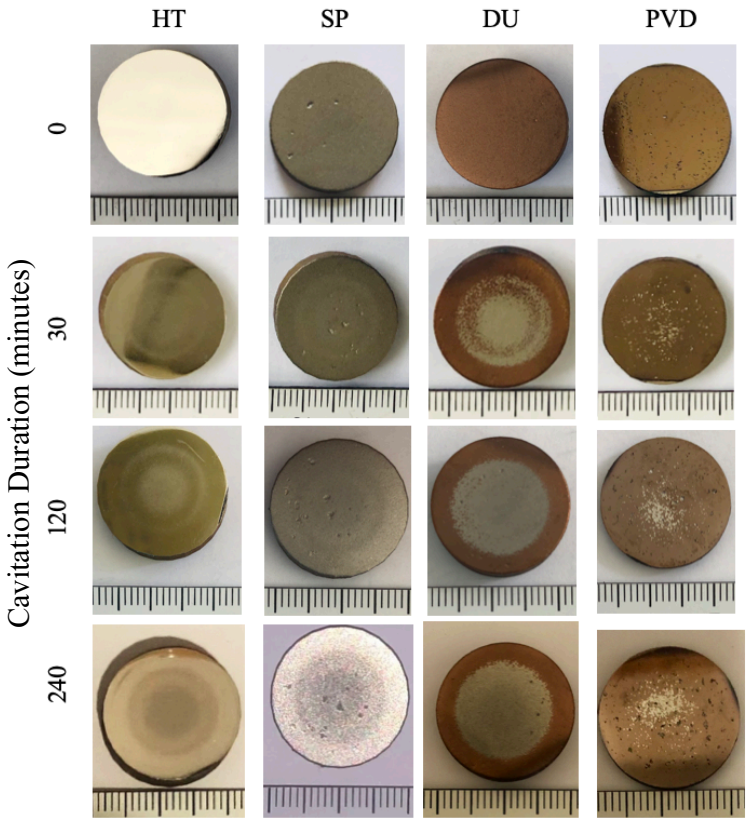

Figure 4.39 Surface condition of the various samples with increased cavitation duration. Each small division is equivalent to 1 mm.

After 30 minutes of cavitation, the test area of the HT sample (Figure 4.40(a)) depicts a higher density of pits compared to the surrounding area. At this stage, any existing pits and pores, observed in Figure 4.40(a), appear to have been enlarged whilst the highlighted areas are likely pits which are in the process of becoming exposed. For the SP sample (Figure 4.40(b)), any changes at this stage are difficult to observe due to the severely plastically deformed surface. However, the test area appears to be populated with a significant number of cavities some of which are likely cavitation pits. Additionally, the surface in the test area also exhibits a rougher morphology, likely a consequence of material detachment due to the erosion experienced. Coating removal,

the majority occurring via delamination, was observed at this stage for the DU sample (Figure 4.40(c)). Several patches of coating were observed to be still well adhered where the underlying substrate was mostly flat. Most of the coating removal occurred at and around various defects present, including pits and craters, confirming the negative influence such features have on the coating's integrity. Additionally, at the exact centre where cavitation is most intense, the exposed substrate exhibited similar characteristics to the SP condition i.e., a greater number of pits. For the PVD sample, minimal coating removal was observed, and removal mainly occurred at areas where there were pre-existing pores (Figure 4.40(d)). Such defects have edges which make it easier for the cavitation bubbles to penetrate between the coating and the substrate. Such pores result from non-optimal build conditions, by reducing porosity the cavitation resistance of the coating may be improved as possible failure sites are eliminated.

After 120 minutes of cavitation, the surface condition of the samples is further aggravated. For the HT sample (Figure 4.41(a)), apart from a further increase in the pit density and the deepening and largening of existing pits (highlighted in the high magnification image embedded on the left-hand side of Figure 4.41(a)), the grains were exposed at this stage. This occurs due to the different wear rates of the phases. The β phase has an inferior hardness and stiffness in comparison to the α phase, thus it is worn first exposing the α lamellae. This was also observed by Wang *et al.* [117] when cavitation testing conventionally manufactured Ti64. The SP sample exhibits similar degradation to the 30-minute interval however, various cracks as highlighted in Figure 4.41(b) and a significant increase in the cavitation pit density were observed. Significant coating removal was observed for the DU sample at this point (Figure 4.41(c)). Additionally, at the centre, the exposed surface exhibited an increased roughness indicating the increased occurrence of material detachment and similar to the SP condition some cracks and tears were observed. For the PVD sample, apart from further coating removal, the formation of cavitation pits was now observed at both exposed and coated areas. In comparison to the coating on the DU sample (Figure 4.41(c)) which appears to have undergone failure via gross delamination, the coating on the PVD sample (Figure 4.41(d)) appears to have failed in a brittle manner and concentrically around existing defects. The brittle nature of the coating's failure is evidenced by the remaining coating fragments which exhibit sharp cleavage facets as

observed in the high magnification image embedded on the left-hand side of Figure 4.41(d).

Following 4 hours of cavitation testing, the wear damage visible on the surfaces was very noticeable. The HT sample (Figure 4.42(a)) exhibited evidence of severe exfoliation with various areas showing significant material detachment and pits became significantly larger. Significant exfoliation was also observed for the SP sample (Figure 4.42(b)) whilst an increase in crack density was exhibited. For the DU sample, complete coating removal was observed at this stage whilst exposed areas had a similar appearance to that of the SP sample at the 120-minute mark as observed in Figure 4.42(c). Complete coating removal was not observed for the PVD sample (Figure 4.42(d)) however at the centre of the test area, degradation was significant exhibited by large cracks. Additionally, at this stage the grains were very visible similar to the HT sample after 120 minutes of cavitation.

(a) Heat-Treated (HT)

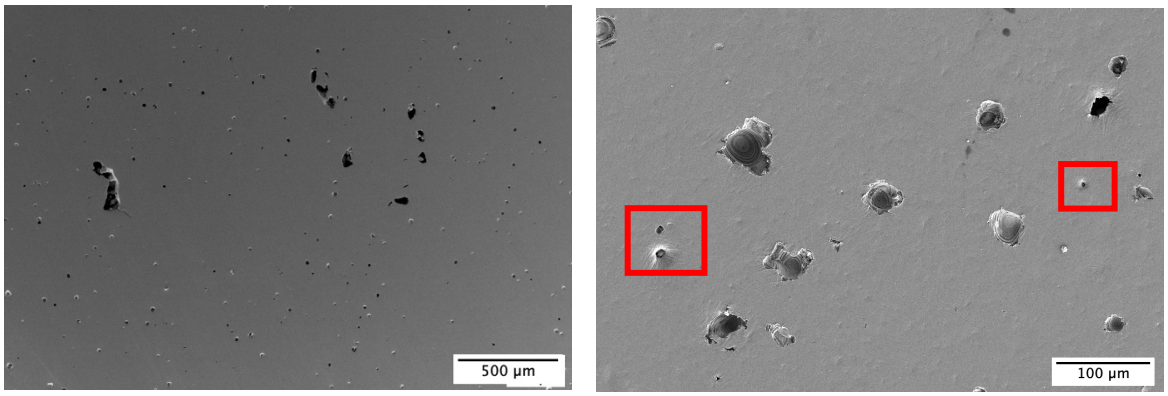

(b) Shot-Peened (SP)

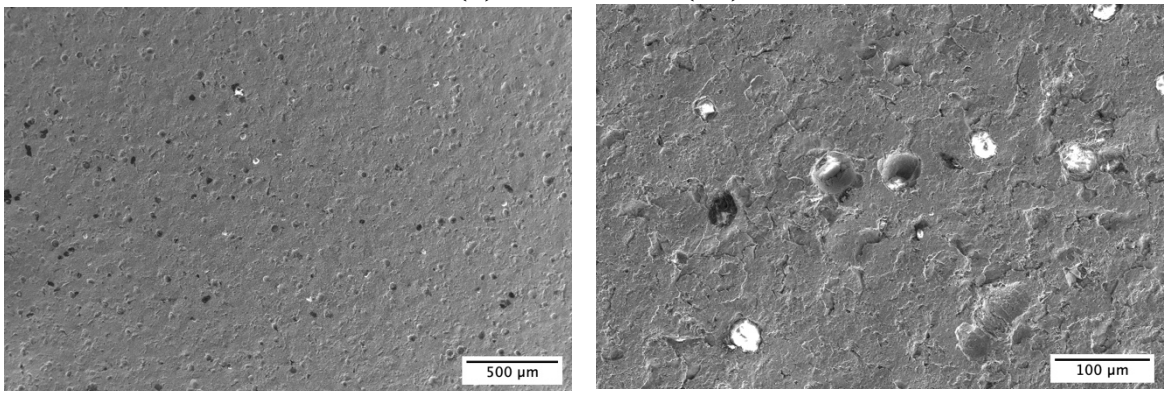

(c) Duplex Treated (DU)

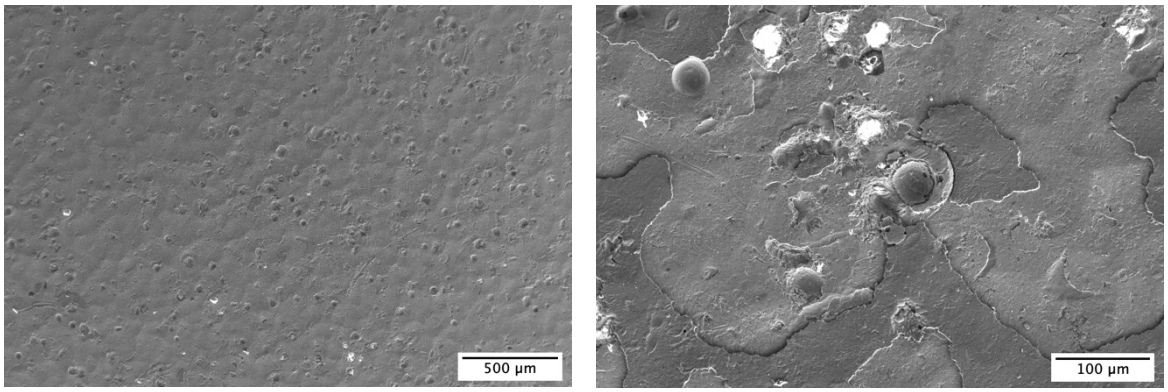

(d) PVD Coated (PVD)

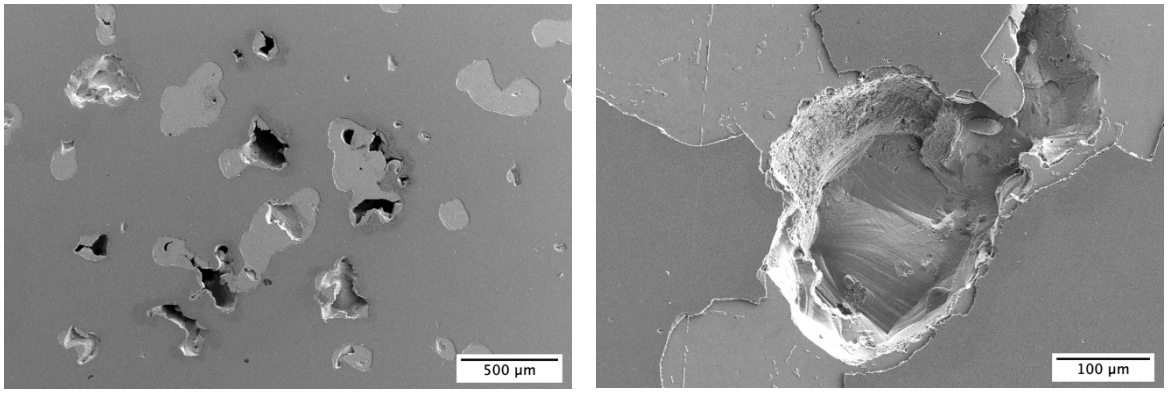

Figure 4.40 SEM micrographs of the a) HT, b) SP , c) DU and d) PVD samples following 30 minutes of cavitation in simulated ocean water. Micrographs on the right are higher magnification images of the test area visualised in the micrographs on the left.

(a) Heat-Treated (HT)

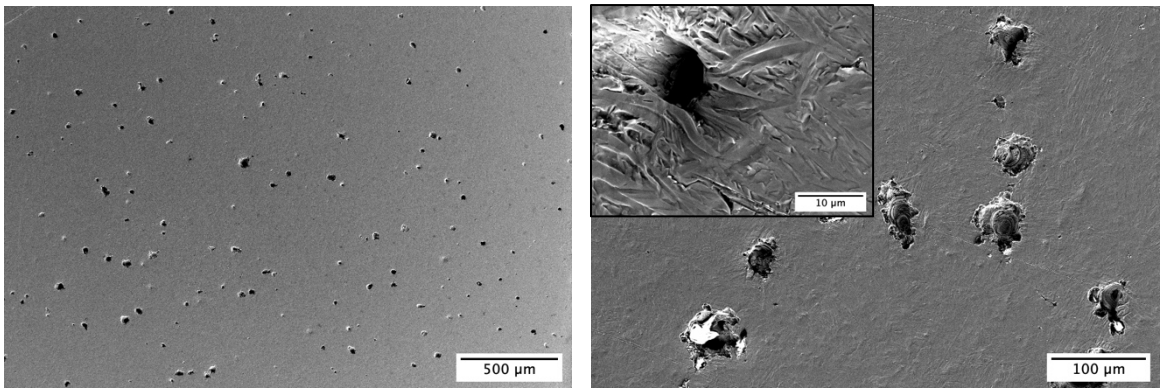

(b) Shot-Peened (SP)

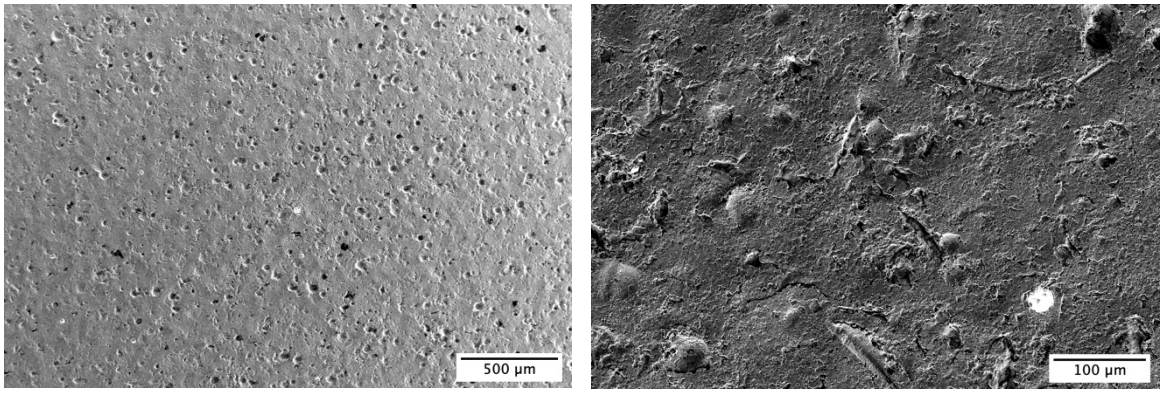

(c) Duplex Treated (DU)

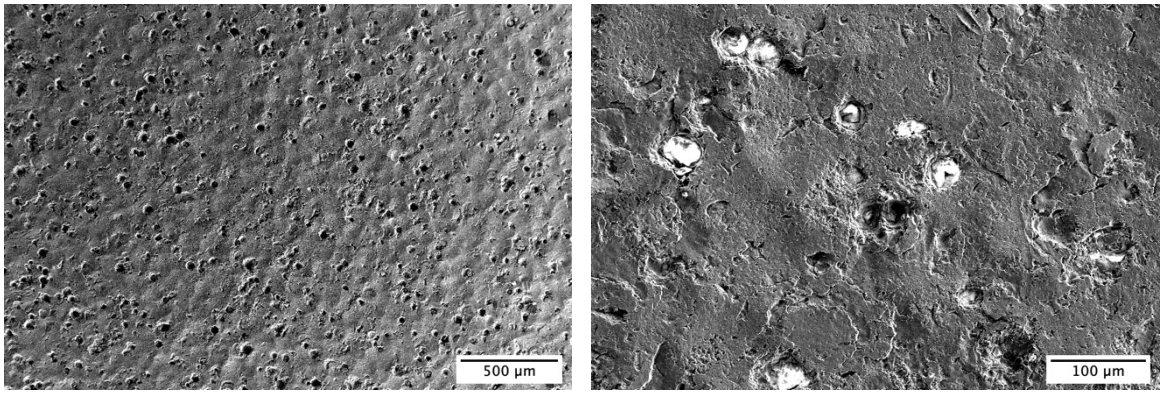

(d) PVD Coated (PVD)

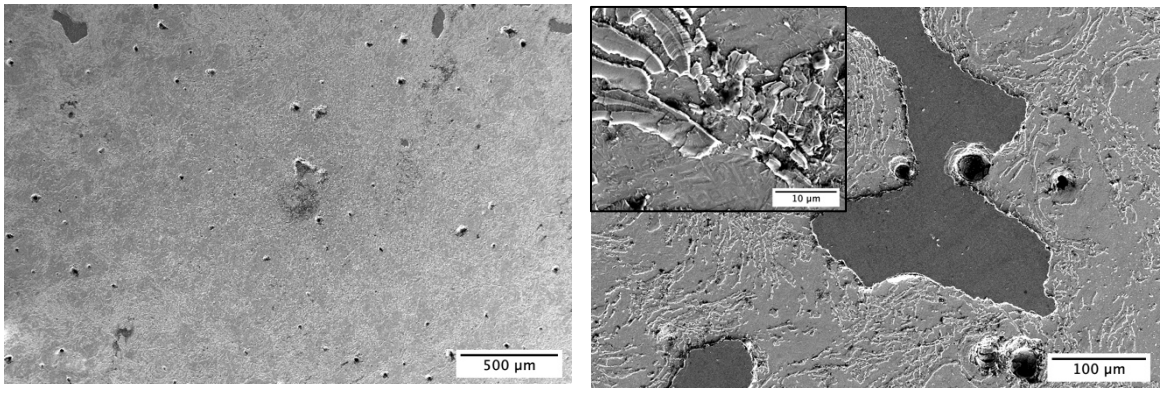

Figure 4.41 SEM micrographs of the a) HT, b) SP , c) DU and d) PVD samples following 120 minutes of cavitation in simulated ocean water. Micrographs on the right are higher magnification images of the test area visualised in the micrographs on the left. Embedded in the higher magnification images for a) HT and d) PVD, are high magnification micrographs of specific features.

(a) Heat-Treated (HT)

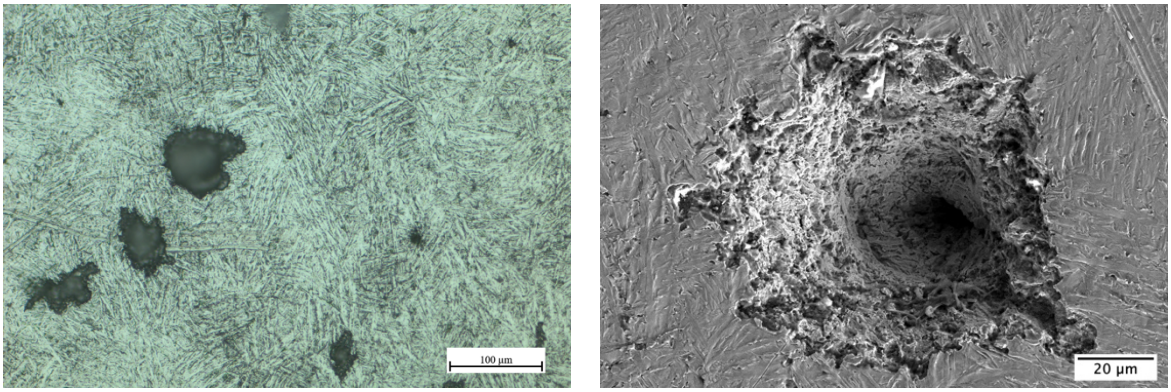

(b) Shot-Peened (SP)

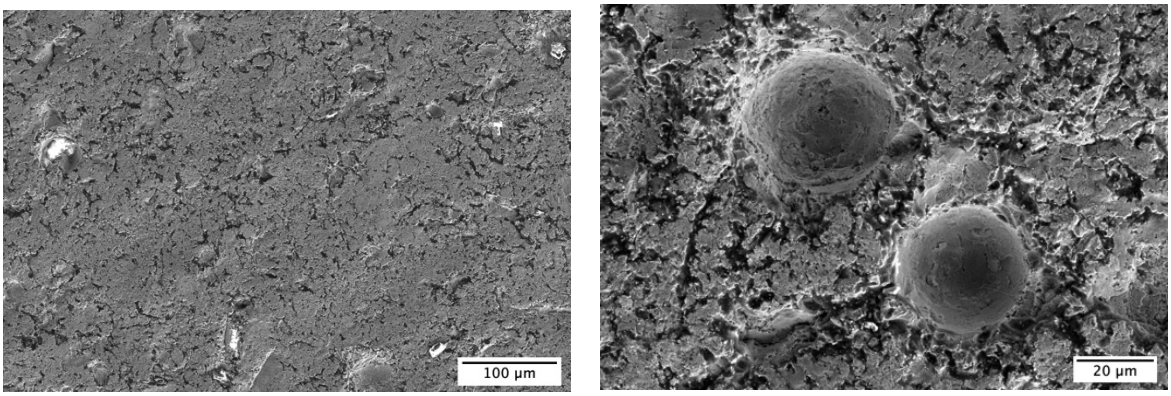

(c) Duplex Treated (DU)

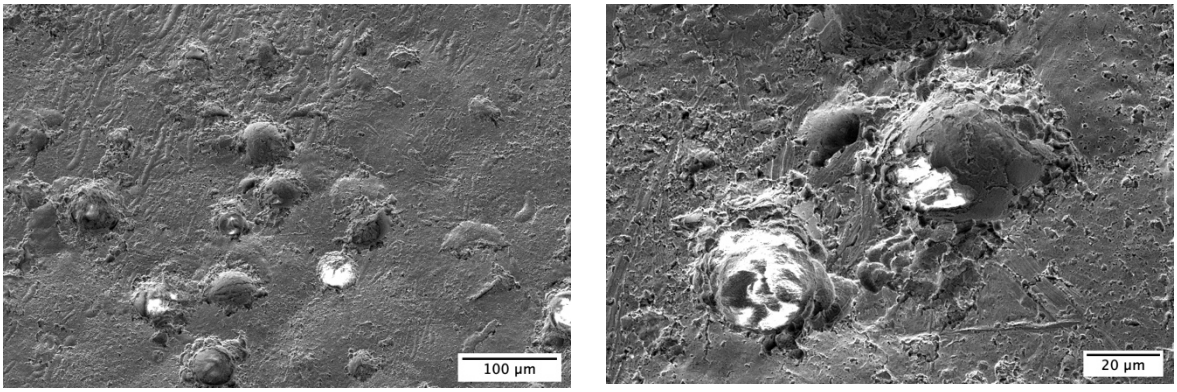

(d) PVD Coated (PVD)

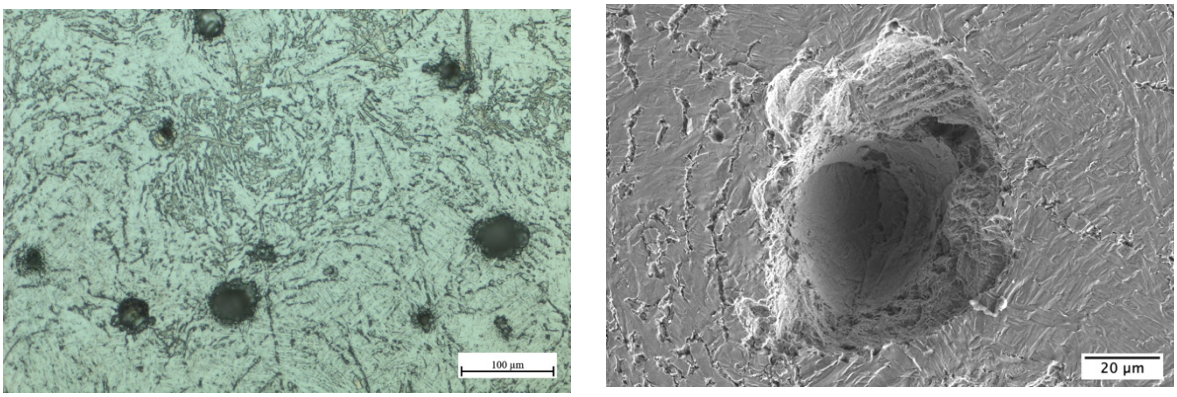

Figure 4.42 SEM micrographs of the a) HT, b) SP , c) DU and d) PVD samples following 240 minutes of cavitation in simulated ocean water. Micrographs on the right are higher magnification images of the test area visualised in the micrographs on the left.

4.6 Cavitation-Corrosion Testing

Testing aimed at investigating the cavitation-corrosion performance of materials and the synergy present between the mechanisms is not yet well established, with limited research existing concerning this issue. The application of cavitation in corrosive environments makes the surface more electrochemically active thus stimulating both anodic and cathodic reactions [222]. Various investigators have conducted testing to observe this effect however, across all existing investigations no standard method was followed each adopting varying methods of inducing and monitoring cavitation-corrosion to quantify synergy. Existing investigations adopted methods such as conducting potentiodynamic testing under cavitation to quantify losses due to corrosion, cavitation testing materials in distilled water or under a cathodic potential to quantify material losses due to pure erosion and cavitation testing materials in artificial seawater, under no induced potential, to quantify total material losses. It appears that the method adopted in the current investigation, where the material undergoes cavitation under an applied anodic potential has not been investigated yet.

Whilst the exact value of material loss due to synergy cannot be quantified using the method adopted in this work, an indication of the effect synergism has, and its significance can be inferred as the adopted testing allows the quantification of total material losses (T) and the losses incurred by the total corrosion (C*) and cavitation (E*) components, which are the addition of losses incurred due to the each mechanism alone (C_0 and E_0) and the losses incurred by the effect the mechanisms have on one another (C_E and E_C).

Figure 4.43 depicts the response of the dynamic corrosion current over time of the various sample conditions. Cavitation was started at 1200 s and kept for a duration of 1800 s, upon which the anodic current is observed to increase from negligible values and settle back to zero once cavitation halts. This response, observed for all conditions, was expected and is identical to that typically observed for tribocorrosion testing whereby sliding wear occurs in conjunction with corrosion [149]. Upon cavitation, cavitation bubbles start impinging the surface and the underlying substrate is exposed to dissolution and erosion: a) via the removal of the present passive layer in case of metallic surfaces or b) in case of coated surfaces, via the removal of the coating [68]. A galvanic couple forms between the mechanically de-passivated areas and the remaining passive areas thus, the increased current values [68]. In addition, initially in

certain instances, the current was observed to spike up to high values before settling at smaller current values. This is attributed to the working mechanism of the sonotrode, which for the first few seconds operates at a higher intensity, before continuing to operate at the set parameters.

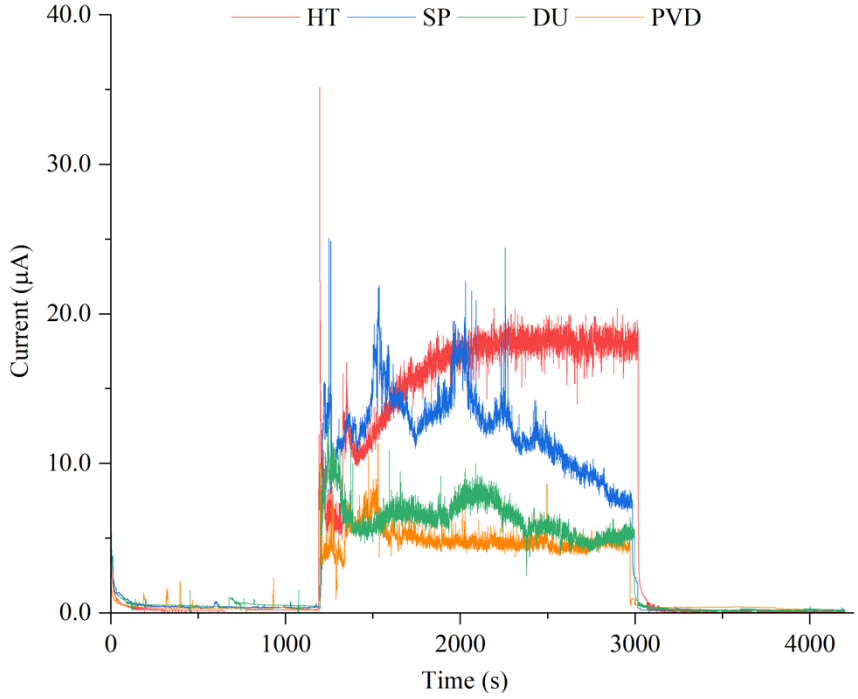

Figure 4.43 The response of the dynamic corrosion current over time of the various sample conditions during cavitation testing under an anodic potential of 0.2V vs. SCE in simulated ocean water.

For all conditions, current values were observed to fluctuate over a small range rather than forming a smooth curve. Such fluctuations are typically attributed to repeated removal and regeneration of the passive film present on the metallic surface, which for the coated sample will have had to be reached through defects induced or exposed due to the removal of the coating [71], [223], [224]. The regeneration results in a slight decrease in current values as the surface is once again being protected from dissolution and erosion. Values then increase slightly again as the layer is rapidly removed due to the continuous impact of the cavitation bubbles [68], [71]. However, compared to the anodic current response observed by Vella *et al.* [149], where the current was observed to fluctuate over a minimum range of 10 µA for corrosion-wear tested heat-treated and shot peened LPBF Ti64, the fluctuations observed in the current investigation are minimal.

In the present study, re-passivation is not occurring since cavitation is non-stop. Amann *et al.* [68] are of the opinion that similar to fretting impact, which has a 100% oxide layer removal efficiency, the mechanical stresses induced by the impingement of

cavitation bubbles is significant enough that it does not allow re-passivation to occur thus the test area is in a completely de-passivated state up until cavitation halts. Similarly, Wang *et al.* [219] theorised that as Ti64 underwent cavitation erosion, the passive layer was removed and eventually the continuous impingement resulted in the formation of microcracks. The artificial seawater propagated through these cracks promoting the formation of a thin passive layer over the damaged surface and in the cracks, which is beneficial in protecting the substrate from further degradation by both erosion and corrosion mechanisms resulting in diminished cavitation-corrosion rates. However, this protective function is also dependent on the layer's generation capacity and the authors noted that despite observing an improvement in the cavitation-corrosion resistance, it is limited due to the significant forces exerted during cavitation which causes the film to constantly peel off [219].

The HT sample exhibited the greatest corrosion currents compared to the other conditions settling at values ranging between 18 and 20 μA. For the SP condition, initially similarly high values to the HT sample which fluctuated over a greater range between around 8 and 20 μA. At instances, a spike in values was recorded throughout the cavitation duration of the SP condition. This may be due to material detachment resulting in the exposure of a significant area, thus its de-passivation, which then undergoes dissolution [225]. The lack of improvement provided by the SP treatment may be attributed to the fact that due to the increased roughness, the test area of the SP sample is greater than that of the HT sample thus, more solution is in contact hence providing the possibility of more corrosion reactions to occur.

High current values are encouraged by the presence of both surface porosity and the induced cavitation pits [51], [224]. Sharma *et al.* [51] related the passive's layer faster dissolution to high surface porosity which was observed to diminish the passive layer's quality resulting in a porous layer more prone to damage. Moreover, pores and cavitation pits, as observed in Figures 4.44(a) and (b), also encourage pitting corrosion to occur as the solution trapped within can become stagnant resulting in a highly corrosive environment due to HCl forming as a by-product of dissolution in NaCl [51]. This can also apply to deformations induced by the peening treatments, which may entrap the corrosive solution encouraging localised corrosion, as previously explained in Section 4.4, thus the treatment's ineffectiveness in diminishing the dynamic corrosion currents recorded. Furthermore, its ineffectiveness can also be attributed to

the induced roughness which encourages the formation of a poorly adhered passive film.

Both coated conditions, DU and PVD, exhibited similar low currents ranging approximately between 5 and 8 μm for the DU condition and 4 and 6 μm for the PVD condition. Thus, from these observations it may be concluded that the SP treatment was ineffective whilst the coating was beneficial as it effectively protected the substrate exhibited by the distinct decrease in recorded current values. Such low values are typically observed when corrosion-wear testing PVD coatings and are attributed to their higher hardness thus their diminished susceptibility to wear and to therefore exposing the underlying substrate to dissolution [15], [16], [226], [227]. Values are then observed to gradually increase over time as the coating is progressively delaminated until complete failure occurs. Coatings exposed to corrosion-wear typically fail via any of the following three mechanisms which can also be applied to the cavitation-corrosion scenario. Failure can occur via [71]:

- Type I: the de-passivation, via damage or complete removal, of the passive layer and its re-passivation. This is also applicable to uncoated substrates which have a naturally occurring passive layer at the surface.
- Type II: corrosion of the underlying substrate resulting in the blistering and possible complete removal of the coating.
- Type III: corrosion of the counter body leading to abrasive wear of the coating.

In the current investigation, the occurrence of Type III is not possible as the counter body is not in contact with substrate. However, Type I occurred for both the HT and SP conditions as evidenced by the anodic current responses observed. For the PVD and DU condition, this type of failure likely occurred in very small quantities given that much of the coating remained intact and only a small proportion of the substrate was exposed. On the other hand, both the PVD and DU condition, could have undergone Type II corrosion-wear encouraged by defects present prior to testing that allowed the propagation of the electrolyte towards the substrate resulting in its dissolution. This attack occurring below the coating may have then encouraged its removal. However, for both coated conditions, no obvious blistering was observed, and the majority of failure appears to have been purely mechanical occurring at existing defects which compromised the coating's adhesion allowing its near

immediate detachment upon impact from the cavitation bubbles. Upon detachment, then the revealed substrate undergoes Type I corrosion-wear.

In addition, the slightly lower current values recorded for the PVD samples may be attributed to the differing roughness of the samples since a greater roughness is accompanied with an increased interaction area and negatively impacts the adhesion of both the coating and the passive film.

Similar to Naghibi *et al.* [227], the minimal current values recorded may be attributed to either the coating's higher chemical stability, thus it is less likely to undergo dissolution or to the diminished active area, due to the coating's high hardness, thus resulting in a minimal active to passive area ratio. The latter is evidenced in Figure 4.44. Aperador *et al.* [228] noted that an excellent corrosion-cavitation resistance can be obtained by increasing the coating's number of layers. The authors noted that a significant number of layers, unlike the 4 layers of the coating in the present study, are beneficial as it increases the coating's overall fracture resistance and improves its nano-crack inhibiting ability. Hence the formation of surface irregularities and damage as a result of the prolonged cavitation, which eventually result in detachment and substrate exposure, leading to its dissolution, can be delayed [228]. Such damage was observed in the current investigation, following 30 minutes of cavitation, as seen in Figures 4.44(c) and (d). Therefore, the coating is likely to perform better if it has a greater number of layers. This would be more beneficial for the DU sample, in particular, due to its higher roughness which is known to enhance the coating's defect density and negatively impact its properties increasing its susceptibility to failure.

(a) Heat-Treated (HT)

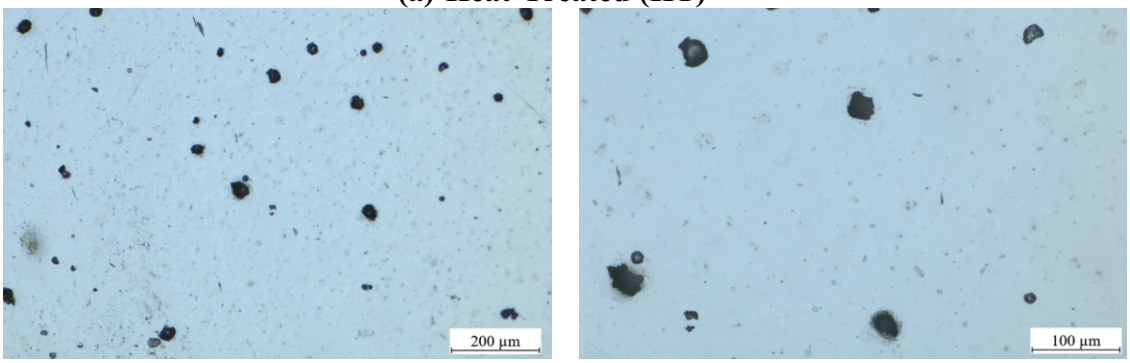

(b) Shot-Peened (SP)

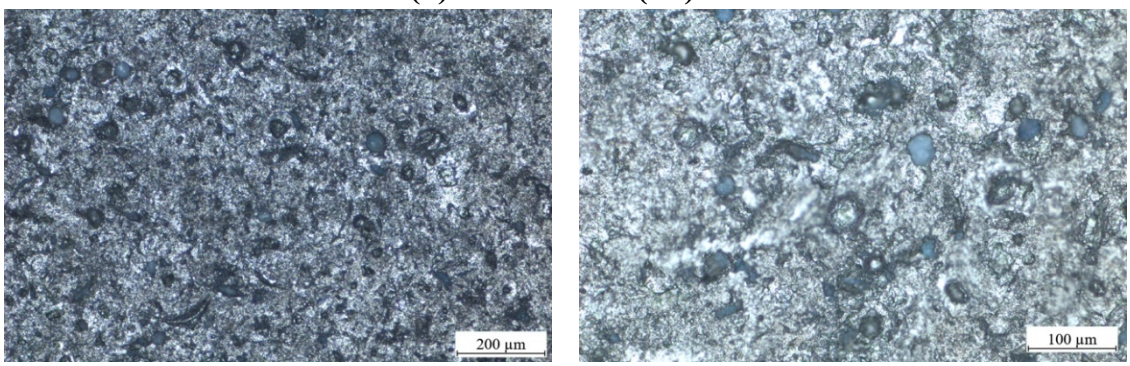

(c) Duplex Treated (DU)

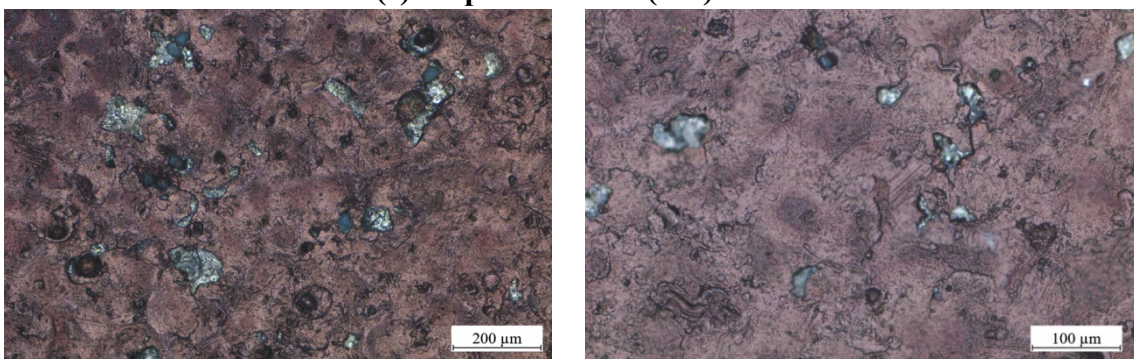

(d) PVD Coated (PVD)

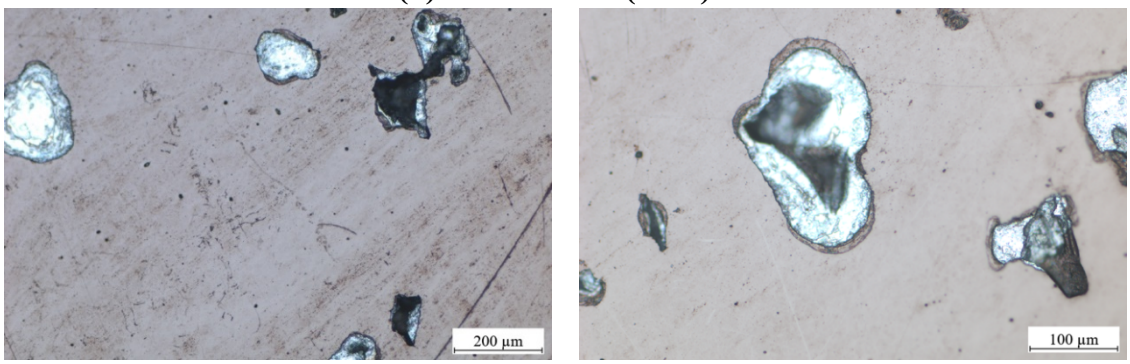

Figure 4.44 Surface condition of the test area of the a) HT, b) SP, c) DU and d) PVD samples following cavitation-corrosion testing carried out in simulated ocean water over a duration of 4200 seconds at an anodic potential of 0.2 V vs. SCE. Micrographs on the right are higher magnification images of the test area visualised in the micrographs on the left.

The total material loss (T) values, obtained from mass measurements following testing, the material loss due to the total corrosion (C*) component, calculated from recorded anodic currents via Faraday's law, and the total erosion (E*) component, measured by the subtraction of C* from T, can be visualised in Figure 4.45 and are also listed in Table 4.8. Moreover, the improvement imparted by the surface treatments relative to the HT condition was quantified. Similar material loss values were recorded for the HT and SP conditions confirming the ineffectiveness of the peening treatment. For the DU condition, whilst diminished material loss values were recorded as compared to the HT sample, values are however similar to those recorded for the SP condition thus, the cavitation-corrosion resistance improvement was minimal, increasing by only 1.2 times that of the polished and heat-treated sample. On the other hand, the PVD condition exhibited minimal material loss, improving the cavitation-corrosion resistance of the polished and heat-treated sample by 2.5 times.

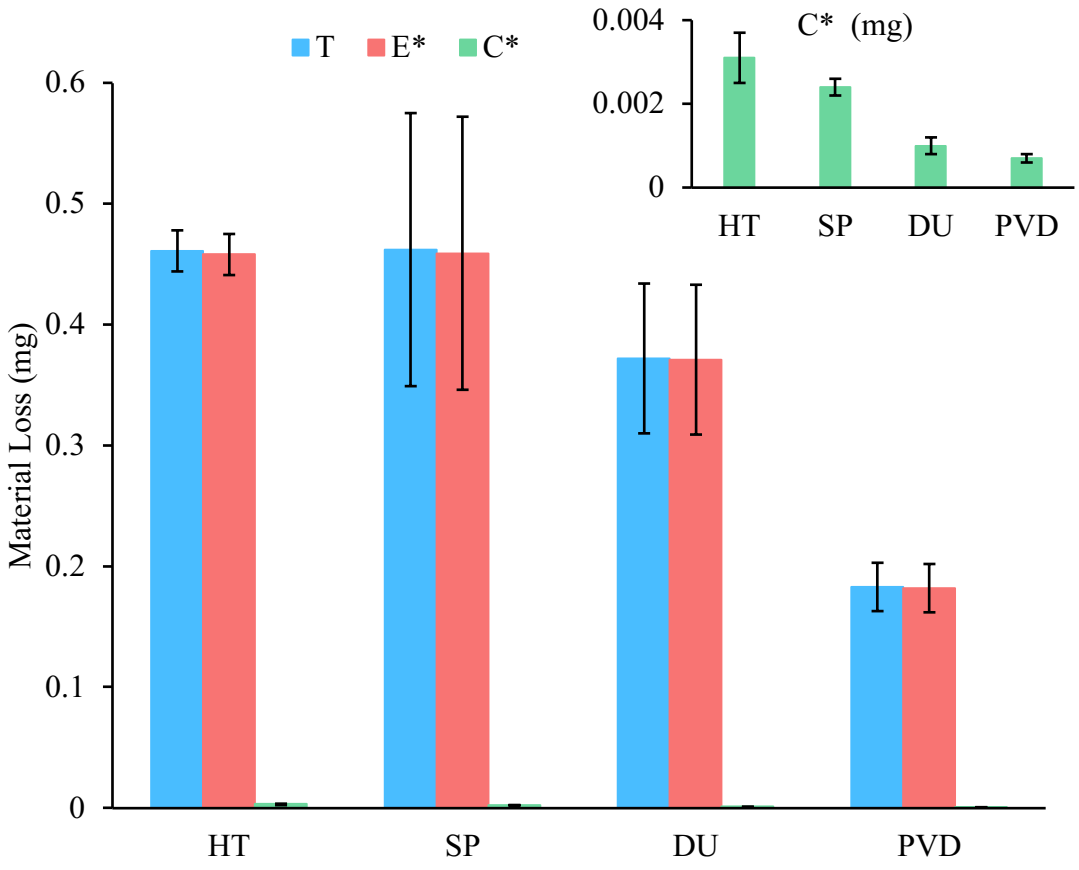

Figure 4.45 A bar chart depicting the total material loss (T), the material loss due to the total erosion (E) component and material loss due to the total corrosion (C*) component. Due to the negligible values of C*, on top right-hand corner, a bar chart of the C* values was provided.*

Table 4.8 Material losses quantified for each condition following cavitation-corrosion testing and the surface treatments' effect on the cavitation-corrosion resistance of the substrate.

Condition	T (mg)	C* (mg)	E* (mg)	Cavitation-corrosion resistance factor relative to HT
HT	0.461 ± 0.017	0.0031 ± 0.0006	0.458 ± 0.017	1.0
SP	0.462 ± 0.113	0.0024 ± 0.0002	0.459 ± 0.113	1.0
DU	0.372 ± 0.062	0.0010 ± 0.0002	0.371 ± 0.062	1.2
PVD	0.183 ± 0.020	0.0007 ± 0.0001	0.182 ± 0.020	2.5

From the results obtained, the contribution to material loss due to corrosion in minimal. Thus, it more important to have a surface or coating of high hardness and toughness which can withstand the impact from the cavitation bubbles. The coated samples exhibited an improvement as the coating could withstand the impact up to a certain extent unlike the peening treatment which did not induce sufficient hardening hence the lack of improvement observed. For the SP condition, the induced roughness may also be contributing, which as stated previously in Section 4.5, was observed to occasionally diminish the material's cavitation resistance. The effect of roughness is also reflected in the material losses obtained for the DU sample. As compared to the PVD sample, the DU samples exhibited greater material losses which could be attributed to the substrate's roughness which encourages the formation of defects and impacts the coating's adhesion strength.

Wang *et al.* [229] investigated the effect of shot peening on the erosion-corrosion of nickel aluminium bronze (NAB) where rather than impinged via cavitation bubbles, the surface was impinged by sand particles. When comparing past erosion-corrosion studies, including erosion via slurry or via cavitation, the authors observed that overall, grain refinement, martensite transformation and the inducing of compressive residual stress were beneficial in improving both the corrosion and erosion-corrosion properties of the material. For the samples shot peened using ceramic shots, at a coverage of 100% and intensities of 0.1 and 0.2 mmA, an increase in erosion-corrosion resistance by 25% and 30% respectively was observed. Thus, the induced roughness had no effect and following erosion-corrosion the surface of the peened samples appeared to be

flatter, as it underwent plastic deformation by the impingement of particles, whilst selective phase corrosion was mitigated due to the combined effect of strain hardening and compressive residual stresses which inhibits the occurrence of further plastic deformation. However, for the dual peened sample a decrease in resistance was observed which was attributed to the occurrence of excessive strain hardening. The authors theorised that this excessive hardening, irrespective of the induced hardness and compressive stresses, resulted in failure at the surface to transform from ductile into brittle exhibited by cleavage-like fractures which contributed to greater material loss. In the current investigation, excessive strain hardening may have occurred due to the adopted 450% coverage which whilst significantly increasing the hardness and induced compressive stresses may have resulted in the over peening of the sample [229].

In comparison, Qin *et al.* [230] observed that compressively loaded Ni-Al-Bronze (NAB) exhibited a diminished cavitation-corrosion resistance in 3.5 wt.% NaCl with increasing stress values. The induced stresses were observed to accelerate the corrosion reaction thus reducing the alloy's strength resulting in the uninhibited formation of cavitation pits which contribute to a greater surface roughness. Consequently, the increased surface roughness was observed to diminish further the surfaces' resistance to wear resulting in significant mass loss. Thus, for an improved cavitation-corrosion resistance, parameter optimisation of the shot peening treatment is paramount as chosen parameters need to result in an ideal combination of hardness, induced compressive stresses and roughness whilst avoiding excessive strain hardening to exhibit minimal material loss rates.

For the coated samples, minimal material losses were still recorded due to coating removal as observed in Figures 4.45(c) and (d). However, the diminished currents recorded for all repeats of the PVD and DU conditions, confirm that the coating removal was not significant enough to affect the current measurements thus, the material loss due to the corrosion component using Faraday's law could be quantified. If delamination were to be significant it would have been evidenced by a sudden spike in current values similar to those recorded for HT. In this case, material loss quantification via Faraday's would have been inaccurate. Additionally, C* values recorded are insignificant compared to the loss due to E* thus, do not bear much impact.

As observed in Table 4.8 and Table 4.9, losses due to the corrosion and cavitation-induced corrosion (C*) were insignificant, confirming that the cavitation and corrosion-induced cavitation (E*) had a more superior effect. This is evidenced by recorded values of percentage of damage induced (Table 4.9), where damage due to the total corrosion component amounted to less than 1% for all conditions with the majority of damage occurring due to the erosion component. It is also worth noting that under cavitation-corrosion conditions, cavitation-induced corrosion can occur in two ways. Apart from occurring due to the increase in ion diffusion, as a result of passive film detachment due to cavitation, it can also occur as a result of the increased oxygen supply generated by the severe stirring effect induced by cavitation bubble generation [230].

Table 4.9 Calculated C/E* ratio and the percentage of damage induced by corrosion (C) and erosion due to cavitation (E) relative to the total material loss (T).*

Condition	C*/E*	% of damage	
		C/T	E/T
HT	0.007	0.67	99.33
SP	0.005	0.52	99.48
DU	0.003	0.26	99.74
PVD	0.004	0.40	99.60

As per Kwok *et al.* [72], this minimal contribution of the corrosion mechanism and the synergistic effect can be attributed to the substrate's excellent corrosion resistance and its high-quality passive film which is capable of resisting detachment and of undergoing dissolution at slow rates. On the other hand, for coated substrates, this may be attributed to the mechanical properties of the coating and such results suggest that having a hard and tough coating is more important than having a coating of excellent corrosion resistance.

The negligible effect of corrosion and the synergy between cavitation and corrosion on the material losses was also confirmed via the ratio of the total erosion component to the total corrosion component (C*/E*). This ratio was adopted by both Runa *et al.* [231] and Toptan *et al.* [224], as it is a mean by which the significance of the synergism

present and the nature of the degradation mechanism can be determined. Depending on the ratio, the dominant degradation mechanism can be either of the following:

- mechanical wear ($C^*/E^* \leq 0.1$), where synergism could be present, but its effect is negligible;
- wear-corrosion ($0.1 < C^*/E^* < 1$), where synergism is present however loss due to wear is more dominant;
- corrosion-wear ($1 < C^*/E^* \leq 10$), where synergism is present however loss due to corrosion is more dominant;
- corrosion ($C^*/E^* > 10$), where synergism could be present, but its effect is negligible.

As observed from the C^*/E^* values listed in Table 4.9, all ratios were below 0.1 thus the dominant degradation mechanism was mechanical wear via cavitation with synergy having a negligible effect. This was observed by Mathew *et al.* [232] and Toptan *et al.* [224] when investigating the interaction of corrosion and wear of a CoCrMo alloy using loads ranging from 0.05 N up to 64 N and of SLM and commercially produced Ti64, respectively. The former observed that with increasing load up to 1 N, mass loss via the synergistic effect of wear and corrosion, with mechanical wear being dominant, increased, however upon reaching loads of 16 N and greater the degradation was observed to shift to the wear-only regime. Mathew *et al.* [232] thus suggested that the impact of synergy is maximised at certain load application but was limited since the corrosion mechanism is limited by its kinetics, whilst material loss due to mechanical wear is dominant at low and high loads and is proportional to the loads applied thus its increase is unlimited. Therefore, in the current investigation, the negligible effect of corrosion and synergism may be attributed to the continuous and simultaneous loads exerted by the numerous cavitation bubbles which significantly outweigh any effects of corrosion.

It is worth noting that as of yet, cavitation-corrosion testing is not yet well established especially for the chosen material and treatments. Whilst obtained results did provide an insight into the mechanisms present and their synergy, cavitation is a very dynamic wear process which consists of numerous simultaneous impact points, unlike for example sliding wear, and is dependent on numerous factors. Thus, further testing is required to confirm the accuracy of the chosen test method.

Chapter 5: Conclusion and Future Work

5.1 Conclusions

The main aim of this investigation was to determine whether the proposed treatments, in particular the duplex treatment of shot peening and a PVD multilayer Ti/TiN/TiAlN/TiAlCuN coating, could enhance the corrosion, cavitation and cavitation-corrosion resistance of the substrate, while simultaneously improving its fatigue performance. The sample conditions analysed and tested were as-built (AB), heat treated (HT), shot peened (SP), duplex treated (DU) an PVD coated (PVD) laser powder bed fusion, LPBF, Ti-6Al-4V.

The main findings from the in-depth characterisation of the sample conditions are summarised as follows:

1. The AB condition was observed to have fine acicular α' martensite laths in prior β columnar grains. Upon heat treating the α' phase broke down, transforming to coarse α and β phases in prior β columnar grains. This transformation was also confirmed by XRD phase analysis. Additionally, the heat treatment led to a 4% decrease in the surface microhardness due to the phase transformation to a softer phase. The SP and DU treatments resulted in a 40% and 210% increase in microhardness, respectively.
2. The initial high surface roughness (R_a) of the AB sample, 8.9 μm, was significantly reduced to 45 nm via polishing. Upon shot peening, the R_a value increased by 41 times to 1.8 μm due to the deformation imparted by the impacting shots. For the DU sample, a similar R_a value of 1.7 μm was recorded indicating that the coating did not result in levelling but rather maintained the rough surface inherited from peening.
3. EBSD analysis revealed increased grain size and decreased misorientations after heat treatment, due to stress relieving. Peening induced compressive residual stresses, also confirmed by XRD phase analysis, and significant misorientations. The misorientations observed for the DU sample confirm that the coating deposition temperature did not result in any stress relief.
4. X-ray diffraction stress measurements showed tensile stresses as high as 128 MPa in the AB condition, induced by the build process. These stresses were relieved after the heat treatment. For the PVD sample, minimal stresses, around 6 MPa, were recorded implying that the coating itself is not highly

stressed. Significant compressive residual stresses equivalent to 700 MPa were induced in the surface of both SP and DU samples, with peak vales being reached at around 30 μm below the surface. Compressive stresses, induced by the impingement of shots, were detected up to approximately 150 μm below the surface for both conditions. From profile hardness measurements, a hardened layer approximately 150 μm deep was also recorded agreeing with the value estimated by residual stress measurements.

Key findings from the analysis of the coating via microscopy, elemental analysis, nanohardness and scratch testing are summarised as follows:

1. The PVD coating structure comprised four different layers: Ti, TiN, TiAlN, TiAlCuN, with a total thickness of approximately 3.9 μm.
2. Nanohardness testing showed the coating's hardness (26 GPa) nearly nine times greater than the heat-treated substrate, with a significant H/E elasticity index of 0.08, indicating its capability to withstand deformation without fracturing when exposed to high cyclic stresses.
3. Overall, the PVD coating exhibited good adhesion characteristics, optimal on a smooth polished surface, with induced roughening by the peening process not conducive to mechanical interlocking rather diminished the coating's integrity due to increased probability of coating defects.

The main findings from the analysis of the substrate's mechanical properties via tensile, impact and axial fatigue testing are summarised as follows:

1. The built and heat-treated material exhibited comparable mechanical properties to its wrought counterpart, except for elongation.
2. Decreased absorbed impact energy for the built and heat-treated material, compared to wrought Ti-6Al-4V, was attributed to build defects and the varying microstructures from different manufacturing processes.
3. Axial fatigue testing revealed enhanced fatigue performance for the SP and DU conditions, though scatter in life cycles dependent on the presence of lack-of-fusion defects and porosity.

Conclusions drawn from polarisation sweeps in artificial seawater at a temperature of 25 ± 2ºC:

1. The PVD coated sample exhibited an overall superior corrosion resistance, whilst the SP and DU treatments did not result in any improvement. High surface roughness contributed to the formation of a non-uniform passive film and increased coating defect density.

The following observation were noted following cavitation testing at a frequency of 20 kHz and amplitude of 50 μm, at a 2 mm horn-to-sample distance, over a test area of 1.99 cm^2 and duration of 4 hours, in artificial seawater at a temperature of 25 ± 2ºC:

1. Ineffectiveness of the treatments in enhancing the substrate's wear resistance was observed due to the rough surface of the SP sample and coating adhesion issues for the PVD and DU conditions.
2. All sample conditions exhibited evidence of cavitation pits after 30 minutes under cavitation, which increased with cavitation time. For the DU and PVD conditions, coating removal mostly occurred at pre-existing surface defects, such as pores, and delamination gradually worsened with time. For the DU condition, coating loss occurred in larger quantities, attributed to its rougher surface.

The following conclusions were drawn following cavitation testing at an anodic potential of 0.2 V vs. reference over a cavitation duration of 4200 s, in artificial seawater at a temperature of 25 ± 2ºC:

1. The cavitation-corrosion resistance increased in the following sequence: HT ≈ SP ≈ DU < PVD, indicating a 2.5-fold improvement for PVD over HT. This was attributed to the high hardness of coating and the better adhesion between the coating and the polished surface.
2. Limited improvement provided by the SP and DU treatments, respectively, was attributed to the induced roughness, resulting in a poorly adhered passive film/ coating and an increased interaction area.
3. For all samples, the contribution of corrosion to material loss was minimal, accounting to less than 1% for all conditions, suggesting that a surface or coating of significant hardness and toughness, capable of withstanding loads induced during cavitation, is more important than having a surface/ coating that exhibits an excellent corrosion resistance. The dominance of

mechanical wear via cavitation, confirmed by a C*/E* ratio of less than 0.1, was exhibited for all conditions.

4. Different failure modes were observed, with Type I failure for HT and SP and likely Type II failure for DU and PVD due to coating defects.

Overall, the applied surface treatments resulted in various desired effects such as an increase in hardness, an improved fatigue performance and induced beneficial compressive residual stresses, in case of shot peening, and an improved corrosion resistance, in case of the PVD coating alone. However, the duplex treatment was ineffective in improving the corrosion, cavitation wear and cavitation-corrosion resistance of the substrate. In all cases, the contributing factor was the peening induced roughness which was observed to result in the formation of a poorly adhered coating having an increased defect density.

5.2 Recommendations for Future Research

As previously mentioned, cavitation-corrosion testing remains relatively unexplored, and the selected test method in this study has not been adopted by other investigators. Consequently, further testing and optimisation are essential to validate the method's accuracy and reliability.

Although the proposed treatments exhibited favourable outcomes in certain aspects, further investigation is warranted, particularly for the duplex treatment's potential use in marine applications. Notably, substrate roughness emerged as a key challenge in shot peening and duplex treatments. Potential remedies may involve refining peening parameters to strike the optimal balance between inducing significant stresses and maintaining minimal roughness. Alternatively, reducing induced roughness could be achieved by incorporating a gentle polishing step post-peening treatment, effectively eliminating asperities without compromising the induced hardening.

Moreover, while there was some improvement observed in the axial fatigue performance of treated LPBF Ti-6Al-4V, it is required to refine the build parameters further. This optimisation is important to diminish the scatter in the fatigue life results, ensuring a consistent and guaranteed improvement through the applied shot peening and duplex treatment.

References

[1] C. Leyens and M. Peters, Eds., *Titanium and Titanium Alloys: Fundamentals and Applications*, 1st ed. Wiley, 2003. doi: 10.1002/3527602119.

[2] D. W. Chalmers, 'The properties and uses of marine structural materials', *Mar. Struct.*, vol. 1, no. 1, pp. 47–70, Jan. 1988, doi: 10.1016/0951-8339(88)90010-X.

[3] Z. Jianwen *et al.*, 'The Application and Prospect of Titanium Materials in Marine Engineering Equipments', presented at the 12th World Conference on Titanium, Jun. 2011, pp. 2268–2271.

[4] B. Vrancken, L. Thijs, J.-P. Kruth, and J. Van Humbeeck, 'Heat treatment of Ti6Al4V produced by Selective Laser Melting: Microstructure and mechanical properties', *J. Alloys Compd.*, vol. 541, pp. 177–185, Nov. 2012, doi: 10.1016/j.jallcom.2012.07.022.

[5] F. Bartolomeu, M. Gasik, F. S. Silva, and G. Miranda, 'Mechanical Properties of Ti6Al4V Fabricated by Laser Powder Bed Fusion: A Review Focused on the Processing and Microstructural Parameters Influence on the Final Properties', *Metals*, vol. 12, no. 6, p. 986, Jun. 2022, doi: 10.3390/met12060986.

[6] S. Liu and Y. C. Shin, 'Additive manufacturing of Ti6Al4V alloy: A review', *Mater. Des.*, vol. 164, p. 107552, Feb. 2019, doi: 10.1016/j.matdes.2018.107552.

[7] S. R. Chauhan and K. Dass, 'Dry Sliding Wear Behaviour of Titanium (Grade 5) Alloy by Using Response Surface Methodology', *Adv. Tribol.*, vol. 2013, pp. 1–9, 2013, doi: 10.1155/2013/272106.

[8] R. Barry Waterhouse and M. Henry Wharton, 'TITANIUM AND TRIBOLOGY', *Ind. Lubr. Tribol.*, vol. 26, no. 1, pp. 20–23, Jan. 1974, doi: 10.1108/eb053055.

[9] J. R. Davis, *Surface engineering for corrosion and wear resistance*. ASM International, 2001.

[10] B. K. C. Ganesh, W. Sha, N. Ramanaiah, and A. Krishnaiah, 'Effect of shotpeening on sliding wear and tensile behavior of titanium implant alloys', *Mater. Des. 1980-2015*, vol. 56, pp. 480–486, Apr. 2014, doi: 10.1016/j.matdes.2013.11.052.

[11] L. Xie, Y. Wen, K. Zhan, L. Wang, C. Jiang, and V. Ji, ‘Characterization on surface mechanical properties of Ti-6Al-4V after shot peening’, *J. Alloys Compd.*, vol. 666, pp. 65–70, May 2016, doi: 10.1016/j.jallcom.2016.01.119.

[12] X. Xie *et al.*, ‘State of the Art and Perspectives on Surface-Strengthening Process and Associated Mechanisms by Shot Peening’, *Coatings*, vol. 13, no. 5, 2023, doi: 10.3390/coatings13050859.

[13] K. Zhan, Y. Zhang, S. Zhao, Z. Yang, B. Zhao, and V. JI, ‘Tribological Behavior and Corrosion Resistance of S30432 Steel after Different Shot Peening Processes’, *J. Mater. Eng. Perform.*, vol. 31, no. 2, pp. 1250–1258, Feb. 2022, doi: 10.1007/s11665-021-06249-3.

[14] A. A. Ahmed, M. Mhaede, M. Wollmann, and L. Wagner, ‘Effect of micro shot peening on the mechanical properties and corrosion behavior of two microstructure Ti–6Al–4V alloy’, *Appl. Surf. Sci.*, vol. 363, pp. 50–58, Feb. 2016, doi: 10.1016/j.apsusc.2015.12.019.

[15] O. Çomaklı, ‘Improved structural, mechanical, corrosion and tribocorrosion properties of Ti45Nb alloys by TiN, TiAlN monolayers, and TiAlN/TiN multilayer ceramic films’, *Ceram. Int.*, vol. 47, no. 3, pp. 4149–4156, Feb. 2021, doi: 10.1016/J.CERAMINT.2020.09.292.

[16] Y. Wang *et al.*, ‘Improvement in the tribocorrosion performance of CrCN coating by multilayered design for marine protective application’, *Appl. Surf. Sci.*, vol. 528, p. 147061, Oct. 2020, doi: 10.1016/J.APSUSC.2020.147061.

[17] F. Ma, J. Li, Z. Zeng, and Y. Gao, ‘Structural, mechanical and tribocorrosion behaviour in artificial seawater of CrN/AlN nano-multilayer coatings on F690 steel substrates’, *Appl. Surf. Sci.*, vol. 428, pp. 404–414, Jan. 2018, doi: 10.1016/J.APSUSC.2017.09.166.

[18] I. V. Gorynin, A. S. Oryshchenko, V. P. Leonov, and V. I. Mikhaylov, ‘Titanium Application in Structures Operating in Sea Water’, in *Proceedings of the 12th World Conference on Titanium*, 2011, pp. 2243–2248.

[19] H. D. Nguyen *et al.*, ‘A critical review on additive manufacturing of Ti-6Al-4V alloy: microstructure and mechanical properties’, *J. Mater. Res. Technol.*, vol. 18, pp. 4641–4661, May 2022, doi: 10.1016/j.jmrt.2022.04.055.

[20] T. R. Bieler, R. M. Trevino, and L. Zeng, ‘Alloys: Titanium’, *Encycl. Condens. Matter Phys.*, pp. 65–76, Jan. 2005, doi: 10.1016/B0-12-369401-9/00536-2.

[21] P. Bocchetta, L.-Y. Chen, J. D. C. Tardelli, A. C. dos Reis, F. Almeraya-Calderón, and P. Leo, 'Passive Layers and Corrosion Resistance of Biomedical Ti-6Al-4V and β-Ti Alloys', *Coatings*, vol. 11, no. 5, p. 487, Apr. 2021, doi: 10.3390/coatings11050487.

[22] R. Yazdi, M. H. Ghasemi, C. Wang, and A. Neville, 'Bio-corrosion behaviour of oxygen diffusion layer on Ti-6Al-4V during tribocorrosion', *Corros. Sci.*, no. 128, pp. 23–32, 2017.

[23] C. Veiga, J. P. Davim, and A. J. R. Loureiro, 'Properties and Applications of Titanium Alloys: A Brief Review', *Rev. Adv. Mater. Sci.*, no. 32, pp. 14–34, 2012.

[24] M. Neikter, A. Huang, and X. Wu, 'Microstructural characterization of binary microstructure pattern in selective laser-melted Ti-6Al-4V', *Int. J. Adv. Manuf. Technol.*, vol. 104, no. 1–4, pp. 1381–1391, Sep. 2019, doi: 10.1007/s00170-019-04002-8.

[25] M. Neikter, 'Microstructure and texture of additive manufactured Ti-6Al-4V', Luleå University of Technology, Luleå, 2017.

[26] C. Zheng *et al.*, 'Effect of microstructures on ballistic impact property of Ti–6Al–4V targets', *Mater. Sci. Eng. A*, vol. 608, pp. 53–62, Jul. 2014, doi: 10.1016/j.msea.2014.04.032.

[27] Y. Fan, W. Tian, Y. Guo, Z. Sun, and J. Xu, 'Relationships among the Microstructure, Mechanical Properties, and Fatigue Behavior in Thin Ti6Al4V', *Adv. Mater. Sci. Eng.*, vol. 2016, pp. 1–9, 2016, doi: 10.1155/2016/7278267.

[28] ASTM International, *ASTM F2792-10 Standard Terminology for Additive Manufacturing Technologies*, ASTM F2792-10. 2010. doi: 10.1520/F2792-10.

[29] P. Ponnusamy, R. A. Rahman Rashid, S. H. Masood, D. Ruan, and S. Palanisamy, 'Mechanical Properties of SLM-Printed Aluminium Alloys: A Review', *Materials*, vol. 13, no. 19, 2020, doi: 10.3390/ma13194301.

[30] J. Yang, H. Yang, H. Yu, Z. Wang, and X. Zeng, 'Corrosion Behavior of Additive Manufactured Ti-6Al-4V Alloy in NaCl Solution', *Metall. Mater. Trans. A*, vol. 48, no. 7, pp. 3583–3593, Jul. 2017, doi: 10.1007/s11661-017-4087-9.

[31] M. Simonelli, Y. Y. Tse, and C. Tuck, 'Effect of the build orientation on the mechanical properties and fracture modes of SLM Ti–6Al–4V', *Mater. Sci. Eng. A*, vol. 616, pp. 1–11, Oct. 2014, doi: 10.1016/j.msea.2014.07.086.

[32] A. Popovich, V. Sufiiarov, I. Polozov, E. Borisov, and D. Masaylo, ‘Producing hip implants of titanium alloys by additive manufacturing’, *Int. J. Bioprinting*, vol. 2, no. 2, Jun. 2016, doi: 10.18063/IJB.2016.02.004.

[33] G. Yu *et al.*, ‘The Effects of Post Heat Treatment on the Microstructural and Mechanical Properties of an Additive-Manufactured Porous Titanium Alloy’, *Materials*, vol. 13, no. 3, 2020, doi: 10.3390/ma13030593.

[34] A. Agapovichev, A. Sotov, V. Kokareva, and V. Smelov, ‘Possibilities and limitations of titanium alloy additive manufacturing’, *MATEC Web Conf.*, vol. 224, p. 01064, 2018, doi: 10.1051/matecconf/201822401064.

[35] E. Maleki, S. Bagherifard, M. Bandini, and M. Guagliano, ‘Surface post-treatments for metal additive manufacturing: Progress, challenges, and opportunities’, *Addit. Manuf.*, vol. 37, p. 101619, Jan. 2021, doi: 10.1016/j.addma.2020.101619.

[36] G. Kasperovich and J. Hausmann, ‘Improvement of fatigue resistance and ductility of TiAl6V4 processed by selective laser melting’, *J. Mater. Process. Technol.*, vol. 220, pp. 202–214, 2015, doi: https://doi.org/10.1016/j.jmatprotec.2015.01.025.

[37] P. Edwards and M. Ramulu, ‘Fatigue performance evaluation of selective laser melted Ti–6Al–4V’, *Mater. Sci. Eng. A*, vol. 598, pp. 327–337, Mar. 2014, doi: 10.1016/j.msea.2014.01.041.

[38] K. S. Chan, M. Koike, R. L. Mason, and T. Okabe, ‘Fatigue Life of Titanium Alloys Fabricated by Additive Layer Manufacturing Techniques for Dental Implants’, *Metall. Mater. Trans. A*, vol. 44, no. 2, pp. 1010–1022, Feb. 2013, doi: 10.1007/s11661-012-1470-4.

[39] P. Li, D. H. Warner, A. Fatemi, and N. Phan, ‘Critical assessment of the fatigue performance of additively manufactured Ti–6Al–4V and perspective for future research’, *Int. J. Fatigue*, vol. 85, pp. 130–143, Apr. 2016, doi: 10.1016/j.ijfatigue.2015.12.003.

[40] ASTM International, *Standard Specification for Wrought Titanium-6Aluminum-4Vanadium ELI (Extra Low Interstitial) Alloy for Surgical Implant Applications (UNS R56401)*, ASTM F136-13(2021)e1. 2021.

[41] ASTM International, *Standard Specification for Additive Manufacturing Titanium-6 Aluminum-4 Vanadium with Powder Bed Fusion*, ASTM F2924-14(2021). 2021.

[42] J. Yang, H. Yu, Z. Wang, and X. Zeng, 'Effect of crystallographic orientation on mechanical anisotropy of selective laser melted Ti-6Al-4V alloy', *Mater. Charact.*, vol. 127, pp. 137–145, May 2017, doi: 10.1016/j.matchar.2017.01.014.

[43] K. F. Walker, Q. Liu, and M. Brandt, 'Evaluation of fatigue crack propagation behaviour in Ti-6Al-4V manufactured by selective laser melting', *Int. J. Fatigue*, vol. 104, pp. 302–308, Nov. 2017, doi: 10.1016/j.ijfatigue.2017.07.014.

[44] S. Leuders *et al.*, 'On the mechanical behaviour of titanium alloy TiAl6V4 manufactured by selective laser melting: Fatigue resistance and crack growth performance', *Int. J. Fatigue*, vol. 48, pp. 300–307, Mar. 2013, doi: 10.1016/j.ijfatigue.2012.11.011.

[45] D. Greitemeier, C. Dalle Donne, F. Syassen, J. Eufinger, and T. Melz, 'Effect of surface roughness on fatigue performance of additive manufactured Ti–6Al–4V', *Mater. Sci. Technol.*, vol. 32, no. 7, pp. 629–634, May 2016, doi: 10.1179/1743284715Y.0000000053.

[46] L.-C. Zhang and H. Attar, 'Selective Laser Melting of Titanium Alloys and Titanium Matrix Composites for Biomedical Applications: A Review', *Adv. Eng. Mater.*, vol. 18, no. 4, pp. 463–475, Apr. 2016, doi: 10.1002/adem.201500419.

[47] P. Lekoadi, M. Tlotleng, K. Annan, N. Maledi, and B. Masina, 'Evaluation of heat treatment parameters on microstructure and hardness properties of high-speed selective laser melted Ti6Al4V', *Metals*, vol. 11, no. 2, pp. 1–15, Feb. 2021, doi: 10.3390/met11020255.

[48] Y. Zhu, X. Chen, J. Zou, and H. Yang, 'Sliding wear of selective laser melting processed Ti6Al4V under boundary lubrication conditions', *Wear*, vol. 368–369, pp. 485–495, Dec. 2016, doi: 10.1016/j.wear.2016.09.020.

[49] K. Bower, S. Murray, A. Reinhart, and A. Nieto, 'Corrosion resistance of selective laser melted Ti–6Al–4V alloy in salt fog environment', *Results Mater.*, vol. 8, p. 100122, Dec. 2020, doi: 10.1016/j.rinma.2020.100122.

[50] N. Dai, L.-C. Zhang, J. Zhang, Q. Chen, and M. Wu, 'Corrosion behavior of selective laser melted Ti-6Al-4 V alloy in NaCl solution', *Corros. Sci.*, vol. 102, pp. 484–489, Jan. 2016, doi: 10.1016/j.corsci.2015.10.041.

[51] A. Sharma, M. C. Oh, J.-T. Kim, A. K. Srivastava, and B. Ahn, 'Investigation of electrochemical corrosion behavior of additive manufactured Ti–6Al–4V alloy for medical implants in different electrolytes', *J. Alloys Compd.*, vol. 830, p. 154620, Jul. 2020, doi: 10.1016/j.jallcom.2020.154620.

[52] H. Dong, 'Tribological properties of titanium-based alloys', in *Surface Engineering of Light Alloys*, Elsevier, 2010, pp. 58–80. doi: 10.1533/9781845699451.1.58.

[53] A. Pramanik and G. Littlefair, 'Machining of Titanium Alloy (Ti-6Al-4V)—Theory to Application', *Mach. Sci. Technol.*, vol. 19, no. 1, pp. 1–49, Jan. 2015, doi: 10.1080/10910344.2014.991031.

[54] A. K. Krella, 'Degradation and Protection of Materials from Cavitation Erosion: A Review', *Materials*, vol. 16, no. 5, p. 2058, Mar. 2023, doi: 10.3390/ma16052058.

[55] J. Basumatary, 'Cavitation erosion-corrosion in marine propeller materials', University of Southampton, 2017.

[56] E. D. D. During, 'Part II: Corrosion Topics', in *Corrosion Atlas Case Studies*, Elsevier, 2020, pp. xliii–lxviii. doi: 10.1016/B978-0-12-818760-9.02003-1.

[57] W. S. Tait, 'Corrosion Prevention and Control of Chemical Processing Equipment', in *Handbook of Environmental Degradation of Materials*, Elsevier, 2012, pp. 863–886. doi: 10.1016/B978-1-4377-3455-3.00028-6.

[58] G. Wang, G. Ma, D. Sun, H. Yu, and H. Meng, 'Numerical study on fatgue damage properties of cavitation erosion for rigid metal materials', *J. Univ. Sci. Technol.*, vol. 15, no. 3, pp. 261–266, Jun. 2008.

[59] W. Będkowski, G. Gasiak, C. Lachowicz, A. Lichtarowicz, T. Łagoda, and E. Macha, 'Relations between cavitation erosion resistance of materials and their fatigue strength under random loading', *Wear*, vol. 230, no. 2, pp. 201–209, May 1999, doi: 10.1016/S0043-1648(99)00105-2.

[60] A. Neville, T. Hodekeiss, and J. T. Dallas, 'A Study of the Erosion---Corrosion Behaviour of Engineering Steel for Marine Pumping Applications', *Wear*, vol. 186, pp. 497–507, 1995.

[61] ASTM International, *Standard Test Method for Cavitation Erosion Using Vibratory Apparatus*, ASTM G32-16(2021)e1. 2021. doi: 10.1520/G0032-16R21E01.

[62] ASTM International, *Standard Test Method for Erosion of Solid Materials by Cavitating Liquid Jet*, ASTM G134-17. 2017. doi: 10.1520/G0134-17.

[63] J. Basumatary and R. J. K. Wood, 'Different methods of measuring synergy between cavitation erosion and corrosion for nickel aluminium bronze in 3.5% NaCl solution', *Tribol. Int.*, vol. 147, p. 104843, 2020, doi: https://doi.org/10.1016/j.triboint.2017.08.006.

[64] J. Basumatary, M. Nie, and R. J. K. Wood, 'The Synergistic Effects of Cavitation Erosion–Corrosion in Ship Propeller Materials', *J. Bio- Tribo-Corros.*, vol. 1, no. 2, p. 12, Jun. 2015, doi: 10.1007/s40735-015-0012-1.

[65] S. Mischler and A. I. Munoz, 'Tribocorrosion', in *Encyclopedia of Interfacial Chemistry*, Elsevier, 2018, pp. 504–514. doi: 10.1016/B978-0-12-409547-2.13424-9.

[66] H. H. Uhlig, 'Passivity in metals and alloys', *Corros. Sci.*, vol. 19, pp. 777–791, 1979.

[67] Z. Zheng, J. Long, S. Wang, H. Li, J. Wang, and K. Zheng, 'Cavitation erosion-corrosion behaviour of Fe-10Cr martensitic steel microalloyed with Zr in 3.5 % NaCl solution', *Corros. Sci.*, vol. 184, p. 109382, May 2021, doi: 10.1016/j.corsci.2021.109382.

[68] T. Amann, M. Waidele, and A. Kailer, 'Analysis of mechanical and chemical mechanisms on cavitation erosion-corrosion of steels in salt water using electrochemical methods', *Tribol. Int.*, vol. 124, pp. 238–246, Aug. 2018, doi: 10.1016/j.triboint.2018.04.012.

[69] Q. N. Song *et al.*, 'Synergistic effect between cavitation erosion and corrosion for various copper alloys in sulphide-containing 3.5% NaCl solutions', *Wear*, vol. 450–451, p. 203258, Jun. 2020, doi: 10.1016/j.wear.2020.203258.

[70] ASTM International, *Standard Guide for Determining Synergism Between Wear and Corrosion*, ASTM G119-09(2021). 2021.

[71] B. Mallia and P. A. Dearnley, 'The corrosion-wear response of Cr-Ti coatings', *Wear*, vol. 263, no. 1-6 SPEC. ISS., pp. 679–690, Sep. 2007, doi: 10.1016/j.wear.2006.12.058.

[72] C. T. Kwok, F. T. Cheng, and H. C. Man, 'Synergistic effect of cavitation erosion and corrosion of various engineering alloys in 3.5% NaCl solution', *Mater. Sci. Eng. A*, vol. 290, no. 1–2, pp. 145–154, Oct. 2000, doi: 10.1016/S0921-5093(00)00899-6.

[73] A. Neville and B. A. B. McDougall, ‘Erosion– and cavitation–corrosion of titanium and its alloys’, *Wear*, vol. 250, no. 1–12, pp. 726–735, Oct. 2001, doi: 10.1016/S0043-1648(01)00709-8.

[74] C. Ye, C. Zhang, J. Zhao, and Y. Dong, ‘Effects of Post-processing on the Surface Finish, Porosity, Residual Stresses, and Fatigue Performance of Additive Manufactured Metals: A Review’, *J. Mater. Eng. Perform.*, vol. 30, no. 9, pp. 6407–6425, Sep. 2021, doi: 10.1007/s11665-021-06021-7.

[75] H. Huang, J. Niu, X. Xing, Q. Lin, H. Chen, and Y. Qiao, ‘Effects of the Shot Peening Process on Corrosion Resistance of Aluminum Alloy: A Review’, *Coatings*, vol. 12, no. 5, 2022, doi: 10.3390/coatings12050629.

[76] V. Fridrici, S. Fouvry, and P. Kapsa, ‘Effect of shot peening on the fretting wear of Ti-6Al-4V’, *Wear*, vol. 250, pp. 642–649, 2001.

[77] O. Lupicka and B. Warcholinski, ‘The Adhesion of CrN Thin Films Deposited on Modified 42CrMo4 Steel’, *Adv. Mater. Sci. Eng.*, vol. 2017, p. 4064208, Dec. 2017, doi: 10.1155/2017/4064208.

[78] X. H. Zhang, D. X. Liu, H. B. Tan, and X. F. Wang, ‘Effect of TiN/Ti composite coating and shot peening on fretting fatigue behavior of TC17 alloy at 350 °C’, *Surf. Coat. Technol.*, vol. 203, no. 16, pp. 2315–2321, May 2009, doi: 10.1016/j.surfcoat.2009.02.058.

[79] N. Ravi, R. Markandeya, and S. V. Joshi, ‘Effect of substrate roughness on adhesion and tribological properties of nc-TiAlN/a-Si3N4 nanocomposite coatings deposited by cathodic arc PVD process’, *Surf. Eng.*, vol. 33, no. 1, pp. 7–19, Jan. 2017, doi: 10.1179/1743294415Y.0000000005.

[80] C. Zhang, M. Zheng, Y. Wang, P. Gao, and B. Gan, ‘Effect of high energy shot peening on the wear resistance of TiN films on a TA2 surface’, *Surf. Coat. Technol.*, vol. 378, Nov. 2019, doi: 10.1016/j.surfcoat.2019.07.045.

[81] A. Zammit *et al.*, ‘Enhancing surface integrity of titanium alloy through hybrid surface modification (HSM) treatments’, *Mater. Chem. Phys.*, vol. 279, p. 125768, Mar. 2022, doi: 10.1016/J.MATCHEMPHYS.2022.125768.

[82] N. Tsuji, S. Tanaka, and T. Takasugi, ‘Effects of combined plasma-carburizing and shot-peening on fatigue and wear properties of Ti–6Al–4V alloy’, *Surf. Coat. Technol.*, vol. 203, no. 10–11, pp. 1400–1405, Feb. 2009, doi: 10.1016/j.surfcoat.2008.11.013.

[83] Q. Zhang, S. Xu, J. Wang, X. Zhang, J. Wang, and C. Si, 'Microstructure change and corrosion resistance of selective laser melted Ti-6Al-4V alloy subjected to pneumatic shot peening and ultrasonic shot peening', *Surf. Topogr. Metrol. Prop.*, vol. 10, no. 1, Mar. 2022, doi: 10.1088/2051-672X/ac4c83.

[84] S. Slawik *et al.*, 'Microstructural analysis of selective laser melted Ti6Al4V modified by laser peening and shot peening for enhanced fatigue characteristics', *Mater. Charact.*, vol. 173, p. 110935, Mar. 2021, doi: 10.1016/j.matchar.2021.110935.

[85] S. Aguado-Montero, C. Navarro, J. Vázquez, F. Lasagni, S. Slawik, and J. Domínguez, 'Fatigue behaviour of PBF additive manufactured TI6AL4V alloy after shot and laser peening', *Int. J. Fatigue*, vol. 154, p. 106536, Jan. 2022, doi: 10.1016/j.ijfatigue.2021.106536.

[86] Q. Lin, H. Liu, C. Zhu, D. Chen, and S. Zhou, 'Effects of different shot peening parameters on residual stress, surface roughness and cell size', *Surf. Coat. Technol.*, vol. 398, p. 126054, Sep. 2020, doi: 10.1016/j.surfcoat.2020.126054.

[87] Y. B. Bozkurt, H. Kovacı, A. F. Yetim, and A. Çelik, 'Tribocorrosion properties and mechanism of a shot peened AISI 4140 low-alloy steel', *Surf. Coat. Technol.*, vol. 440, p. 128444, 2022, doi: https://doi.org/10.1016/j.surfcoat.2022.128444.

[88] M. Kahlin *et al.*, 'Improved fatigue strength of additively manufactured Ti6Al4V by surface post processing', *Int. J. Fatigue*, vol. 134, p. 105497, May 2020, doi: 10.1016/j.ijfatigue.2020.105497.

[89] E. Wysick, A. Solbach, S. Siddique, D. Herzog, F. Walther, and C. Emmelmann, 'Effects of defects in laser additive manufactured Ti-6Al-4V on fatigue properties', *Phys Procedia*, vol. 56, pp. 371–378, 2014.

[90] A. Zammit, 'Shot Peening of Austempered Ductile Iron', in *Advanced Surface Engineering Research*, M. A. Chowdhury, Ed., Rijeka: IntechOpen, 2018. doi: 10.5772/intechopen.79316.

[91] W. J. Tomlinson, R. T. Moule, and G. N. Blount, 'THE EFFECT OF SHOT PEENING ON THE CAVITATION EROSION OF PURE IRON AND AUSTENITIC STAINLESS STEEL IN DISTILUED AND 1% SALT WATERS', *Wear*, no. 118, pp. 233–242, 1987.

[92] H. Sasaki, F. Takeo, and H. Soyama, 'Cavitation erosion resistance of the titanium alloy Ti–6Al–4V manufactured through additive manufacturing with

various peening methods', *Wear*, vol. 462–463, p. 203518, Dec. 2020, doi: 10.1016/j.wear.2020.203518.

[93] S. Zeng, S. Hu, and G. Cheng, 'Effect of shot peening on surface characterization and cavitation resistance of nickel aluminum bronze', *Mater. Today Commun.*, vol. 33, p. 104767, Dec. 2022, doi: 10.1016/j.mtcomm.2022.104767.

[94] A. Baptista, F. Silva, J. Porteiro, J. Míguez, and G. Pinto, 'Sputtering Physical Vapour Deposition (PVD) Coatings: A Critical Review on Process Improvement and Market Trend Demands', *Coatings*, vol. 8, no. 11, 2018, doi: 10.3390/coatings8110402.

[95] H. Hoche, S. Groß, and M. Oechsner, 'Development of new PVD coatings for magnesium alloys with improved corrosion properties', *9th Asian-Eur. Int. Conf. Plasma Surf. Eng.*, vol. 259, pp. 102–108, Nov. 2014, doi: 10.1016/j.surfcoat.2014.04.038.

[96] I. Petrov, P. B. Barna, L. Hultman, and J. E. Greene, 'Microstructural evolution during film growth', *J. Vac. Sci. Technol. A*, vol. 21, no. 5, pp. 117–128, Sep. 2003, doi: 10.1116/1.1601610.

[97] W. Chang, H. Cai, Y. Xue, X. Lei, and H. Li, 'Effects of Deposition Pressure on the Microstructural and Tribological Properties of CrAgCeN Coatings Prepared by Magnetron Sputtering', *Materials*, vol. 16, no. 3, 2023, doi: 10.3390/ma16031141.

[98] A. R. M. Nizam, P. T. Swanson, M. M. Razali, B. Esmar, and H. Hakim, 'Effect of PVD Process Parameters on the TiAlN Coating Roughness', 2010. [Online]. Available: https://api.semanticscholar.org/CorpusID:138705927

[99] E. Lugscheider, C. Barimani, C. Wolff, S. Guerreiro, and G. Doepper, 'Comparison of the structure of PVD-thin films deposited with different deposition energies', *Surf. Coat. Technol.*, vol. 86–87, pp. 177–183, Dec. 1996, doi: 10.1016/S0257-8972(96)03041-1.

[100] P. Panjan, A. Drnovšek, N. Mahne, M. Čekada, and M. Panjan, 'Surface Topography of PVD Hard Coatings', *Coatings*, vol. 11, no. 11, 2021, doi: 10.3390/coatings11111387.

[101] Y. Liu, S. Yu, Q. Shi, X. Ge, and W. Wang, 'Multilayer Coatings for Tribology: A Mini Review', *Nanomaterials*, vol. 12, no. 9, p. 1388, Apr. 2022, doi: 10.3390/nano12091388.

[102] A. Krella, ‘Resistance of PVD Coatings to Erosive and Wear Processes: A Review’, *Coatings*, vol. 10, no. 10, p. 921, Sep. 2020, doi: 10.3390/coatings10100921.

[103] H. Elmkhah, A. Fattah-alhosseini, K. Babaei, A. Abdollah-zadeh, and F. Mahboubi, ‘Correlation between the Al content and corrosion resistance of TiAlN coatings applied using a PACVD technique’, *J. Asian Ceram. Soc.*, vol. 8, pp. 1–9, Jan. 2020, doi: 10.1080/21870764.2019.1709274.

[104] I. V. Blinkov, D. S. Belov, A. O. Volkhonskii, Yu. A. Pustov, F. V. Kiryukhantsev-Korneev, and E. A. Skryleva, ‘Thermal stability, heat resistivity, and electrochemical corrosion resistance of (Ti,Al)N-Cu nanostructural coatings’, *Prot. Met. Phys. Chem. Surf.*, vol. 51, no. 4, pp. 550–557, Jul. 2015, doi: 10.1134/S207020511504005X.

[105] D. S. Belov *et al.*, ‘Abrasive, hydroabrasive, and erosion wear behaviour of nanostructured (Ti,Al)N-Cu and (Ti,Al)N-Ni coatings’, *Surf. Coat. Technol.*, vol. 338, pp. 1–13, Mar. 2018, doi: 10.1016/j.surfcoat.2018.01.066.

[106] L. Ceschini, E. Lanzoni, C. Martini, D. Prandstraller, and G. Sambogna, ‘Comparison of dry sliding friction and wear of Ti6Al4V alloy treated by plasma electrolytic oxidation and PVD coating’, *Wear*, vol. 264, no. 1–2, pp. 86–95, Jan. 2008, doi: 10.1016/j.wear.2007.01.045.

[107] D. S. Belov, I. V. Blinkov, and A. O. Volkhonskii, ‘The effect of Cu and Ni on the nanostructure and properties of arc-PVD coatings based on titanium nitride’, *41st Int. Conf. Metall. Coat. Thin Films*, vol. 260, pp. 186–197, Dec. 2014, doi: 10.1016/j.surfcoat.2014.09.069.

[108] H. Mei *et al.*, ‘Effect of Cu doping on the microstructure and mechanical properties of AlTiVN-Cu nanocomposite coatings’, *Surf. Coat. Technol.*, vol. 402, p. 126490, Nov. 2020, doi: 10.1016/j.surfcoat.2020.126490.

[109] A. García *et al.*, ‘Copper-modified polymeric membranes for water treatment: A comprehensive review’, *Membranes*, vol. 11, no. 2, pp. 1–47, Jan. 2021, doi: 10.3390/membranes11020093.

[110] V. Aruoja, H. C. Dubourguier, K. Kasemets, and A. Kahru, ‘Toxicity of nanoparticles of CuO, ZnO and TiO2 to microalgae Pseudokirchneriella subcapitata’, *Sci. Total Environ.*, vol. 407, no. 4, pp. 1461–1468, Feb. 2009, doi: 10.1016/J.SCITOTENV.2008.10.053.

[111] V. M. C. A. Oliveira, C. Aguiar, A. M. Vazquez, A. Robin, and M. J. R. Barboza, 'Improving corrosion resistance of Ti-6Al-4V alloy through plasma-assisted PVD deposited nitride coatings', *Corros. Sci.*, vol. 88, pp. 317–327, 2014, doi: 10.1016/j.corsci.2014.07.047.

[112] O. Durst, J. Ellermeier, and C. Berger, 'Influence of plasma-nitriding and surface roughness on the wear and corrosion resistance of thin films (PVD/PECVD)', *Proc. 35th Int. Conf. Metall. Coat. Thin Films*, vol. 203, no. 5, pp. 848–854, Dec. 2008, doi: 10.1016/j.surfcoat.2008.05.022.

[113] J. L. Daure, K. T. Voisey, P. H. Shipway, and D. A. Stewart, 'The effect of coating architecture and defects on the corrosion behaviour of a PVD multilayer Inconel 625/Cr coating', *Surf. Coat. Technol.*, vol. 324, pp. 403–412, Sep. 2017, doi: 10.1016/j.surfcoat.2017.06.009.

[114] J. Munemasa and T. Kumakiri, 'Effect of the surface roughness of substrates on the corrosion properties of films coated by physical vapour deposition', *Surf. Coat. Technol.*, vol. 49, no. 1, pp. 496–499, Dec. 1991, doi: 10.1016/0257-8972(91)90106-7.

[115] M. Hein *et al.*, 'On the influence of physical vapor deposited thin coatings on the low-cycle fatigue behavior of additively processed Ti-6Al-7Nb alloy', *Int. J. Fatigue*, vol. 166, p. 107235, Jan. 2023, doi: 10.1016/j.ijfatigue.2022.107235.

[116] S. Glodež, M. Podgrajšek, B. Podgornik, and Z. Ren, 'The influence of PVD coating on the low cycle fatigue behaviour of Cr-Mo-V steel at elevated temperatures', *Surf. Coat. Technol.*, vol. 321, pp. 358–365, 2017, doi: https://doi.org/10.1016/j.surfcoat.2017.05.008.

[117] A. P. Gopkalo, N. R. Muzyka, A. V. Rutkovskii, and V. P. Shvets, 'Effect of PVD coatings on the strain and low-cycle fatigue resistance of stainless steel and titanium alloys', *Strength Mater.*, vol. 43, no. 6, pp. 604–614, Oct. 2011, doi: 10.1007/s11223-011-9333-6.

[118] M. J. Twu, C. C. Hu, D. W. Liu, C. Y. Hsu, and C. G. Kuo, 'Effects of TiN, CrN and TiAlN coatings using reactive sputtering on the fatigue behaviour of AA2024 and medium carbon steel specimens', *J. Exp. Nanosci.*, vol. 11, no. 7, pp. 581–592, 2016, doi: 10.1080/17458080.2015.1100332.

[119] E. S. Puchi-Cabrera, F. Matínez, I. Herrera, J. A. Berríos, S. Dixit, and D. Bhat, 'On the fatigue behavior of an AISI 316L stainless steel coated with a PVD TiN

deposit', *Surf. Coat. Technol.*, vol. 182, no. 2, pp. 276–286, Apr. 2004, doi: 10.1016/j.surfcoat.2003.07.003.

[120] M. Y. P. Costa, M. L. R. Venditti, M. O. H. Cioffi, H. J. C. Voorwald, V. A. Guimarães, and R. Ruas, 'Fatigue behavior of PVD coated Ti–6Al–4V alloy', *Int. J. Fatigue*, vol. 33, no. 6, pp. 759–765, Jun. 2011, doi: 10.1016/j.ijfatigue.2010.11.007.

[121] D. Ma *et al.*, 'Cavitation erosion performance of CrAlYN/CrN nanoscale multilayer coatings deposited on Ti6Al4V by HIPIMS', *J. Alloys Compd.*, vol. 788, pp. 719–728, Jun. 2019, doi: 10.1016/j.jallcom.2019.02.238.

[122] B. D. Beake, 'The influence of the H/E ratio on wear resistance of coating systems – Insights from small-scale testing', *Surf. Coat. Technol.*, vol. 442, p. 128272, 2022, doi: https://doi.org/10.1016/j.surfcoat.2022.128272.

[123] A. Krella, 'The influence of TiN coatings properties on cavitation erosion resistance', *Surf. Coat. Technol.*, vol. 204, no. 3, pp. 263–270, Oct. 2009, doi: 10.1016/j.surfcoat.2009.07.014.

[124] A. K. Krella, 'Cavitation erosion resistance of Ti/TiN multilayer coatings', *Surf. Coat. Technol.*, vol. 228, pp. 115–123, Aug. 2013, doi: 10.1016/j.surfcoat.2013.04.016.

[125] P. Wiecinski, J. Smolik, H. Garbacz, J. Bonarski, A. Mazurkiewicz, and K. J. Kurzydłowski, 'Microstructure and properties of metal/ceramic and ceramic/ceramic multilayer coatings on titanium alloy Ti6Al4V', *Surf. Coat. Technol.*, vol. 309, pp. 709–718, Jan. 2017, doi: 10.1016/j.surfcoat.2016.11.003.

[126] A. Zammit *et al.*, 'Investigations on the adhesion and fatigue characteristics of hybrid surface-treated titanium alloy', *Surf. Coat. Technol.*, vol. 431, p. 128002, 2022, doi: https://doi.org/10.1016/j.surfcoat.2021.128002.

[127] J. Jiang and R. D. Arnell, 'The effect of substrate surface roughness on the wear of DLC coatings', 2000. [Online]. Available: www.elsevier.comrlocaterwear

[128] X. Cao *et al.*, 'Effect of TiN/Ti coating combined with laser shock peening pre-treatment on the fatigue strength of Ti-6Al-4V titanium alloy', *Surf. Coat. Technol.*, vol. 403, p. 126393, Dec. 2020, doi: 10.1016/j.surfcoat.2020.126393.

[129] Avimetal Powder Metallurgy Technology Co. Ltd., 'TC4 Powder Datasheet'.

[130] European Additive Manufacturing Group, *INTRODUCTION TO ADDITIVE MANUFACTURING TECHNOLOGY: A Guide for Designers and Engineers*, 3rd ed. 2019.

[131] C. Zhang, W. Song, F. Li, X. Zhao, Y. Wang, and G. Xiao, 'Microstructure and Corrosion Properties of Ti-6Al-4V alloy by Ultrasonic Shot Peening', *Int. J. Electrochem. Sci.*, vol. 10, pp. 9167–9178, 2015.

[132] S. J. Lainé, K. M. Knowles, P. J. Doorbar, R. D. Cutts, and D. Rugg, 'Microstructural characterisation of metallic shot peened and laser shock peened Ti–6Al–4V', *Acta Mater.*, vol. 123, pp. 350–361, Jan. 2017, doi: 10.1016/j.actamat.2016.10.044.

[133] Z. Zhang *et al.*, 'Fatigue life enhancement in alpha/beta Ti–6Al–4V after shot peening: An EBSD and TEM crystallographic orientation mapping study of surface layer', *Materialia*, vol. 12, p. 100813, 2020, doi: https://doi.org/10.1016/j.mtla.2020.100813.

[134] H. Y. Miao, D. Demers, S. Larose, C. Perron, and M. Levesque, 'Experimental study of shot peening and stress peen forming', *J. Mater. Process. Technol.*, vol. 210, no. 15, pp. 2089–2102, Nov. 2010, doi: 10.1016/J.JMATPROTEC.2010.07.016.

[135] International Organization for Standardization, *ISO 20502:2005: Fine ceramics (advanced ceramics, advanced technical ceramics) — Determination of adhesion of ceramic coatings by scratch testing*, 1st ed. 2005.

[136] D. Shindo and H. Kenji, *High-Resolution Electron Microscopy for Materials Science*. Springer Japan, 2012. [Online]. Available: https://books.google.com.mt/books?id=tCHpCAAAQBAJ

[137] *Non-destructive testing. Test method for residual stress analysis by X-ray diffraction*, Confirmed. 2009.

[138] M. Fitzpatrick, A. Fry, P. Holdway, F. Kandil, J. Shackleton, and L. Suominen, 'Determination of Residual Stresses by X-ray Diffraction', vol. 52, Jan. 2002.

[139] P. S. Prevéy, 'X-ray diffraction characterization of residual stresses produced by shot peening', *Shot Peen.*, vol. 15, no. 1, pp. 4–8, 2001.

[140] A. D. Krawitz, *Introduction to Diffraction in Materials Science and Engineering*. New York: John Wiley & Sons, 2001.

[141] ASTM International, 'Test Methods for Vickers Hardness and Knoop Hardness of Metallic Materials', ASTM International. doi: 10.1520/E0092-17.

[142] M.-W. Wu and P.-H. Lai, 'The positive effect of hot isostatic pressing on improving the anisotropies of bending and impact properties in selective laser melted Ti-6Al-4V alloy', *Mater. Sci. Eng. A*, vol. 658, pp. 429–438, Mar. 2016, doi: 10.1016/j.msea.2016.02.023.

[143] ASTM International, *Test Methods for Tension Testing of Metallic Materials*, ASTM E8/E8M-16. 2016. doi: 10.1520/E0008_E0008M-16A.

[144] ASTM International, *Test Methods for Notched Bar Impact Testing of Metallic Materials*, ASTM E23-16. 2016. doi: 10.1520/E0023-16B.

[145] International Organization for Standardization, *ISO 1099:2017(E): Metallic materials — Fatigue testing Axial force-controlled method*, 3rd ed. International Organization for Standardization, 2017.

[146] P. Webb, *Introduction to Oceanography*. [Online]. Available: https://books.google.com.mt/books?id=OcI5zQEACAAJ

[147] D. Gregory *et al.*, 'Of time and tide: the complex impacts of climate change on coastal and underwater cultural heritage', *Antiquity*, vol. 96, pp. 1–16, Nov. 2022, doi: 10.15184/aqy.2022.115.

[148] ASTM International, *Standard Practice for the Preparation of Substitute Ocean Water*, ASTM D1141-98 (2003). 1998.

[149] K. A. Vella *et al.*, 'The Effect of a Duplex Surface Treatment on the Corrosion and Tribocorrosion Characteristics of Additively Manufactured Ti-6Al-4V', *Materials*, vol. 16, no. 5, 2023, doi: 10.3390/ma16052098.

[150] Kelsey Ann Vella, 'Investigating the Corrosion-Wear Characteristics of a 3D Printed Surface Engineered Titanium Alloy', University of Malta, 2022.

[151] Antonella Scerri, 'Corrosion and Corrosion-Wear Response of PIRAC-treated Ti-6Al-4V in a Simulated Body Fluid', University of Malta, 2015.

[152] D. Surovtseva and K. Kannoorpatti, 'Benefits and drawbacks of pourbaix diagram', *Annu. Conf. Australas. Corros. Assoc. 2014 Corros. Prev. 2014*, Jan. 2014.

[153] T. Vilaro, C. Colin, and J. D. Bartout, 'As-Fabricated and Heat-Treated Microstructures of the Ti-6Al-4V Alloy Processed by Selective Laser Melting', *Metall. Mater. Trans. A*, vol. 42, no. 10, pp. 3190–3199, Oct. 2011, doi: 10.1007/s11661-011-0731-y.

[154] Z. Yu *et al.*, ‘Microstructure and Electrochemical Behavior of a 3D-Printed Ti-6Al-4V Alloy’, *Materials*, vol. 15, no. 13, p. 4473, Jun. 2022, doi: 10.3390/ma15134473.

[155] F. I. Jamhari *et al.*, ‘Influence of heat treatment parameters on microstructure and mechanical performance of titanium alloy in LPBF: A brief review’, *J. Mater. Res. Technol.*, vol. 24, pp. 4091–4110, May 2023, doi: 10.1016/j.jmrt.2023.04.090.

[156] B. Ahn, ‘Microstructural Tailoring and Enhancement in Compressive Properties of Additive Manufactured Ti-6Al-4V Alloy through Heat Treatment’, *Materials*, vol. 14, no. 19, 2021, doi: 10.3390/ma14195524.

[157] H. Bai *et al.*, ‘Effect of Heat Treatment on the Microstructure and Mechanical Properties of Selective Laser-Melted Ti64 and Ti-5Al-5Mo-5V-1Cr-1Fe’, *Metals*, vol. 11, no. 4, 2021, doi: 10.3390/met11040534.

[158] X.-Y. Wang, M. Li, and Z.-X. Wen, ‘The Effect of the Cooling Rates on the Microstructure and High-Temperature Mechanical Properties of a Nickel-Based Single Crystal Superalloy’, *Materials*, vol. 13, no. 19, 2020, doi: 10.3390/ma13194256.

[159] A. K. Saxena, M. Anupoju, A. Tewari, and P. Pant, ‘Effect of grain size on deformation twinning behavior of Ti6Al4V alloy’, in *Materials Science Forum*, Trans Tech Publications Ltd, 2015, pp. 337–340. doi: 10.4028/www.scientific.net/MSF.830-831.337.

[160] P. Panjan, M. Čekada, M. Panjan, and D. Kek-Merl, ‘Growth defects in PVD hard coatings’, *Vacuum*, vol. 84, no. 1, pp. 209–214, Aug. 2009, doi: 10.1016/j.vacuum.2009.05.018.

[161] M. Čekada, P. Panjan, A. Drnovšek, M. Panjan, and P. Gselman, ‘Growth Defects in PVD Hard Coatings’, in *Recent Advances in Thin Films*, S. Kumar and D. K. Aswal, Eds., Singapore: Springer Singapore, 2020, pp. 35–73. doi: 10.1007/978-981-15-6116-0_3.

[162] G. Ongtrakulkij, A. Khantachawana, and K. Kondoh, ‘Effects of media parameters on enhance ability of hardness and residual stress of Ti6Al4V by fine shot peening’, *Surf. Interfaces*, vol. 18, p. 100424, Mar. 2020, doi: 10.1016/j.surfin.2019.100424.

[163] Y. Sun and R. Bailey, ‘Improvement in tribocorrosion behavior of 304 stainless steel by surface mechanical attrition treatment’, *Surf. Coat. Technol.*, vol. 253, pp. 284–291, Aug. 2014, doi: 10.1016/j.surfcoat.2014.05.057.

[164] J. Tomastik and R. Ctvrtlik, ‘Nanoscratch test — A tool for evaluation of cohesive and adhesive properties of thin films and coatings’, *EPJ Web Conf.*, vol. 48, p. 00027, 2013, doi: 10.1051/epjconf/20134800027.

[165] G. Cassar, S. Banfield, J. C. Avelar-Batista Wilson, J. Housden, A. Matthews, and A. Leyland, ‘Tribological Properties of Duplex Plasma Oxidised, Nitrided and PVD Coated Ti-6Al4V’, *Surf. Coat. Technol.*, vol. 206, pp. 395–404, Oct. 2011, doi: 10.1016/j.surfcoat.2011.07.037.

[166] J. C. Avelar-Batista Wilson, S. Wu, I. Gotman, J. Housden, and E. Y. Gutmanas, ‘Duplex coatings with enhanced adhesion to Ti alloy substrate prepared by powder immersion nitriding and TiN/Ti multilayer deposition’, *Mater. Lett.*, vol. 157, pp. 45–49, Oct. 2015, doi: 10.1016/j.matlet.2015.05.054.

[167] L. Bonnici *et al.*, ‘Additively Manufactured 316L Stainless Steel Subjected to a Duplex Peening-PVD Coating Treatment’, *Materials*, vol. 16, no. 2, 2023, doi: 10.3390/ma16020663.

[168] H. Ruan *et al.*, ‘Designed Ti/TiN sub-layers suppressing the crack and erosion of TiAlN coatings’, *Surf. Coat. Technol.*, vol. 438, p. 128419, May 2022, doi: 10.1016/J.SURFCOAT.2022.128419.

[169] M. Wang *et al.*, ‘Fabrication and characterization of selective laser melting printed Ti–6Al–4V alloys subjected to heat treatment for customized implants design’, *Prog. Nat. Sci. Mater. Int.*, vol. 26, no. 6, pp. 671–677, Dec. 2016, doi: 10.1016/J.PNSC.2016.12.006.

[170] P. Harlin, P. Carlsson, U. Bexell, and M. Olsson, ‘Influence of surface roughness of PVD coatings on tribological performance in sliding contacts’, *Proc. 33rd Int. Conf. Metall. Coat. Thin Films*, vol. 201, no. 7, pp. 4253–4259, Dec. 2006, doi: 10.1016/j.surfcoat.2006.08.103.

[171] K. Bobzin, C. Kalscheuer, M. Carlet, D. C. Hoffmann, T. Bergs, and L. Uhlmann, ‘Low-Temperature Physical Vapor Deposition TiAlCrSiN Coated High-Speed Steel: Comparison Between Shot-Peened and Polished Substrate Condition’, *Adv. Eng. Mater.*, vol. 24, no. 9, p. 2200099, Sep. 2022, doi: 10.1002/adem.202200099.

[172] T. Hanabusa, K. Kusaka, T. Matsue, M. Nishida, O. Sakata, and T. Sato, ‘Evaluation of internal stresses in single-, double- and multi-layered TiN and TiAlN thin films by synchrotron radiation’, *JSME Int. J. Ser. Solid Mech. Mater. Eng.*, vol. 47, no. 3, pp. 312–317, 2004.

[173] O. Zimmer and F. Kaulfuß, ‘Hard coatings with elevated film thickness prepared by PVD’. 2008. [Online]. Available: https://publica.fraunhofer.de/handle/publica/360041

[174] T. DebRoy *et al.*, ‘Additive manufacturing of metallic components – Process, structure and properties’, *Prog. Mater. Sci.*, vol. 92, pp. 112–224, 2018, doi: https://doi.org/10.1016/j.pmatsci.2017.10.001.

[175] S. Cao, Y. H. Zou, C. V. S. Lim, and X. Wu, ‘Review of laser powder bed fusion (LPBF) fabricated Ti-6Al-4V: process, post-process treatment, microstructure, and property’, *Light Adv. Manuf.*, 2021.

[176] Y. Hu, M. Lai, Z. Hu, and Z. Yao, ‘Effect of multiple laser peening on surface integrity and microstructure of laser additive manufactured Ti6Al4V titanium alloy’, *Rapid Prototyp. J.*, vol. 25, no. 8, pp. 1379–1387, Sep. 2019, doi: 10.1108/RPJ-09-2018-0250.

[177] I. Yeo, S. Bae, A. Amanov, and S. Jeong, ‘Effect of Laser Shock Peening on Properties of Heat-Treated Ti–6Al–4V Manufactured by Laser Powder Bed Fusion’, *Int. J. Precis. Eng. Manuf.-Green Technol.*, vol. 8, no. 4, pp. 1137–1150, Jul. 2021, doi: 10.1007/s40684-020-00234-2.

[178] W. Chen, L. Xiao, Q. Sun, and J. Sun, ‘Effect of the initial grain size on grain refinement in Ti–2Al–2.5Zr alloy subjected to multi-impact process’, *Mater. Sci. Eng. A*, vol. 554, pp. 86–94, 2012, doi: https://doi.org/10.1016/j.msea.2012.06.019.

[179] K.-A. Lee, Y.-K. Kim, J.-H. Yu, S.-H. Park, and M.-C. Kim, ‘Effect of Heat Treatment on Microstructure and Impact Toughness of Ti-6Al-4V Manufactured by Selective Laser Melting Process’, *Arch. Metall. Mater.*, vol. 62, no. 2, pp. 1341–1346, Jun. 2017, doi: 10.1515/amm-2017-0205.

[180] H. K. Rafi, N. V. Karthik, H. Gong, T. L. Starr, and B. E. Stucker, ‘Microstructures and Mechanical Properties of Ti6Al4V Parts Fabricated by Selective Laser Melting and Electron Beam Melting’, *J. Mater. Eng. Perform.*, vol. 22, no. 12, pp. 3872–3883, Dec. 2013, doi: 10.1007/s11665-013-0658-0.

[181] X. Yan *et al.*, 'Effect of heat treatment on the phase transformation and mechanical properties of Ti6Al4V fabricated by selective laser melting', *J. Alloys Compd.*, vol. 764, pp. 1056–1071, Oct. 2018, doi: 10.1016/j.jallcom.2018.06.076.

[182] A. D. Prasetya, M. Rifai, Mujamilah, and H. Miyamoto, 'X-ray diffraction (XRD) profile analysis of pure ECAP-annealing Nickel samples', *J. Phys. Conf. Ser.*, vol. 1436, no. 1, p. 012113, Jan. 2020, doi: 10.1088/1742-6596/1436/1/012113.

[183] F. Kaschel *et al.*, 'Mechanism of Stress Relaxation and Phase Transformation in Additively Manufactured Ti-6Al-4V via in situ High Temperature XRD and TEM Analyses', *Acta Mater.*, vol. 188, Feb. 2020, doi: 10.1016/j.actamat.2020.02.056.

[184] D. Zhang *et al.*, 'Effect of heat treatment on the tensile behavior of selective laser melted Ti-6Al-4V by in situ X-ray characterization', *Acta Mater.*, vol. 189, Mar. 2020, doi: 10.1016/j.actamat.2020.03.003.

[185] M. Attard, 'Study of Shot-peened and PVD coated Aerospace-grade Titanium Alloy', University of Malta, 2019.

[186] B. D. Cullity, *Elements of X-ray Diffraction*. in Addison-Wesley metallurgy series. Addison-Wesley Publishing Company, 1956. [Online]. Available: https://books.google.com.mt/books?id=XJVCgGFTODMC

[187] A. Mikrajuddin and K. Khairurrijal, 'Derivation of Scherrer Relation Using an Approach in Basic Physics Course', *J. Nanosains Nanoteknologi*, vol. 1, Jan. 2008.

[188] E. Maawad, Y. Sano, L. Wagner, H.-G. Brokmeier, and C. Genzel, 'Investigation of laser shock peening effects on residual stress state and fatigue performance of titanium alloys', *Mater. Sci. Eng. A*, vol. 536, pp. 82–91, 2012, doi: https://doi.org/10.1016/j.msea.2011.12.072.

[189] C. J. Feng, X. Hu, Y. F. Jiang, and Q. Zhao, 'Effects of Cu Addition on Microstructure and Adhesion Properties of Ti-Al-N Nanocomposite Films Deposited by Magnetron Sputtering', *Adv. Mater. Res.*, vol. 652–654, pp. 1751–1754, Jan. 2013, doi: 10.4028/www.scientific.net/AMR.652-654.1751.

[190] S. Pugal Mani, M. Kalaiarasan, K. Ravichandran, N. Rajendran, and Y. Meng, 'Corrosion resistant and conductive TiN/TiAlN multilayer coating on 316L SS: a promising metallic bipolar plate for proton exchange membrane fuel cell', *J.*

Mater. Sci., vol. 56, no. 17, pp. 10575–10596, Jun. 2021, doi: 10.1007/s10853-020-05682-4.

[191] K. Carpenter and A. Tabei, 'On residual stress development, prevention, and compensation in metal additive manufacturing', *Materials*, vol. 13, no. 255, pp. 1–38, 2020.

[192] W. Yanfeng, L. Zhengxian, W. Haonan, D. Jihong, and Z. Changwei, 'Effect of Multilayered Structure on Properties of Ti/TiN Coating', *Rare Met. Mater. Eng.*, vol. 46, no. 5, pp. 1219–1224, May 2017, doi: 10.1016/S1875-5372(17)30140-6.

[193] T. Sprute, W. Tillmann, D. Grisales, U. Selvadurai, and G. Fischer, 'Influence of substrate pre-treatments on residual stresses and tribo-mechanical properties of TiAlN-based PVD coatings', *Surf. Coat. Technol.*, vol. 260, pp. 369–379, 2014, doi: https://doi.org/10.1016/j.surfcoat.2014.08.075.

[194] E. Vogli, W. Tillmann, U. Selvadurai-Lassl, G. Fischer, and J. Herper, 'Influence of Ti/TiAlN-multilayer designs on their residual stresses and mechanical properties', *Appl. Surf. Sci.*, vol. 257, no. 20, pp. 8550–8557, 2011, doi: https://doi.org/10.1016/j.apsusc.2011.05.013.

[195] A. Hattal *et al.*, 'Effect of hot isostatic pressing on microstructure and mechanical properties of Ti6Al4V-zirconia nanocomposites processed by laser-powder bed fusion', *Mater. Des.*, vol. 214, p. 110392, 2022, doi: https://doi.org/10.1016/j.matdes.2022.110392.

[196] H. Li *et al.*, 'Effect of heat treatment on microstructure evolution and mechanical properties of selective laser melted Ti–6Al–4V and TiB/Ti–6Al–4V composite: A comparative study', *Mater. Sci. Eng. A*, vol. 801, p. 140415, 2021, doi: https://doi.org/10.1016/j.msea.2020.140415.

[197] Y. Yıldıran Avcu, O. Yetik, M. Guney, E. Iakovakis, T. Sınmazçelik, and E. Avcu, 'Surface, Subsurface and Tribological Properties of Ti6Al4V Alloy Shot Peened under Different Parameters', *Materials*, vol. 13, no. 19, p. 4363, Sep. 2020, doi: 10.3390/ma13194363.

[198] Y. M. Wang, J. P. Cheng, H. P. Yang, C. H. Zhang, and B. X. Wang, 'Influence of Microstructure on Shot Peening Effects of Ti-6Al-4V Alloy', *Mater. Sci. Forum*, vol. 921, pp. 177–183, 2018, doi: 10.4028/www.scientific.net/MSF.921.177.

[199] G. Cassar *et al.*, ‘A study of the reciprocating-sliding wear performance of plasma surface treated titanium alloy’, *Wear*, vol. 269, pp. 60–70, May 2010, doi: 10.1016/j.wear.2010.03.008.

[200] C. T. Wang *et al.*, ‘An investigation into the effect of substrate on the load-bearing capacity of thin hard coatings’, *J. Mater. Sci.*, vol. 51, no. 9, pp. 4390–4398, May 2016, doi: 10.1007/s10853-016-9751-8.

[201] D. Moskovskikh *et al.*, ‘Extremely hard and tough high entropy nitride ceramics’, *Sci. Rep.*, vol. 10, no. 1, p. 19874, Nov. 2020, doi: 10.1038/s41598-020-76945-y.

[202] K.-D. Bouzakis *et al.*, ‘Ambient and elevated temperature properties of TiN, TiAlN and TiSiN PVD films and their impact on the cutting performance of coated carbide tools’, *ICMCTF 2009*, vol. 204, no. 6, pp. 1061–1065, Dec. 2009, doi: 10.1016/j.surfcoat.2009.07.001.

[203] J. M. Lackner, L. Major, and M. Kot, ‘Microscale interpretation of tribological phenomena in Ti/TiN soft-hard multilayer coatings on soft austenite steel substrates’, *Bull. Pol. Acad. Sci. Tech. Sci.*, vol. 59, Sep. 2011, doi: 10.2478/v10175-011-0042-x.

[204] Q. Yang *et al.*, ‘Effect of different surface asperities and surface hardness induced by shot-peening on the fretting wear behavior of Ti-6Al-4V’, *Surf. Coat. Technol.*, vol. 349, pp. 1098–1106, Sep. 2018, doi: 10.1016/J.SURFCOAT.2018.06.092.

[205] P. Tao, H. Li, B. Huang, Q. Hu, S. Gong, and Q. Xu, ‘Tensile behavior of Ti-6Al-4V alloy fabricated by selective laser melting: effects of microstructures and as-built surface quality’, *China Foundry*, vol. 15, no. 4, pp. 243–252, Jul. 2018, doi: 10.1007/s41230-018-8064-8.

[206] J. He *et al.*, ‘The Martensitic Transformation and Mechanical Properties of Ti6Al4V Prepared via Selective Laser Melting’, *Materials*, vol. 12, no. 2, p. 321, Jan. 2019, doi: 10.3390/ma12020321.

[207] A. du Plessis, I. Yadroitsava, and I. Yadroitsev, ‘Effects of defects on mechanical properties in metal additive manufacturing: A review focusing on X-ray tomography insights’, *Mater. Des.*, vol. 187, p. 108385, 2020, doi: https://doi.org/10.1016/j.matdes.2019.108385.

[208] E. Yasa, J. Deckers, J.-P. Kruth, M. Rombouts, and J. Luyten, ‘Charpy impact testing of metallic selective laser melting parts’, *Virtual Phys. Prototyp.*, vol. 5, no. 2, pp. 89–98, Jun. 2010, doi: 10.1080/17452751003703894.

[209] D. G. Hernández, ‘Mechanical behaviour assessment of the Ti6Al4V alloy obtained by additive manufacturing towards aeronautical industry’, p. 10.

[210] A. M. Muiruri, M. Maringa, W. du Preez, and L. Masu, ‘VARIATION OF IMPACT TOUGHNESS OF AS-BUILT DMLS TI6AL4V (ELI) SPECIMENS WITH TEMPERATURE’, *South Afr. J. Ind. Eng.*, vol. 29, no. 3, Nov. 2018, doi: 10.7166/29-3-2076.

[211] I. Hacısalihoğlu, F. Yıldiz, and A. Çelik, ‘The effects of build orientation and hatch spacing on mechanical properties of medical Ti–6Al–4V alloy manufactured by selective laser melting’, *Mater. Sci. Eng. A*, vol. 802, p. 140649, Jan. 2021, doi: 10.1016/j.msea.2020.140649.

[212] M. Kazachenok, A. Panin, S. Panin, and I. Vlasov, ‘Impact toughness of Ti–6Al–4V parts fabricated by additive manufacturing’, presented at the PROCEEDINGS OF THE INTERNATIONAL CONFERENCE ON ADVANCED MATERIALS WITH HIERARCHICAL STRUCTURE FOR NEW TECHNOLOGIES AND RELIABLE STRUCTURES 2019, Tomsk, Russia, 2019, p. 020153. doi: 10.1063/1.5132020.

[213] M.-W. Wu, P.-H. Lai, and J.-K. Chen, ‘Anisotropy in the impact toughness of selective laser melted Ti–6Al–4V alloy’, *Mater. Sci. Eng. A*, vol. 650, pp. 295–299, Jan. 2016, doi: 10.1016/j.msea.2015.10.045.

[214] V. Chastand, A. Tezenas, Y. Cadoret, P. Quaegebeur, W. Maia, and E. Charkaluk, ‘Fatigue characterization of Titanium Ti-6Al-4V samples produced by Additive Manufacturing’, *Procedia Struct. Integr.*, vol. 2, pp. 3168–3176, 2016, doi: 10.1016/j.prostr.2016.06.395.

[215] N. Dai, J. Zhang, Y. Chen, and L.-C. Zhang, ‘Heat Treatment Degrading the Corrosion Resistance of Selective Laser Melted Ti-6Al-4V Alloy’, *J. Electrochem. Soc.*, vol. 164, no. 7, pp. C428–C434, 2017, doi: 10.1149/2.1481707jes.

[216] P. Renner, S. Jha, Y. Chen, A. Raut, S. G. Mehta, and H. Liang, ‘A Review on Corrosion and Wear of Additively Manufactured Alloys’, *J. Tribol.*, vol. 143, no. 5, p. 050802, May 2021, doi: 10.1115/1.4050503.

[217] K. D. Ralston and N. Birbilis, ‘Effect of Grain Size on Corrosion: A Review’, *CORROSION*, vol. 66, no. 7, pp. 075005-075005–13, Jul. 2010, doi: 10.5006/1.3462912.

[218] S. Bagherifard *et al.*, ‘Effects of nanofeatures induced by severe shot peening (SSP) on mechanical, corrosion and cytocompatibility properties of magnesium alloy AZ31’, *Acta Biomater.*, vol. 66, pp. 93–108, 2018, doi: https://doi.org/10.1016/j.actbio.2017.11.032.

[219] Y. Wang, E. Hao, X. Zhao, Y. Xue, Y. An, and H. Zhou, ‘Effect of microstructure evolution of Ti6Al4V alloy on its cavitation erosion and corrosion resistance in artificial seawater’, *J. Mater. Sci. Technol.*, vol. 100, pp. 169–181, Feb. 2022, doi: 10.1016/j.jmst.2021.06.005.

[220] C. Si, W. Sun, Y. Tian, and J. Cai, ‘Cavitation erosion resistance enhancement of the surface modified 2024T351 Al alloy by ultrasonic shot peening’, *Surf. Coat. Technol.*, vol. 452, p. 129122, Jan. 2023, doi: 10.1016/j.surfcoat.2022.129122.

[221] D. Ma, T. J. Harvey, Y. N. Zhuk, R. G. Wellman, and R. J. K. Wood, ‘Cavitation erosion performance of CVD W/WC coatings’, *Wear*, vol. 452–453, p. 203276, Jul. 2020, doi: 10.1016/j.wear.2020.203276.

[222] J. Xu, S. K. Zhang, X. L. Lu, S. Jiang, P. Munroe, and Z.-H. Xie, ‘Effect of Al alloying on cavitation erosion behavior of TaSi2 nanocrystalline coatings’, *Ultrason. Sonochem.*, vol. 59, p. 104742, Dec. 2019, doi: 10.1016/j.ultsonch.2019.104742.

[223] F. Pougoum, A. Jedrzejczak, M. Azzi, L. Martinu, and J. E. Klemberg-Sapieha, ‘Effect of interface roughness on the tribo-corrosion behavior of diamond like carbon coatings on titanium alloy’, *J. Vac. Sci. Technol. A*, vol. 40, no. 3, p. 033405, May 2022, doi: 10.1116/6.0001657.

[224] F. Toptan *et al.*, ‘Corrosion and tribocorrosion behaviour of Ti6Al4V produced by selective laser melting and hot pressing in comparison with the commercial alloy’, *J. Mater. Process. Technol.*, vol. 266, pp. 239–245, Apr. 2019, doi: 10.1016/j.jmatprotec.2018.11.008.

[225] D. Landolt, ‘Electrochemical and materials aspects of tribocorrosion systems’, *J. Phys. Appl. Phys.*, vol. 39, no. 15, pp. 3121–3127, Aug. 2006, doi: 10.1088/0022-3727/39/15/S01.

[226] R. Chetcuti, P. A. Dearnley, A. Mazzonello, J. Buhagiar, and B. Mallia, ‘Tribocorrosion response of duplex layered CoCrMoC/CrN and CrN/CoCrMoC coatings on implant grade 316LVM stainless steel’, *Surf. Coat. Technol.*, vol. 384, p. 125313, Feb. 2020, doi: 10.1016/j.surfcoat.2019.125313.

[227] S. A. Naghibi, K. Raeissi, and M. H. Fathi, ‘Corrosion and tribocorrosion behavior of Ti/TiN PVD coating on 316L stainless steel substrate in Ringer’s solution’, *Mater. Chem. Phys.*, vol. 148, no. 3, pp. 614–623, 2014, doi: 10.1016/j.matchemphys.2014.08.025.

[228] W. Aperador, E. Ruiz, and A. Delgado, ‘Diagnostic of the Erosion Corrosion Evolution by Cavitation of [TiN-TiAlN]200 Thin Coatings’, *Int. J. Electrochem. Sci.*, vol. 9, no. 7, pp. 3876–3884, Jul. 2014, doi: 10.1016/S1452-3981(23)08058-6.

[229] C. Wang *et al.*, ‘Erosion-corrosion behaviour of shot peening treated nickel-aluminium bronze in simulated sand-containing seawater’, *Corros. Sci.*, vol. 211, p. 110908, Feb. 2023, doi: 10.1016/j.corsci.2022.110908.

[230] Z. Qin *et al.*, ‘Effect of compressive stress on cavitation erosion-corrosion behavior of nickel-aluminum bronze alloy’, *Ultrason. Sonochem.*, vol. 89, p. 106143, Sep. 2022, doi: 10.1016/j.ultsonch.2022.106143.

[231] M. J. Runa, M. T. Mathew, and L. A. Rocha, ‘Tribocorrosion response of the Ti6Al4V alloys commonly used in femoral stems’, *3rd Int. Conf. Tribocorrosion – Atlanta 2012*, vol. 68, pp. 85–93, Dec. 2013, doi: 10.1016/j.triboint.2013.09.022.

[232] M. T. Mathew, M. J. Runa, M. Laurent, J. J. Jacobs, L. A. Rocha, and M. A. Wimmer, ‘Tribocorrosion behavior of CoCrMo alloy for hip prosthesis as a function of loads: A comparison between two testing systems’, *Wear*, vol. 271, no. 9–10, pp. 1210–1219, Jul. 2011, doi: 10.1016/j.wear.2011.01.086.